The Spatial Distribution of Post-blast Condensed Phase Explosive Residues

Nadia Abdul-Karim

Submitted in partial fulfilment of the requirements for the degree of Doctor of Philosophy at University College London

2015

Declaration

I, Nadia Abdul-Karim, confirm that the work presented in this thesis is my own. Where information has been derived from other sources, I confirm that this has been indicated in the thesis.

2015.

Abstract

During bomb scene investigation the collection of trace explosive residue is a principal forensic task which allows the cause of the explosion to be determined. However the optimum locations around a detonation from *where* these undetonated trace residues should be sampled has not been determined scientifically. Crime scene investigation guides describe several methods for collecting and analysing explosive residues, but literature regarding the most efficacious areas to sample from is relatively scarce. In this thesis, analysis of the spatial distribution patterns of post-blast explosive residues from detonation and simulation experiments with 0.5 kg, 1 kg and 2 kg aluminised ammonium nitrate and RDX composition charges are the primary original contributions to the literature.

Residue samples were collected by swabbing sample sites positioned around the explosive charges and condensed phase particles were collected onto smaller sample sites in order to ascertain the physical morphology of the residues. Both organic and inorganic residues ultimately decreased in concentration nonlinearly with increasing distance from the charge centre. However, the distribution trends between different explosive analytes varied, suggesting the dispersal mechanisms or factors which affected the distribution for each were different. The post-blast particles had varying morphologies at different distances from the detonation and also exhibited different features based on the explosive type. Computational simulations of residue distributions compared well to the experimental results; substantiating the capability of numerical methods to be used as a forensic investigation aid.

The key findings from this thesis have provided empirical evidence which validates the current forensic practice of concentrating trace evidence collection near the central region of a detonation area during bomb scene investigation. The findings also imply that surfaces which are downwind of the detonation should be focused on for residue sampling and that microscopic examination of items in the vicinity of a detonation may allow identification of the explosive used based on particle morphology, prior to any chemical analyses. Furthermore, having demonstrated the reliability and capability of simulation techniques to model explosive residue distribution, these can now be developed and validated through further tests which also assess the detonations of further explosives under different conditions.

Table of contents

List of Figures

List of Tables

Acknowledgements

First and foremost I thank my supervisor Dr Chris Blackman for his support, guidance and advice during my PhD. From him I have learnt, and am still learning, a great deal. Thank you for your patience and allowing me to develop my research ideas, it has been a pleasure to work with you. I also thank my second supervisor Dr Ruth Morgan for useful discussions regarding forensic science. I thank you both for always being there and encouraging me during challenging times. I would also like to thank Dr Phil Gill at Cranfield University for advice during experiments and explosive related discussions.

Special thanks to collaborators who have helped in various ways in the past three years, without you this research would not have been possible and certainly would not have been so much fun! I'm very grateful to all the staff who have helped with detonations at the Cranfield, Porton Down and Kineton firing ranges. I also appreciate the interest and advice with research designs from staff at the Forensic Explosives Laboratory at DSTL. I thank the UK Metropolitan Police and the US Federal Bureau of Investigation for allowing me to attend and take part in post-blast investigation courses. I'm much obliged to Lidija Matjacic at the Surrey Ion Beam Centre for collecting SIMS measurements and huge thanks to Professor Bjorn Anders Reif, Dr Magnus Vartdal and Hannibal Fossum from the Norwegian Defence Research Establishment for collaborating on simulation studies and making me feel so welcome in Norway.

For assistance with technical aspects of the research I thank: Dr Kersti Karu for helping me fix the mass spectrometer (so many times!) and for help with mass spectrometry measurements; Kevin Reeves for your dry sense of humour and excellent taste in music which made SEM analysis in a cold basement an enjoyable experience; Anjum Agha and Nathalie Mai for assistance with chromatographic analyses; Steve Firth for chats during Raman analysis; Jim for cutting many metal plates in the workshop; and Jo Cleaves from Vision Research for helping with high-speed imaging calculations.

Thank you to Francesco, Carlos, Ana, Chiaki, John and all other friends in the Chemistry and Security Science departments; your friendship and jokes have made the past 3 years so enjoyable. Special thanks to Amy who has always been there for me – you are my rock. And last but by no means least I thank my family; my brother Juneid, my sister Sophie and my parents, Fatma and Iqbal. Your love, support and encouragement throughout my whole academic career has spurred me on. I dedicate this thesis to you. Asante sana!!!

Presentations and Publications

Aspects of this thesis have been presented and published in the following:

Abdul-Karim, N., Blackman, C., Gill, P., Wingstedt, E. & Reif, B. A. P. (2014) "Post-Blast Explosive Residue – A Review of Formation and Dispersion Theories and Experimental Research", *Royal Society of Chemistry Advances*, Accepted Manuscript, October 2014.

Abdul-Karim, N., Blackman, C. & Morgan, R. (2014) Keynote Presentation: "Post-blast Aftermath: Forensic, Chemical and Physical Aspects of Explosion – the Particles and the Patterns", *ANZFSS International Conference,* Adelaide, Australia.

Abdul-Karim, N. & Blackman, C. (2014) "Incomplete Reactions during Detonation: Survival of Particulate Material from Condensed Phase Charges", *The Institute of Physics: Pressure, Energy, Temperature and Extreme Rates Conference*, London, UK.

Matjacic, L., **Abdul Karim, N**., Jones, B., Palitsin, V., Demarche, J. & Webb, R. (2014) "Chemical Characterisation of Explosive Residues by Ambient Pressure MeV-SIMS", *CAARI*, Texas, USA.

Abdul-Karim, N. & Blackman, C. (2013) Invited Talk: "Condensed Phase Particulate Residues from Small-Scale Detonations of PETN and RDX-based Detonators", *Forensic Explosives Laboratory*, DSTL, UK.

Abdul-Karim, N., Blackman, C. & Morgan, R. (2012) "CSI Explosives: Finding Hidden Clues", *ANZFSS Conference*, Hobart, Tasmania. (Best Oral Presentation Award Winner).

Manuscripts in preparation

Abdul-Karim, N., Blackman, C. & Morgan, R. "The Spatial Distribution of Post-blast Explosive Residues: Studies with Unconfined and Confined Organic and Inorganic Explosive Charges".

Abdul-Karim, N., Blackman, C. & Morgan, R. "Morphological and Chemical Characteristics of Condensed Phase Post–blast Explosive Residue Particles from Detonations of RDX Compositions and Aluminised Ammonium Nitrate Charges".

Abdul-Karim, N., Blackman, C., Reif, B. A. P., Fossum, H. & Vartdal, M., "Application of Computational Fluid Dynamics to the Simulation of Bomb Residue Deposition".

Thesis outline

This thesis contains 7 chapters:

Chapter 1: Introduction. The premise for the research is provided in the introduction as well as fundamental background information on explosives, and the chemical and physical aspects of explosion phenomenon pertinent to the research are detailed.

Chapter 2: Literature Review. Literature regarding explosive residue formation mechanisms and theoretical and experimental work conducted is reviewed. Forensic practices at post-blast crime scenes are outlined, as well as analytical techniques used in this thesis with reference to their forensic application. A summary of the research field and the research required to develop it further, including the aims and objectives of this thesis, is presented.

Chapter 3: Materials and Methods. Details of the explosive charges used in the project and the experimental designs for detonation and sampling procedures for swabbing of post-blast residues and collection of particulate material are explained. The analytical methods used for both inorganic and organic analysis methods are detailed. The method for the simulation experiments is provided.

Chapter 4: Experiments with Unconfined Charges. Results of residue concentrations and distribution patterns from repeated firings of 0.5 kg AlAN and PE4 charges are presented here. The residue results are compared against potential factors which could affect distribution such as the blast overpressure, the fireball and the weather conditions. The results from each explosive material are compared and discussed against each factor.

Chapter 5: Complementary Experiments. Results from experiments conducted with unconfined larger charge masses (1 kg, 2 kg) of AlAN and PE7 are presented here alongside experiments with results from charges confined in vehicles. The results are discussed in relation to factors which may affect residue distribution.

Chapter 6: Particle Characterisation and Simulation Experiments. Results of the morphology and composition of condensed phase particles found around the detonation centre are presented. Particle distribution plots from numerical simulation experiments are compared to experimental data and discussed.

Chapter 7: Summary and Conclusions. The results and discussion generated are summarised; the limitations of the research are discussed and avenues for future research in this area are outlined. The conclusions from this thesis are presented in this chapter.

CHAPTER 1: INTRODUCTION

One of the main priorities at a post-blast bomb scene is to establish the cause of the incident as soon as possible and a principle method of doing so is via the collection and analysis of explosive residues. The term 'explosive residue' here refers to the *undetonated* microscopic particles[1] which remain following an explosion as opposed to the partially reacted or decomposition products of the original explosive material. In forensic contexts the products formed from an explosive are usually vapours and salts of limited diagnostic value[2,3] and therefore it is the undetonated material which provides invaluable chemical signatures at post-blast bomb scenes.

Trace explosive residues have high evidentiary value as they can denote the chemical composition of the explosive material and thereby indicate whether it was commercially available or home-made, domestic or foreign material, or associated with a particular terrorist or criminal organisation[4]. The importance of locating explosive residue is reflected in current forensic texts and guidelines, with some stating it is the most important task[5] as these explosive particles are one of the first things to be analysed in the laboratory[6], and even noting that the "key to success lies primarily with the collection of residues at the scene of an explosion" (pg. 108)[1]. It is also becoming increasingly important to identify this residual material *in situ*, from samples taken from fixed areas at the scene rather than that adhered to transportable objects, in order to proffer evidence in court that the material was found at the scene and not placed there after the event[7].

Experience has led to the practice of focusing the collection of explosive residues from items based on their proximity to the explosion centre, but no rigid rules are in place[2,8]. Surfaces or objects sometimes display visual signs of having been close to the explosion, such as cratering or pitting damage, and these may yield residue. If no visible signs of damage are present however this does not negate the possibility of recovering residue from a particular item as explosions can leave invisible traces of explosive residue[9,10]. The issue therefore is to know where to look for it. Whilst residue sample collection and analysis procedures have been widely researched in the open literature, a scientific basis for *where* to locate explosive residues has not yet been established. The focus of this research was to provide an experimentally verified rationale of where to sample for explosive residue. In order to understand residue dispersal during detonation, firstly the background information on explosives and explosions is provided, with a focus on RDX and ammonium nitrate (explosives to be used in the thesis).

1.1 Background Information

1.1.1 Explosives

An explosive material contains sufficient potential energy which can cause an explosion when released rapidly. The potential energy can be chemical (chemical explosives), physical (pressurised gases) or nuclear (fissile materials). Chemical explosives require a fuel and oxidising component, either within the molecular structure of the compound or provided by two or more components mixed together, and are usually solids or liquids in a metastable state which are capable of undergoing a rapid exothermic reaction yielding heat and gas upon the application of heat or shock[11–13].

Several criteria can be used to classify chemical explosives. For instance, by reference to their rate of reaction, 'low' explosives burn rapidly (deflagrate) at subsonic reaction speeds (40 m/s to 1500 m/s) and require confinement to do useful work during explosion whilst 'high' explosives can undergo almost instantaneous reactions at supersonic rates (1500 m/s to 9000 m/s) when unconfined[11,12]. Explosives can also be categorised into primary, secondary and tertiary explosives: primary explosives (e.g. lead azide and mercury fulminate) are extremely sensitive to heat, shock and friction stimuli and small amounts of them are used as the explosive components of detonators; secondary explosives (e.g. SEMTEX, dynamites) are relatively insensitive to external stimuli and detonate with the aid of primary explosives in detonators; and tertiary explosives (e.g. ammonium nitrate fuel oil) are very insensitive and require an explosive booster comprised of a secondary explosive (such as a pentaerythritol-tetranitrate booster charge) which in turn is initiated by a primary explosive detonator in order to undergo detonation[14].

Chemical explosives can also be classified by their usage into military, commercial or home-made explosives. Military explosives are required to have an appropriate sensitivity and stability (so they can be handled safely), power (so they can do the work required), and availability and cost (so they are accessible when required)[12]. High, secondary explosives such as RDX (1,3,5-Trinitroperhydro-1,3,5-triazine) (figure 1.1) are embedded into polymer matrices to produce polymer-bonded explosives (PBX) and are combined with plasticisers to produce malleable plastic explosive compositions suitable for handling[11]. RDX based explosive charges have been used as military compositions since World War 2[15], and whilst primarily for military use, have also been used in terrorist attacks including during the 2006 Mumbai train bombings, the 2008 Jaipur bombings and the 2011 Moscow bombings.

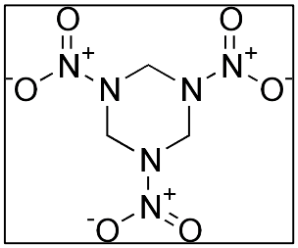

Figure 1.1*: RDX molecule (1,3,5-Trinitroperhydro-1,3,5-triazine: $C_3H_6N_6O_6$). Both the oxidising (NO_2) and fuel components (hydrocarbon fragments) are within the molecular structure of this nitramine explosive.*

Commercial explosives, such as ammonium nitrate fuel oil (ANFO), are used for blasting purposes in the mining industries and are usually insensitive, requiring booster charges and detonators to initiate them (thus detonated by a shockwave)[14]. They have a weaker shattering effect (brisance) compared to the military explosives as their reactions propagate slower[11], hence their suitability for doing rock heaving work. Ammonium nitrate (AN) (figure 1.2) has also been widely used in terrorist attacks, particularly by the Irish Republican Army and more recently in al-Qaeda inspired attacks, due to its relative ease of purchase as fertiliser and low cost[16].

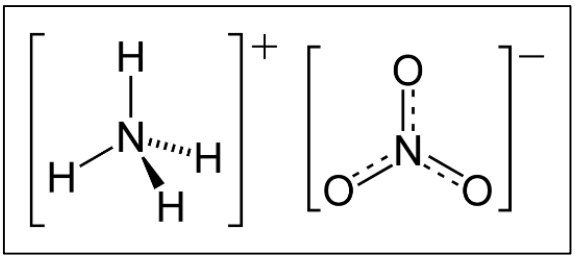

Figure 1.2*: The ammonium nitrate (NH_4NO_3) molecule is the oxidising component of the explosive charge and with the addition of a fuel and initiation by detonator will undergo explosion.*

Improvised explosive devices (IEDs) can contain explosive components which are military, commercial or home-made. Home-made explosives (HMEs) have no military or commercial purpose. Recently peroxide based materials have been used in terrorist incidents including during the 2005 London bombings, however less sensitive compositions such as fertilizer and fuel mixtures, e.g. ammonium nitrate/metal mixtures, have also been used as they are safer (less sensitive) to handle than peroxide mixtures[16].

1.1.2 Chemical Aspects of Explosion

Chemical explosions are a result of rapid chemical reactions driven by large exothermic and positive entropy changes in going from reactants to products[11]. Energy input to a chemical explosive by an external stimulus (friction, heat, shock, etc.) can initiate ignition by causing the temperature of the explosive to rise as the stimulus energy is converted to heat, producing localised regions of heat called hotspots[17]. Mechanisms for hotspot formation include adiabatic compression of small entrapped bubbles of gas in the explosive, friction caused between sliding surfaces such as grit particles or explosive crystals, or cavity collapse of the surrounding matrix material[11,17,18]. If there is sufficient energy increase in the hotspots, heat will be transmitted and reactions will develop[18].

During the decomposition of the reactants the atoms of the explosive molecules separate; the exact specifics of the chemical reactions occurring during detonation of condensed phase explosives are unknown due to the extreme pressures (20 GPa to 40 GPa) and temperatures (3000 K to 5000 K) generated during their decomposition[19,20]. Ongoing experimental work using spectroscopic techniques employing picosecond time resolution aims to understand detonation chemistry in more detail[21–23], although elementary theoretical constructs are recognised for some materials.

1.1.2.1 RDX (1,3,5–Trinitroperhydro–1,3,5–triazine)

The decomposition mechanism for the RDX molecule depends on the physical state of the material (gas or solid phase) and the temperature[24,25]. In the solid state, the most supported mechanism for the initial unimolecular step is that decomposition of RDX begins with the loss of a single NO_2 molecule[25] via homolytic cleavage of an N–NO_2 bond[26,27], which is followed by the rupture of the chain into intermediate products.

The final gaseous products formed through these decompositions are energetically stable and form strongly bonded species such as carbon monoxide, carbon dioxide and di-nitrogen gas[28]. The products formed depend on the quantity of oxidising atoms present in the original molecule[11,13] and therefore the oxygen balance (OB) of the explosive. Oxygen deficient, or fuel rich, explosives such as RDX (OB = –21.6 %) will not combust fully; there is not enough oxygen within the molecule for the fuel to be fully oxidised and the primary reactions progress too quickly for atmospheric oxygen to be used for full combustion[29], hence the resulting carbon monoxide (equation 1.1).

$$C_3H_6N_6O_6 \rightarrow 3CO + 3H_2O + 3N_2 \quad (1.1)$$

Some of the energy produced during the detonation is released as heat and light; the fireball consists of the hot incandescent gases, typically fuel-rich for oxygen negative explosives such as RDX which results in afterburning of the detonation by-products with atmospheric oxygen facilitated by turbulent mixing within the fireball[30]. Upon decay of the fireball, the subsequent smoke plume produced will also likely contain carbon residues and therefore exhibit a black/grey colour.

1.1.2.2 Ammonium Nitrate (AN)

The decomposition of AN has been studied broadly[31,32] and whilst thermal decomposition mechanisms have been theorised, a clear understanding of the detonation decomposition mechanism is unknown. Studies investigating the effect of the shock stimulus on ammonium nitrate decomposition have indicated the break-up of the NH_4^+ ion occurs initially, possibly followed by decomposition of the NO_3^- ion[33]. Ultimately, the gaseous products formed through these decompositions are energetically stable species such as di-nitrogen gas, oxygen and water[11]. Oxygen positive, or fuel lean, explosives such as AN (OB = +20 %) combust fully[29] as seen in reaction 1.2.

$$NH_4NO_3 \rightarrow N_2 + 2H_2O + 1/2O_2 \quad (1.2)$$

AN has a lower decomposition rate compared to the unimolecular explosive RDX[29,34]. The addition of high energy combustible light metals (e.g. aluminium) to non-ideal bimolecular explosives such as AN improves their energetic efficiency by increasing the reaction velocity and temperature[11]. In the case of aluminised ammonium nitrate (AlAN), the high temperature AN decomposition products heat the aluminium particles which evaporate upon reaching their ignition temperature and subsequently react in the gaseous phase; either aerobically with oxygen in shock compressed air or anaerobically with oxidants in the detonation products[35,36]. Reactions occur behind the principle reaction front during the expansion of the gases[37–40], with the main combustion product being aluminium oxide[38]. The burning of aluminium releases energy which further enhances the blast effects by increasing the overpressure impulse produced[11,39], and the energy release therefore occurs over a longer time period due to the afterburning of the aluminium. Upon decay of the fireball the smoke plumes are a light grey/white colour, indicating an oxygen positive explosive composition.

1.1.3 Physical Aspects of Explosion

The above reactions propagate supersonically and so the explosions are termed detonations; they are 'low-order' detonations if the reaction rate is below the maximum detonation velocity possible for the explosive and 'high-order' detonations if the rate is at the explosives highest possible detonation velocity[11]. The decomposition of the explosive during detonation occurs due to a shockwave; the pressures generated within the primary reaction zone increase the speed of the reaction, thus increasing the pressure in the reacting material which in turn produces the shockwave[11,12,28]. The shockwave has regions of compression and rarefaction, and is led by a shock front progressing at a constant velocity into the unreacted material and is sustained by the decomposition of the explosive material behind it[28,41–43].

The velocity of detonation (VOD) is the speed at which the shock front travels through the explosive and is affected by the type of explosive material; the VOD of RDX is ~8440 m/s, higher than that of AN, which is ~5000 m/s[2,11]. Generally, as the density of the material increases so does the VOD, particularly for homogenous explosives, and the material has to be at or above a critical diameter (characteristic of each explosive) for the wave front to be sustained and move through the explosive charge[11,41,43,44].

On reaching the periphery of the explosive the shockwave passes into the surrounding medium and exerts a sudden and intense pressure upon it, forming craters on the ground, bubbles in water, and blast waves in air[28,44]. The brisance, or shattering effect, of the explosive is determined by this detonation overpressure produced. The velocity of the initial blast wave in air is high, but the shock decays with distance to the speed of sound in air and the blast wave undergoes systematic changes in amplitude, duration and profile. After a rapid rise in pressure followed by decay, there is a negative duration where the pressure is below atmospheric level due to the inertial effect caused by the initial outward movement of air[28,44]. Air then rushes back in to this 'void' and the pressure returns to ambient level[44]. A typical pressure-time history profile (the Friedlander waveform[28,45]) is shown in figure 1.3.

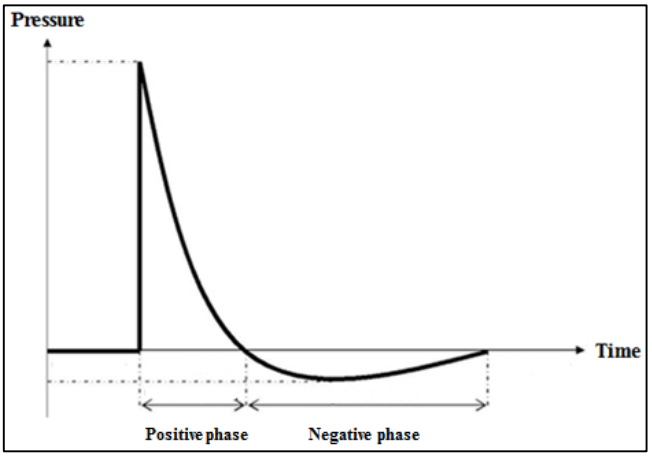

***Figure 1.3**: Friedlander waveform profile for blast-wave showing the initial positive overpressure impulse followed by the negative pressure phase of longer duration.*

As the principle shockwave moves through the explosive, a rarefaction wave propagates inward simultaneously[35,46]. The movement of the rarefaction wave back into the centre causes an over-expansion of the gas flow, causing a weaker secondary shock to form which is pushed out and strengthened by the detonation gases[28,46]. The outward propagation of the secondary shock generates instabilities in the gas flow due to misaligned pressure and density gradients[35,47]. The growth of these instabilities at the surface between the fireball and shocked air is caused by multi-dimensional perturbations[35,48–50].

1.1.3.1 Fireball Morphology

Instabilities grow with time[51] and occur if the explosive charge has a rough surface, but also occur on the molecular scale for explosive charges which are smooth; producing turbulent mixing layers between detonation products and the shock-compressed air. Instabilities also occur in the particle cloud during explosive detonations which contain metal particles[47,52]. The growth of the perturbations enhances the mixing with the surrounding air and the afterburning of the combustion products[47,52] (oxidation of aluminium in the case of aluminised charges). Metal particles can also form filamentary jets which protrude outward from the product gases and subsequently ignite; resulting in fireballs with 'spiky' appearances due to the remnants of particle jets[47]. Additionally, if the buoyant gases rise, further instabilities are produced and air is drawn up into the plume centre, whilst at the edge of the fireball a vortex ring is formed as turbulent vortices curl downwards and draw further air up into the centre[53]. Therefore spherical charges do not always produce spherical fireballs. As the temperature in the fireball decreases, the remaining mass of airborne particulates then forms the smoke plume which contains both solid and gaseous

particles including the decomposition products of the reaction and the surrounding entrained air[11]. The size of the smoke plume initially depends on the volume of product gases formed, with the movement of the smoke plume determined by the wind field.

1.1.3.2 Confinement

Confinement of the explosive charge in an encasement (e.g. a pipe) or confinement of a bomb in an enclosed area (e.g. a room within a building) can increase the pressures produced during detonation, compared to those produced during open-air or free-field detonations[28]. At higher levels of confinement the final pressure and temperature during the explosion can be higher, resulting in more vaporization, better mixing of reaction products, and stronger dispersion of products in the surrounding atmosphere[54]. The strength of the holding confinement affects these pressures – stronger confinement (e.g. in dense metals) can cause higher pressures to be produced[28,41].

Given the chemical and physical aspects of detonation outlined above it would seem counter-intuitive to expect unreacted particles of the original explosive to survive during such high pressure, high temperature reactions and yet this is often the case for both RDX and ammonium nitrate based compositions[44,55,56]. The review in the following chapter outlines potential mechanisms as to how this may occur and discusses the literature regarding the subsequent distribution of undetonated residues, from which the aims and objectives of this thesis are drawn.

CHAPTER 2: LITERATURE REVIEW

2.1 Introduction

The literature review starts with the initial formation of undetonated residues, highlighting the potential factors which may affect their formation during high-order detonations. This is followed by a discussion of the theoretical constructs which govern their subsequent dispersal and a synthesis and critique of the experimental work conducted to date in this field. Subsequently, the post-blast crime scene procedures informed by the literature are detailed; including information regarding the analytical techniques used in forensic practice which will be used in this research. Finally, a summary of the literature review precedes the aim and objectives of this thesis.

2.2 Explosive Residue Formation

The most recognisable undetonated explosive material at a post-blast scene is that which remains following a partial or 'low-order' detonation, which could be caused by a failure in the booster or detonator or some inhomogeneity in the main charge[57]. Low-order detonations leave undetonated residues in the form of large deposits that are easier to identify. Nevertheless, even when a complete or high-order detonation has occurred, undetonated explosive residues are still found[3].

No experimental results have been published in the open literature which assess the mechanism(s) by which undetonated explosive residues can remain from high-order detonations, however some theoretical concepts are described. It has been posited that the width of the reaction zone in a detonating explosive charge affords an explanation as to how this may occur[57]. Thinner reaction zones move quickly through the unreacted material, releasing chemical energy at a faster rate than that needed to sustain the shockwave[58] and therefore result in a greater consumption or decomposition of the explosive molecules[57]. Wider reaction zones are less likely to release chemical energy at a rate needed to exceed that which can sustain the wave[59] and therefore move through unreacted material slower and would not decompose material as efficiently. If undetonated molecules do persist because of reaction zone sizes, even infinitesimally thin reaction zones would produce undetonated molecules. Based on this theory, the factor affecting the amount of undetonated material generated would be the velocity of detonation (VOD) of an explosive charge.

Another potential mechanism for the formation of undetonated residues is based on the reflection of the shockwave at the boundary of the charge. It has been suggested that as the shock front passes from the periphery of the explosive into the surrounding medium the shock wave can be partially reflected at this discontinuity[43] and the surface layers of the charge may not react completely – particles may 'survive' here and remain unreacted[57]. The exact details of how a shockwave reflection at the surface interface could limit the decomposition of explosive molecules are not fully explained, nonetheless, this would suggest the amount of undetonated material remaining following a detonation would vary depending on factors including the charge mass, charge diameter and the number of interfaces within the charge[57].

2.2.1 Factors Affecting Undetonated Residue Formation

Both theories described above lack comprehensive explanations, however if either is the cause of undetonated explosive residue remaining from high-order detonation events then the following factors would affect the amount of material generated:

Velocity of Detonation: Based on the width of the reaction zone, explosives which decompose faster (have a higher VOD) would produce fewer undetonated residues than those which react slower and have a relatively lower VOD. For example, RDX (VOD ~8440 m/s) would be expected to produce less undetonated residue than explosives such as AN (VOD ~5000 m/s)[11].

Charge Mass: Based on the theory of shockwave reflection at boundary layers, the amount of undetonated residues produced would be proportional to the surface area of the charge. The ratio of surface area to volume is inversely proportional to size. Therefore larger charge masses would produce fewer undetonated residues relative to their mass and volume compared to smaller charge masses[3,57].

Charge Diameter: As the charge diameter increases, the velocity of detonation increases up to a limiting point[42] thereby decreasing the size of the reaction zone and narrowing the interaction zone at the explosive–air boundary layer where unreacted material may survive[57,60] potentially producing fewer residues.

Number of Interfaces: If the undetonated residue is formed at the boundary layer between the charge surface and the surrounding medium, it follows then that more interfaces between these two surfaces would produce more undetonated material to remain. A charge

comprised of multiple stacked cartridges (such as bags of AN fertilizer) would therefore generate more residue than if the explosive was encased only once[57].

Despite the aforementioned theories and factors regarding undetonated residue formation, no verified reason for the presence of undetonated material following high-order detonation reactions is evidenced in the literature. The mechanisms for residue dispersal nonetheless are also theorised.

2.3 Explosive Residue Distribution

Two distinct mechanisms for the distribution of explosive residues are posited in the literature; those which are adhered to fragments of the explosive device such as the casing and those which move freely, i.e. unattached to any other material. The focus of this thesis is residues which move unattached to fragmented casings; therefore the movement of fragments will be covered briefly with more emphasis applied to free-moving residues.

2.3.1 Theoretical Studies

2.3.1.1 Fragment Based Residue Dispersion Theory

When the forces acting on any material used to contain an explosive exceed the holding strength of that confining material, the stress and resulting strain upon it will cause it to fragment and these fragments will be ejected. Assuming any undetonated residues ejected from the charge surface adhere to this confinement, their subsequent distribution depends on the fragment movement. The dispersal of the fragments is governed by the initial velocity and energy imparted to them as well as their mass, shape and trajectory[61].

The initial velocity of metal fragments has been related to both the mass of the explosive charge and metal casing[62,63] and has been found to be specific to explosive materials; derived by modelling the energy distribution between metal shells and detonation gases of different explosives[41,63,64]. From this work, a series of equations ('Gurney equations', which are reported fully in the cited texts[63,64]) were generated for the dispersal of solid casing fragments with simple geometries. With the development of these equations, it has been suggested that the distribution of fragments (which may harbour explosive residues) would be based on the inverse square law[65], i.e. the quantity of fragmented material found would be inversely proportional to the square of the distance from their origin.

The maximum distances (R_{max}) moved by fragments have been predicted for different metals[66], where the relationship between distance and fragment was determined to be only a function of fragment density and maximum fragment mass[66]. Based on the results of this work, equation 2.1 was stated in another report[57] to relate the fragment density, (called 'r' and measured in the cited text in g/cm^3), and the maximum fragment mass, (called 'w' and measured in the cited text in kg), to the maximum fragment range, R_{max}. In contrast to the Gurney equations, the relationship does not take into account the effect of the explosive type or mass.

$$R_{max} = 190\ r^{-0.112}\ w + 52\ r^{0.858} \quad (2.1)$$

Equation 2.1 fits well with results from computed models[67] of fragment distribution with fragment densities of 0.8 mg m^{-3} to 1.2 mg m^{-3} (common density range for explosives[57]), however these computations were based on the detonations of gas, liquid and vapour clouds rather than solid explosives and so may not be wholly applicable to condensed explosive charges. Nonetheless, the equation may be able to indicate the movement of free-moving undetonated residues (those which are not adhered to any casing fragments). From equation 2.1, if the mass of the fragment decreases to almost nil, a limiting value of '$52r^{0.858}$' remains; based on this the approximate maximum radius within which fragments with densities of ~1.2 mg m^{-3} could be found would be ~60 metres[57]. This could hypothetically be applied to estimate the distance moved by undetonated residue 'fragments'. Whilst equation 2.1 is said to fit the computational experiments[67] and is based on data from the fragment range experiments[66], it's derivation from the actual data is not provided in the report in which it is presented[57] and the terms cannot therefore be theoretically justified here.

Whilst the inverse square law theory of fragment distribution and the hypothetical radius of 60 metres within which fragments may be found provide a basis for fragmentation distribution, little experimental work has been produced to fully validate either. Furthermore, not all fragments of an encasing material may contain undetonated explosive particles, and it is necessary to understand the method by which these particles move independently during detonation.

2.3.1.2 'Free Moving' Particle Dispersion Theory

The dispersal of particulate explosive residue is explained in the literature as being potentially due to two of the detonation stages: the blast-wave phases and the smoke

plume. Each potential dispersal mechanism has factors which would affect the explosive residue distribution patterns.

It is posited that residue particles are expelled and could be pushed outward from the detonation centre due to the positive pressure impulses produced by the detonation and subsequently impeded or pulled back into the centre by the negative impulses[3,57]. If this theory is correct the factors that would affect the residue distribution pattern around the detonation centre would be the concentration of the original explosive material and the fireball dynamics.

Concentration: If the undetonated residues are formed on the surface of the explosive charge and subsequently dispersed due to the blast, approximations could be made that residues are equally distributed and spread over the surface of a sphere (if the charge is spherical)[3]. The amount, 'c', of material (measured in the cited text[3] in grams) on 0.01 m^2 of a surface is said to be determined by equation 2.2 where 'W' denotes the total mass of distribution material (reported in grams) and 'r' is the distance from the charge in metres.

$$c = \frac{(10^{-4} W)}{(4 \pi r^2)} \qquad (2.2)$$

The amount of residue expelled by the blast-wave per any unit area around the detonation would decrease proportionally to the reciprocal of the square of the distance of that unit area from the charge (i.e. the inverse square law model which was also hypothesised for fragment distribution patterns). Based on this, it has been suggested that the distance at which residue concentrations will be lower than instrumental detection limits is relatively short and so undetonated residues would be found close to the explosion seat or centre, particularly if the negative phase of the blast-wave causes particles to be pulled back in towards the centre[3]. Whilst indicating a generic trend of residue distribution, equation 2.2 would apply only for perfectly spherical unconfined systems, where no other variables such as a charge shape, confinement or surrounding environmental conditions were encountered, however in reality this is almost always not the case.

Conversely, the inverse square model has been developed with the use of ballistics equations to further explain the potential trajectory paths of residues and their distribution if they are ejected initially due to the blast-wave[57]. By considering the movement of residues within a hemisphere above the point of detonation and assuming the particles are of equal mass, moving at equal speeds and projected at all angles above the horizontal, the

angle of projection can be plotted against the range of the material[57]. If the trajectory of the explosive residue terminates at this theoretical hemisphere, the residue distributed within a particular segment would be equivalent to that which falls on the section of ground covered between the two angles, i.e. the mass of material at longer range from the centre would be concentrated in a smaller area compared to closer to the centre (figure 2.1). This indicates more residue by mass may actually be found further away from the centre contrary to suggestions that most undetonated residue will be found near the detonation centre[8,68].

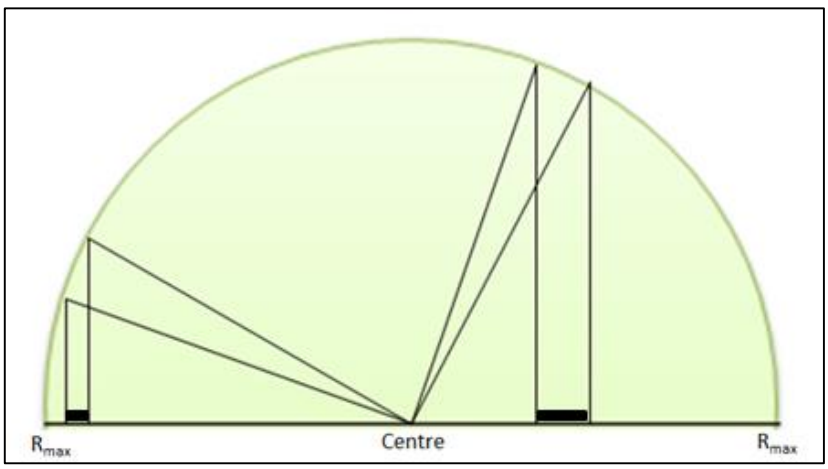

Figure 2.1: *Distribution of residue based on dispersion angle: the same segments cover different sized areas on the ground, further away less area is covered and therefore more residues by mass is found further compared to closer to the centre.*

From both the inverse square model of distribution and the developed trajectory model, contradictory indications of residue distribution patterns are deduced. However, neither model takes into account potential factors which may affect distribution such as different shapes of the original explosive charge, the morphology of the explosive residues being dispersed, the residue trajectory angles (other than above the horizontal), or directionally biased particle movements due to the irregular expansion of the product gases for example[60].

Fireball: The inner zone consists of hot incandescent gases (the fireball). Any undecomposed explosive which is ejected initially due to the positive blast overpressures and adheres to a surface close to the detonation centre may subsequently be engulfed in the fireball and decomposed in this later stage[3]. This is also reiterated elsewhere where it is stated that the exposure of the flame front can impinge on close surfaces, depending on their thermal inertia[69]. Equation 2.3 has been suggested for estimating fireball radius

(called 'r' in the cited text[3]) and includes a term for the explosive charge mass ('W', measured in kg in the cited text[3]).

$$r = W/3 \tag{2.3}$$

Equation 2.3 does not however explain the relationship between charge mass and fireball radius effectively; no terms which factor in the explosive type or charge shape are included and these may affect such calculations. Nonetheless, if the blast is the mechanism by which the residues disperse, and the fireball radius does affect the amount of residue on closer surfaces, the distribution of undetonated residues would again vary from the inverse square law and the highest concentrations may not be found at the closest or central regions of the detonation where the temperatures are the highest.

The second residue dispersal mechanism is theorised as being due to the movement of the smoke plume[60,70] which forms upon the decay of the fireball, counter-intuitively assuming unreacted particles remain within it. The factor which would affect the residue distribution if the smoke plume dispersed undetonated material would be the environmental conditions, principally governed by the wind field.

Environmental conditions: The weather can have variable effects on different phases of detonation. During the detonation, changes in relative humidity, heavy fog or rain have been found to have insignificant effects on blast waves whereas severe wind has been found to cause a focusing of the blast in the downwind direction[71]. The smoke plume movement is affected by the wind velocity and direction; the higher the wind velocity, the faster the movement and dispersal of the smoke plume. The wind moves at a lower relative velocity on the ground due to friction and turbulence that occurs as air moves over the ground, and structures such as buildings and trees produce localised effects which can increase or decrease the wind velocity or alter its direction[72]. If the movement of the smoke plume is the predominant mechanism by which the undetonated explosive residues are dispersed, attention during post-blast investigations should be focused to collection of residue material downwind whilst taking into account potential structural effects.

Whilst either stage of the detonation, the blast-wave or smoke plume, could be the principal dispersal mechanisms of undetonated explosive residues, it is not implausible that both may have an effect on the particle movement. Some empirical evidence to support these theoretical constructs has been obtained through experimental research.

2.3.2 Experimental Research

Experimental studies which discuss the distribution of explosive residues have been conducted from both an environmental perspective, investigating the distribution of residues on the ground, and also from a forensic perspective, investigating the dispersal of chemical evidence during detonation.

2.3.2.1 Environmental Studies

The fate and distribution of energetic material residues on military training grounds has been investigated extensively in order to better maintain and ensure thorough management and remediation of training ranges, and to control the leaching of toxic residues into groundwater. Studies have been based on sampling in and around areas of known detonations on firing ranges as well as immediately following the detonations of military explosives, including various sized mortar rounds and shells, and have focused on ground sampling; incorporating techniques such as multi-increment sampling[73–75], sampling on tarpaulin[76,77], snow[78–80], soil[73,75], and trays[81,82]. Table 2.1 contains the key data synthesised from aspects of this set of experimental research.

The residue concentrations reported in studies from which samples were not collected immediately after detonations[73–75,83], but rather from areas known to have had detonations occur in the past (indicated with an asterisk in table 2.1), were subject to degradation of residues over time and also cannot be assigned to one particular detonation event due to multiple firings occurring on such military ranges. In order to circumvent the issue of knowing whether or not collected residues were from a particular detonation or not, studies have used snow as a sampling medium and focused sample collection on the darker soot regions left on the snow around the detonation centre[80], possibly introducing density bias into the collection strategy.

In general, findings from the studies indicated low-order detonations produced heterogeneous residue distributions around the detonation centre[76,84] compared to high-order detonations from which the residue distribution trends were principally of decreasing concentration as a function of increasing distance from the detonation centre[77,84]. These experimental findings support theoretical constructs which state fewer residues will be deposited further from the detonation than closer to it[3,57].

Explosive	Sampling Method	Key Results	Ref
Mortar rounds (low-order firings)	Tarpaulin sweeping: collective amounts reported within radii around centre	• Larger rounds produced more residues • Heterogeneous distribution of particles: no consistent relationship between mass deposition and distance. No orientation bias could be reported. • 18 m radius within which majority of residues from low-order firings were detected.	76
Mortar rounds, C4, TNT & binary explosives.	Tarpaulin: Sand from tarp swept from 3, 9, 18 and 21 m incremental radii for residue analysis.	• total mass of residue recovered per firings < 100 mg, (binary charges produced more) • limited mass within 5 m of the detonation centre for most mortar rounds • 105 mm rounds: mg quantities of RDX and TNT within crater and at 3 m from it. • Peak residue mass between 5 m and 15 m, with maximum perimeter of 15 m • For the larger charges, RDX mass exhibited less of a distribution trend	77
Comp B rounds (low and high-order firings)	Tarpaulin and trays: Particles counted at 2 m intervals in one direction from centre	• Residue concentrations decreased with increasing distance from centre • Residue mass per m^2 constant to 13 m distance, then decreased by 2 orders of magnitude at 21 m • Low-order distributions asymmetrical compared to high order • Estimated mass of recovered residue increased with increasing charge size	84
NG	Soil: incremental samples in 1 direction	• Highest NG concentrations found near firing point and at target • 4,200 mg/kg at firing point → 142 mg/kg at furthest sampled distance.	73 *
TNT	Soil	• High order = 0.02 mg/kg to 7.5 mg/kg near firing point. No residue detected elsewhere. • Low order = 6500 mg/kg and 4400 mg/kg near firing point	74 *
RDX, TNT	Soil	• 0.004 µg/g detected 5 m from the known firing point; No residue detected 10 m to 50 m • Average RDX concentration ~ 0.021 µg/g. Average TNT concentration ~ 0.004 µg/g.	75 *
Mortars, grenade, C4	Snow: from $1m^2$ blackened areas	• Only concentration ranges reported: RDX: 0.0052 ng to 17 mg, TNT: 0.0011 mg to 2.2 mg • Blow in place firings: RDX = 0.77 – 120 mg, TNT = 0.0053 – 100 000 mg	80
Landmines	Snow and plate sampling in 3 orientations	• TNT: decreased with distance in all orientations, e.g. 199 µg/m^2 (4 m) → 25.2 µg/m^2 (10 m) → 0.1 µg/m^2 (~24 m) • RDX: heterogeneous distributions (non-linear decreases), e.g. 11.9 in centre → 0.27 → 0.20 → 1.56 → 1.00 → 1.78 → 0.13 → 0.45 µg/m^2	79
RDX, TNT, others	Soil	• Crater area concentrations below detection limits (1 µg/kg) and always below 100 µg/kg • RDX had spatially heterogenous distributions at training grounds	83 *

Table 2.1*: Summary of methods and key results from environmental residue distribution research studies. *Samples from these studies were not collected immediately after firing but at areas of known firings in the past*

When comparing different charge sizes, smaller munitions were found to deposit less residues which were recovered closer to the detonation centre, compared to larger munitions[84]; thus countering theories which state the larger the charge, the less likely it will be to find undetonated material[3].

Limiting radii within which explosive residues could be sampled for were also inferred from the data. A distribution radius of 18 metres within which residues could be found from low-order detonations of artillery munitions rounds was suggested[76]. A 15 metre radius resulted from the corresponding high-order detonations[77]. The radii determined from these studies may have been dependent on the limit of detection (LOD) of analytical equipment used in the studies; however these were not reported in either study. Whilst the difference between the two radii was not great (3 metres), they implied low-order detonations distribute residues at greater distances than high-order detonations. The greater kinetic energy of the larger mass deposits produced from low-order detonations would cause them to be deposited further away from the centre compared to the smaller particles generated from high-order detonations[76]. The findings also indicate that theoretical limits of 60 metres may exceed distribution radii for smaller charge masses.

The findings from these environmental studies demonstrate that whilst the residue concentrations from high-order detonations is low (in the mg/L or µg/L range), it is possible to detect them and define distribution patterns. As the primary goal of the research was to assess contamination of training grounds, the results do not include information which would be pertinent to a forensic scenario such as perpendicular site sampling, which has been noted as more lucrative for forensic sampling of explosive residues[85]. However they do highlight pertinent methodological requirements such as the use of multi-increment sampling in numerous orientations around the detonation centre in order to optimise representative sampling techniques.

Most of the studies cited here form a set of experiments conducted by the US Army Corps of Engineers, Engineer Research and Development Centre (ERDC), of which the final report[86] contains further information.

2.3.2.2 Forensic Studies

A notable set of experiments was conducted by the UK Forensic Explosives Laboratory (FEL) and US Federal Bureau of Investigation (FBI) assessing the physical and chemical evidence remaining after explosions of improvised bombs[70,87,88]. The studies utilised metal road signs and cars as sampling materials from which residue concentrations of mainly ammonium nitrate/fuel mixtures were measured. Further to this collaborative set of

experiments, studies designed to assess the application of analytical techniques to the detection of residues[60] and those aiming to elucidate dynamite brands from post-blast residues[68] have also commented on distribution trends. A summary of the pertinent methodological aspects of the forensic research as well as the key results synthesised from it is provided in table 2.2.

The FEL/FBI collaborative investigations tested mainly large (454 kg and 2268 kg) inorganic improvised charges. The sampling sites (mainly non-porous) were generally positioned at various incremental distances and four orientations around the charge centre for most experiments, similarly to the environmental studies. Overall, these collaborative studies found residue concentrations decreased as a function of increasing distance from the charge centre in the majority of cases; figures 2.2 and 2.3 show some of the reported residue recoveries from this series of papers.

As with the environmental studies, the concentration levels detected following these high-order detonations were low; the nitrate concentration range detected (0 mg to 11 mg) was higher overall than the ammonium (0 μg to 330 μg)[70]. No consistent stoichiometric relationship was determined between the two ions and this was explained as being due to the potential oxidation of ammonium to nitrogen and nitrogen oxides which would have reduced the ammonium content within samples. However it is more likely that the lower ammonium concentration range was due to the nonlinear response of the ion chromatography detector used during the experiments, which as the authors stated would have caused the ammonium to be underestimated[70,87]. Furthermore, the calibration used for analyte quantification in this study was based on a single-point curve and therefore the accuracy of the ammonium quantification was unknown.

No fuels from the inorganic charges (sucrose or glucose) were detected in the residues, however some analysis was noted to have occurred weeks after sampling and the time lag may have contributed to the non-detection of the fuel components[87], thus highlighting the importance of sampling and analysing post-blast residues as quickly as possible. TNT and RDX detected from organic charges were in the nano-gram mass range. The variations between residue mass from the inorganic and organic charges were not discussed in the reports, but the findings support theoretical constructs that improvised mixed charges (such as ANFO) would generate more undetonated material than military explosive compositions due to their respective VODs. The general distribution trend between the analytes was similar.

Charges & mass, /kg	Analytes	Sample sites	Distances / m	Key results	Ref
AN/S (x3 repeats) 455	NH_4^+, NO_3^-	metal signs & cars	2.1, 4.6, 7.6, 15.2, 22.9, 30.5	• Concentration ranges: NO_3^-: 12 µg to 5 mg from vehicles, 3 µg to 5.5 mg from road-signs; NH_4^+: 26 µg to 161 µg from vehicles, 3 µg to 366 µg from signs; no sugar detected • Distribution trend: signposts = residue concentrations decreased with increasing distance; car doors = residue increased with increasing distance • lowest concentrations detected at 60 m.	87
CAN/S (x3 repeats) 454, 2268	NH_4^+, NO_3^-, glucose	metal signs & cars	5, 8, 15, 23, 30, 46, 60	• More nitrate than ammonium, (not stoichiometric). No sucrose or glucose detected from larger charges. Recoveries from road-signs lower than from cars. • Residue concentrations decreased with increasing distance from road-signs. • From vehicles facing the charge residues increased with increasing distance • Quantities recovered at equal distance but different orientations not comparable • Higher residue concentrations on back of signs than on front in some cases	70
ANFO (x1), LAN/S (x3) TNT (x1) 454, 2268	NH_4^+, NO_3^- Ca, Mg, glucose, fructose	metal signs & cars	5, 8, 15, 23, 30, 46, 60	• No NH_4^+ or NO_3^- from 2268 kg ANFO charge apart from 17 µg of NO_3^- 30 m away in one orientation • Lower organic concentrations than inorganic: RDX (0 ng to 76 ng), TNT (0 ng to 1700 ng) • Residue decreased with distance (in some cases increased) but orientations weren't comparable • organic residues detected on front and back of road-signs (higher concentrations on the front) • fructose (18 µg) and glucose (19 µg) recovered 30 m from 454 kg inorganic charge. No sucrose detected from vehicles.	88
TNT, Dynamite (x3 repeats) 0.2/ 0.4/0.6	TNT, DNT, EGDN, NH_4^+, NO_3^-, Na^+	stone surfaces & 1 m^2 metal plates	0, 1, 2	• unreacted particles at all sites, irregularly dispersed on the 1 m^2 surfaces • distribution varied between different charge masses and explosive types. • Residue concentrations found to both increase and decrease with increasing distance, e.g. 6.44 (0 m) → 48.46 (1 m) → 23.96 (2 m) mg/L TNT (from 400 g charge) • 6 mg/L to 50 mg/l concentration range for TNT	60*
Dynamite: 6 brands (1 firing each) 0.5	EGDN, DNT, TNT, NG	1 m^2 steel plates	1, 2.5, 5, 7.5, 10	• damage to plates positioned 1 m from centre; residue (grey coatings) at 2.5 m, visible residue particles at 5 m and few residue particles at 7.5 m and 10 m. • 2.5 m to 5 m distances were optimal for obtaining highest residue concentrations: 185.62 µg EGDN, 143.21 µg TNT, 50.03 µg NG, 32.97 µg DNT	68*

Table 2.2: *Methodological aspects of forensic research and key results to date. *Not primarily testing for residue distribution.*

Danubit = industrial plastic explosive dynamite; S = sugar; AN = ammonium nitrate; CAN = calcium ammonium nitrate; LAN = limestone ammonium nitrate; ANFO = ammonium nitrate fuel oil; TNT = trinitrotoluene; DNT = 2,4-Dinitrotoluene; EGDN = ethylene glycol dinitrate; NG = nitroglycerine.

Figures 2.2 and 2.3 show that whilst the residue concentrations decreased with distance overall, the trend was not linear in all cases, with higher concentrations being detected from some of the mid-sampled distances (23 m and 30 m from the centre) compared to the closer sampled distances (15 m from centre).

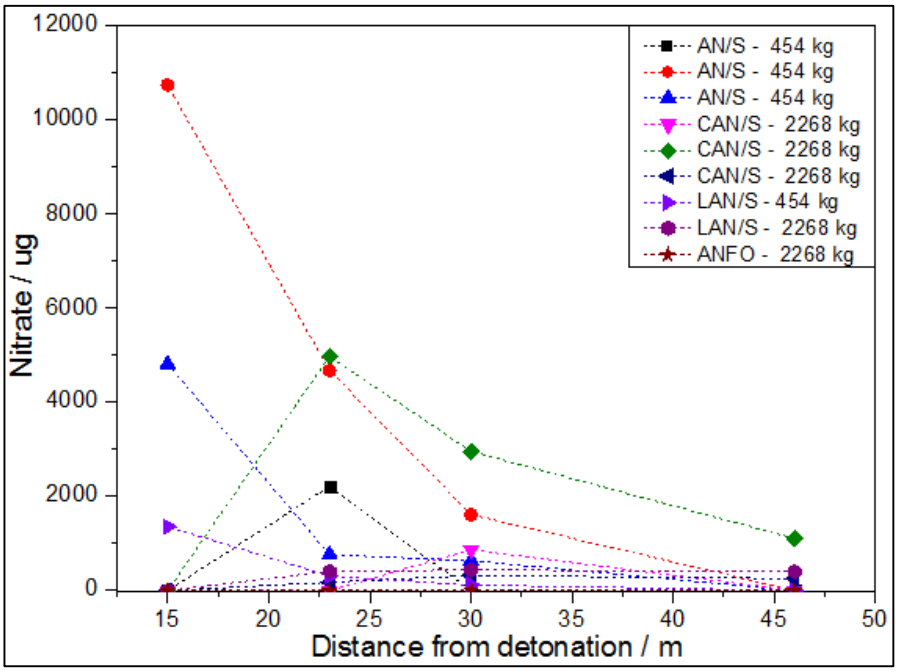

Figure 2.2: *Recovery of nitrate (µg) from sites positioned at increasing distances from detonations of inorganic charges from refs*[7,70,87,88].

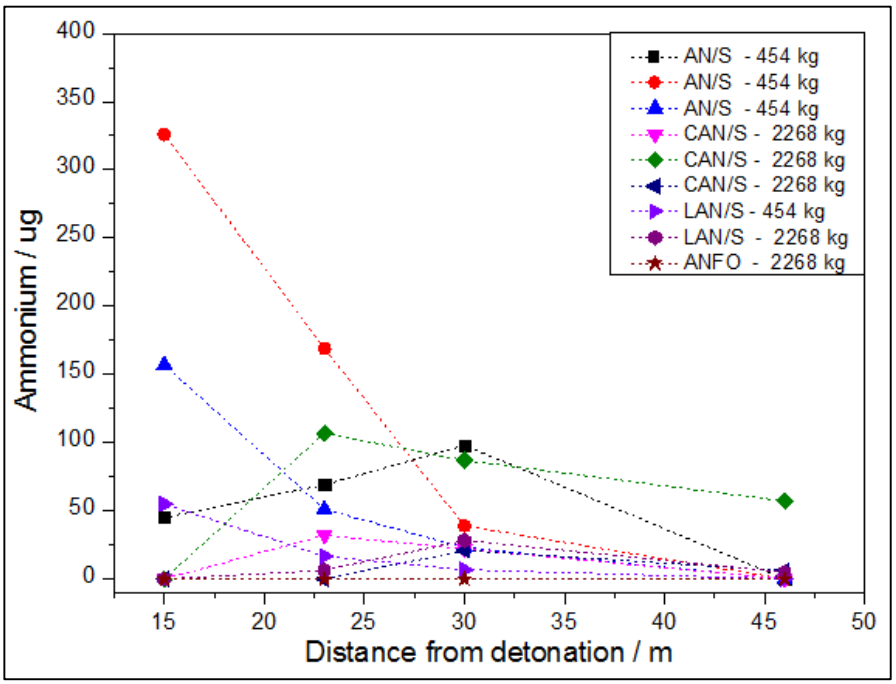

Figure 2.3: *Recovery of ammonium (µg) from sites positioned at increasing distances from detonations of inorganic charges from refs*[7,70,87,88].

The finding of this 'spike' in concentration at the mid-sampled distances was not explained in the reports, but may be caused by the degradation of residues on closer sampling sites due to higher temperatures closer to the detonation centre[3,69] creating an apparent increase in the amount detected further away. With no use of visual recording equipment during the firings however this could not be confirmed. Furthermore, not all residue distributions decreased with increasing distance; residue concentrations from vehicles sampled around the detonations in these studies increased with increasing distance[70,87]. This finding indicates that the height of the sampling site relative to the initial explosive charge placement may be an important consideration when sampling for residues and establishing distribution trends, potentially due to the varying wind currents at different heights which may affect the residue dispersal.

Additionally, from most firings, concentrations from similar distances at different orientations around the centre were not comparable. The variations in residue amounts were explained as indicating residue deposition occurred primarily due to the dust or smoke cloud and not the initial shock wave (the blast overpressures from which were measured during the firings), thus contradicting theories which discuss the effects of the positive and negative blast pressures on the pushing and impedance of particles[3,57]. However, whilst blast overpressures from the firings were recorded, the results between pressure and residue concentration were not compared, furthermore the details of the wind speed and direction were also absent in the reports.

A drop in residue concentration was detected 60 m from the charge centre following most firings, thus supporting the theoretical radius within which residues may be found[57], however no sites further than 60 m sampled so the trend beyond this point is unknown.

Further to this set of studies, figure 2.4 displays the data gathered from experimental work assessing the application of analytical techniques to the recovery of dynamite and TNT residues[60], and illustrates both the trend of decreasing residue concentration with increasing distance as well as those of higher concentrations detected at the mid-sampled distances (as exhibited in the FEL/FBI research). The recovered amounts of the different analytes would have been dependent on the chemical nature of the analytes themselves and the sensitivity of the analytical technique. The authors reported limits of detection of 0.05 mg/L for TNT, 0.1 mg/L for DNT (2,4-dinitrotoluene), 2.5 μg/L for EGDN (ethylene glycol dinitrate) and 5 μg/L for NG (nitroglycerine) (all in hexane) using gas chromatography coupled to an electron capture detector[60].

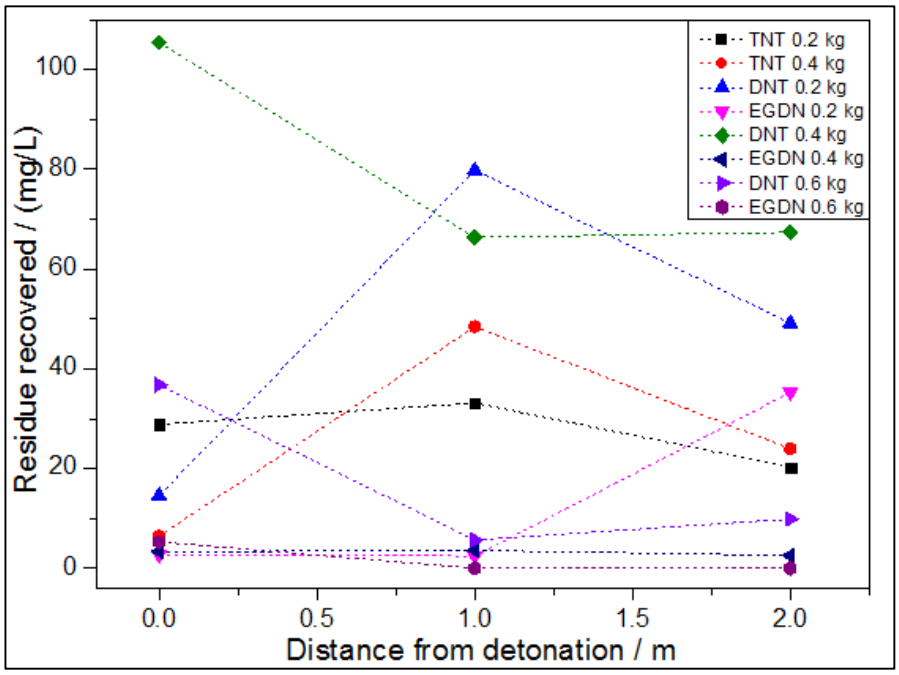

Figure 2.4: *Recovery of dynamite explosive residues from detonation centres and 1 m and 2 m from them, data from Varga & Ulbrich[60], figure adapted from[7].*

The data presented in figure 2.4 however requires verification as only one firing of each charge was conducted and only two distances from the detonation centre (1 m and 2 m) were assessed. Moreover, with only one direction from the charge placement tested, any findings regarding distribution have assumed homogeneous residue deposition about the centre which, as found from the environmental research[76,79], was not always the case. The distribution pattern, or limiting radius around the charge centre within which the residues could be detected from these firings, was therefore unknown. Residue movement however was explained as being due to the acceleration of particles due to the expansion of gases with the final phase of movement determined by the wind. The authors suggested the particles became heated by the shock wave, as in some cases they had the form of droplets, which appeared to have subsequently condensed and solidified on cooler adjacent surfaces of the surrounding environment[60].

Conversely, the authors of a study aiming to elucidate different dynamite brands from post-blast residues described the finding of particles from a 0.5 kg charge at 10 m from the centre to be due to their ejection and dispersal by the shockwave when it reached the boundary between the explosive charge and air. Because of the higher mass of residues compared to micro-droplets in the explosion gases, these particles would have had a higher kinetic energy and moved further to be deposited at ten metres[68]. The findings from this experiment were however based on firings that were initiated in a manner which biased the directional expansion of the gaseous products towards the sampling sites, and therefore potentially influenced residue deposition.

One method of clearly testing the distribution patterns of post-blast explosive residue would be with the use of taggants (such as particulate, isotopic and biological[89] additives) incorporated into the charges. Taggants which can be used to identify explosives both pre and post-blast has been investigated extensively[89–91] and identification taggants which can survive an explosion have been used in Switzerland to aid post-blast investigations[92,93]. Whilst taggant use is technically feasible, due to cost and safety concerns it has not been widely implemented[94,95]. Lanthanide taggants have however recently been used to assess the spatial distribution of post-blast explosive residues following detonations of homemade explosive mixtures and were collected from uniformly positioned collection media on the ground surrounding the charge and subsequently analysed with inductively coupled plasma mass spectrometry (ICP-MS)[96]. Despite attempts at establishing the spatial distribution of the explosive residue, it was the distribution of the lanthanide taggant which was actually reportable and as the correlation between the two remained unverified, the taggant was not a valid representation of the explosive residue distribution. This highlights an important point to consider when using taggant material for identifying spatial residue trends – the taggant must be incorporated as a part of, or bound to, the explosive molecule in order to conclude the distribution of the explosive itself rather than that of the taggant. No other studies which have examined the spatial distribution trends of post-blast residues using taggants were found at the time of writing.

In sum, the experimental studies detailed thus far are an important foundation for residue distribution research as they demonstrate generic distribution patterns of decreasing concentrations as a function of distance from the centre and also provide a good basis for methodological considerations for experimental work, such as the use of incremental sampling of non-porous sites, consideration of sampling height position and the measurement of blast overpressures during firing. The findings from these experiments were however limited to either very large inorganic charges or smaller dynamite charges and the applicability of the distribution trends to further materials of varying charge mass is unknown. The studies also did not conclusively identify the dispersal mechanisms for post-blast residue, with only indications of mechanisms provided with no evidence to support these. The use of imaging technologies capable of recording the detonations (in order to observe the potential movement of particles for example) were not considered, furthermore the recording of environmental conditions at the time of firing was suggested but detailed results of this were not included in the reports. Additionally, no attempt was made to characterise the condensed residues which were detected on the sample site surfaces in terms of their morphology and composition which could potentially imply the mechanism by which they were formed.

Whilst further experimental studies are fundamental to the development of a data set establishing the spatial distribution of post-blast residues, the expense of the investigations and firing trial requirements such as access to explosive ranges, explosive material and personnel authorised to handle and detonate the charges are understandably difficult necessities to overcome. Furthermore, the need to replicate experiments in order to produce verifiable findings and therefore generate significant conclusions is hampered by these constraints. Computer aided simulation techniques have been applied to model various explosion phenomena and offer a useful tool for investigating multiple scenarios and allow for numerous repeat measurements to be obtained.

2.3.2.3 Simulation Studies

Detonation and shock modelling capabilities have been developed over decades to produce models that can improve knowledge and understanding of the processes occurring during detonation, in both chemical and physical terms. Models for various detonation modelling purposes, for example evolved from research into effects of blast on buildings[97], have predominantly focused on calculating peak pressures from the leading shock wave. Despite the wealth of detonation modelling literature and knowledge, relatively little research has been carried out in the area of condensed phase residue particle distribution.

The distribution of solid particles from the point of detonation to post-blast movement in the smoke plume and wind field is a complex problem to solve computationally, requiring extensive computing power, an understanding of the quantity of material which could become airborne[98,99], and expressions which consider factors such as the explosive strength and total mass of other materials present[100]. Computational fluid dynamic (CFD) techniques have however been used to simulate the dispersion of solid particles.

Atmospheric dispersion models initially developed to predict the downwind concentration of air pollutants emitted from sources such as industrial plants have been applied to explosive releases. An dispersion modelling system named Quic–plume, developed at Lawrence Livermore National Laboratories, is capable of simulating the distribution of gases[101] and has potential application for modelling post-blast explosive residues as aerosol. Quic-plume consists of a code which uses multiple terms to address the movement of particles in a built environment by tracking each particle's trajectory in an instantaneous wind field whilst incorporating codes for turbulence modelling[101]. Whilst Quic-plume has been evaluated experimentally[102,103], the empirical work has been based on sulphur releases and their subsequent sampling in a built environment[102] and the release of airborne contaminants[103] rather than actual explosive releases. The full equations and theory behind

the Quic-plume model are beyond the scope of this review but are provided in the theory guide[101] of the code.

Models which have assessed the dispersal of solid particles during the detonation of a spherical explosive charge have discussed the movement of these particles, in particular the way in which during the reactions, they can overtake not only the detonation products but also the shock wave[104,105]. These experiments however have been based on a packed bed of inert solid particles moulded around a spherical explosive charge and it was the velocities of these which was reported rather than the unreacted particles of the explosive material itself.

Relevant work in modelling particle distribution following a detonation also includes research into the dispersal of radiological material from 'dirty' bombs[106], modelling the velocity of explosive products[107] and estimations of dispersal based on the smoke cloud volume and height, however they do not directly or fully address the distribution of undetonated explosive residues upon and following detonation. Recently, aerosol dispersion models developed from the dispersal around biological treatment plants[108], have been applied to model explosive residue particle releases, in particular the deposition of post-blast residue following the 2011 Oslo bombings has been simulated[85].

These simulations included the movement of the particle cloud following the detonation focusing on the wind as the dominant transport mechanism and were based on spherical residue particle sizes smaller than 20 μm with a high density (1000 kg/m^3)[85]. Simulation results indicated perpendicular areas which the cloud had passed over to have the highest residue depositions (15 %), with only 5 % of the total residue particles emitted being deposited on the ground[85]. This trend was consistent with the experimental finding of low concentrations of residue on the ground from some of the environmental studies. The deposition of particles has been concluded to depend more on the source location (for example high on a roof, or low on the ground) and the dispersal mechanism to be based more on the wind direction and velocity[85,109]. Figure 2.5 shows an example output from the computation, showing the particle distribution amongst the built-up area.

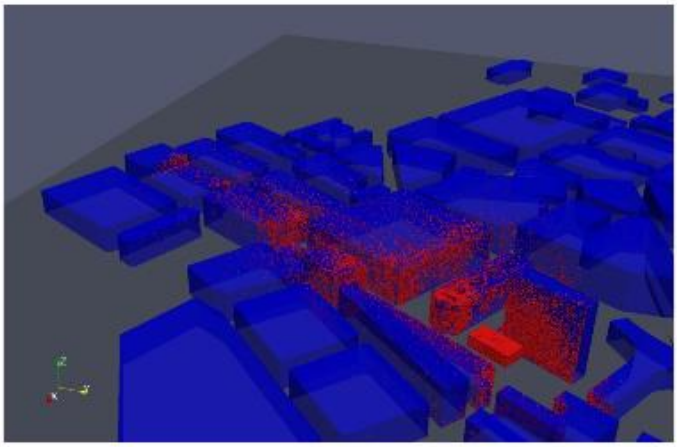

Figure 2.5: *Bomb residue particles deposited in built environment generated with simulation techniques[85]. Reprint permission provided by the Norwegian Defence Research Establishment (FFI).*

This work constitutes the only known research which directly models the dispersal of explosive particles and attempts to establish their distribution patterns. However, with no direct comparisons of the numerical simulations with experimental data, the models have not yet been validated.

The theoretical and experimental work discussed thus far somewhat informs current forensic practice at post-blast crime scenes with regard to locating explosive residues, which are summarised in the next section.

2.4 Forensic Crime Scene Procedures

General forensic crime scene investigation procedures include conducting preliminary safety and security assessments of the scene alongside initial surveys during which notes of the time, date and location of the incident are made as well as any particular resources which may be required to support the investigations[55,110]. The scene investigation then involves photography, documentation of initial observations, and evidence identification, packaging and collection. Logs of all activities within the crime scene (including entry/exit to the scene, photography and evidence logs) are maintained throughout the investigation[44,111,112]. Prioritisation of evidence collection depends principally on the nature of the scene and the evidence item in particular; for example, the collection of potential biological evidence located outdoors where prevailing environmental conditions could compromise the evidence would give the item priority[55,113].

2.4.1 Post-blast Investigations

The identification of potential evidence items at any crime scene can be a challenging task, one which is further complicated by the inherently complex nature of a post-blast scene where debris, structural and thermal damage can dominate the scene. Evidence

identification is achieved through organised searches using grid, line or spiral search techniques[55]. As well as identifying components of the explosive device such as the power supply (e.g. batteries), initiator (e.g. switch) and container (e.g. fragments of a pipe), residue of the explosive material itself is also sought[44,55,114].

2.4.2 Explosive Residue Evidence

The morphological appearances of trace post-blast explosive residues from high-order detonation events are not detailed extensively in the literature. Microscopic observations from one study assessing high order detonations of Composition B (RDX and TNT based explosive composition) found melted metal spheres, fragments of wood and soil in the residues[84] but no further morphological or chemical information was provided. Research from related fields may however provide insight into the appearance of post-blast residues. Both pyrotechnic and gunshot residues (GSR) have been found to produce spherical and spheroidal particles, the sizes of which have varied depending on the material and level of confinement. GSR particles have been found to be 0.5 μm to 5 μm in diameter[115], pyrotechnic residues have been found to <1 μm[54] or between 5 μm and 20 μm[115–117]. The elemental compositions of each have been characteristic of the unburnt material[115,116,118].

The altered morphology of particles from their original form has been explained as being due to the initial melting of the particles and their subsequent solidification during dispersion[115,116]. Increased confinement of pyrotechnics was found to produce smaller residue particles[54] which was explained as being due to the pressure and temperature during explosion being higher and therefore resulting in increased vaporization[54]. These findings indicated that the appearance of undetonated post-blast residues from high-order detonations may vary from that of the undetonated material. Nonetheless, given the particle sizes, they would not be obviously apparent at a post-blast scene, raising the question of where they should be sought.

2.4.2.1 Locating Explosive Residues

Due to the multivariate nature of explosion scenes no definitive guide to locating explosive residue has been determined as each scene is generally considered unique. Current forensic practices focus residue collection efforts towards the crater or central region of the explosion as it is thought to be a typically forensically rich area[7,55,119]. Multiple samples are collected of the ground material in the central region of the detonation and of areas close around it, including nearby vertical surfaces such as signs and on ceilings if present. This practice contradicts theory that the temperatures evolved in the central area would decompose residues[3,69] and sites further from the centre should be sampled.

Items in close proximity to the detonation centre, or 'witness materials', are also sampled for residues of the explosive material[55]. Sometimes surfaces or objects can display visual signs of having been close to the explosion such as cratering or pitting, but these do not always yield explosive residue[55]. Additionally, if there are no visible signs of damage, this does not negate the possibility of recovering evidence on a particular item as explosions also leave invisible traces of residue[10]. The issue therefore is to know where to look for this residue. A scientifically sound way to locate items or surfaces which are thought to harbour explosive residues has not yet been established[2,7].

2.4.2.2. Sampling Techniques

No surfaces within the zone in which detectable residues and traces may be expected should be neglected[3] and if the item thought to potentially harbour explosive residues can be removed from the scene, it will be packaged appropriately in a labelled metal container and nylon bag to be transported away for microscopic inspection and chemical analysis at a laboratory[10,114]. If this is not possible sampling can be conducted at the scene. *In situ* sampling of porous materials can be conducted by vacuum sampling[120,121] and non-porous materials, such as car doors or street signs, can be swabbed[55,122]. Numerous swabbing materials have been investigated in the literature[123], including, wipes[124,125] and cotton swabs[126,127], the latter of which are often used to collect trace explosive residues due to their low cost, ease of use and availability[124]. However, the choice of sampling medium at a crime scene would inevitably depend on the availability of material and the nature of the sampling site encountered.

Research conducted to optimise swabbing techniques has found solvent moistened swabs can collect more explosive residue than dry swabs[124,127] as some explosives are readily dissolved[126]. The suitability of various solvents has also been investigated[128], and deionised water was found most appropriate for inorganic explosives such as ammonium nitrate (solubility of approximately 0.2 kg in 1 m^3 of water at 20 °C) and acetone for organic explosives[2,56] such as RDX (solubility of approximately 0.008 kg in 1 m^3 of acetone at 25 °C)[2,10]. Ultimately, the choice of solvent depends on the type of explosive used, and as this is usually undetermined at a crime scene, solvents which are suitable for both organic and inorganic explosives, (mixtures of water and an organic solvent) are often used[120,129]. The manner of swabbing, and the optimum swabbing procedure, has also been commented on; swabbing repeatedly over a surface with considerable pressure has been found to be a more efficient collection procedure than lightly brushing swabs over surfaces[10,55].

The amount of explosive residue ultimately recovered from a particular surface is governed by the efficiency of the sampling technique used. If no prior knowledge of the explosive material used is available, sampling procedures must be able to collect residues from a wide range of potential explosives, which in turn can potentially raise the detection limit. Swabbing capability studies based on the use of different surfaces, multiple target explosive analytes, and various swab supports and solvents have found that the efficiency levels can vary very greatly (Δ = ~10 % to > 90 %)[123,124,127,130–132]. This further highlights the importance of understanding where explosive residues are likely to have deposited in order to ensure sampling in, and from, optimum locations.

2.4.2.3 Trace Explosive Residue Analysis

Following residue collection, the samples are extracted from their supports. Post-explosion analysis usually consists of both an aqueous and organic extraction as the explosive type is usually unknown, and therefore in order to ensure recovery of either material, both are carried out[2,56] prior to instrumental analysis. A vast amount of literature is available on the various methods used to analyse post-blast trace explosive residues, both qualitatively and quantitatively. They vary in their sensitivity, selectivity, resolution, cost, timeliness and availability. Some require extensive preparation procedures, whilst others need additional clean-up and extraction procedures to remove impurities. Comprehensive reviews[2,133,134] encapsulate the key analytical techniques in this area and their applicability, advantages and disadvantages to explosive analysis. A brief outline of the analytical techniques used in this thesis (both during firing experiments and laboratory analysis) is included in the following section with reference to their use in relevant literature.

2.5 Technical Information

2.5.1 Diagnostic Techniques during Firing

High Speed Imaging

High speed photography technology allows the motion of transient phenomenon to be studied at slower rates with high spatial resolution, and high speed imaging (HSI) has been used to capture detonation phenomenon[135]. The technique allows observation of the shockwave as well as the growth of the fireball and smoke plume to be monitored over small time scales[136]. The high speed cameras can be operated in either colour or monochromatic mode; the latter requiring less light during exposure and ultimately producing better resolution.

Blast Pressure Measurements

Measurement of the blast overpressures produced during detonation is possible with pressure gauges which offer the capability of measuring a wide range of frequencies and amplitudes adequate for recording fast transient phenomenon and have been used in previous blast research[70,88]. The numerical outputs can be converted into pressure-time plots which allow assessment of blast profile characteristics such as the peak overpressure, impulse and time of arrival[28].

2.5.2 Laboratory Analysis Techniques

Inorganic Analysis

Ion chromatography (IC)

Inorganic ions from post-blast explosive residue samples have been detected with IC in multiple studies[137–142]; the technique has high sensitivity and selectivity to the residues and a review of the use of IC to post-blast analysis is provided elsewhere[143,144]. In particular, IC is a robust and reliable tool which has been used to successfully detect ammonium and nitrate ions from the detonations of slurries[145,146], pipe bombs[147–149], and other explosive devices[140,149,150]. For ammonium nitrate based residues, cation exchange chromatography involves the retention of the ammonium ion on the negatively charged functional groups of a stationary phase; whilst anion exchange chromatography involves retention of the nitrate ion on positively charged functional groups[2,44]. The ions are eluted from the column by displacement with similarly charged species of higher concentrations to be detected by Ultraviolet/Visible light based or conductivity detectors.

Inductively Coupled Plasma – Atomic Emission Spectroscopy (ICP-AES)

Trace elemental analysis of metals, such as aluminium, can be conducted with ICP-AES; the technique has been used to analyse the metallic content of post-blast residues in order to differentiate between similar samples[151]. Samples are required to be in a solution, and an acid digestion (for example with nitric acid) stabilises any metals dissolved in the sample[152]. Aerosolised sample particles are heated, and following electron excitation, emit specific energy wavelengths characteristic of the elemental composition of the sample[153].

Organic Analysis

High Performance Liquid Chromatography–Mass Spectrometry (HPLC-MS)

Liquid chromatography is a well-established technique for the analysis of trace organic explosives and has been used extensively; standardised methods[154] for the analysis of nitramine analytes such as RDX in complex matrices state the requirement of a sample sonication and filtration step prior to HPLC analysis[2,133,154]. Sample component separation is then based on the retention of target analytes on stationary phase columns; RDX

separation is achieved via 'reverse-phase' chromatography whereby the stationary phase column (usually a C-18 column)[154] is hydrophobic, to which the RDX molecules adsorb, and are then eluted with a polar mobile phase[2].

The coupling of the chromatographic equipment to a detector allows peak purity to be ascertained and mass spectrometry (MS) detectors offer precise molecular identification and high sensitivity[2,155]. Samples are ionised prior to detection using, for example, electrospray ionisation (ESI) techniques. ESI is a 'soft-ionisation' technique as little fragmentation occurs during the process, which allows a pseudo-molecular ion to be observed, however it provides little structural information to be gained[156]. Tandem MS overcomes this by allowing structural determination of analytes to be achieved; two spectrometers are positioned in line with each other with a collision cell between them. The precursor ions from the first MS (MS1) analyses collide with a high pressure gas (such as helium) in the cell and fragment; the fragmented ions are then analysed again (MS2)[156].

HPLC-MS of RDX can be problematic due to the thermally labile nature of the RDX molecule[2,157]. RDX-adduct formation, via the addition of chloride ions for example, has proven a successful technique in overcoming this by producing characteristic ions during ionisation[157]. With the addition of chloride into eluents or samples matrices, the resulting major ionic species have mass-to-charge (*m/z*) values of 257 and 259 corresponding to the $[M+^{35}Cl]^-$ and $[M+^{37}Cl]^-$ ions, which significantly improve detection signals (M being the molecular ion, RDX, with a mass of 222 Da)[158–162].

Particle Analysis

Scanning Electron Microscopy – Energy Dispersive X-ray Analysis (SEM-EDS)

The combined use of SEM and EDS is a well-established technique in the forensic sciences, particularly in the application to gunshot residue (GSR) analysis[163] and whilst literature regarding the application of SEM-EDS to the analysis of explosives residues is comparatively sparse, it has the potential to be effective. SEM usually requires an electrically conductive sample which promotes the conduction of electrons away from the sample surface to prevent charge build-up and degradation of the image. Non-conductive forensic samples, such as post-blast explosive residues which may require further analyses, can be analysed under variable pressure (as opposed to a vacuum). The inclusion of air into the sample chamber neutralises negative charge on surfaces and therefore samples can be analysed without a metal coating which could otherwise compromise the analysis[164].

Raman Spectroscopy

Raman spectroscopy provides information about molecular vibrations which allow sample identification and quantification; the intensity of the Raman spectral features are proportional to the concentration of material analysed. RDX and AN each produce characteristic Raman spectra which provide a chemical fingerprint of the molecules and both materials have been analysed with a 785 nm laser at low power successfully[165–167].

Particle Induced X-ray Emission (PIXE)

PIXE techniques have been successfully applied in the forensic analysis of PE4 (plastic explosive containing RDX)[168]. PIXE is a non-destructive elemental analysis technique which has a higher sensitivity to trace elements than EDS and can also be operated at atmospheric pressure. Analysis of a number of spots on non-ideal samples (those which are not flat or homogeneous) followed by averaging can provide a semi-quantitative analysis[169].

Mega–electronvolt – Secondary Ion Mass Spectrometry (MeV SIMS)

Secondary ion mass spectrometry (SIMS) is a sensitive analytical technique capable of detecting trace elements in the surface layer at < 1 mg/kg concentration. The application of SIMS analysis to the identification and differentiation of explosive samples has been successfully determined through experiments[170,171]. The technique is based on the ejection of secondary ions (both positive and negative) from a sample surface when bombarded with primary ions from a source.

2.5.3 Computational Simulation

Computational Fluid Dynamics (CFD) is a branch of fluid mechanics which solves and analyses problems involving fluid flow. CFD has been used to simulate the dispersion of solid particles[99] and their subsequent deposition following the detonation events which occurred in Oslo in 2011[85]. Computer based simulations incorporate mathematical modelling and software tools in a controlled virtual environment and offer many advantages over experimental approaches, including potential reductions in time and cost, greater levels of detail in the results and the ability to provide insight into systems which would otherwise be unfeasible to assess due to physical impracticalities or hazards. The CFD workflow process is divided into three stages. The 'pre-processing' stage involves the formation of the computational domain geometry and it's subdivision into smaller cells. The initial conditions within each cell (e.g. velocity, pressure and fluid density) and the boundary conditions of the domain are prescribed at this point. The equations which govern the flow of material (which in the case of detonation are the product gases produced and the surrounding air) are formulated as a closed set of equations which can be solved

numerically in each of the cells at pre-determined time steps[172]. The 'solving' stage uses numerical algorithms to solve the previously determined equations. The actual amount of time taken to complete a computation depends on many variables including the problem, number of cells, the chosen algorithms and hardware etc. The final stage, 'post-processing', involves the extraction of data from the computed flow field and producing a physical interpretation of the results, i.e. multi-dimensional graphical plots[172].

2.6 Summary

Whilst the reason for why undetonated explosive particles remain following high-order detonation events is only partially theorised in the literature, it is generally accepted that they can be found in the vicinity of a detonation. Explosive residue distribution is theoretically attributed to two distinct mechanisms; residue movement due to blast-wave effects and movement due to the smoke cloud directed by the wind. The distribution trends are suggested to decrease from the centre based on an inverse square law of particle distribution or increase from the centre based on residue trajectory models or the thermal effects of the fireball (decomposing residues) on closer sampling sites.

The empirical evidence to support either notion is limited to a set of environmental and forensic studies, from which the varying results principally demonstrate distribution trends of decreasing residue concentrations with increasing distance from the detonation centre (not always linearly) with potential directional influences attributed to the wind. The data set to date is based on a small range of tested explosive charges and masses and few sampling points around the detonation centre. Furthermore, the amount of explosive residue in each case has been dependent on the analytical technique employed; the resulting values reported are therefore not reliably comparable across datasets from different studies.

The theoretical and experimental research loosely informs forensic practice at post-blast crime scenes which focuses sample collection on the central and surrounding areas of detonation with no rigid or empirical evidence based rules in place. In order to develop the knowledge base in this area and therefore better inform, or support, forensic practices, the residue distribution trends should be tested via repeated experiments with further explosives, of different masses in varying confinements. Experiments which incorporate measurement of and account for both meteorological conditions and blast overpressure at the time of firing are necessary to allow the mechanism of residue distribution to be determined. A morphological and chemical assessment of the condensed phase particulate material sampled for would also enhance this field by generating knowledge regarding the appearance of the condensed phase particles which can be found at post-blast scenes.

2.7 Aim and Objectives

The aim of this research was to develop the empirical data-set regarding the spatial distribution of post-blast explosive residues in order to better inform forensic sampling procedures for residues at post-blast crime scenes. The relationship between detected residue concentration trends and potential influential factors such as the blast-wave, fireball and wind direction were investigated. The morphological and chemical characteristics of the condensed phase residues were assessed.

In order to do so, the following objectives were defined:

- Detonation experiments were conducted using RDX based military explosive compositions and improvised explosive mixtures of aluminized ammonium nitrate. These explosives were chosen as they allowed variation in VOD to be tested. Unconfined spherical charges (0.5 kg) were tested initially; complementary tests involving unconfined larger masses (1 kg and 2 kg) and 1 kg charges confined in vehicles were also conducted.
- Diagnostic tools were used to measure the blast overpressures produced (using piezoelectric pressure gauges), fireball sizes (using high-speed imaging) and environmental conditions during the firings.
- Residue samples were collected by swabbing sampling sites from around the detonation centre at incremental distances from it. Samples were chemically analysed (with HPLC-MS, IC and ICP-AES) to generate a relative concentration of residue per each sampled area.
- The data sets were synthesised to establish if correlation points existed between the detected residue concentrations and theoretical distribution trends or the potential factors thought to influence distribution.
- The morphology and chemical composition of condensed phase residue particles were assessed by collecting particulate matter onto smaller stub surfaces positioned around the detonations. Particles were analysed with SEM-EDX, Raman spectroscopy and MeV SIMS.
- The potential to couple experimental data with simulations of residue deposition was evaluated by comparing data sets from field trials with numerical simulations of particle distribution generated using computational fluid dynamics (carried out by researchers at the Norwegian Defence Research Establishment (FFI)).

CHAPTER 3: MATERIALS AND METHODS

This chapter contains details of all explosive materials used in this thesis followed by the methods in which they were positioned and detonated. The experimental design for collecting explosive residue samples from around the detonations is explained as well as the techniques for collecting and processing diagnostic measurements during firing. The analytical methods used in the laboratory analysis of all samples are detailed. Finally, the simulation parameters inputted into numerical calculations of particle distribution are outlined. Experiments with 0.5 kg unconfined charges were conducted at the explosives range and demonstration area (ERDA) at the UK Defence Academy. Experiments with 1 kg and 2 kg charges were conducted at an explosive test range facility at Porton Down. Confined firings were conducted at the Defence Explosive Ordnance Disposal, Munitions and Search School (DEMSS) regiment in Kineton.

3.1 Explosive Charges

Two different explosives were tested in this thesis; organic military compositions of RDX and improvised inorganic compositions of aluminised ammonium nitrate. These explosives were chosen as both have been used in previous terrorist attacks and so are forensically applicable, and because the detonation chemistry and physics for each varies.

Aluminised Ammonium Nitrate (AlAN) Charges

Fertilizer grade ammonium nitrate (AN) prills (33.5 % mass fraction of nitrogen; Hydro Agri Ltd., UK) were ground to less than 1 mm in diameter (average particle size; 0.8 mm) using electric processors. Aluminium powder (flake particle size range; 10 μm to 150 μm diameter, provided by DSTL, UK) was mixed into the AN in a 10:90 (mass fraction) Al:AN ratio to produce the composition for the 0.5 kg aluminised AN (AlAN) charges. The charges were moulded into spheres; six charges were made in total and the mass of each was weighed using an analytical balance ($\pm$ 0.0001 kg).

The composition of the 1 kg and 2 kg charges consisted of atomised aluminium powder (spherical particle size range; 20 μm to 63 μm in diameter, provided by DSTL, UK) mixed to produce a 30:70 (mass fraction) Al:AN ratio. All mixing was performed remotely using a rolling steel drum. The variation in the type of aluminium powder for each composition was due to differences in available materials at the different sites where the charges were produced. The 1 kg and 2 kg charges were moulded into cylindrical charges with a near 1:1 aspect ratio, producing almost spherical charges. One of each of the larger charge masses was fired; more firings were not possible due to restrictions on the availability of explosive material during the Porton Down experiments.

RDX Composition Charges

Plastic Explosive Number 4 (PE4), consisting of RDX (mass fraction of 88 %) as the explosive ingredient and hydroxyl–terminated polybutadiene (HTPB) (mass fraction of ~12 %) as the binder, (provided by Cranfield Defence Academy) was moulded from its cylindrical forms into six 0.5 kg spherical charges at the ERDA facility. Plastic Explosive Number 7 (PE7), also consisting of RDX (mass fraction of 88 %), (provided by DSTL, UK) was moulded into near spherical 1 kg and 2 kg charges – one of each was made. Charge masses were weighed using analytical balances ($\pm$ 0.0001 kg).

RDX Composition Charges for Confined Firings

A charge demolition device commonly known as MAXI-CANDLE (Charge Demolition EOD HE L6A1, supplied by Kineton DEMSS) was used for the confined vehicle firings. The MAXI-CANDLES contained two explosive pellets, each consisting of 86 g RDX/wax (mass fractions of 88:12) and a 26 g DEBRIX 18AS booster charge (consisting of 95 % RDX mass and 5 % wax binder mass). The MAXI-CANDLES functioned as charge demolition devices and therefore also contained fire suppressant powder (Centrimax ABC Plus, consisting of 85 % ammonium phosphate by mass and 15 % moisture inhibitors).

The outer body of the cartridges consisted of a single polythene moulding with a detonator chamber designed to hold the detonator. The outer body was sealed with an end cap which enclosed the fire suppressant powder and inner container. The inner polythene container housed the explosive charge (figure 3.1). In order to fire a charge mass consistent with previous experiments, six MAXI-CANDLE cartridges were used per firing, equating to the detonation of approximately 1.06 kg of explosive mass. The cartridges were held together with cord to form a cylindrical charge (near spherical).

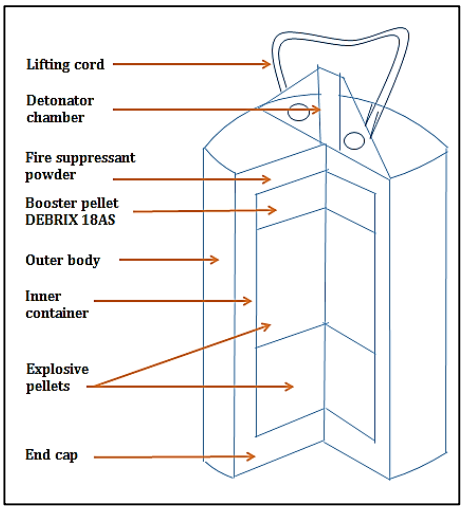

***Figure 3.1**: Inner build of charge demolition EOD HE L6A1 (MAXI CANDLE)*

Booster Charges and Detonators

All unconfined charges were detonated with SX2 booster charges (mass fractions of 88 % RDX and 12 % non-explosive plasticiser) and detonators. The 0.5 kg charges fired at ERDA were detonated with No. 8 Instant Electric detonators (containing 0.720 g Pentaerythritol-tetranitrate (PETN)). The 1 kg and 2 kg charges fired at Porton Down were detonated with RP83 high voltage detonators (containing 0.08 g PETN and 1.03 g RDX). The confined MAXI-CANDLE charges were detonated with L2A2 electric detonators (containing 1.40 g PETN). The variation in detonator types used was due to the availability of materials at each firing range.

The booster charges and detonators in all cases were positioned directly underneath the charge centre; the initiation was therefore directed vertically upward in order to avoid directional bias of the expansion gases in any horizontal orientations.

3.2 Experimental Designs

3.2.1 Charge Positioning

Unconfined charges

All of the 0.5 kg, 1 kg and 2 kg charges fired at both ERDA and Porton Down were positioned 2 m above the ground on wooden firing poles placed in the centre of the firing area; measurements were made with measuring tape from the ground to the charge centre. All charges were required to be no less than 2 m from the ground surface of the firing pads in order to ensure the prevention of crater formation and therefore comply with each of the explosive range operating procedures. New firing poles were used per detonation. The charges were secured in place upon the firing poles for the time between positioning and initiation by wrapping adhesive tape around the base of the charge and the top of the pole.

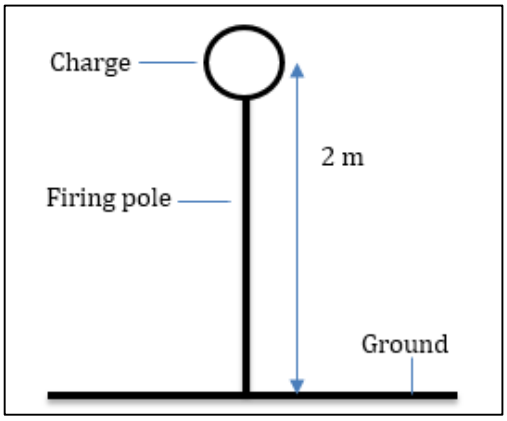

***Figure 3.2**: Schematic of spherical explosive charge positioning 2 m above ground.*

Confined Charges

The MAXI CANDLE charges were positioned within the centre of cars prior to detonation. Cars were used for the confined firings as they represented a forensically valid scenario which could be tested outdoors. The charges were tied to 3 m wooden firing poles which were placed horizontally through the front car door windows (figure 3.3). The height of the charge for each was measured at approximately 1.5 m (± 0.2 m) from the ground. Slight variations in charge height placement were due to different models and makes of vehicles used per firing. Six experiments were conducted in total.

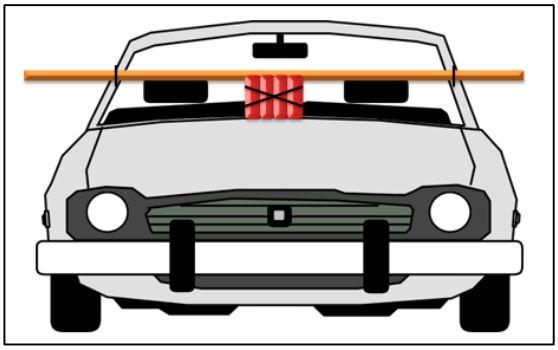

***Figure 3.3**: MAXI-CANDLE charges (red, attached to wooden firing pole) positioned within car. Six MAXI-CANDLES (equating to ~1.06 kg RDX) were positioned and fired at the same time in each car.*

3.2.2 Residue Sampling Sites

Sampling Positions

Sampling poles (2.4 m steel scaffold poles) were positioned around the central firing pole at various orientations around the centre and at incremental distances (1 m, 2 m, 3 m, 4 m, 5 m, 6 m, 7 m, and 10 m) from it. These distances around the 0.5 kg charge were chosen as they allowed the residue to be collected 'close in' to the detonation centre as well as further from it whilst reflecting the practice of using incremental sampling conducted in previous trials[173–175]. Distances were measured with measuring tape along the ground from the firing centre. Figure 3.4 illustrates the orientations, positions and distances of the sampling poles for the 0.5 kg AlAN and PE4 charges fired at the ERDA range.

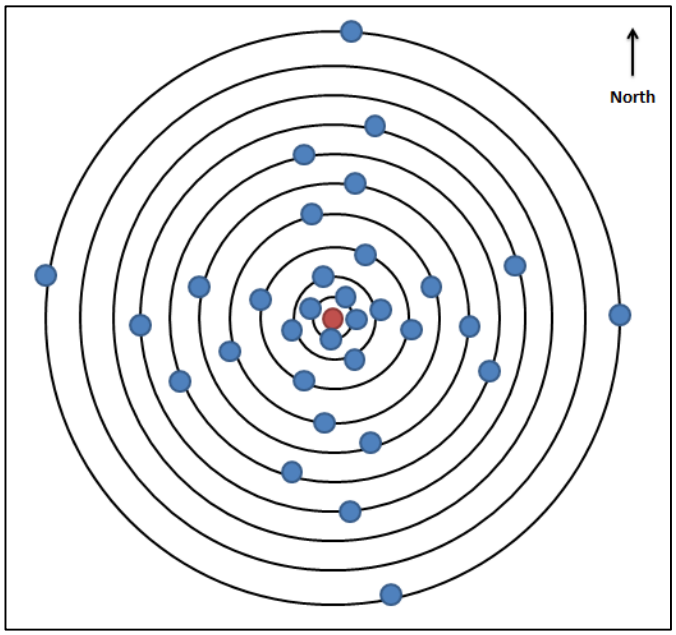

***Figure 3.4**: Aerial view of sampling pole placement around 0.5 kg charges at ERDA. Each black ring marks a 1 m increment from the centre. Poles (blue) were positioned offset* with each other at North, East, South and West orientations, 1 m to 10 m from the charge centre (red). *The diagram is not to scale and therefore does not show that each plate front was completely unobstructed by others.*

The same pole orientations were arranged around the 1 kg and 2 kg charges at the Porton Down Range and the confined 1 kg charges placed in vehicles on the Kineton range. The sampling pole distances for these larger charges were at 3 m, 4 m, 5 m, 6 m, 7 m, 10 m, 15 m, 20 m, 25 m and 30 m. The placement of poles closer than 3 m was not possible around the 1 kg and 2 kg charges at Porton or the confined charges at Kineton due to their destruction at these closer distances to the centre, whilst due to the larger firing ranges it was possible to extend the sampling distances up to 30 m for these larger charge masses and therefore assess the movement of residues at these further distances.

All sampling poles were positioned offset with each other (i.e. not directly in front or behind each other) to avoid obstruction of the furthest sampling sites by those closer to the centre.

In order to later compare the residue distribution directly to numerical simulations of residue movement due to the wind field (explained in section 3.6), as well as positioning sampling poles at the compass points, sampling poles were also positioned at incremental distances in further orientations in line with the wind direction (NW and SW orientations) during some of the 0.5 kg AlAN firings. Figure 3.5 shows an aerial view schematic of the layout of these sites.

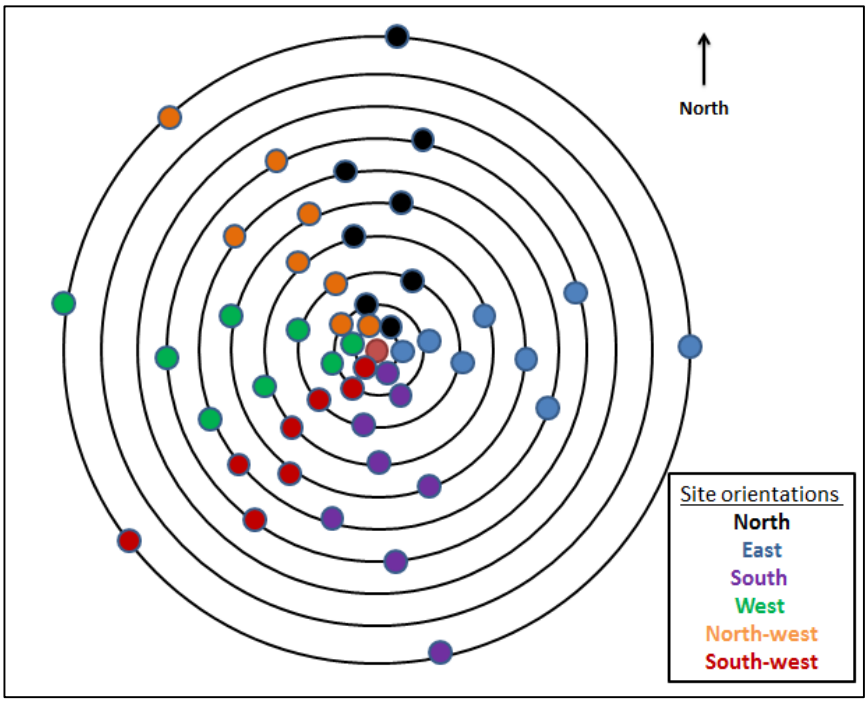

Figure 3.5: *Aerial view of sampling site positions* around detonation centre. The sites were positioned at 1 m to 10 m distances and are marked according to their orientation around the centre. Additional sample sites were positioned in line with the west/north-westerly wind direction. Residue was collected at the points at the ground level and 2 m above it. *The diagram is not to scale and therefore does not show that each plate front was completely unobstructed by others.*

Swabbing Sites

In order to sample for explosive residues following each firing, steel sampling (or 'witness') plates (mild sheet steel: 300 mm x 200 mm x 0.80 mm; Metalstore, UK) were placed upon each of the sampling poles. Prior to positioning, each plate was cleaned thoroughly by washing and wiping the surface with deionised water (Sigma Aldrich, UK) followed by acetone (> 99.5 %, Sigma Aldrich, UK) before arrival at the firing range. Once dried, the plates were sealed into new nylon bags (provided by DSTL, UK) in order to ensure the surfaces were free from explosive residue contamination prior to the firings. Plates were positioned onto poles immediately prior to the detonator being placed within the charges in order to minimise the amount of time sampling surfaces were exposed; the exposure time was between 10 and 45 minutes.

Sampling plates were placed on the poles at 2 m from the ground and therefore in line with the position of the explosive charges; each 2 m point was measured from the ground to the centre of each plate with measuring tape. Each plate was secured in place with heavy duty cable ties, pulled through two 120 mm holes drilled (using a Roland CNC MDX-40A milling machine) into the centre of each plate (figure 3.6).

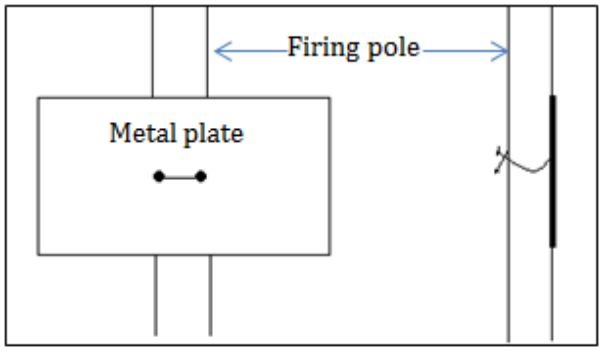

Figure 3.6: *Schematic of steel sampling plate affixed to sampling pole with cable tie pulled through drilled holes in plate front and tied at the back; view from the front (left) and view from the side (right).*

For the experiments with the 1 kg and 2 kg charges at Porton Down, further steel sampling materials were available and plates were also positioned 0.75 m from the ground on all sampling poles. For the experiments conducted to directly compare experimental residue data to numerical simulations, sampling plates were also positioned at ground level.

Particles

Post-blast particulate material was collected onto the surfaces of aluminium SEM specimen stubs (12.5 mm diameter and 3.20 mm diameter pin with groove; Taab Laboratories, UK). This novel technique of post-blast particle collection afforded a sampling medium upon which particulates could be collected but also subsequently analysed without the need for transfer or removal of particles from their surface. The stubs were positioned onto the sampling poles which surrounded the detonation centre; each stub was placed above the residue collection steel plate (figure 3.7). The stub was affixed in place using an adhesive Blu–tack mount. Double sided adhesive carbon discs (3.00 mm thick, 12.5 mm diameter, Taab Laboratories, UK) were applied to each stub in order to provide a surface for particulate matter to adhere to. Prior to placing stubs on sampling poles, each was individually stored in a sample tube holder with a lid (single SEM pin stub storage tube, 25 mm diameter, 55 mm height; Taab Laboratories, UK) (figure 3.7).

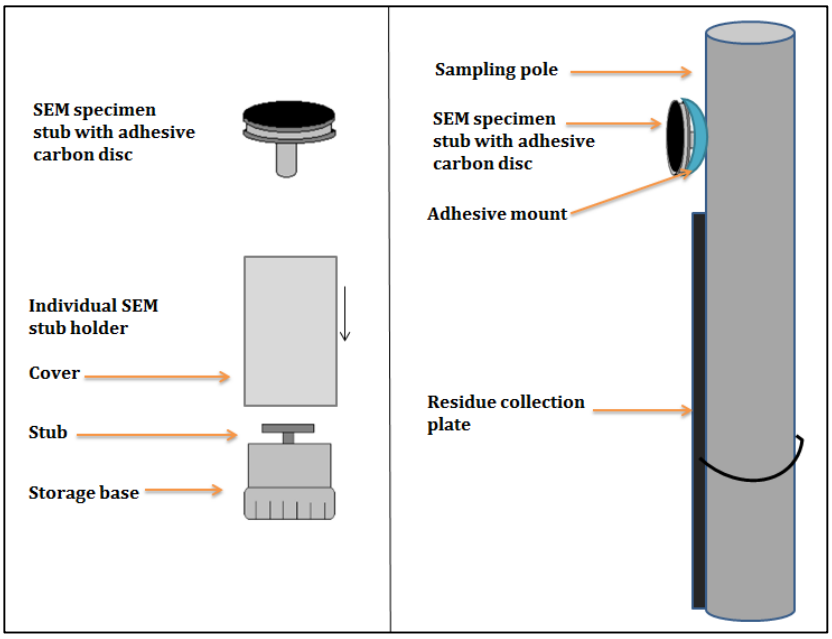

***Figure 3.7**: Left: SEM stub with carbon disc and individual stub holder. Right: SEM stub positioning on sampling pole; positioned above steel plates from which residues were swabbed.*

3.2.3 Blast Pressure Measurements

Quartz piezoelectric pressure gauges (Piezotron® type 211B, Kistler, USA) were mounted on 2 m high supports and positioned in the south-east orientation around the 0.5 kg charges at ERDA (figure 3.8). The distance of each gauge (1 m, 2 m, 3 m and 4 m) was measured with a laser distance measurer (Leica Disto D210) and each was aligned directly behind the other in order to accurately record the blast wave profile produced.

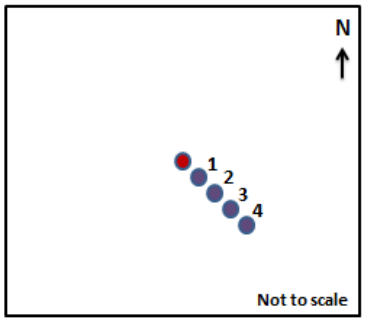

***Figure 3.8**: Mounted pressure gauges (purple) aligned at 1 m to 4 m south-west from the charge centre (red).*

Data was collected for a duration of 20 ms and was processed with a 25.0 MHz digital oscilloscope (Nicolet Technologies Sigma 90-8) and based on the waveforms from each firing the peak positive pressures and integrated impulses were calculated. It was not possible to obtain the blast pressure data from the 1 kg and 2 kg charges fired at Porton Down or the confined firings at Kineton due to the unavailability of blast pressure recording facilities.

3.2.4 High Speed Imaging

Each firing was recorded using a high speed imaging (HSI) camera in order to estimate sizes of the fireballs and smoke plumes produced during detonations. On the ERDA range, the 0.5 kg AlAN and PE4 detonations were captured with a Phantom V12.1 camera (Vision Research, UK), operating in monochromatic mode, at 1280 x 800 full widescreen resolution and 6000 frames per second (fps). The camera was situated 75 m south from the firing area, facing north for each of these firings. GoPro camera footage was also acquired for the firings at ERDA; the GoPro camera was positioned 2 m (north-east) from the charge on a 2 m high mount and protected with a blast screen.

The HSI technology available at Porton Down during the 1 kg and 2 kg firings was operated in polychromatic mode, 800 x 600 resolution and 4000 fps. The camera was situated 130 m south-west of the firing area, facing east. All data obtained from HSI footage was analysed using Cine Viewer 2.5 software (Ametek, USA) capable of assessing individual frames. The 'real time' steps were calculated and a series of frames (or 'HSI stills') compiled to show the growth of the fireball and the subsequent smoke cloud, the volumes of which were then estimated.

No HSI recording equipment was available at Kineton DEMSS firing range. Firings were recorded with a digital camera recording in 'real-time' positioned ~120 m south-west from the firing centre. Stills of the smoke cloud allowed its approximate size and movement following detonation to be estimated.

3.2.5 Meteorological Conditions

The temperature, wind speed and direction, humidity and barometric pressure were measured and recorded in the centre of the firing area at 2 m from the ground prior to each firing using a Kestrel 3500 weather meter. The data was evaluated against the residue distribution results in order to assess the effect of environmental conditions on the dispersal of post-blast residues.

3.3 Sample Collection

3.3.1 Residue Collection from Unconfined and Confined Firings

As solvent moistened swabbing has been found to be an effective method for recovering trace explosive residues[124,127], sterile cotton balls (300 mm diameter, Medline Industries, USA), were used to swab the entire plate surface facing the detonation. Swabs were moistened with 5 cm^3 deionised (DI) water (Sigma Aldrich, UK), for the inorganic AlAN firings and moistened with 5 cm^3 of acetone (> 99.8 %; Sigma-Aldrich, UK) for the RDX composition firings. The swabs and solvents were within 10.5 cm^3 glass squat vials with

snap on plastic caps (Scientific Glass Laboratories, UK). For swabbing, each swab was held with sterile polystyrene disposable tweezers (VWR, PA, USA) which were individually packed and opened only prior to sampling. The surfaces were swabbed with the same consistent procedure for 30 seconds; the swab was applied with pressure horizontally back and forth across the plate and then vertically ensuring the whole plate surface had been sampled and therefore in accordance with procedures considered to collect the most residues[10,55]. Following sampling, individual swabs were replaced into the vials containing solvent.

Prior to conducting firings, control samples were taken of each of the steel sample plates in order to assess whether any contaminants were present before detonation. Control samples were collected on bench-guard covered laboratory benches. Samples of the blank swabs (directly from the packaging) and samples of the DI water and acetone used were also collected into labelled glass vials for control purposes.

Samples collected following the detonations were labelled with the position of the plate relative to the central firing area and the firing number. Once swabbed, plates were removed from the support poles by cutting the cable ties. Samples were transported back to the laboratory where all samples were stored at ~4 °C. All sampling was conducted within 45 minutes of each detonation.

Following the confined vehicle firings, samples (control and test) were also collected from the vehicles prior to and following each detonation. The cars were sampled on the outer areas of the bonnet and boot and the inner areas near the dashboard, centre of the car (near to the charge placement) and the roof of each car. Five samples were collected from each car to compare residue concentrations detected on the cars to those from the surrounding sample plates. These points were chosen on each car as they presented both inner and outer areas of each car which remained intact and from which sampling could be conducted.

3.3.2 Particle Collection

Following detonations the stubs were collected by removing the base pin of each stub from the adhesive mount using stainless steel tweezers specifically designed to grip SEM stubs (Agar Scientific, UK). Using the tweezers, each stub was replaced into its holder, which was then labelled with the position around the detonation from which the sample had been collected. Care was taken not to touch the stub surface during the procedure.

3.4 Residue Analysis

3.4.1 Swab Extraction Procedure

The extraction procedure employed was based on established techniques known to remove explosive residues from sampling supports[133,154]. The vials containing the swab samples and solvent were sonicated (Grant MXB22 Ultrasonic bath) at 25 °C for 30 minutes. Following sonication, the vials were removed and each one individually opened and the swab inside further agitated using a new glass Pasteur pipette; each swab was pounded with a pipette for 2 minutes in order to further promote the removal of explosive residue from the swab support into the solvent. The extract was then drawn, through the swab, into the pipette and deposited into a 10 cm^3 disposable polypropylene syringe (Sigma Aldrich, UK) fitted with a 0.2 μm nylon filter, 30 mm in diameter (Chromacol, UK). Each filtrate was deposited into new, clean 10.5 cm^3 rolled rim glass vials (Scientific Glass Laboratories, UK) and labelled with the sample number. The same technique was applied to the control and blank swab samples.

To samples from the inorganic AlAN firings, DI water (5 cm^3) was added to each vial containing a swab from which extract had been removed. Vials were recapped and the agitation via sonication and pipette was repeated for each swab sample. This second extract was also removed through the swab until it was dry and filtered into the labelled glass vial containing filtrate. The total volume of the filtrate in each glass vial was 10 cm^3 (± 0.1 cm^3). A 1.5 cm^3 aliquot of the aqueous samples was pipetted from the glass vials into new 1.8 cm^3 chromatography vials (Chromacol, UK) labelled with the sample number for analysis of NH_4^+ and NO_3^- via Ion Chromatography. The remaining aqueous samples in the glass vials, at a volume of 8.5 cm^3 (± 0.1 cm^3), were recapped and all samples were refrigerated at 4 °C.

The residue samples collected following the organic explosive firings were extracted in a similar manner, with acetone in place of DI water. Following agitation and filtration, the vials were positioned uncapped within a fume-hood in a clean area and upon new bench-guard; the acetone in each vial (~10 cm^3) was evaporated.

When dry, 1.5 cm^3 of HPLC grade acetonitrile (ACN) (99.8 %, Sigma Aldrich, UK) was pipetted into each vial to dissolve any residues. The side and bottom of each vial was scraped with the Pipette tip in order to remove any undissolved residues which may have adhered to the glass vials. Samples were then transferred into labelled 1.8 cm^3 chromatography vials (Chromacol, UK) and refrigerated at 4 °C.

3.4.2 Ion Chromatography: NH_4^+ and NO_3^- Ions

Analysis of NO_3^- and NH_4^+ content from extracted post-blast samples was performed using Ion Chromatography (IC). A DIONEX ICS-2000 reagent free IC system with eluent generation (Thermo Scientific, USA) coupled to an SRS-300 auto-suppression device and conductivity detector was used for these analyses. Table 3.1 displays the system conditions for both the anion and cation analysis. All data was analysed using Chromeleon 6.8 chromatography data system software.

Instrument aspect	Anion (NO_3^-) settings	Cation (NH_4^+) settings
Column	IonPac AS19; 4.0 mm x 250 mm	IonPac CS16; 5 mm x 250 mm
Mobile phase	Isochratic 22 mM KOH	Isochratic 30 mM MSA
Flow rate	1 ml/min	1 ml/min
Injection volume	100 µl	100 µl
Cell heater	35°C	40°C
Pump (backpressure)	2344 psi	2300 psi
Detector	Suppressed conductivity (ECD)	Suppressed conductivity
Suppressor type	ASRS (4 mm) at 112 mA	CSRS-ULTRA (4 mm) at 100 mA
Sample run time	20 minutes	30 minutes

Table 3.1: *System conditions for isochratic analysis of NO_3^- and NH_4^+ ions by Ion Chromatography*

In order to quantify any post-blast residues detected in the test samples, a range of calibration standards were produced. NO_3^- and NH_4^+ IC standards (1000 mg/L; Fisher Chemical, UK), were used to make calibration standards (0.5, 1, 10, 25, 50, 75, 100, 250, 500, 750 and 1000 mg/L) by serial dilution of 1000 mg/L stock solutions into clean 10 cm^3 and 25 cm^3 volumetric flasks, made up to volume with 18 MΩ DI water. Calibration lines were constructed by plotting the peak area against the concentration of each ion injected onto the column and linearity was evaluated via the R^2 regression coefficient of determination. Quality assurance (QA) samples of each ion (90 mg/L and 650 mg/L) were also produced in order to assess the accuracy of the calibration. Calibration standards were analysed at the beginning and end of each sequence and QA samples analysed at multiple points throughout. All calibration and QA standards were injected in triplicate.

Calibration: Ammonium

The retention time of the NH_4^+ ion was ~8.44 minutes. Figure 3.9 shows a calibration graph for the 12 ammonium standards (between 0.5 mg/L and 1000 mg/L) injected. The accuracy of the calibration was tested by injecting QA standards; which as seen in figure 3.9, did not accurately fit the calibrant plot, which was slightly curved at higher concentrations due to the suppressed mode settings used on the IC (discussed further in chapter 4, section 4.5).

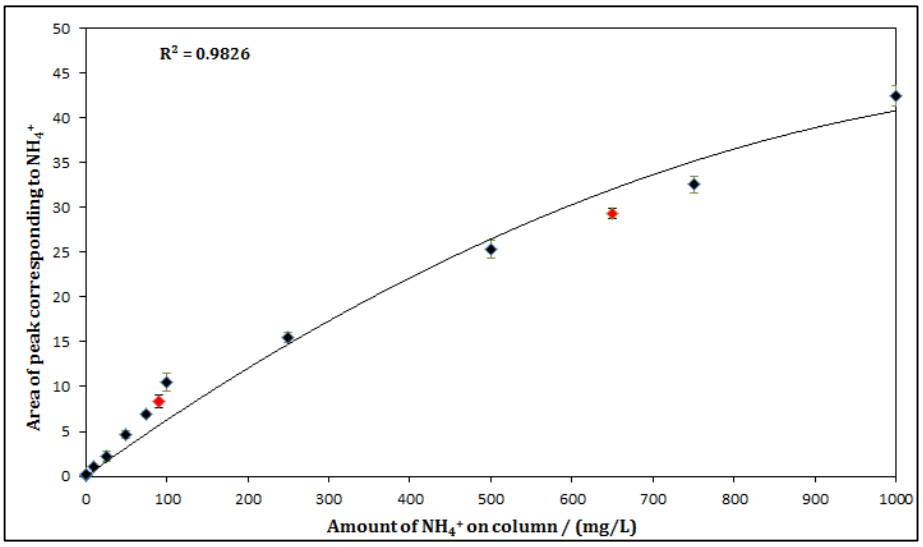

Figure 3.9*: Calibration graph of ammonium standards. R² value is inset. Calibrants were made up at concentrations of 0.5, 1, 10, 25, 50, 75, 100, 250, 500, 750 and 1000 mg/L. Calibrants marked in red were QA standards (90 mg/L and 650 mg/L) injected to assess the accuracy of the calibration.*

The lower ammonium concentrations alone (0.5 mg/L to 50 mg/L) produced a linear calibration fit (R^2 of 0.9973; figure 3.10). The mass of a NH_4^+ in the majority of experimentally generated samples was calculated using this calibration fit.

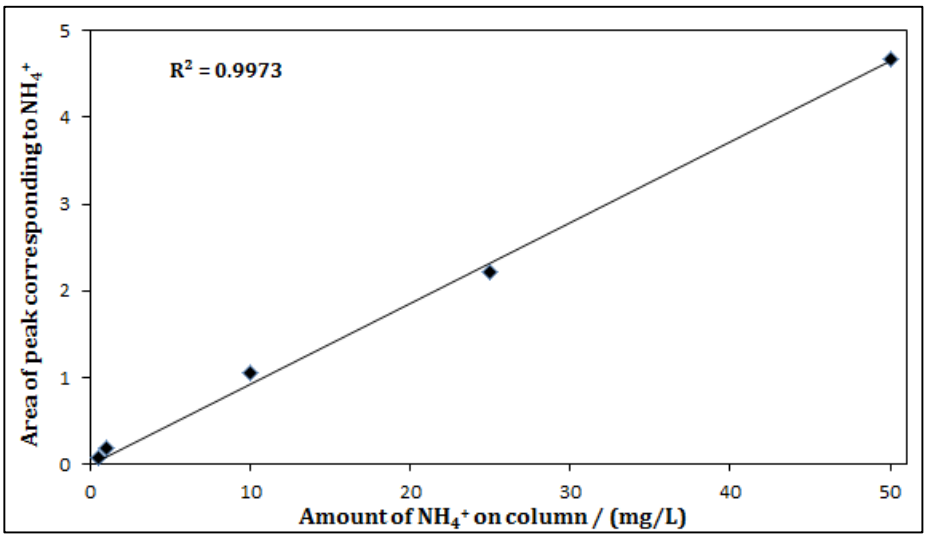

Figure 3.10*: Calibration graph of 0.5 to 50 mg/L ammonium standards. R² value is inset. The calibration fit at lower concentrations was linear compared to that including higher concentrations.*

The higher range of ammonium concentrations (200 mg/L to 1000 mg/L) produced a linear calibration (R^2 of 0.9869; figure 3.11). The mass within experimental samples which produced greater peak areas were calculated using this separate calibration fit.

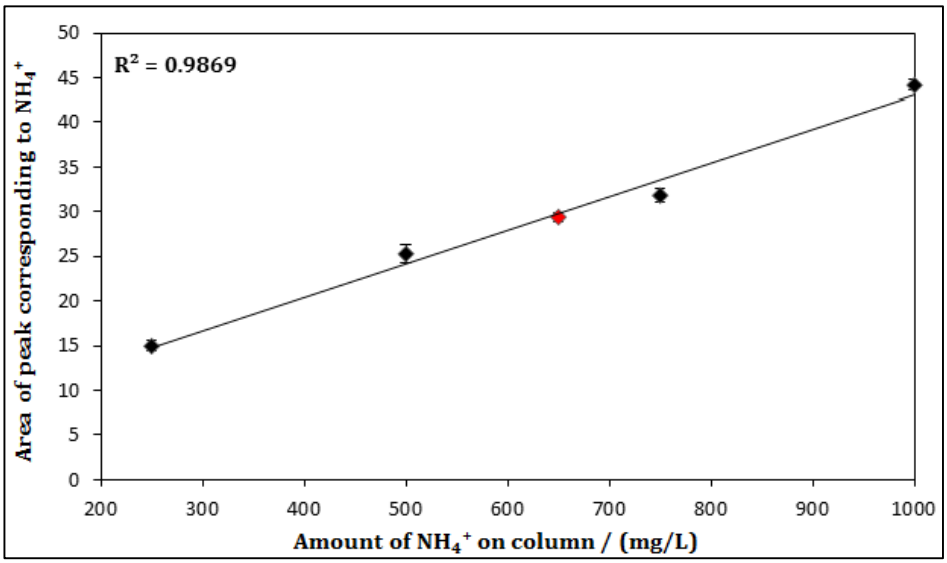

Figure 3.11*: Calibration graph of 200 to 1000 mg/L ammonium standards. R^2 value is inset. The calibration fit at higher concentrations was linear compared to that including lower concentrations.*

The precision of the technique was validated by injecting all samples in triplicate and at different times throughout a sequence – the responses were reproducible with similar peak areas produced for each of the repeated injections (indicated by the small error bars on figures 3.9, 3.10 and 3.11). The standard deviations of repeated injections of calibration and QA samples ranged between 0.09 mg/L and 3.5 mg/L, indication high level of precision for each of the detected concentrations from the sample vials. The limit of detection (LOD) for NH_4^+ was within the range of 0.1 mg/L and 0.5 mg/L of NH_4^+; test samples therefore containing less than 0.5 mg/L would not have produced peak resolution sufficient for quantification of ammonium.

Calibration: Nitrate

The retention time of the NO_3^- ion detected in samples was ~5.8 minutes. The R^2 value (0.9819) for the nitrate indicated a high degree of linearity in the response of the detector between 0.1 mg/L and 1000 mg/L of NO_3^- loaded onto the column (figure 3.12).

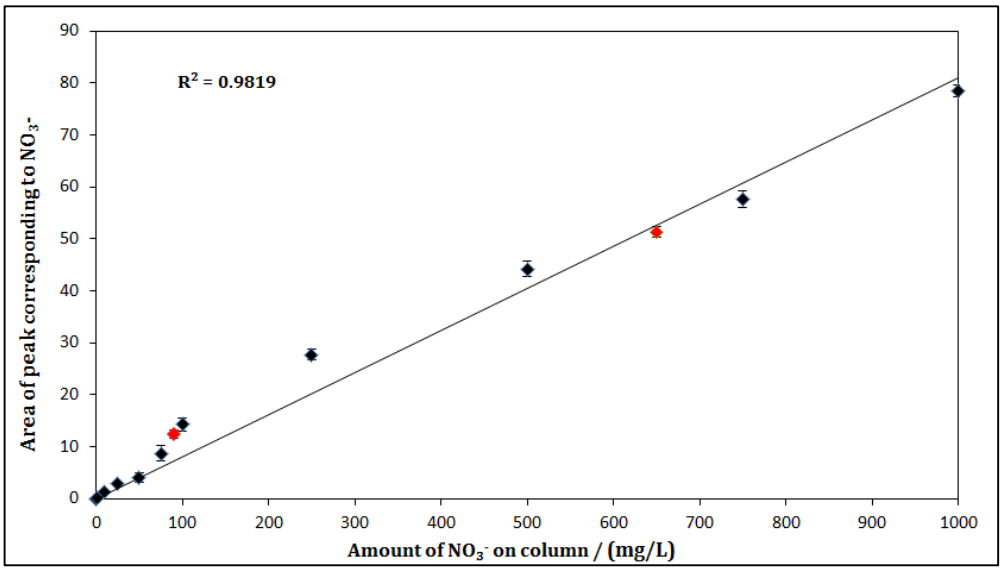

***Figure 3.12**: Calibration graph of nitrate standards. R^2 values are inset. Calibrants were made up at concentrations of 0.1, 1, 10, 25, 50, 75, 100, 250, 500, 750 and 1000 mg/L. Calibrants marked in red are the QA standards (90 mg/L and 650 mg/L) injected to assess the accuracy of the calibration.*

The accuracy of the calibration, which was tested by injecting QA standards (90 mg/L and 650 mg/L, marked in red on figure 3.12), was not reliable for the nitrate ions; indicated by the varying fit of the QA data points to the calibration line. The 650 mg/L QA standard fit the calibration line well, however the lower concentration QA standard did not (figure 3.12). The lower concentration region alone (0.1 mg/L to 50 mg/L) showed that whilst the data points did not fit the calibration line exactly, the linearity of the standards was still high with an R^2 value of 0.9525 (figure 3.13). A linear calibration was therefore used for quantification of test samples.

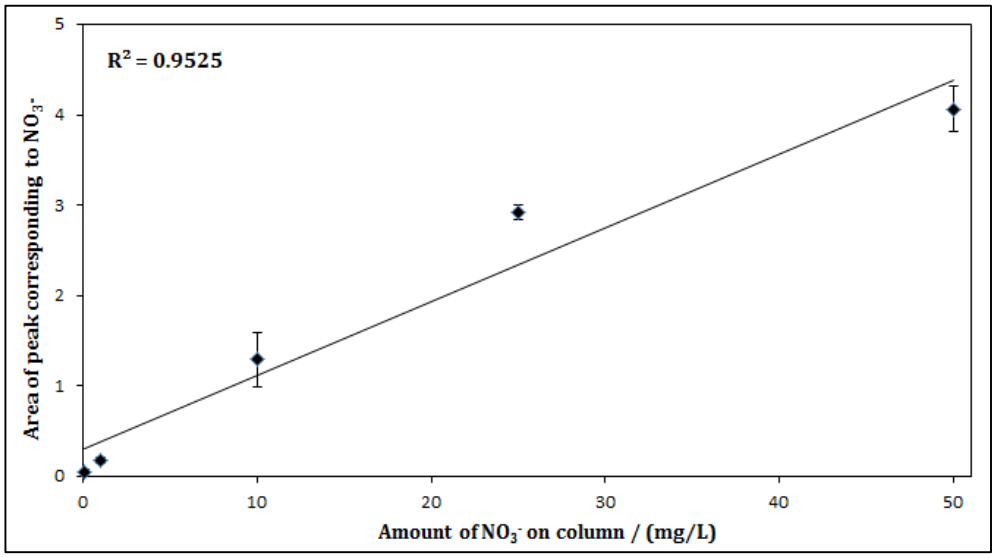

***Figure 3.13**: Calibration graph of 0.1mg/L to 50 mg/L nitrate standards. R^2 value inset.*

Responses for all triplicate injections of standards at different times were reproducible with little deviation observed in the measured peak areas (indicated by the small error bars on data points in figures 3.12 and 3.13). The limit of detection for NO_3^- was determined to be 0.1 mg/L of NO_3^-; nitrate concentrations lower than this in test samples would not have been detected.

Blank deionised water samples were run in-between each test sample in order to minimise sample carry over. All test, control and blank samples were analysed in triplicate. The mass of each ion in test samples was calculated by interpolating results from the calibration curves. The average residue mass of the triplicate injections were plotted against the distance from the centre at which the sample was collected.

3.4.3 Inductively Coupled Plasma –Atomic Emission Spectroscopy: Aluminium

Of the remaining 8.5 cm^3 aqueous residue samples in the glass vials, 4.95 cm^3 aliquots of each were pipetted into 10 cm^3 conical polypropylene auto-sampler tubes with snap cap lids (PerkinElmer, UK). Samples were made up to 5 cm^3 with the addition of 0.05 cm^3 nitric acid (ACS reagent, >90 %, Sigma Aldrich, UK). Samples were analysed for aluminium content using ICP–AES (Varian 720–ES with SPS3 autosampler) against matrix matched standards of 1 % (volume fraction) nitric acid, which was added to each sample to stabilise any aluminium present. Readings were 2 second integrations repeated 4 times with a 1 minute wash between samples with 1 % nitric acid in 18 MΩ DI water to minimise carry-over. All sample data was analysed using Bruker Expert software (version 2.3).

3.4.4 High Performance Liquid Chromatography – Mass Spectrometry: RDX

Analysis of post-blast residues was performed using HPLC-MS with electrospray ionisation (ESI).

3.4.4.1 Direct Infusion ESI Mass Spectrometry Analysis of RDX

The ionisation, fragmentation and selectivity for RDX detection was established with direct infusion methods. ESI-MS analyses were performed on an LTQ Ion Trap instrument (Thermo Finnigan, San Jose, CA, USA) fitted with an ESI source. RDX standards (1 mg/L, 5 mg/L, 10 mg/L and 100 mg/L made in ACN) were spiked with 0.1 % hydrochloric acid (HCl) in order to form $[M+^{35}Cl]^-$ and $[M+^{37}Cl]^-$ adducts amenable to ESI and injected using a 250 µl Hamilton syringe. For direct infusion and fragmentation tests the LTQ mass spectrometer was operated as detailed in table 3.2. A full scan was initially conducted followed by manual collection of MS^2 (fragmentation) spectra of the $[M+^{35}Cl]^-$ ion, corresponding to m/z 257, in order to verify the molecule as RDX.

Instrument Aspect	Setting
Scan mode	Full (for MS experiments)
Ion mode	Negative
ESI spray voltage	~5 kV
Capillary temperature	275 °C
Sheath gas flow rate	N/A
Auxiliary gas flow rate	N/A
m/z range scanned	100 to 1000 (then 100 to 700)
Data collection mode	Centroid
Number of scans	3 averaged 'micro-scans'
Injection time	200 ms
MS2 experiments	
Collision energy	35.0
Isolation widths	2.00
Number of scans	3 averaged 'micro-scans'
Injection time	200 ms

Table 3.2: *Direct Infusion and fragmentation test settings, other conditions of the LTQ were tuned automatically using the auto-tune function for m/z 257 of the [M+^{35}Cl]$^{-}$ precursor ion in order to increase sensitivity for RDX.*

An automated program was then set-up based on these acquisitions. The data system of the LTQ used a data processing and instrument control software called Xcalibur™; consisting of instrument set-up, acquisition and data processing. All data files generated were reviewed with the qualitative browser. The fragmentation results from the direct infusion tests can be found in Appendix A (section A.1).

3.4.4.2 HPLC–MS Analysis of Post-Blast RDX Samples

Chromatographic separation was performed with a Dionex UltiMate 3000 single capillary LC system (Camberley, Surrey, UK). The LC system consisted of SRD-3600 solvent rack with on-line vacuum degasser, LPG-3600 low pressure dual gradient micro-pumping 76 system, WPS-3000 auto-sampler and FLM-3100 thermostated flow manager.

LC was conducted using an Acquity BEH C-18 column (2.1 mm x 50 mm, 1.7 µm particles, 130 Å, Waters, Ireland). The mobile phases were 0.1 % HCl in DI water (mobile phase A) and 0.1 % HCl in acetonitrile (mobile phase B); the flow rate was 200 µl/min. A gradient program is shown in figure 3.14 and table 3.3. The total sample run time was 10 minutes. Samples were held in an auto-sampler tray kept at 4 °C and 10 µl injections were loaded onto the column via a partial sample loop mechanism. Between sample injections, the injector and needle were flushed and washed with methanol to minimise carry-over of RDX between injections. Blank acetone and acetonitrile samples were also run throughout the sample sequence to ensure minimal carry over.

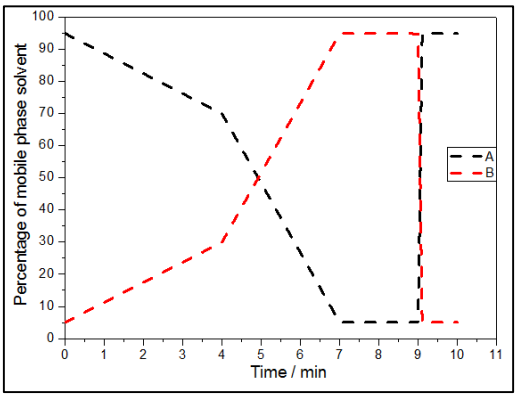

Time /min	Flow rate/ (µl/min)	%A[a]	%B[b]
0	200	95	5
4	200	70	30
7	200	5	95
9	200	5	95
9.1	200	95	5
10	200	95	5

[a]Mobile phase A: DI H_2O + 0.1% HCl
[b]Mobile phase B: ACN + 0.1% HCl

Figure 3.14 *(left),* ***Table 3.3*** *(right): Gradient profile used for the separation of RDX using HPLC.*

The reconstructed ion chromatogram of a 10 mg/L injection of RDX showed the retention time (RT) was ~2.39 minutes (figure 3.15) using the mobile phase program detailed above (table 3.3).

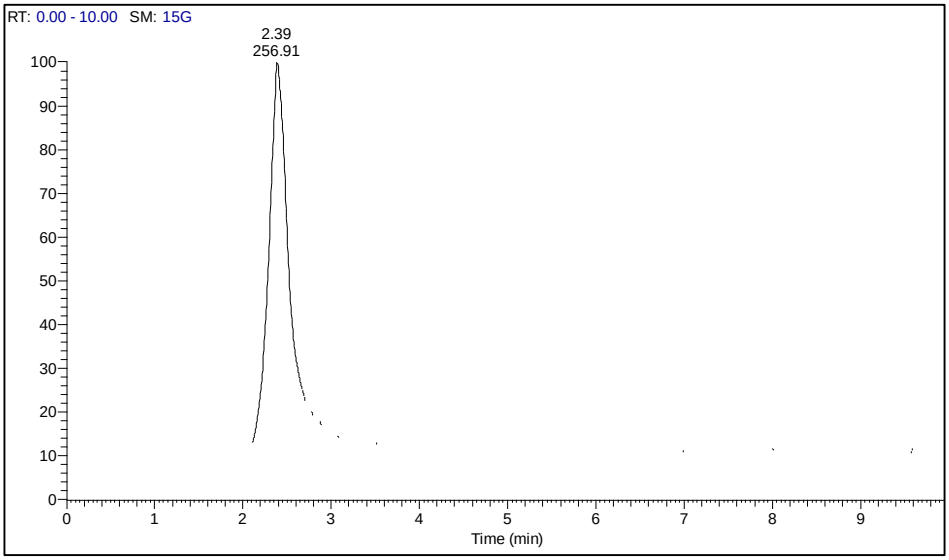

Figure 3.15*: RIC for m/z 256.91 (RT: 2.39 minutes, signal intensity: 5.74 x 10^6). Separation achieved on a 2.1 mm (i.d.) x 50 mm, C18 (1.7 µm, 130 Å) column at a flow rate of 200 µL/min. Mobile phase A was DI H_2O, 0.1% HCl, and B was ACN, 0.1% HCl. Total sample run time was 10 minutes.*

For the analysis of test samples, adducts were generated by spiking each sample with HCl (0.1 % volume fraction). The samples were loaded via a sample loop by means of a six-port valve, and the column eluent was continuously directed into the electrospray source of the LTQ mass spectrometer. For MS analyses coupled to the chromatography instrumentation the LTQ mass spectrometer was operated as detailed in table 3.4.

Instrument Aspect	Setting
Scan mode	Selected ion monitoring (SIM)
SIM settings	For *m/z* 257 and *m/z* 259
Ion mode	Negative
ESI spray voltage	5.00 kV
Spray current	30 µA
Capillary temperature	275 °C
Sheath gas flow rate	30.0
Auxiliary gas flow rate	10.0
Collision energy	35.0
Isolation widths	2.00
Number of scans	5 averaged 'micro-scans'
Injection time	200 ms

Table 3.4: *LTQ instrument settings for HPLC-MS analyses of RDX samples over the 10 minute HPLC time period; the SIM mode was set for m/z 257 and m/z 259 corresponding to the [M+^{35}Cl]⁻ and [M+^{37}Cl]⁻ precursor ions, respectively. Scans were obtained over 200 ms to ensure enough data points were obtained across the chromatographic peaks. Scans (typically 30) were averaged for each spectra.*

Using this method, the mass spectrum (figure 3.16) at RT 2.39 minutes corresponding to the peak in the above RIC (figure 3.15), displayed a high signal intensity (1.07 x 10^6) for ions of *m/z* 257 and 259 confirming its origin as RDX.

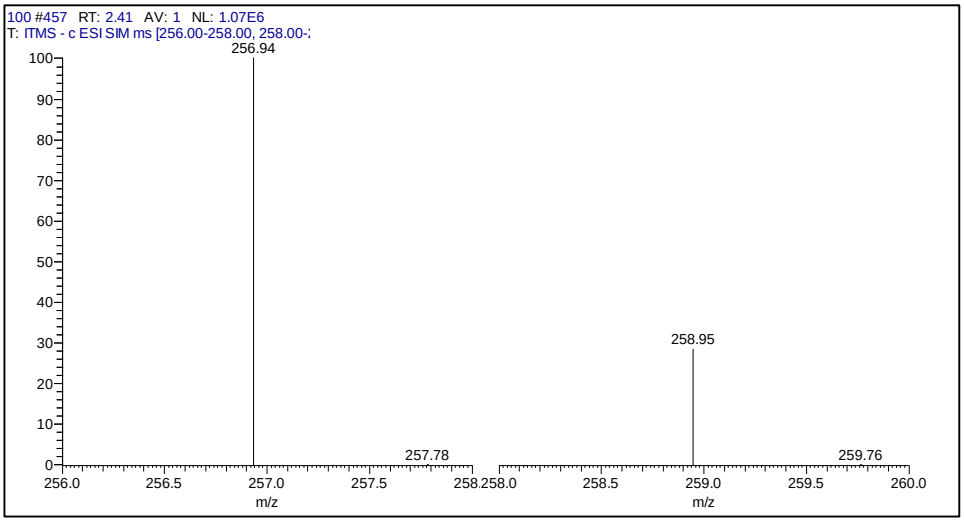

Figure 3.16: *Mass spectrum of peak at RT of 2.39 (from figure 3.14). SIM scan collision energy was 35, spray voltage 5 kV, spray current 30 µA, sheath and auxiliary gases had flow rates of 30 and 10, capillary temperature 275 °C. Isolation widths were 2.00 and scans consisted of 5 averaged 'micro-scans' per scan event, each with a maximum injection time of 200 ms.*

3.4.4.3 Validation of HPLC-MS method

Calibration standards (0.1, 0.5, 1, 2.5, 5, 10, 25, 50, 75, 100, 250, 500, 750 and 1000 mg/L) and quality control (8 mg/L, 125 mg/L and 300 mg/L) samples of RDX were made in ACN by serial dilution of a primary stock solution of 1000 mg/L of RDX in ACN. Each calibration standard was analysed at the start, middle and end of each sequence, and quality control samples were injected throughout the sequence in triplicate. Quantification was performed

using the ion chromatograms generated for the $[M+^{35}Cl]^-$ and $[M+^{37}Cl]^-$ parent ions. Triplicate analyses were performed on the same day. All generated data files were analysed using XCalibur™ software.

Calibration lines were constructed by plotting the peak area against the concentration of RDX injected onto the column and calculated using linear regression. Figure 3.17 shows a calibration graph of the RDX standards, the R^2 value (0.9971) indicated a high degree of linearity in the response of the detector between 0.1 mg/L and 500 mg/L of RDX loaded onto the column.

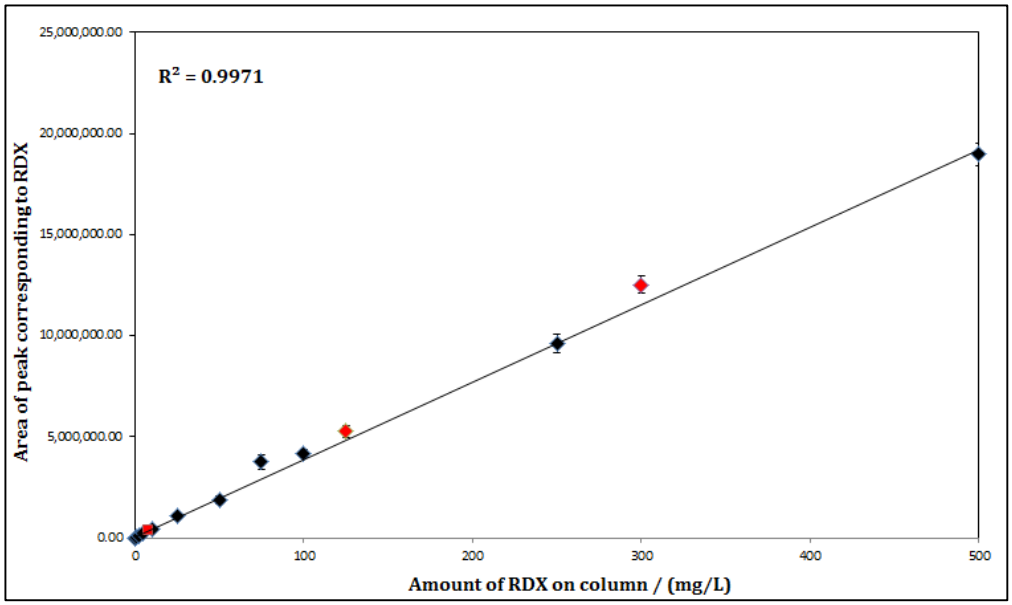

***Figure 3.17**: Calibration graph of RDX standards. R^2 value is inset. Calibrants were made up at concentrations of 0.1, 0.5, 1, 5, 10, 25, 50, 75, 100, 250 and 500 mg/L. Calibrants marked in red are the QA standards (8 mg/L, 125 mg/L and 300 mg/L) injected to assess the accuracy of the calibration.*

The 0.1 mg/L to 50 mg/L lower RDX concentration region, depicted in figure 3.18 for clarity, showed the response of most calibrants, including the 8 mg/L QA standard, was close to the calibration line. The error bars represent the standard deviation of the mean average of the measurements from triplicate injections.

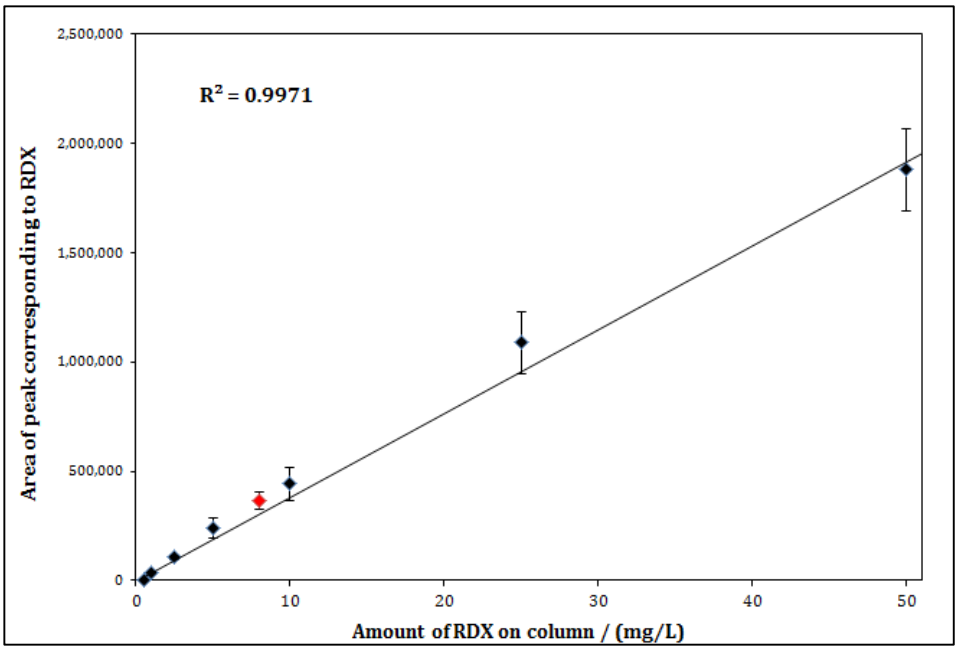

***Figure 3.18**: Calibration graph of 0.1 mg/L to 50 mg/L RDX standards. R^2 value is inset. Calibrant marked in red is the QA standards (8 mg/L) injected to assess the accuracy of the calibration.*

The QA standards (8 mg/L, 125 mg/L and 300 mg/L, marked in red points on figure 3.17) fitted the calibration well demonstrating a more accurate calibration, particularly at lower concentrations (< 150 mg/L) than from that of the nitrate or ammonium ions. Responses for repeated injections of all standards were reproducible with similar peak areas produced indicating suitable precision of the calibration. The LOD for RDX was determined to be within the range of 0.1 mg/L and 0.5 mg/L of RDX (see Appendix A, section A.2, for further details).

All post-blast RDX samples collected following the unconfined 0.5 kg, 1 kg and 2 kg composition firings, as well as the confined vehicle firings were analysed with HPLC-MS. A typical analytical sample also consisted of triplicate injections of RDX calibration standards, quality control standards run throughout the sequence, and blank samples of deionised water and acetonitrile injected twice between test samples. All test samples results are reported in the absolute mass of RDX within each sample, calculated based on the concentration of residue compared to the calibration, and the amount (2 cm^2) of total sample collected from each sampling plate.

3.4.4.4 Recovery of RDX: Method efficiency

The efficiency of recovering RDX throughout various aspects of the sampling and extraction procedure was assessed by conducting tests with known amounts of RDX (this was not possible to do with the AlAN explosive compositions). Here, the steps that were evaluated and the corresponding average percentage of RDX recovered are provided (table 3.5). Full method details and results for the recovery tests are presented in Appendix A (section A.3).

The results indicated the efficiency of the procedures in recovering RDX from a sampling plate were not 100 %, with the majority of sample loss occurring during the swabbing phase itself, and losses occurring subsequently throughout the extraction procedure. Reported values of RDX amounts detected in post-blast samples would therefore not be an accurate indication of the actual mass of residue material deposited upon the sampling plate but rather a relative value due to loss of analyte during sampling and analysis. The estimated error of the residue measurements based on the average losses incurred (table 3.5) was approximately 25 % overall.

Efficiency test	Percentage of RDX recovered
Swabbing efficiency (from spiked plates)	40 % to 70 %
Extraction procedure (from spiked swabs)	44 % to 73%
Filtering process (from spiked solvent)	66 % to 85%
Evaporation process (from spiked solvent)	80 % to 93%

Table 3.5*: Recovery tests of RDX per efficiency test. Test were conducted by spiking known amounts of RDX at different stages of the sampling and extraction procedure and analysed by HPLC-MS.*

3.5 Particle Analysis

The SEM stubs collected from the sampling poles around each of the detonation centres were analysed to assess the deposition of any particulate matter upon them and ascertain the morphology, elemental composition and chemical composition of any deposited material.

3.5.1 Morphology and Elemental Composition (SEM-EDX)

The stub surfaces were scanned for particulate residues with a scanning electron microscope. A Hitachi S-3400N Variable Pressure SEM with Energy Dispersive X-ray Spectrometer (EDS) was used for this analysis and allowed the study of the non-conductive samples without a metal or carbon coating. The SEM was operated with a beam current of 10 nA; spot size of 30 μm; chamber pressure of 20 Pa to 30 Pa (air); and working distance of 10 mm with accelerating potential voltage of 5 kV to 15 kV to minimise charging. Imaging was conducted in secondary electron imaging (SEI) mode and magnifications required to identify particles ranged between 50 to >4500. The EDS spectrometer consisted of a silicon detector. All data was processed using Oxford Instruments Microanalysis System user interface.

Stubs were removed from holders using tweezers and placed onto the stage. The morphology of the post-blast particles was compared to that of the explosive prior to detonation; specimens of the 'raw' material, or original explosive compositions, were also mounted onto aluminium SEM stubs upon which double sided adhesive carbon discs were

attached. The elemental composition of detected particles via EDS analysis was also compared to that of the raw material.

3.5.2 Chemical Identity

Raman Spectroscopy

Raman spectroscopy was used to obtain chemical composition information for the particles observed with SEM. Analyses were conducted on a Renishaw InVia Raman microscope with a 785 nm near infrared laser operated at 0.1 % to 10 % intensity. Five accumulations were collected over 10 second exposures. Stubs were not removed from their individual holders; the caps were removed and the stub kept within the bottom of the holder which itself was placed onto the Raman microscope stage. Both the raw materials (undetonated samples of the PE4 and AlAN) and post-blast samples collected after the firings were analysed.

SEM – Structural Chemical Analyser

Particles which could not be seen with the resolution of the Raman microscope, but were apparent on the stubs when assessed with SEM (principally those retrieved following the RDX based detonations), were analysed with a combined SEM-Raman system using a Structural and Chemical Analyser for scanning electron microscopes (SEM–SCA) (Renishaw). The operating conditions for the SEM component and the Raman system were as the conditions described for each above.

Particle Induced X-Ray Emission (PIXE)

PIXE was used to map the elements present in particles on the stub surfaces. PIXE measurements were collected with a 2.5 MeV proton beam and an 80 mm^2 Si(Li) detector with a 12.5 mm Be window installed at an angle of 45° at a distance of between 25 mm and 70 mm from the sample. Multiple points on the SEM stub surfaces were measured and three accumulations of each spot were obtained.

MeV Secondary Ion Mass Spectrometry (MeV SIMS)

Further compositional analyses were attempted on the particles recovered following the RDX based detonations with ambient pressure MeV-SIMS at the University of Surrey Ion Beam Centre using a 2 MV Tandetron (High Voltage Engineering, Europe). As a primary ion source a 8.8 MeV O_4^+ beam, focused to 4 mm resolution, was used; the focusing system was a quadrupole triplet system (Oxford Microbeams Ltd.). The MeV ion beam exited the vacuum system through a Si_3N_4 window (100 nm thick) and was scanned electrostatically over an area of 2 mm^2. Secondary ions generated at atmospheric pressure were transferred through the capillary (50 cm length, 700 mm and 2 mm distance from spot size) carried by Helium flow into Q-TOF orthogonal mass spectrometer. The detection interval was from

m/z 50 to *m/z* 1000. The working current was <50 pA and spectra were collected for *t* = 5 min.

3.6 Simulation

Simulation experiments of residue distribution were conducted by the Norwegian Defence Research Establishment (FFI) using Computational Fluid Dynamics (CFD) techniques, the results were compared to range experiments with 0.5 kg AlAN charges fired at ERDA. The simulation experiment was based on detonations of a spherical 0.5 kg explosive charge (TNT equivalent to AlAN). TNT was used for the simulation experiments as the detonation characteristics in the literature[176,177] are better defined compared to improvised mixtures such as AlAN. Due to the novelty of this comparative study, this was therefore deemed an appropriate initial methodology.

The simulation was conducted in two steps; the first was of the initial detonation in a hemispherical domain (figures 3.19 and 3.20) without any wind effects. The flow data (velocity, pressure, temperature, air density) and particle data (location and speed) was computed for the first ~3 ms of the detonation.

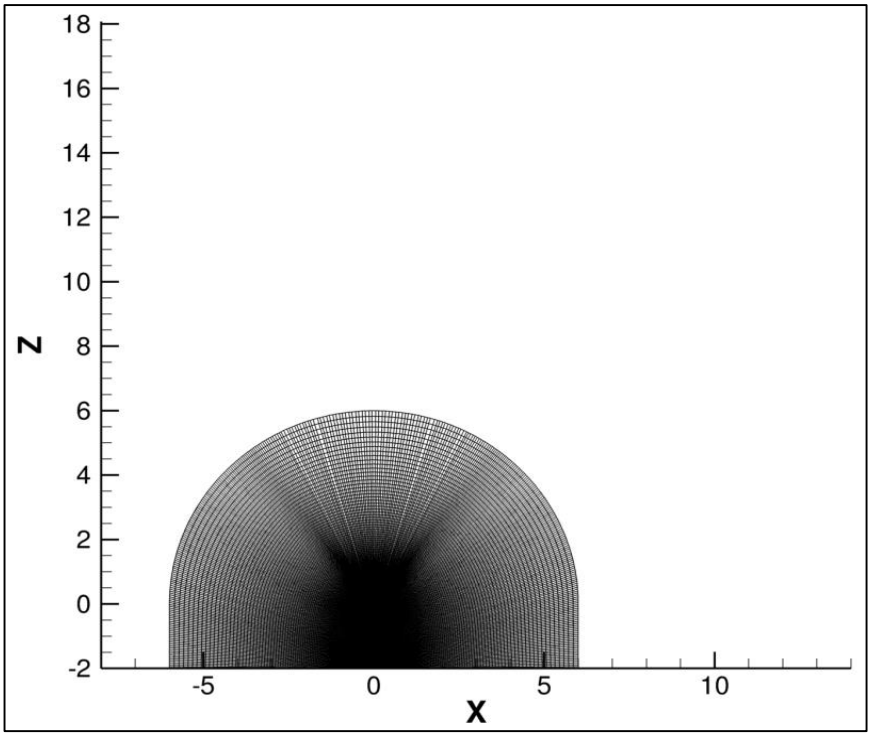

***Figure 3.19**: XZ mesh for simulation in step 1.*

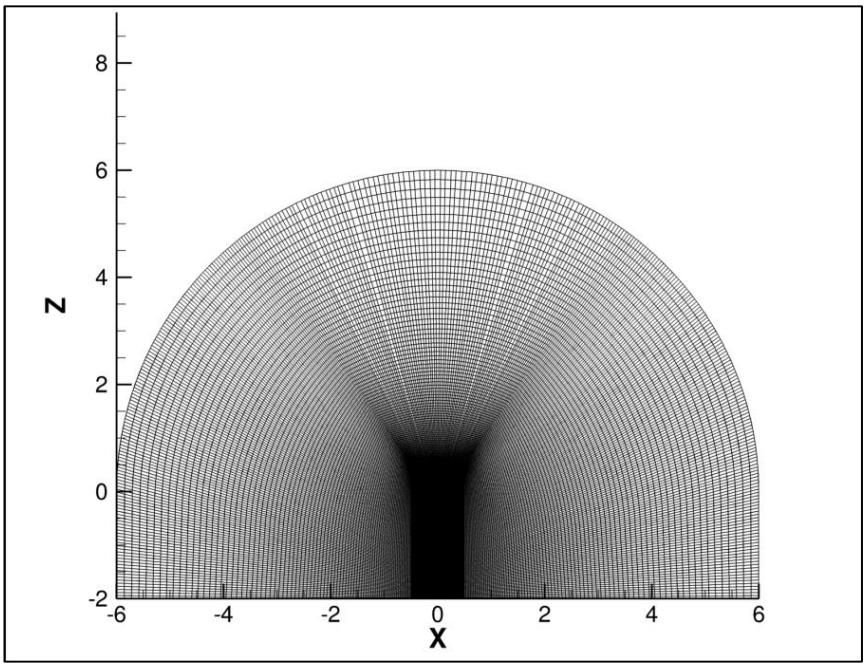

Figure 3.20*: Closer view of XZ mesh for simulation in step 1showing individual grids in the domain.*

This data was then interpolated onto a larger rectangular domain for the remainder of the simulation (the second step), when wind/buoyancy was factored in. This second mesh (figure 3.21) was coarser and larger in terms of physical dimensions than the first spherical mesh. The simulation process for each of the two steps was based on pre-processing, solving and post-processing phases.

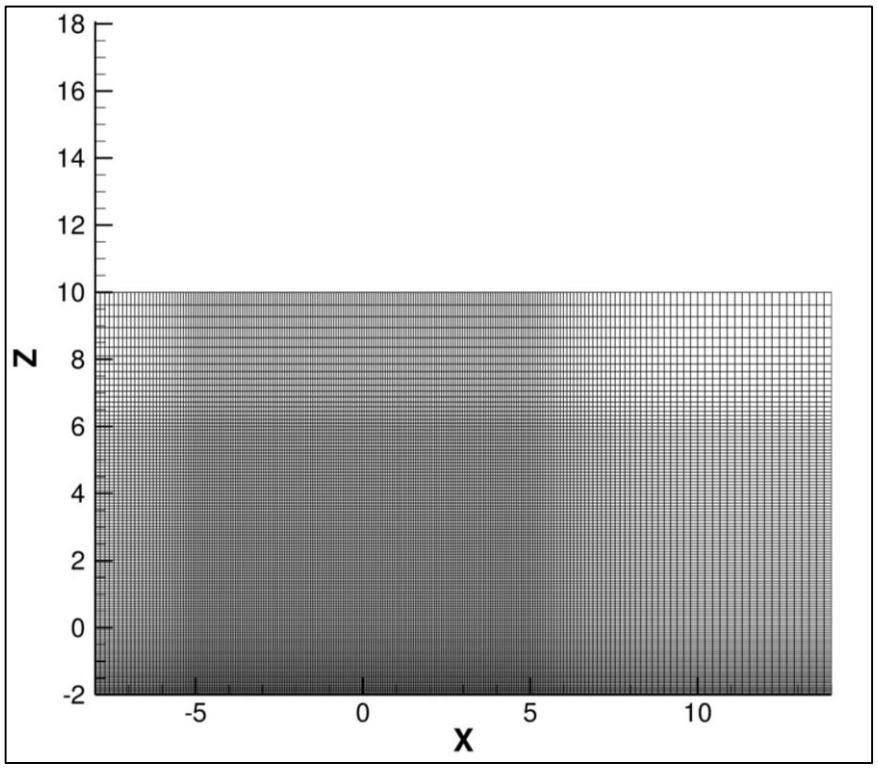

Figure 3.21*: XZ mesh for simulation in step 2.*

The simulation data inputted into each step is given in table 3.6.

	STEP 1	**STEP 2**
Initial conditions		
Motion	Zero velocity	Initialized with data from the end of the first simulation (by interpolation).
Atmospheric pressure	101,200 Pa	"
Temperature	300 K	"
Density of air	1.225 kg/m^3	"
Charge initialisation	from Autodyn data (external software)	"
Boundary	**STEP 1**	**STEP 2**
Ground	Adiabatic walls on all sides*	Adiabatic wall (reflect pressure waves).
Inflow		Turbulence boundary layer inflow with wind velocity***
Outflow and top boundaries		"Sponge" zone to absorb pressure waves and prevent reflection; so flow will largely exit the domain.
Side boundaries:		Periodic with a dissipative upwind numerical scheme to try to damp out pressure fluctuations.
Particles	**STEP 1**	**STEP 2**
Number	2 million particles**	Initialized at the same locations (and velocities) as at the end of step 1.
Size	1, 10, 50, 100, 200 μm in diameter	"
Density	As water (998 kg/m^3)	"
Position	Initially on spherical "shell"	"
Domain (mesh) extent	**STEP 1**	**STEP 2**
(x,y,z)-coordinates	From (-6,-6,-2) to (6,6,6) (units [m]).	From (-8,-11,-2) to (14,11,10) (units [m])
Mesh size		
Cell number	5.3 million cells	6 million cells
Size	Smallest cell approx. 1 x 1 x 1 cm^3	Smallest cell approx. 7 x 7 x 4 cm^3.
Time step		
Step	Constant time step of 0.0005 ms	Approx. between 0.01 ms and 0.1 ms.
Time simulated	Simulated from 0 to 3 ms.	From 3 ms 5.5 s

Table 3.6*: Step 1 and step 2 conditions for the numerical simulation of residue distribution*

*Suitable when the simulation is stopped before any information from the detonation (e.g. the pressure wave) reaches the domain boundaries).

**This many particles were used in order to ensure at least a few hundred particles (on average) would hit each of the simulated "collection plates" used to compare with experimental data.

***(corresponding to experimental measurements)

3.6.2.1 Pre-processing

As information such as pressure fluctuations travelled with the speed of sound in dry air (330 m/s) and the smallest mesh size used for the second step was 4 cm, the time step was no more than 0.1 ms ($0.004/330 = 10^{-4}$ s). It therefore took approximately one week to simulate wind of ~2 m/s propagating through the ~10 m mesh.

3.6.2.2 Solving

Due to the highly turbulent nature of a detonation event, the governing equations for the fluid flow (in the form of the Navier-Stokes equations) were coupled with a turbulence model. A Large Eddy Simulation (LES) model was used, which solved Navier-Stokes equations for compressible fluids accounting explicitly for the large turbulent scale and used a model to estimate the effects of the smaller scales. The governing equations were solved in an Eulerian frame of reference, i.e. considering the fluid flow in time and space from a fixed position.

As well as the movement of the flow field, the movement of the explosive residue particles was also computed. Particle transport was simulated in a Lagrangian frame of reference whereby each individual particle was tracked in space and time, thus producing a pathline for each particle. The force balance for each particle, based on Newton's second law, was integrated in time to determine the particle trajectory. The governing equations were solved using the Charles flow solver, which solves the compressible Navier-Stokes equation using an explicit time stepping scheme.

3.6.2.3 Post-processing

The flow and particle data at the end of the first step of the simulation was saved to disk and interpolated onto the mesh used in step 2. Data from the simulation was saved to disk at regular time intervals so that the data could be analysed after the whole simulation was completed. All the flow variables at these times were then available to be inspected.

The main post-processing of the present particle data consisted of computing particle trajectories for the duration of the simulation. These trajectories were used to determine how many particles would pass through a plate of size 20 cm x 30 cm and therefore equal to the ones used in the experiments, placed at regular intervals of 1 m in multiple directions, at a height of 2 m from the ground and at ground level. This data was compared with the relative particle deposition (in logscale) obtained from the experiments.

CHAPTER 4: STUDIES WITH 0.5 KG ALAN AND PE4 CHARGES

4.1 Introduction

The results from repeated unconfined firings of spherical 0.5 kg AlAN and PE4 (RDX-based) explosive compositions are presented here. Residues were collected from sampling sites positioned 2 m high from the ground (and therefore at the charge height) in four different orientations around the charge centre and multi-increment distances up to 10 m from it. Sampling plates were swabbed for residues, and samples collected following the AlAN firings were analysed with IC for nitrate and ammonium analytes and with ICP-AES for aluminium content. HPLC-MS was used to analyse RDX content from samples collected following the PE4 firings.

Results of the AlAN charges are presented first (section 4.2) followed by those of the RDX composition (section 4.3). Within each set of results, the residue concentrations are compared to the physical aspects of the detonation in order of their occurrence; the blast overpressures produced, the fireball volume and the subsequent movement of the smoke plume. The results are then summarised (section 4.4) and discussed in comparison to relevant theory and studies in the literature (section 4.5).

4.2 Results from 0.5 kg AlAN Firings

4.2.1 Inorganic Post-blast Residue Results

No nitrate, ammonium or aluminium were detected in the control samples of blank DI water, blank swab samples, blank steel plate samples or in DI water injected between test samples. Therefore any target analytes detected in post-blast samples were attributed to the explosive residue in that sample. All results regarding residue amount are reported in absolute mass (i.e. either mg or μg) recovered from each sampled plate around the detonations.

The total residue amounts (i.e. the summed nitrate, ammonium and aluminium masses from all four measured orientations around the charge centre and averaged across all six repeated firings) are presented in comparison to the theoretically proposed inverse square law distribution in figure 4.1.

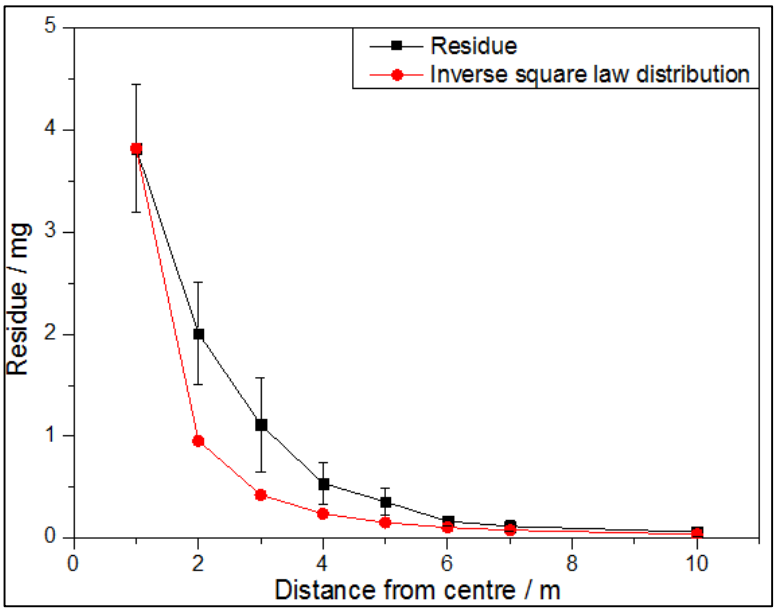

***Figure 4.1**: Averaged inorganic residue concentrations (summed NO_3^-, NH_4^+ and Al) from all 0.5 kg AlAN firings (in black) compared to the theoretical inverse square distribution pattern (in red). Values for each distance were the totals from four sampled orientations. Both trends were similar, however experimental values at 2 m, 3 m, 4 m and 5 m were higher than the theoretical values.*

The theoretical trend was calculated using the experimental value from 1 m around the charge centre (3.82 ± 0.63 mg). Clearly, the experimental results (based on the summed initial residue amount at the 1 m point) followed the same trend as the theoretical data (decreasing with increasing distance), however the absolute values are the relevant parameter and based on these, the experimental measurements did not appear to follow an inverse square distribution. The summed and averaged experimental values were higher at the 2 m, 3 m, 4 m and 5 m measured points (2.00 ± 0.5 mg, 1.11 ± 0.46 mg, 0.54 ± 0.20 mg, 0.36 ± 0.13 mg) than the theoretical ones (0.96 mg, 0.42 mg, 0.24 mg, 0.15 mg). The measured and theoretical values further from the charge centre (at 6 m, 7 m and 10 m) were similar.

However, by comparing the experimental results without the value obtained from the closest measured point (at 1 m from the charge centre), against the inverse square law (1/d^2; where d is the distance from the charge centre), the theoretical and experimental datasets showed a strongly positive correlation with an R^2 value of 0.9838 (figure 4.2).

Having compared the totalled residue values, the individual trends from each inorganic analyte were plotted to assess each distribution when compared against the theoretically proposed trend.

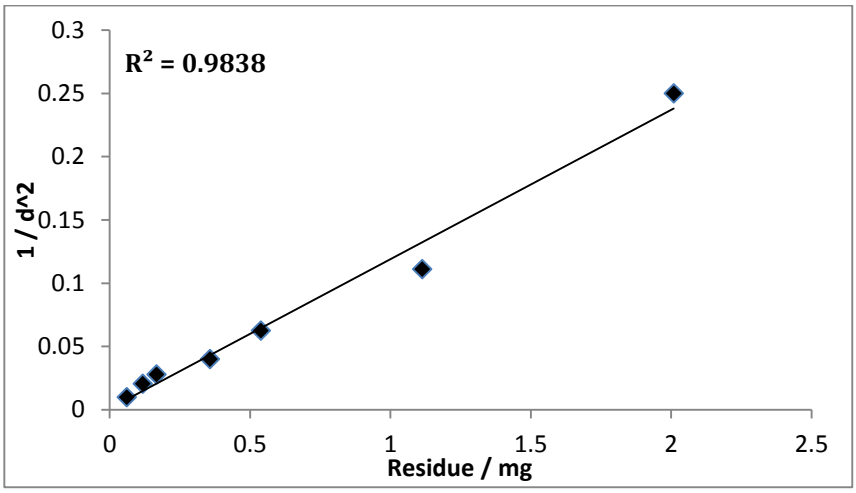

***Figure 4.2**: The (averaged) experimental data fit to the theoretical model (1/d^2) generated an R^2 of 0.9838 (plotted without the experimental measurement obtained at 1m from the charge).*

Nitrate

The nitrate mass range detected from post-blast samples was between 0 mg and 14 mg; the limit of detection for the nitrate anion was established as 0.2 µg, no samples containing lower nitrate amounts were quantified. The nitrate amounts between 1 m and 10 m, (summed from all four sampled orientations around the charge centre and averaged across the repeated firings), decreased with increasing distance from the centre, similarly to the theoretical trend of nitrate distribution (figure 4.3).

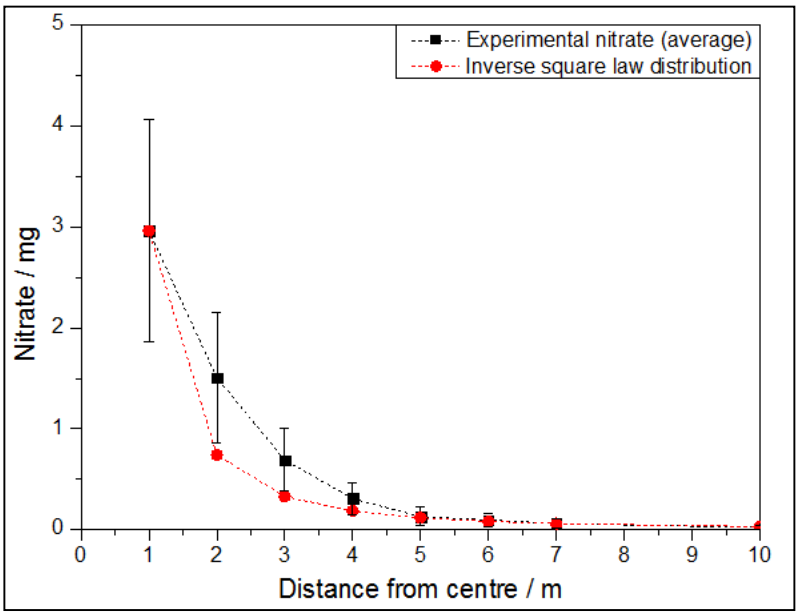

***Figure 4.3**: Averaged nitrate amounts from 0.5 kg AlAN firings (in black) compared to the theoretical inverse square law distribution pattern (in red). Values for each distance were totals from all four sampled orientations. Both trends were similar, however the experimental values at 2 m to 4 m were higher than the theoretical values. The error bars represent standard deviations based on the mean average measurement of the mass recovered from six repeated firings.*

The theoretical inverse square distribution was initiated with the experimental measurement at 1 m (2.96 ± 1.31 mg); it was clear that the two distributions followed the same trend (figure 4.3). However, the absolute mass in experimental samples at 2 m, 3 m and 4 m was larger (2 m; 1.51 ± 0.65 mg, 3 m; 0.69 ± 0.35 mg, 4 m; 0.31 ± 0.19 mg) than the respective theoretical ones (2 m; 0.74 mg, 3 m; 0.33 mg, 4 m; 0.19 mg) and therefore the experimental results did not appear to correspond to the model.

By excluding the experimental datum obtained from the sample collected at 1 m from the charge, and plotting the results against '1/d^2' (where d is the distance from the charge placement), the averaged nitrate distribution was shown to correspond well with the inverse square law, generating an R^2 coefficient of 0.9958 (figure 4.4).

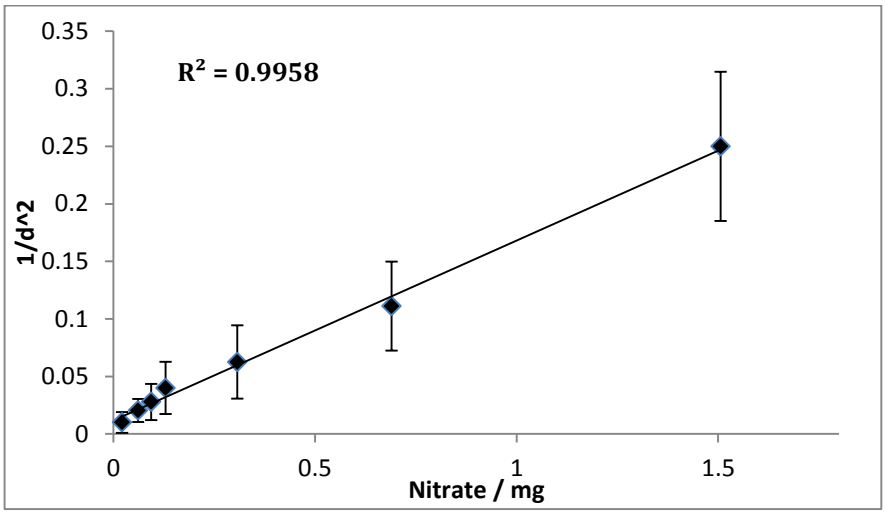

Figure 4.4:*Plot of experimentally determined nitrate amounts recovered 2 m to 10 m from the charges against 1/d^2 demonstrating linearity between the two datasets (R^2 inset).*

The error bars on figures 4.3 and 4.4 represented the standard deviation of the mean average amount of nitrate recovered from the six repeated firings of the 0.5 kg AlAN charges. The amounts recovered between the firings were not comparable; with greater deviations at the closer sampled distances (Δ = at 1 m: ± 40 %, at 2 m: ± 50 % and at 3 m: ± ~60 %). Figure 4.5 shows the individual nitrate plots from each firing.

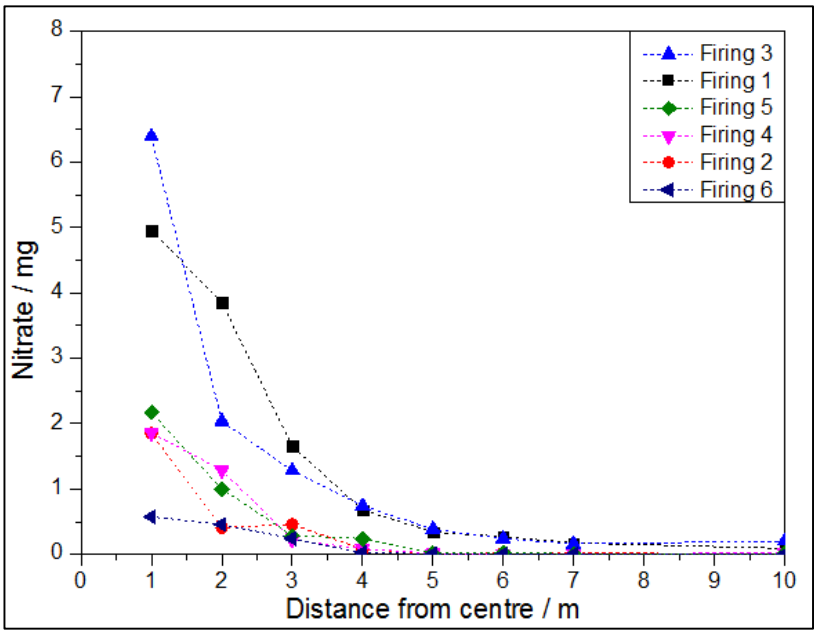

***Figure 4.5**: Nitrate mass recovered from each 0.5 kg AlAN firing. Each value is the totalled amount from all four sampled orientations around the charge centre. The trend of decreasing nitrate mass with increasing distance from the centre was apparent from all firings. The actual mass detected from each measured distance was not reproducible between firings.*

The trend of decreasing mass with increasing distance from the centre was still apparent following each of the individual firings; however, each firing produced varying amounts of residue (figure 4.5). The masses detected in samples collected at 1 m and 2 m following firings 1 and 3 (black and blue plots in figure 4.5) were higher (firing 1: 4.95 mg and 3.85 mg; firing 3: 6.39 mg and 2.04 mg, respectively) than all other amounts (0.0005 mg and 2.17 mg) (figure 4.5). The majority of the highest nitrate amounts from each distribution were detected within five metres from the detonation.

Ammonium

The ammonium mass range detected from post-blast samples varied between 0 mg and 3 mg; the limit of detection for the ammonium anion was established as 1 µg, no samples containing less ammonium than this were quantified. The summed ammonium amounts detected from the four sampled orientations around the detonation centre were averaged across the repeated firings (figure 4.6); the ammonium decreased in mass with increasing distance from the centre.

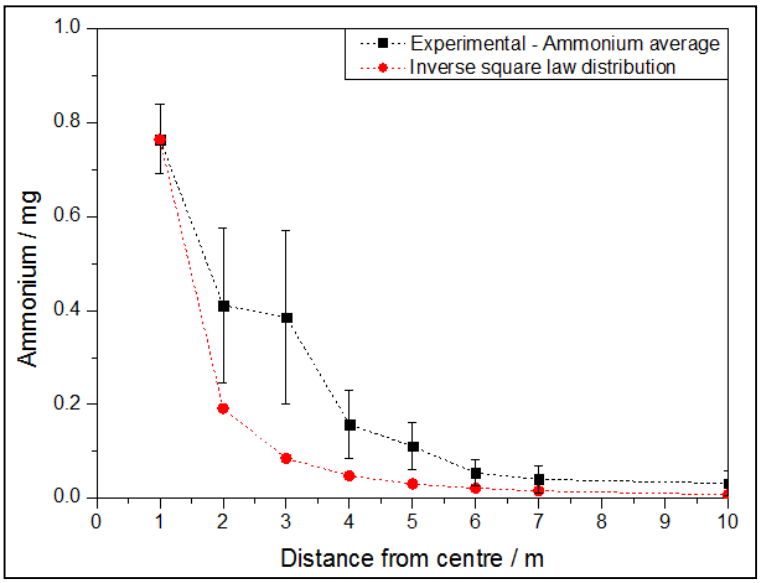

***Figure 4.6**: Averaged ammonium amounts detected following all 0.5 kg AlAN firings (in black) compared to the theoretical inverse square law distribution pattern (in red). Values for each distance were totals from all four sampled orientations. The trends were more dissimilar than the nitrate comparisons. The error bars represent standard deviations based on the mean average measurement of the mass recovered from six repeated firings.*

The experimental results were compared to the theoretical inverse square law with both plots starting with the measured experimental value at 1 m (0.77 ± 0.15 mg). Whilst both plots decreased with increasing distance, the experimentally determined ammonium amounts between 2 m and 7 m were at least double (0.41 ± 0.16 mg, 0.39 ± 0.2 mg, 0.16 ± 0.07 mg, 0.11 ± 0.05 mg, 0.05 ± 0.03 mg and 0.04 ± 0.03 mg) than the theoretically generated values (0.19 mg, 0.09 mg, 0.05 mg, 0.03 mg, 0.02 mg and 0.01 mg) (figure 4.6). Excluding the datum from 1 m, the plot of experimental data against '1/d^2' showed a positive correlation with the inverse square law (figure 4.7), although less linear (R^2 of 0.8047) than that found with the nitrate previously (cf. figure 4.4).

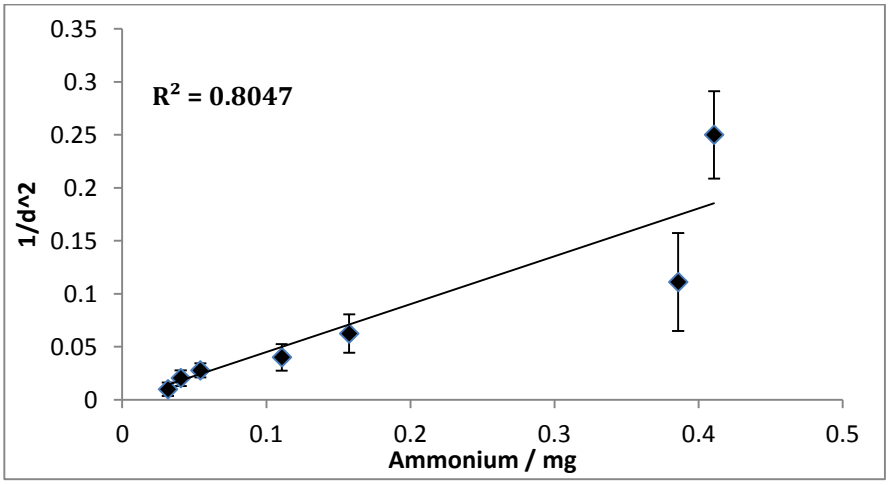

***Figure 4.7:** Plot of experimentally determined ammonium mass detected 2 m to 10 m from the charge centres against 1/d^2. The plot was not as linear as that produced from the nitrate analysis (R^2 inset).*

The majority of the highest ammonium masses were detected within six metres from the detonation centres. The error bars on figures 4.6 and 4.7 represented the standard deviation of the mean average amounts of ammonium detected from the six repeated firings of the 0.5 kg AlAN charges. The amounts recovered between firings were not comparable however, with greater deviations at closer (1 m to 4 m) sampled distances (Δ = at 1 m; ± ~14 %, at 2 m; ± ~40 %, at 3 m; ± 48 % and at 4 m; ± 45 %). Figure 4.8 shows the distributions from each individual firing; the majority of plots exhibited similar trends and the outlier was firing 3. Following firing 3 the amount of ammonium increased between 1 m and 3 m from the centre (1 m; 0.79 mg → 2 m; 0.99 mg → 3 m; 1.09 mg) after which it decreased at further sampled distances.

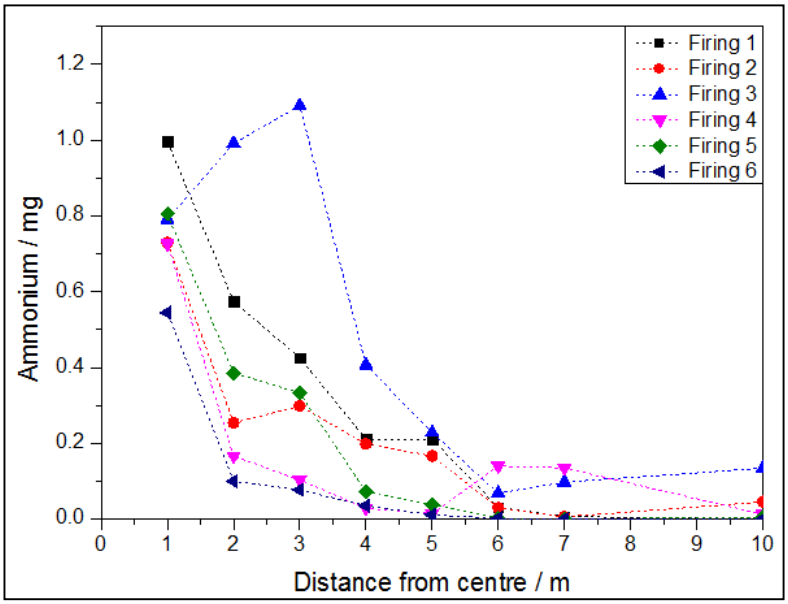

***Figure 4.8**: Ammonium mass distribution following each 0.5 kg AlAN firing. Each value is the totalled amount from all four sampled orientations around the charge centre. The trend of decreasing ammonium mass with increasing distance from the centre was apparent from most firings. Actual masses for each measured distance were not reproducible between firings.*

Without the anomalous data from firing 3, the trend of ammonium mass (averaged across the other five firings) did not vary greatly from previous comparisons to the theoretical model; the R^2 value (0.8562) showed a slightly more linear fit however (figure 4.9).

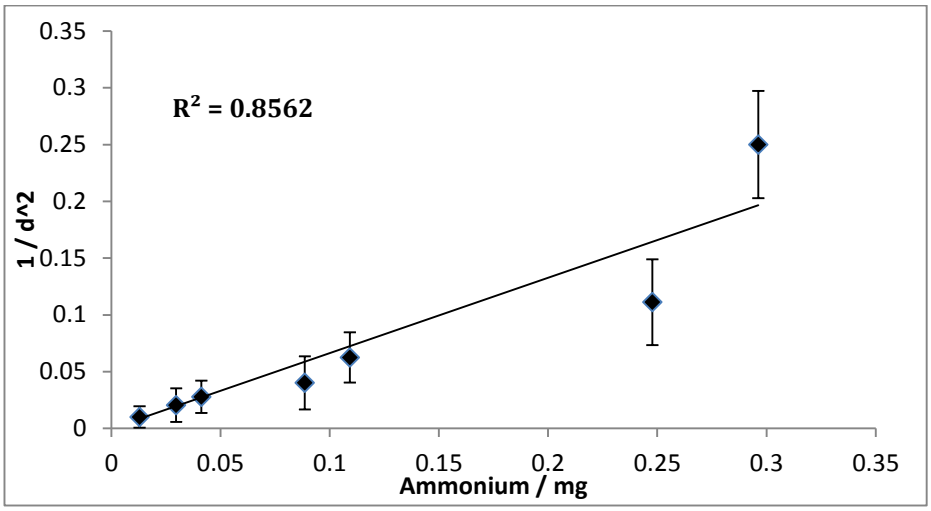

***Figure 4.9**: As for figure 4.7, without the anomalous results from firing #3. The plot against the inverse square law distribution was slightly more linear than previously. Experimental and theoretical data fit generated an R^2 of 0.8562.*

Aluminium

The overall mass range of aluminium detected in post-blast samples was between 0 µg and 1 µg. The amounts of aluminium (summed from all four sampled orientations around the centre) were averaged across the repeated firings; figure 4.10 shows the aluminium did not decrease linearly with increasing distance as the nitrate and ammonium analytes did.

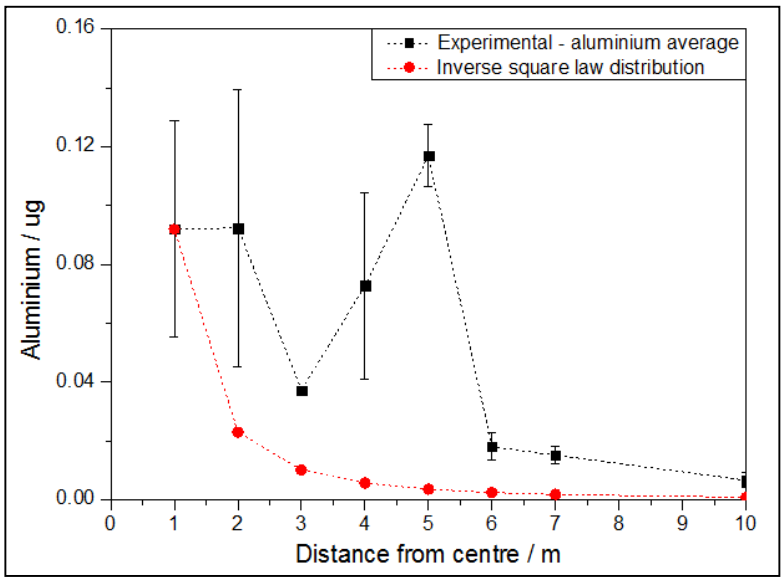

***Figure 4.10**: Averaged aluminium amounts detected from all 0.5 kg AlAN firings (black) compared to the theoretical inverse square law distribution pattern (red) which was generated using the experimental datum obtained at 1 m. Values for each distance were totals from all four sampled orientations. The experimental trend was not consistent with the theoretical comparison. The error bars represent standard deviations of the mean average based on 6 repeated firings.*

The experimental results were compared to the theoretical inverse square law (figure 4.10) where both plots started with the first measured experimental value from 1 m (0.09 ± 0.04 µg). The averaged experimental results for aluminium were clearly inconsistent with the theoretical pattern. Even when omitting the datum from sites sampled at 1 m, the plot against the inverse square distribution did not improve (figure 4.11), unlike the case of the nitrate and ammonium mass comparisons. Furthermore, unlike the nitrate and ammonium trends, the largest amounts of aluminium were detected five metres from the centre as opposed to the closest sampled distance of one metre.

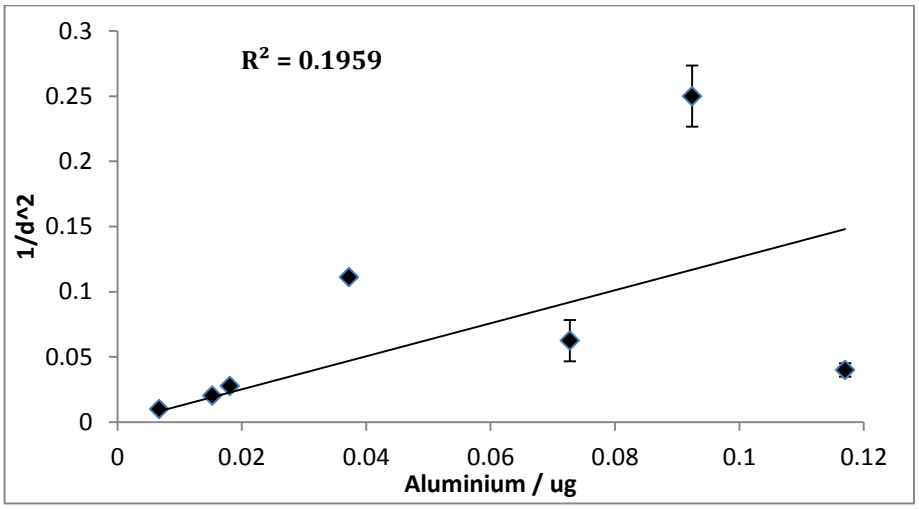

***Figure 4.11**: Plot of experimentally determined aluminium mass against the inverse square law distribution. Linearity was not as good (R^2 of 0.1959) as demonstrated by the nitrate or ammonium.*

The error bars on figures 4.10 and 4.11 represented the standard deviation of the aluminium amounts recovered from the six repeated firings of the 0.5 kg AlAN charges. Based on these, the masses detected between firings appeared incomparable; however when assessing the trend from each individual firing (figure 4.12) it was clear that aluminium concentrations from all firings, apart from firing 1 (black plot in figure 4.12), were reproducible.

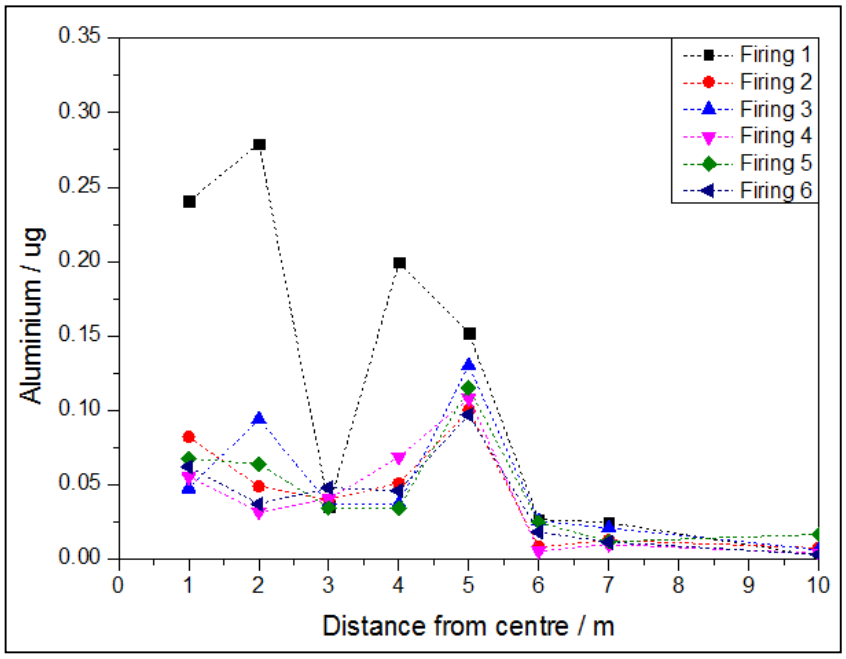

***Figure 4.12**: Aluminium amounts detected following each 0.5 kg AlAN firing. Each value is the totalled amount from all four sampled orientations. No firings exhibited a linear decrease in residue mass, most had a 'spike' in mass at 5 m. All firings produced reproducible Al amounts apart from firing 1.*

No firings produced linear aluminium distributions and the outliers from firing 1 were the values at 1 m, 2 m and 4 m (0.24 µg, 0.28 µg and 0.20 µg) (figure 4.12). No improvement was observed between the theoretical and averaged experimental comparisons when data from firing 1 was excluded (figure 4.13) although the error margins for the average aluminium mass detected at each measured distance were smaller.

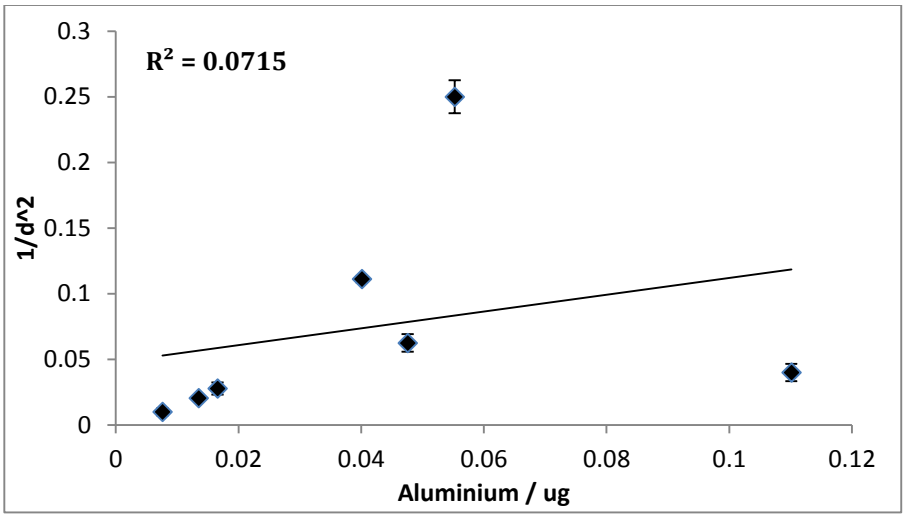

***Figure 4.13**: As for figure 4.11, without the anomalous results of aluminium mass from firing #1. The fit between the experimentally determined aluminium and the inverse square distribution was not linear (R^2 = 0.0715).*

Comparison between Inorganic Analytes

The anomalous results from the nitrate recovery were from firings 1 and 3, for ammonium this was the case for firing 3, and for aluminium the outliers were detected following firing 1. No methodological inconsistencies were apparent between any of the firings.

The overall mass range of NO_3^- detected (0 mg to 14 mg) was higher than that of the NH_4^+ levels (0 mg to 3 mg). Based on the molar masses of each ion in the AN molecule (nitrate:ammonium ~4:1), an exact stoichiometric relationship between the two analytes was not observed, the approximate ratio between the two analytes here was ~7:1. The mass range of aluminium detected (0 µg to 1 µg) was three orders of magnitude lower than that of the nitrate and ammonium (figure 4.14). The error bars in figure 4.14 represented the standard deviations of the mean average mass of residues recovered from each sampled distance between repeated firings.

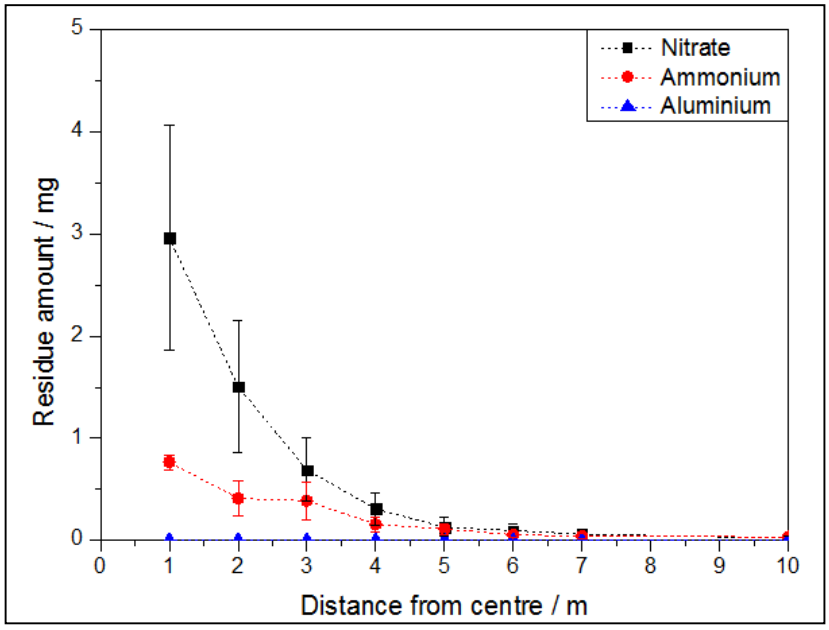

Figure 4.14*: Comparison between the average nitrate, ammonium and aluminium mass. The amounts are based on the totalled masses from four sampled orientations around each firing and averaged across six repeated firings. The error bars represent the deviation of the mean average between the results from repeated firings. The mass of nitrate detected was higher than ammonium, which was higher than aluminium, particularly between 1m and 5 m.*

Having established the general distribution trends from the inorganic analytes, the effects of the various blast phenomena (overpressure, fireball dynamics and smoke plume movement) were compared to the residue concentrations.

4.2.2 Blast Overpressure

Blast pressure profiles were measured with piezoelectric gauges at 1 m, 2 m, 3 m and 4 m from the detonation centres during each firing. All pressure profiles exhibited an initial overpressure peak with a positive phase duration followed by a negative pressure phase. The arrival times of the blast wave, peak overpressures, duration of positive phases and impulse areas for each sensor are displayed in table 4.1; the mean average values from all six repeat firing are presented with the standard deviation of the measurements. Data tables of measurements from each individual sensor during each firing are in appendix B.

Sensor position / m		Arrival time /ms	Positive duration /ms	Impulse area/ (kPa/ms)	Peak over-pressure /kPa
1	**Mean**	**0.981**	**1.31**	**35.6**	**167**
	S.D.	0.112	0.110	7.13	28.6
2	**Mean**	**3.15**	**1.70**	**29.9**	**61.3**
	S.D.	0.270	0.116	6.04	13.7
3	**Mean**	**5.60**	**1.82**	**20.4**	**32.8**
	S.D.	0.280	0.130	3.33	4.86
4	**Mean**	**8.39**	**2.03**	**16.6**	**21.4**
	S.D.	0.322	0.0663	2.83	2.66

Table 4.1: *Mean average and standard deviations (S.D.) of measurements of blast wave arrival time, positive duration, impulse and overpressure from sensors positioned 1 m to 4 m from charge centre from six repeat firings of 0.5 kg AlAN charges (3 sig. figs.). Measurements were made using piezoelectric pressure gauges and data recorded on a 25.0 MHz Nicolet oscilloscope.*

The average peak overpressure decreased with increasing distance from the charge centre (167 kPa → 61.3 kPa → 32.8 kPa → 21.4 kPa), as did the impulse areas, whilst the duration of each positive phase increased with increasing distance (table 4.1). Based on the arrival times and sensor positions the speed of the blast wave was calculated to be 1020 m s^{-1}, 635 m s^{-1}, 536 m s^{-1} and 477 m s^{-1} at 1 m, 2 m, 3 m and 4 m, respectively and therefore reduced in speed with increasing distance from the centre as expected. The standard deviation of the peak overpressure measurements decreased with increasing distance at which the measurement was recorded, a similar trend was produced for the calculated impulse areas; the reproducibility of the results improved further from the detonation centre.

The blast pressure profiles of each 0.5 kg AlAN firing are presented in figure 4.15. The pressure values had returned to stable ambient pressure by 10 ms at 1 m from the charge centre (figure 4.15a). Figure 4.15b shows the pressure returned to ambient between 14 ms and 16 ms at 2 m from the charge centre. At 3 m, the pressure returned to ambient level between 16 ms and 18 ms (figure 4.15c), and at 4 m the sensor measurements were not stable (figure 4.15d).

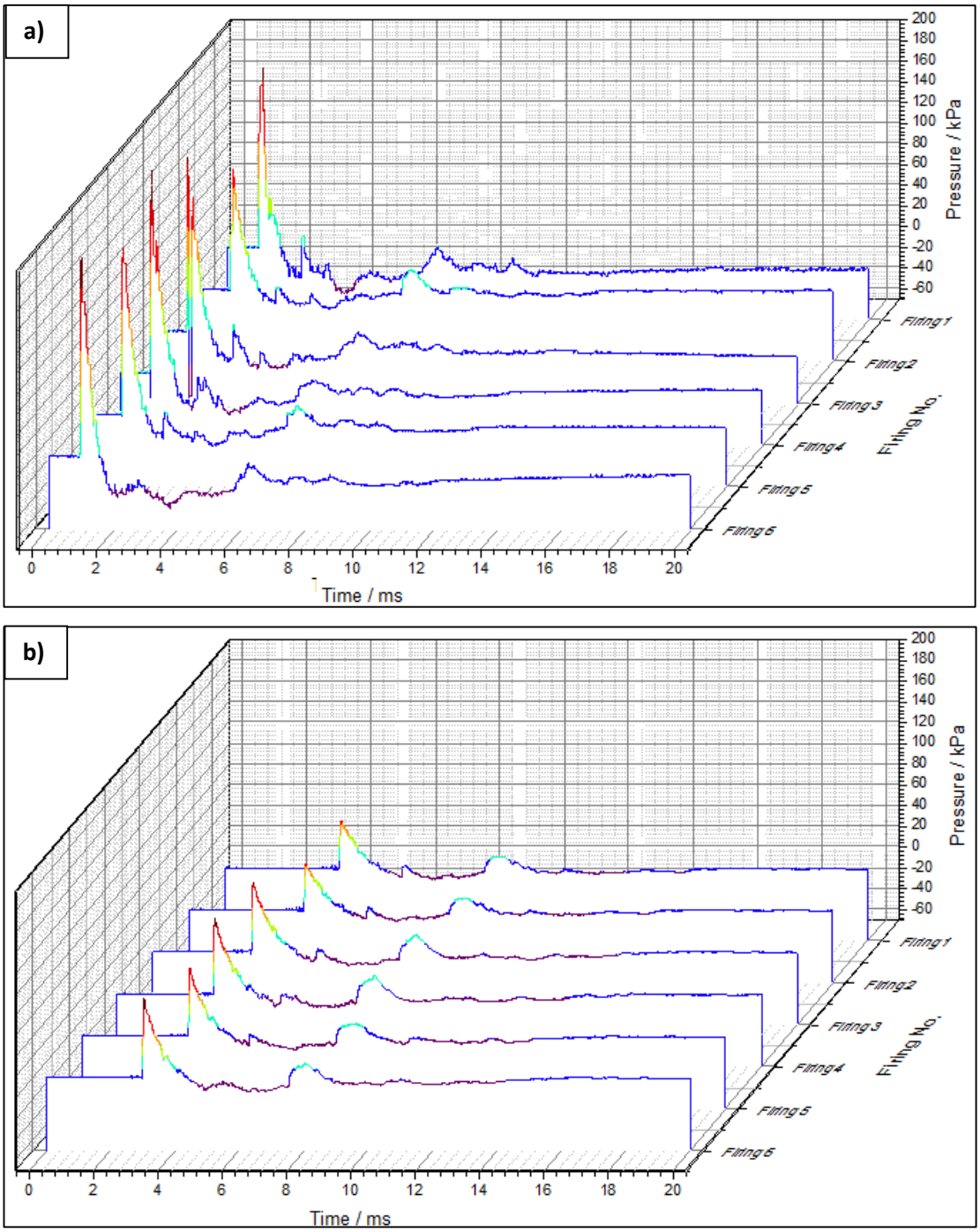

***Figure 4.15**: Blast pressure profiles (time /ms v. pressure /kPa) from sensors positioned 1 m (a) and 2 m (b) from the detonation centre of six repeated 0.5 kg AlAN firings. Measurements were recorded with piezoelectric gauges and processed with a Nicolet oscilloscope.*

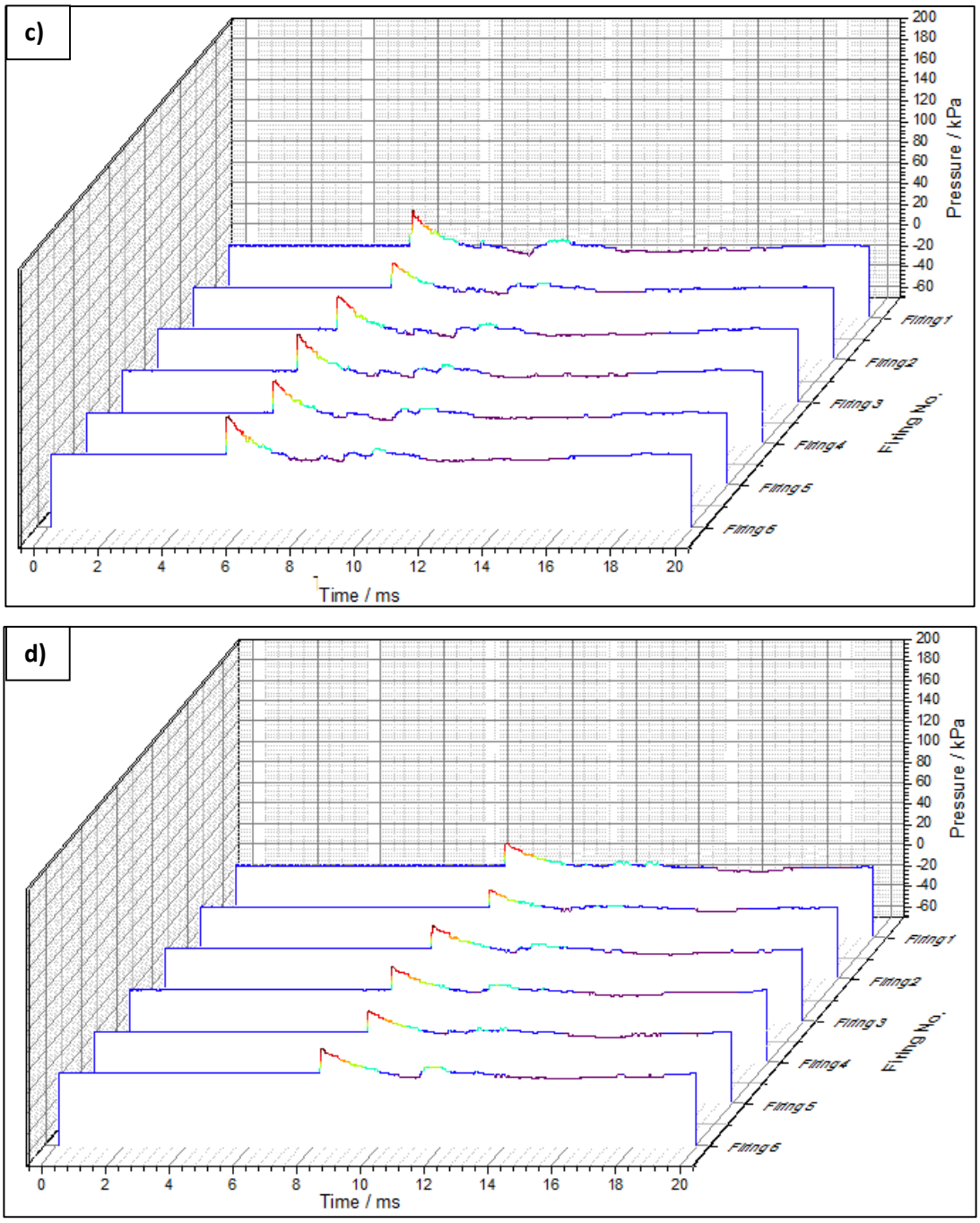

***Figure 4.15 cont'd**: Blast pressure profiles (time /ms v. pressure /kPa) from sensors positioned 3 m (c) and 4 m (d) from the detonation centre of six repeated 0.5 kg AlAN firings.*

Comparison between Overpressures and Post-blast Residues

Figure 4.16 shows the average blast overpressures (black solid line) recorded from the six firings of 0.5 kg AlAN at 1 m to 4 m compared to the averaged inorganic analyte concentrations (each depicted with a blue dashed line). The pressure trend was similar to that of the nitrate recovery between one and four metres in that both decreased with increasing distance. No other distinct comparisons were clear between overpressure and residue mass at each sampled distance.

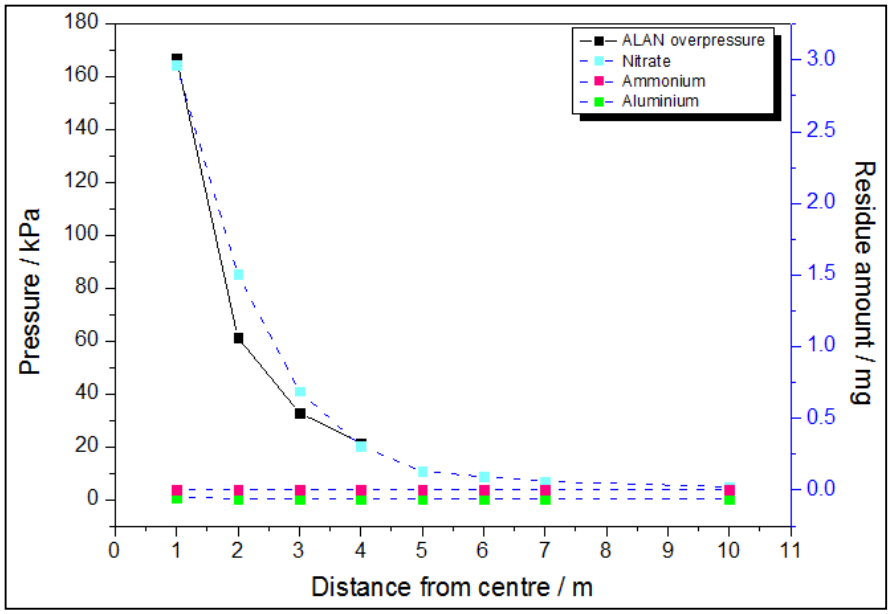

***Figure 4.16**: Comparison between average peak AlAN overpressure and inorganic analyte mass distributions.*

4.2.3 Fireball

In this section some representative stills from the AlAN detonations are presented, alongside estimates of the fireball volumes based on observations through the imaging footage. The observations are compared to the explosive residue distribution data. A full set of high speed imaging (HSI) and GoPro footage stills can be seen in appendix C.

Table 4.2 shows the approximated fireball and smoke plume volumes based on radii observed through HSI and GoPro footage of the detonations. Measurements were estimated at the time (t) when the largest fireball and smoke cloud radii were observed through the imaging in order to approximate the maximum radius around the charge where the highest temperatures may have extended (and assess if this correlated with the residue distribution patterns). For the 0.5 kg charges this was approximately at t = 24 ms and t = 800 ms for the fireball and smoke cloud, respectively, which were both assumed to have a spherical shape. The average fireball volume estimated for the 0.5 kg AlAN charges was ~10.0 m^3; the average smoke cloud was ~39.1 m^3.

Firing No.	Fireball radius /m	Fireball volume /m³	Smoke plume radius /m	Smoke plume volume /m³
1	1.20	7.20	1.90	28.7
2	1.50	14.1	1.80	24.4
3	1.60	17.2	2.00	33.5
4	1.20	7.20	2.20	44.6
5	1.20	7.20	2.00	33.5
6	1.20	7.20	2.50	65.4

***Table 4.2**: Estimated fireball and smoke cloud sizes based on HSI and GoPro footage of the 0.5 kg AlAN firings. All estimates are based on spherical volumes and given to 3 sig. figs.*

Figure 4.17, comprised of HSI stills a–d, show some of the phases of the AlAN detonations. In 4.17a (t = 1.01 ms) the edges of the fireball were not smooth but had a spiked appearance. Figure 4.17b shows the blast-wave (t = 1.67 ms); possible particulate matter was visible in the region between the blast-wave and fireball surface. At 3.00 ms (figure 4.17c) the blast-wave had moved further through the surrounding air and possible particulate matter was still visible as ejecta near the fireball surface. One of the closest sampling plates was seen to be partially engulfed at this stage by the fireball. The smoke plume (figure 4.17d) was also seen to engulf the closest positioned sampling plates southward from the detonation centre.

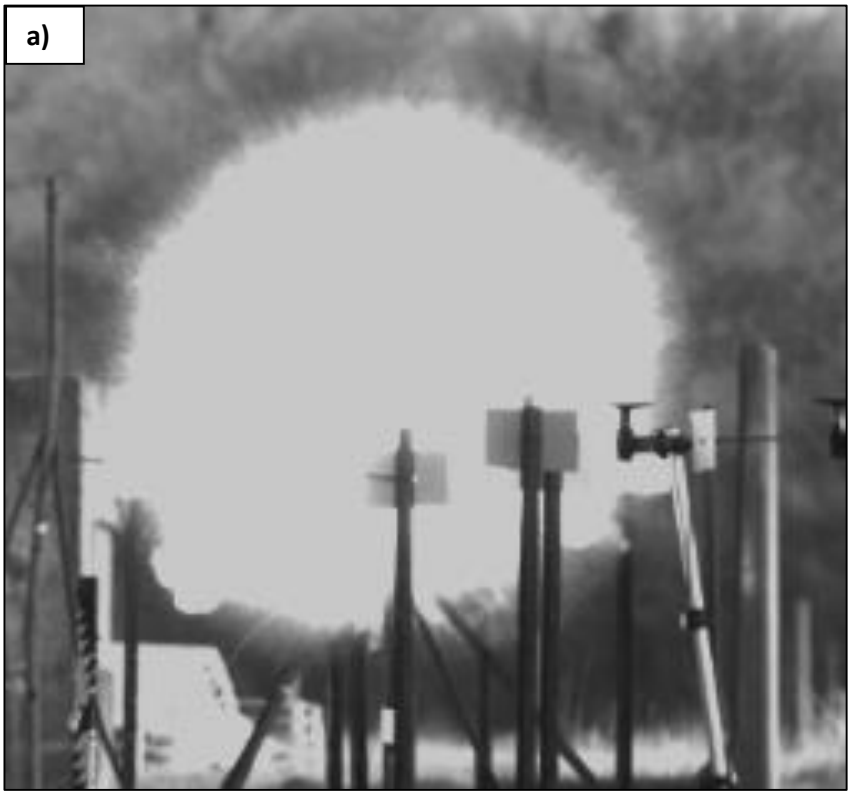

***Figure 4.17**: High speed footage stills of a representative 0.5 kg AlAN firing. a) t = 1.01 ms: the fireball did not have smooth edges but more of a spiky appearance.*

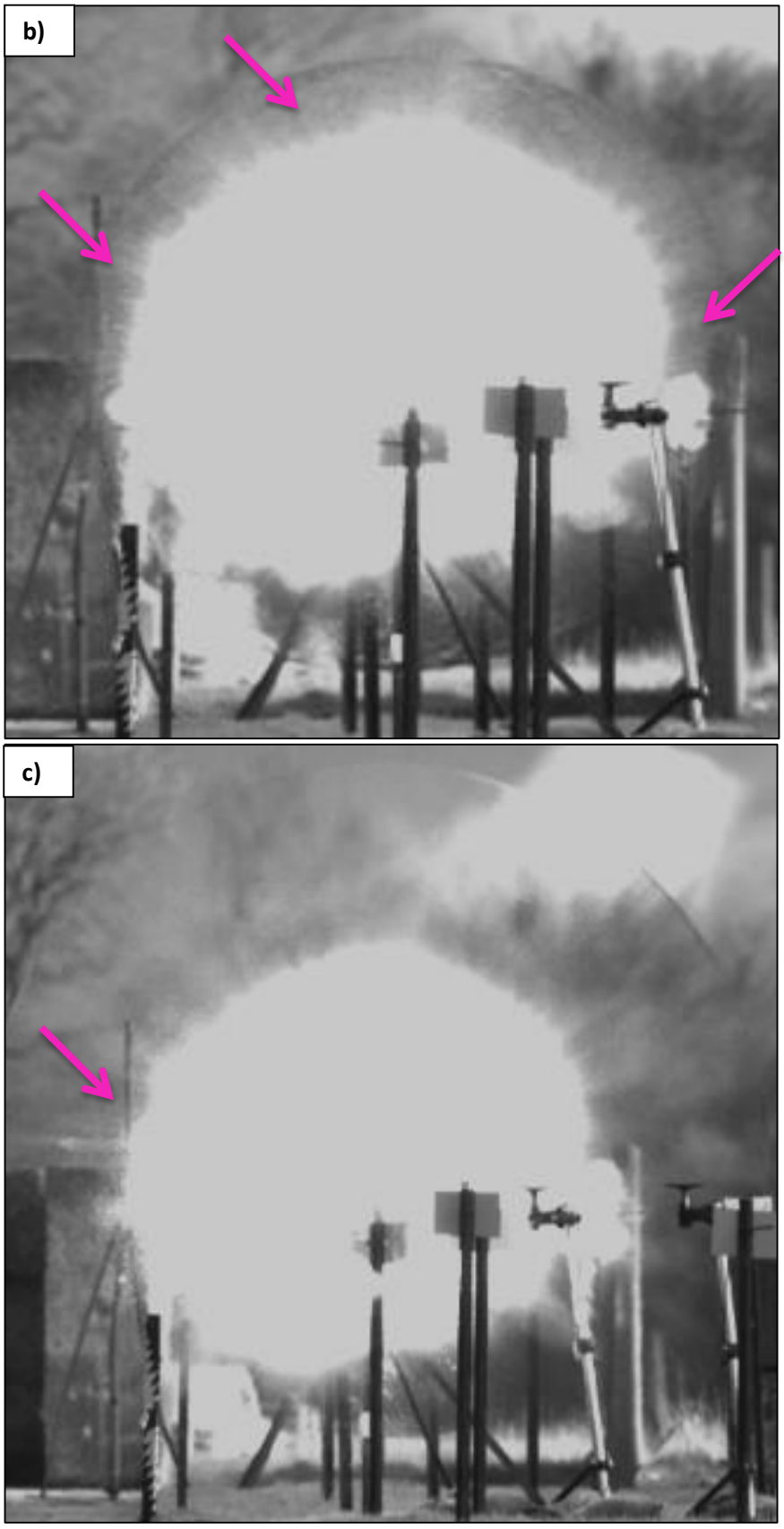

Figure 4.17 cont'd: *b) t = 1.67 ms: the blast wave was moving away from the fireball, between the fireball edge and blast, particulate material was visible (arrows). c) t = 3.00 ms: the arrow shows one of the areas where particulate matter was still visible between the blast and the fireball.*

Figure 4.17 cont'd*: d) t = 48.2 ms; smoke plume engulfed closest plates visible from the camera angle.*

Comparison between Fireballs and Post-blast Residues

The extent of the fireball growth was compared to the residue distribution trends in order to assess any effects of temperature on the persistence of undetonated residues potentially deposited on the closest sampling sites. Figures 4.18 and 4.19 show the comparison of fireball radius with the detected nitrate and ammonium amounts – neither distribution appeared affected by the temperatures of the fireball, with the majority of the greatest residue masses following each firing detected on sampling plates within the region that the fireball was observed to extend over. The only case for which this was not true, was from the anomalous results of ammonium following firing 3 (figure 4.19), after which lower ammonium amounts were detected within the fireball region (1 m from the detonation centre) than outside of it (at 2 m and 3 m).

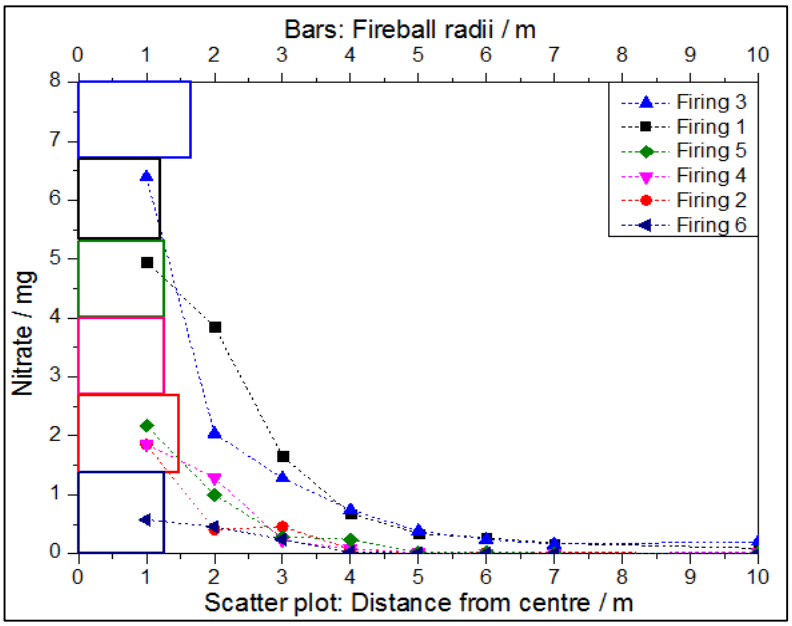

***Figure 4.18**: Nitrate distributions (scatter plots) from six repeated firings of AlAN. The bars indicate the extent of the fireball (radius in metres) as observed through the HSI recordings for each detonation. The largest amounts of nitrate were detected on 1 m sampling plates (within the range of the fireball).*

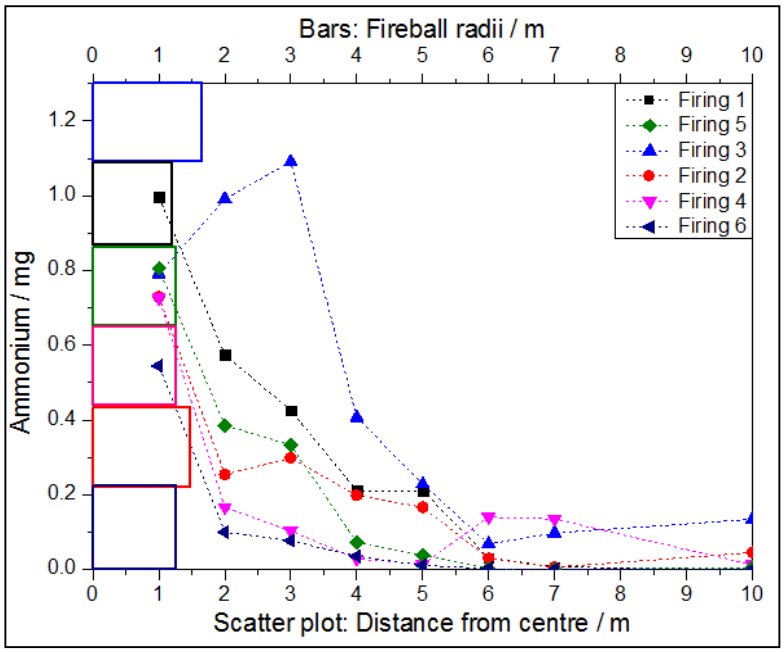

***Figure 4.19**: Ammonium distributions (scatter plots) six repeated firings of AlAN. The bars indicate the extent of the fireball (radius in metres) as observed through the HSI recordings for each detonation. The majority of the highest ammonium amounts detected, which were at 1 m, were in the region of the fireball. The anomaly to this was from firing 3.*

The majority of the detected aluminium was lower in mass within the fireball region (1 m) and increased in mass further from it (figure 4.20). A rise in the amount of aluminium immediately outside of the fireball region was apparent following firings 1 and 3, however more aluminium was detected on sampling plates positioned at distances further (4 m and 5 m) from the fireball (figure 4.20) following the majority of firings.

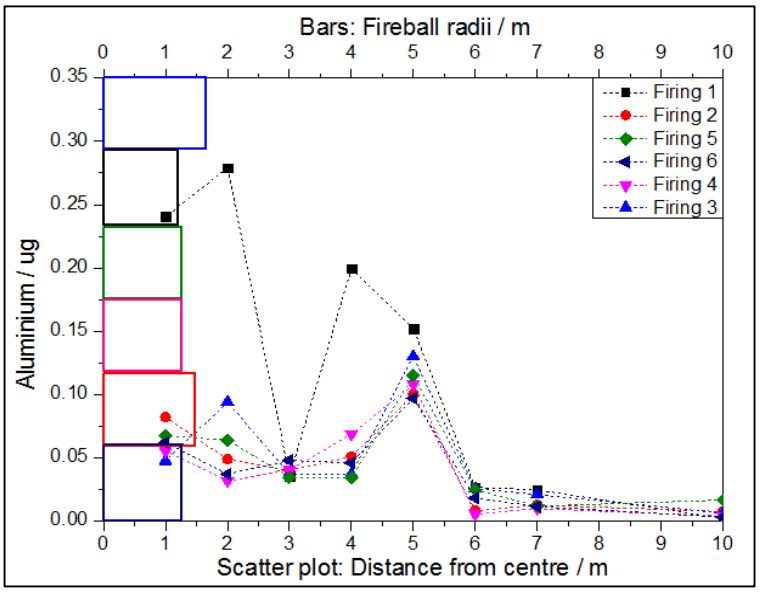

***Figure 4.20**: Aluminium distributions (scatter plots) from six repeated firings of AlAN. Bars indicate the extent of the fireball (radius in m) as observed through the HSI recordings. Lower aluminium amounts were detected within the fireball region than at further distances (5 m).*

4.2.4 Meteorological conditions

The effect of the smoke plume movement (as observed through the HSI images) on the residue mass distribution was assessed by measuring the meteorological conditions at the time of each AlAN firing. Table 4.3 shows the wind direction was consistently toward the west and north-westerly directions throughout the firings and the wind speed varied between 2.5 m/s and 5.8 m/s. The temperature, barometric pressure and humidity were similar across the repeated firings.

Firing No.	Wind Speed / (m/s)	Wind Direction	Temperature /°C	Humidity /%	Pressure /mbar
1	5.80	NW	15.0	65.0	1010
2	4.20	WNW	14.0	65.0	1013
3	2.50	NW	14.0	62.0	1013
4	3.40	NW	16.0	69.0	1013
5	3.60	WNW	13.0	64.0	1010
6	4.20	NW	15.0	58.0	1012

***Table 4.3**: Meteorological conditions recorded at the time of each firing of 0.5 kg AlAN.*

Comparison between Wind Direction and Post-blast Residues

Figure 4.21 shows the nitrate distributions from each of the four sampled orientations (N, E, S and W) following each firing. The error bars in the plots represent the standard

deviation of the measurements determined through triplicate injections of each sample; the majority of which indicated high precision. The highest wind speed (5.80 ms/s) during firing 1 correlated with the highest amounts of nitrate (figure 4.21a) in the north and westerly directions. The majority of nitrate recovered following all firings was greater from sites sampled in line with the wind directions during firing. More was also detected from the north and west positioned sites at the further sampled distances (~6 m).

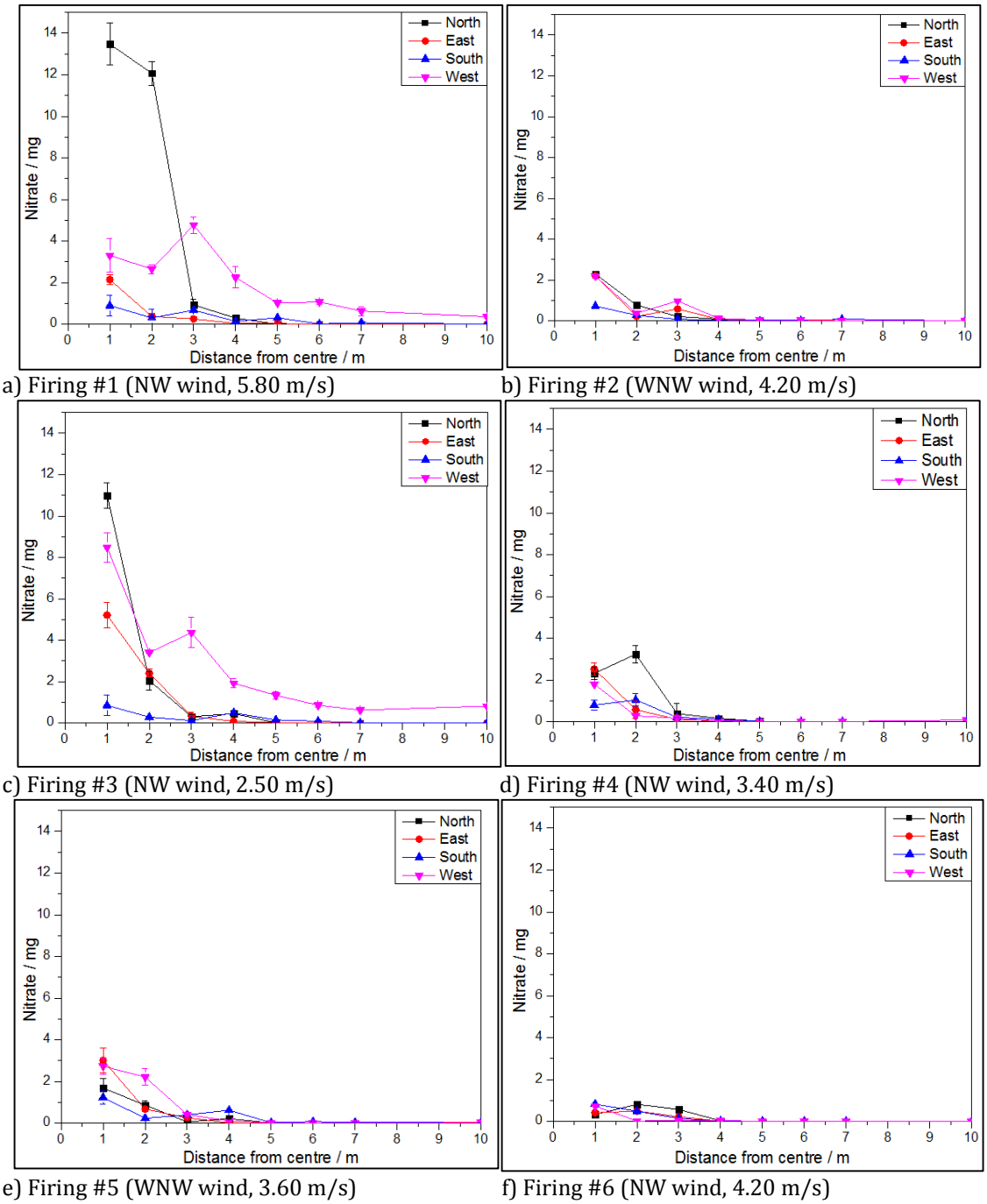

a) Firing #1 (NW wind, 5.80 m/s)
b) Firing #2 (WNW wind, 4.20 m/s)
c) Firing #3 (NW wind, 2.50 m/s)
d) Firing #4 (NW wind, 3.40 m/s)
e) Firing #5 (WNW wind, 3.60 m/s)
f) Firing #6 (NW wind, 4.20 m/s)

Figure 4.21: *Nitrate distributions per sampled orientation around the charge centre. The wind moved consistently towards the north/north-westerly directions, corresponding with more nitrate detected from sampling sites in the north (black) and west (pink) orientations following most firings.*

Figure 4.22 shows the corresponding ammonium mass distributions from each sampled orientation. The precision of the each measurement was determined through triplicate sample analyses, and is shown to be high based on the small error bars on the plots. Similarly to the nitrate, the largest ammonium amounts around the detonation centre were recovered from sites positioned in line with the wind direction at the time of firing (north and west directions). And at furthest sampled distances (figure 4.22 b, c, d) it was these directions which yielded the highest ammonium masses.

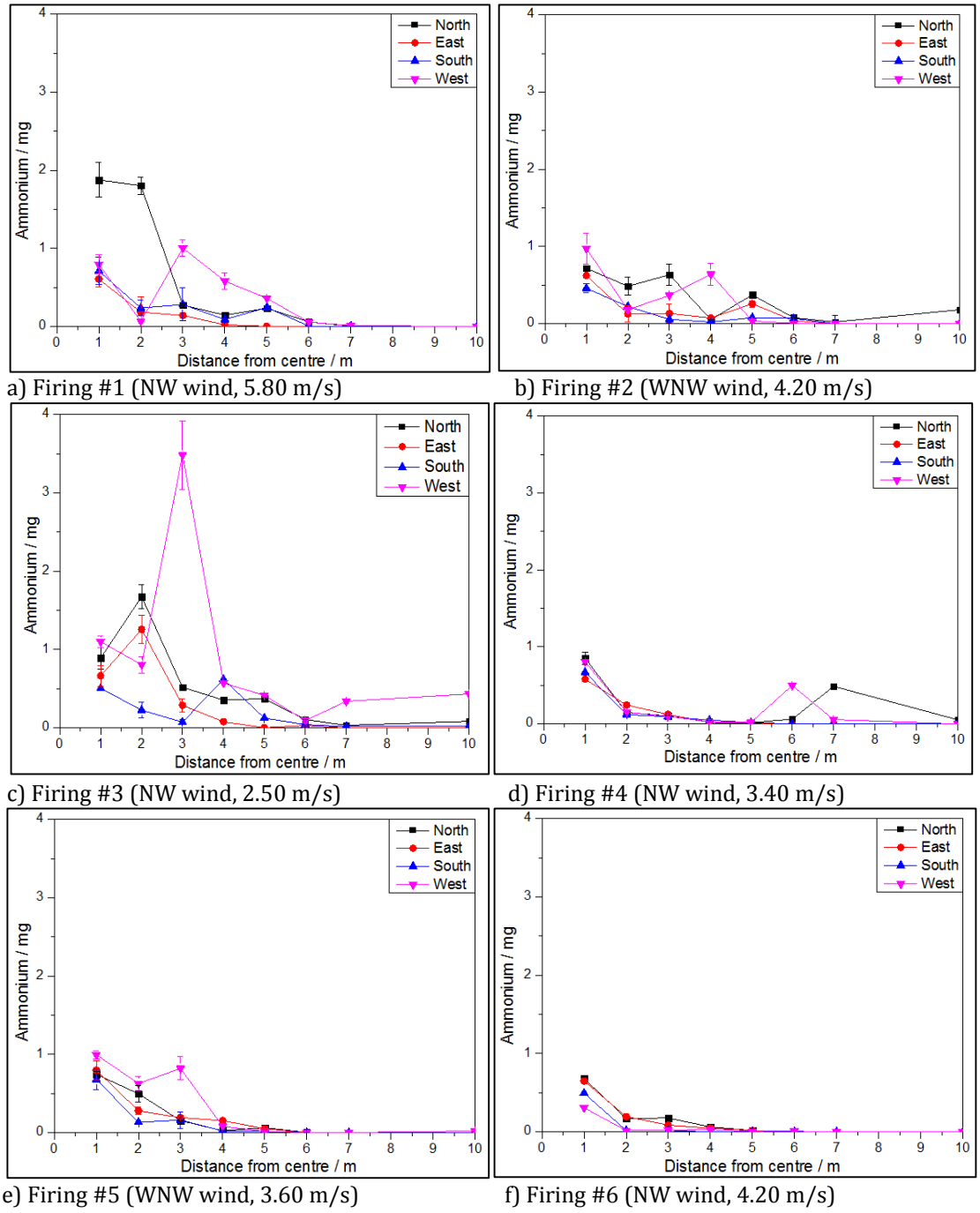

a) Firing #1 (NW wind, 5.80 m/s)
b) Firing #2 (WNW wind, 4.20 m/s)
c) Firing #3 (NW wind, 2.50 m/s)
d) Firing #4 (NW wind, 3.40 m/s)
e) Firing #5 (WNW wind, 3.60 m/s)
f) Firing #6 (NW wind, 4.20 m/s)

Figure 4.22: *Ammonium distributions per sampled orientation around the charge centre. The wind was consistently towards the N/N-W directions and corresponded with more ammonium detected from sampling sites in the north (black) and west (pink) orientations following the majority of firings.*

The lowest aluminium amounts were detected in the southward direction (figure 4.23), and therefore opposite the wind direction, but noticeably higher amounts were not detected from the north and westward sites following every firing, for example firings 1 and 6 showed more aluminium was detected from the eastward sites (figure 4.23 a and e). It was not possible to establish the precision of the aluminium measurements as only one sample injection was possible during this analysis.

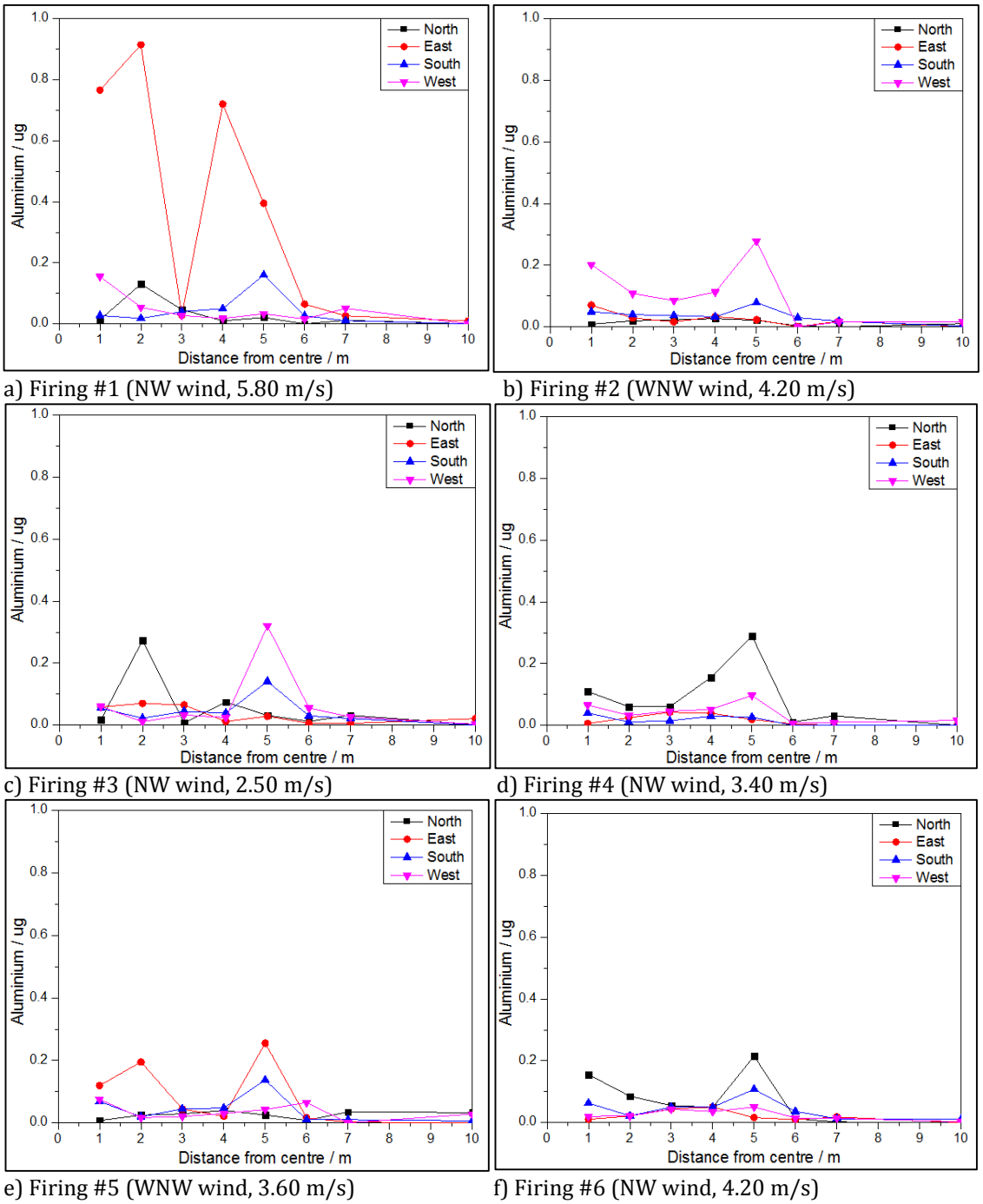

a) Firing #1 (NW wind, 5.80 m/s)
b) Firing #2 (WNW wind, 4.20 m/s)
c) Firing #3 (NW wind, 2.50 m/s)
d) Firing #4 (NW wind, 3.40 m/s)
e) Firing #5 (WNW wind, 3.60 m/s)
f) Firing #6 (NW wind, 4.20 m/s)

***Figure 4.23**: Aluminium distributions per sampled orientation around the charge centre. The wind was consistently towards the north/north-westerly directions. Smallest amounts of aluminium were detected from sites in the southward direction.*

4.3 Results from 0.5 kg PE4 Firings

4.3.1 Organic Post-blast Residue Results

No RDX was detected in the control samples of blank acetone or ACN, swab blanks or steel plate blanks, or in blank ACN and water samples injected between test samples. Therefore any RDX detected in each post-blast sample was attributed to the explosive residue in that sample.

The error associated with each measurement is based predominantly on the varying efficiencies of residue collection (occurring during the sampling phases) and the losses of material incurred during the extraction procedure. Full details regarding RDX sampling and extraction efficiencies (obtained through controlled studies of residue deposition) are presented in Appendix A, section A.3; it is of note that the reported residue measurements herein are estimated (based on the above mentioned tests in Appendix A) to be only approximately 25 % of the actual deposited residue amount.

The overall mass range of RDX detected in post-blast samples was between 0 μg and 20 μg, the limit of detection of RDX was established as 0.1 μg and samples containing lower amounts than this would not have been quantified. The averaged RDX amounts detected from all four sampled orientations, 1 m to 10 m from the charge centre of the 0.5 kg PE4 firings, showed an overall trend of decreasing mass with increasing distance from the centre (figure 4.24). The averaged experimental results appeared to vary from the inverse square law distribution model which was initially generated using the experimental measurement at 1 m (3.06 ± 1.4 μg), in that the mass of RDX at 2 m (4.82 ± 1.8 μg) was overall greater than that at 1 m. The experimental values were also inconsistent at 3 m and 4 m (2.88 ± 1.0 μg and 1.97 ± 0.9 μg) than the theoretical values (0.77 μg, 0.34 μg and 0.19 μg) (figure 4.24).

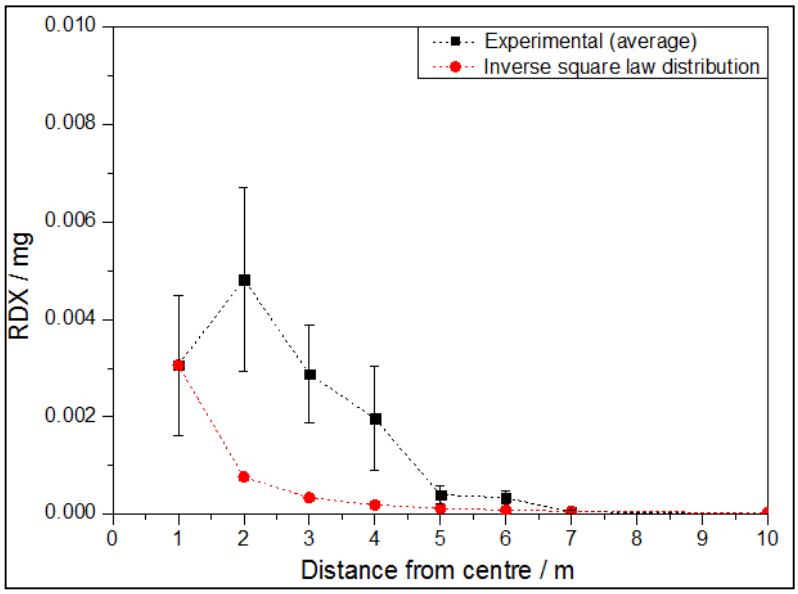

***Figure 4.24**: Averaged RDX amounts detected following 0.5 kg PE4 firings (in black) compared to the theoretical inverse square law distribution pattern (in red). Values for each distance were totals from four sampled orientations. The experimental trend was inconsistent with the theoretical comparison. Error bars represent standard deviations of the mean average RDX mass from repeated firings.*

Omitting the datum from 1 m and plotting the experimentally generated data against 1/d^2 (inverse square law) demonstrated that the RDX distribution was a linear fit to the theoretical model, producing an R^2 of 0.928 (figure 4.25).

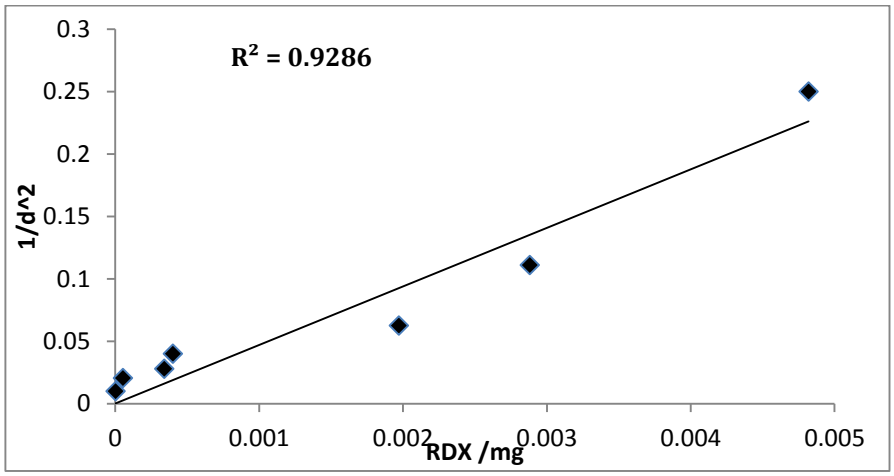

***Figure 4.25:** Plot of RDX mass (without datum from 1 sampling point) against 1/d^2, demonstrating linearity with an R^2 of 0.9286.*

The error bars on figure 4.24 represented the standard deviation of the mean average RDX mass from the six repeated firings; individual residue plots from each firing are shown in figure 4.26. The RDX distribution trends were not as linear as the nitrate (cf. figure 4.5) or ammonium trends (cf. figure 4.8). From most firings a greater mass of RDX was detected at distances further than 1 m and residue amounts fluctuated up to 7 m from the centre (figure 4.26). The only anomaly to this was from firing 6, where the greatest mass was detected at 1 m.

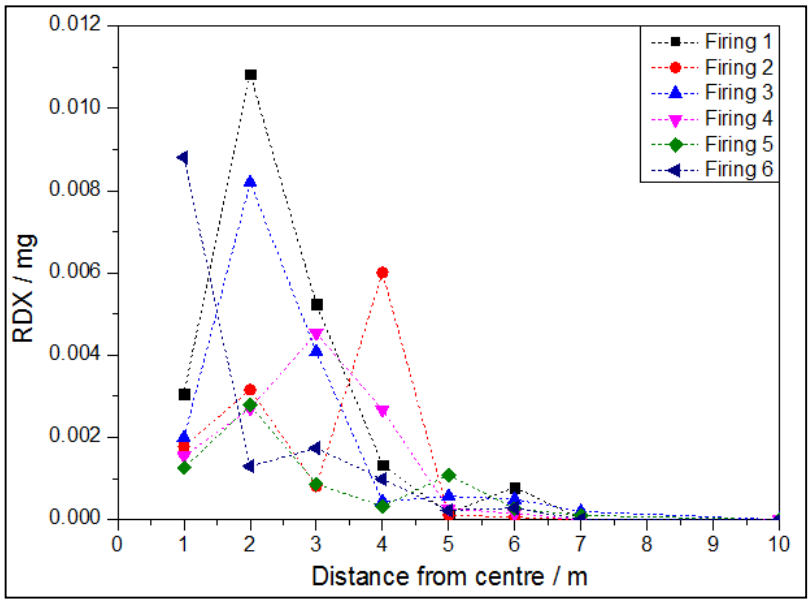

***Figure 4.26**: RDX mass detected from each 0.5 kg PE4 firing. Each value is the totalled amount from all four sampled orientations around the charge centre. No firings exhibited a linear decrease in residue mass with increasing distance; most had a 'spike' in RDX mass at distances further than 1 m.*

Comparison between Organic and Inorganic analytes

The mass range of RDX detected (0 µg to 20 µg) was lower than that of the nitrate (0 mg to 14 mg) and ammonium (0 mg to 3 mg), but higher than the aluminium (0 µg to 1 µg) from the AlAN firings (averaged data from repeated firings presented in figure 4.27).

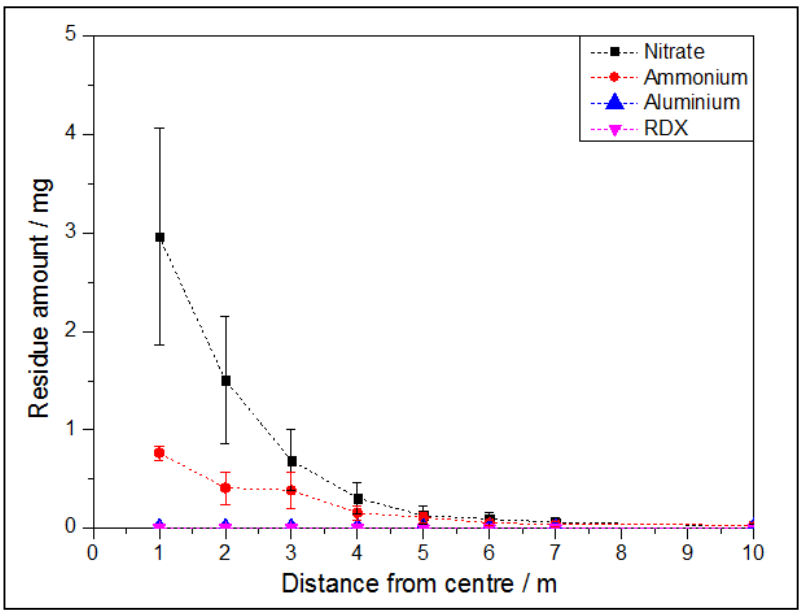

***Figure 4.27**: Comparison between the average inorganic and organic residue mass. The amounts were based on totalled sample results from the four sampled orientations around each firing and then averaged across the six repeated firings. The error bars represent the deviation of the mean average from repeated firings. Analyte comparisons showed: nitrate > ammonium > RDX > aluminium.*

Having established the general RDX distribution trends, these were compared to various blast phenomena, starting with the blast overpressure.

4.3.2 Blast Overpressure

The arrival times of the blast wave, peak overpressures, duration of positive phases and impulse areas for each sensor are displayed in table 4.4; the mean average values from all six repeat firing are presented with the standard deviation of the measurements. Data collected from each individual sensor during every firing is presented in appendix B.

Sensor position /m		Arrival time /ms	Positive duration /ms	Impulse area/ (kPa/ms)	Peak over-pressure /kPa
1	**Mean**	**0.481**	**1.00**	**64.9**	**479**
	S.D.	0.0513	0.194	12.7	97.6
2	**Mean**	**2.27**	**1.56**	**52.9**	**119**
	S.D.	0.0876	0.0314	0.657	6.18
3	**Mean**	**4.54**	**1.93**	**38.2**	**55.0**
	S.D.	0.0729	0.0889	1.02	1.31
4	**Mean**	**7.09**	**2.21**	**29.9**	**36.2**
	S.D.	0.0731	0.0831	0.796	1.00

Table 4.4*: Mean average measurements and standard deviations (S.D.) of blast wave arrival time, positive duration, impulse and overpressure from sensors positioned 1 m, 2 m, 3 m and 4 m from charge centre from six repeat firings of 0.5 kg PE4 charges (3 sf).*

The average peak overpressure decreased with increasing distance from the charge centre (479 kPa → 119 kPa → 55.0 kPa → 36.2 kPa), as did the impulse areas, whilst the duration of each positive phase increased with increasing distance (table 4.4). Based on the arrival times and sensor positions the speed of the blast wave was calculated to be moving at 2080 m s^{-1}, 881 m s^{-1}, 661 m s^{-1} and 564 m s^{-1} at 1 m, 2 m, 3 m and 4 m, respectively. The standard deviation of the peak overpressure measurements decreased with increasing distance at which the measurement was recorded; the reproducibility of the results improved further from the detonation centre (as was the case for the inorganic blast-waves).

The blast pressure profiles from the 0.5 kg PE4 charge firings are presented in figure 4.28. The negative phase durations recorded from the 1 m sensors did not return to ambient pressure (figure 4.28a). Figure 4.28b shows the pressure returned to ambient after 15 ms at 2 m from the charge centre. At 3 m, the pressure returned to ambient level after 16 ms (figure 4.28c) and at 4 m, pressure fluctuations were apparent between 18 ms and 20 ms towards the end of the data measurement and had not yet returned to a stable ambient pressure (figure 4.28d).

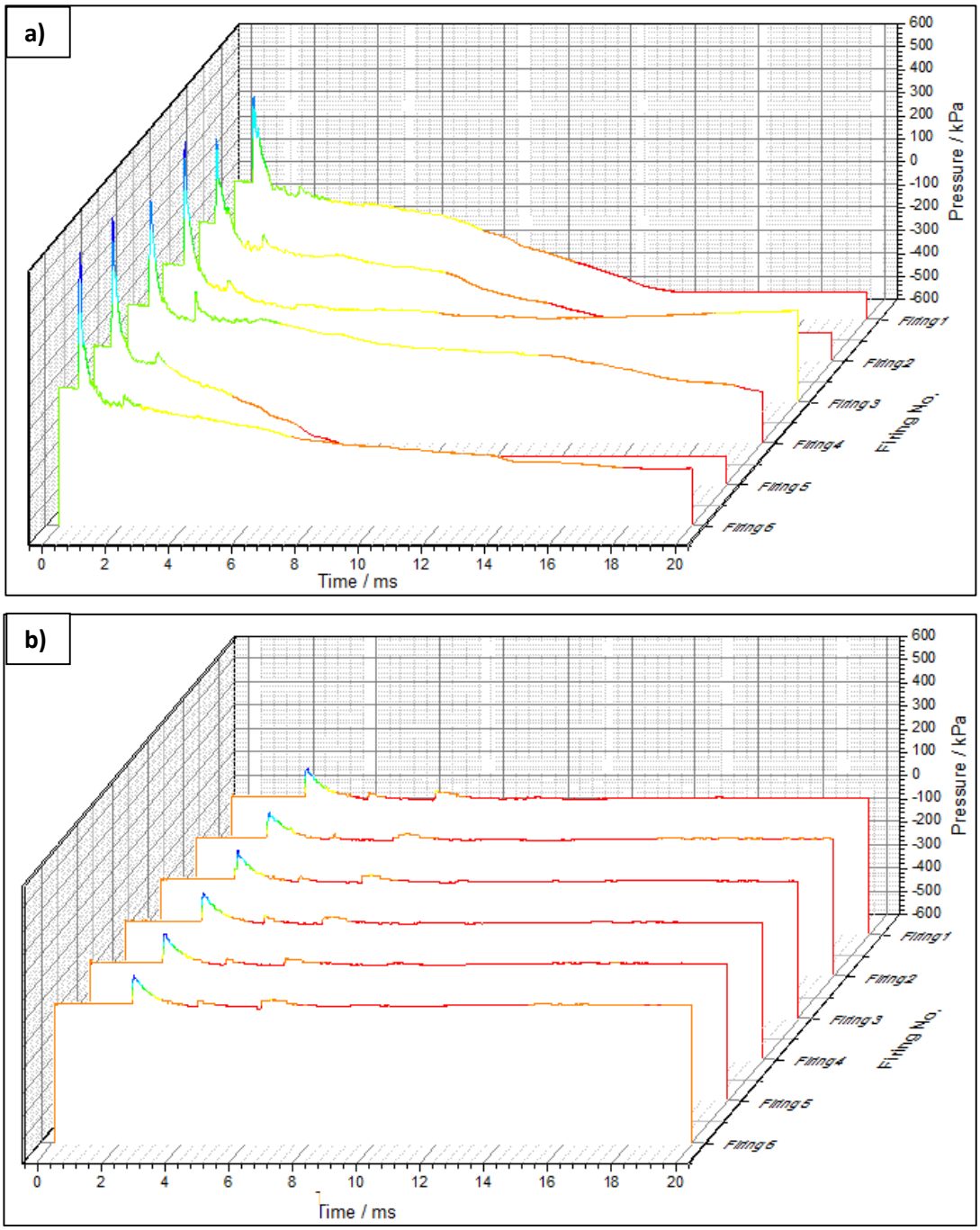

***Figure 4.28**: a) Blast pressure profiles (time /ms v. pressure /kPa) from sensors positioned 1 m from the detonation centre of six repeated 0.5 kg PE4 firings and b) at 2 m from the detonations. Measurements were recorded with piezoelectric gauges and processed with a Nicolet oscilloscope.*

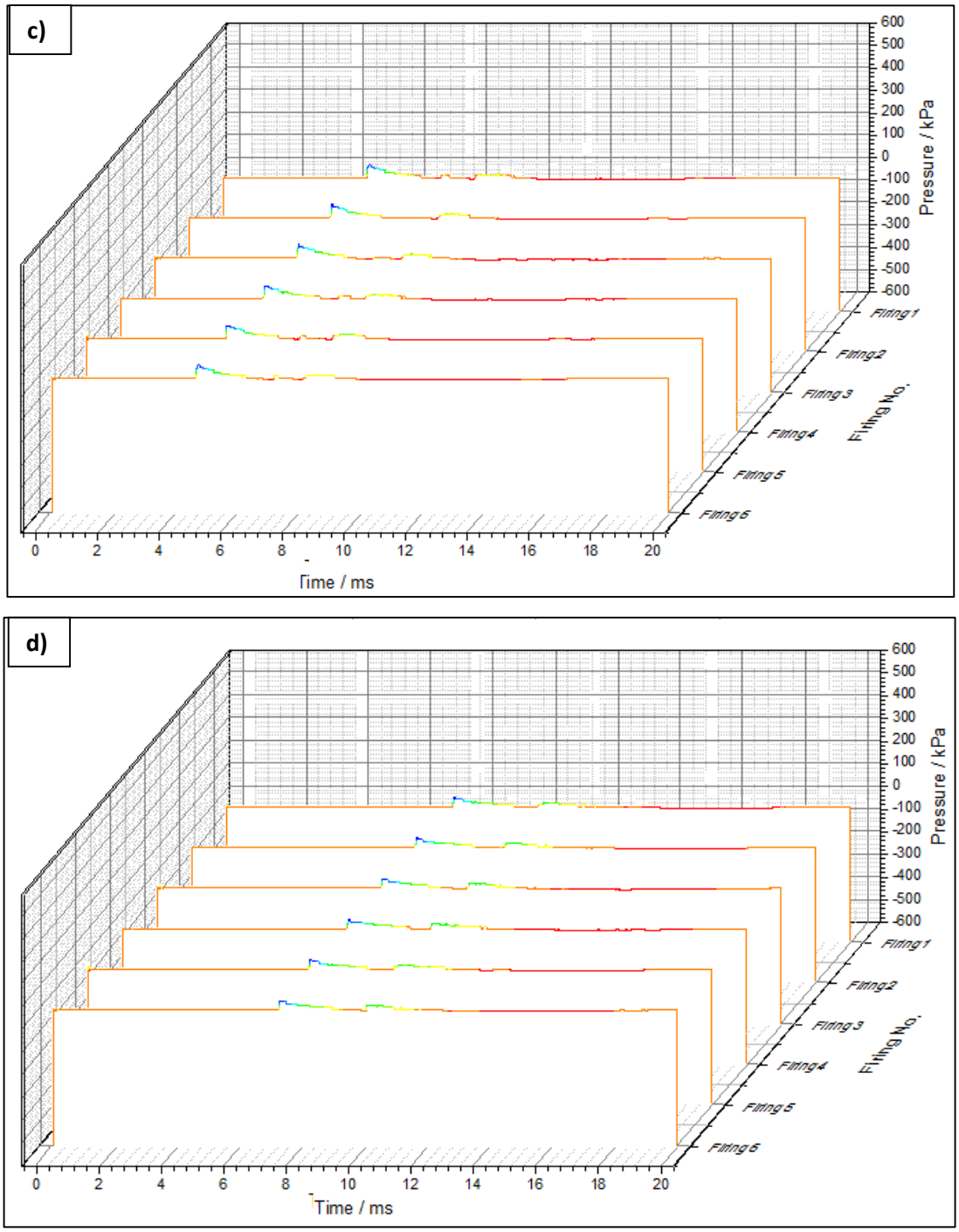

***Figure 4.28 cont'd**: c) Blast pressure profiles (time /ms v. pressure /kPa) from sensors positioned 3 m from the detonation centre of six repeated 0.5 kg PE4 firings d) 4 m from the detonation centre of six repeated 0.5 kg PE4 firings.*

Comparison between Overpressures and Post-blast Residues

Figure 4.29 shows the average blast overpressures (black line) recorded from the six firings of 0.5 kg PE4 at 1 m to 4 m compared to the average RDX amounts (blue line) recovered at 1 m to 10 m. As the average overpressure decreased between 1 m and 2 m (479 kPa → 119 kPa), the RDX mass increased (3.06 µg → 4.82 µg).

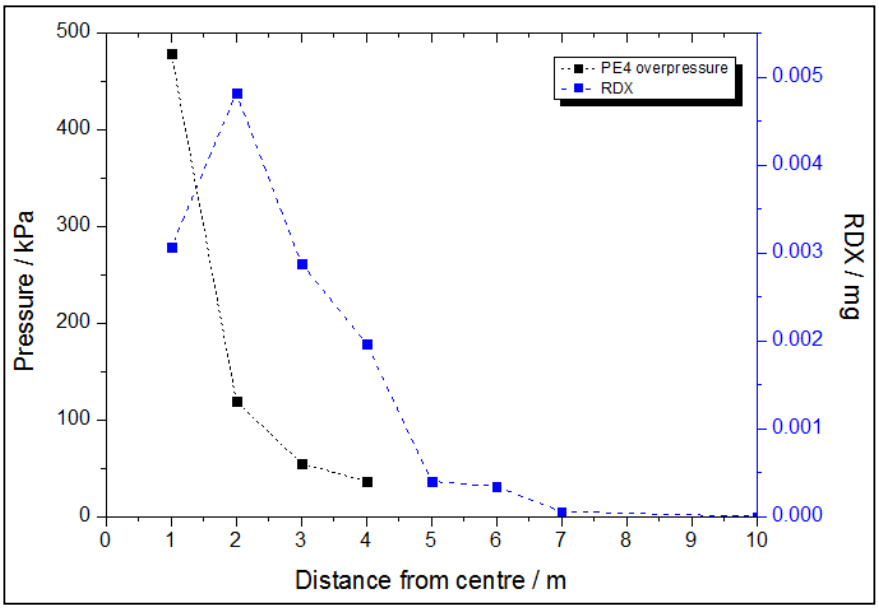

***Figure 4.29**: Comparison between average peak PE4 overpressure and RDX mass. As the blast pressure initially decayed (from 1 m to 2 m), the residue mass increased, following which both the pressure and residue decreased with increasing distance.*

Comparison of Overpressures between Explosive Charges

The average peak overpressures produced from the 0.5 kg PE4 (RDX-based) charges were higher than the 0.5 kg AlAN charges at all measured distances (figure 4.30), as were the peak impulses. The blast waves moved at a faster speed compared to the AlAN charges. The reproducibility of the measurements from repeated firings improved further from the detonation centre (3 m and 4 m sensors) for both explosive types.

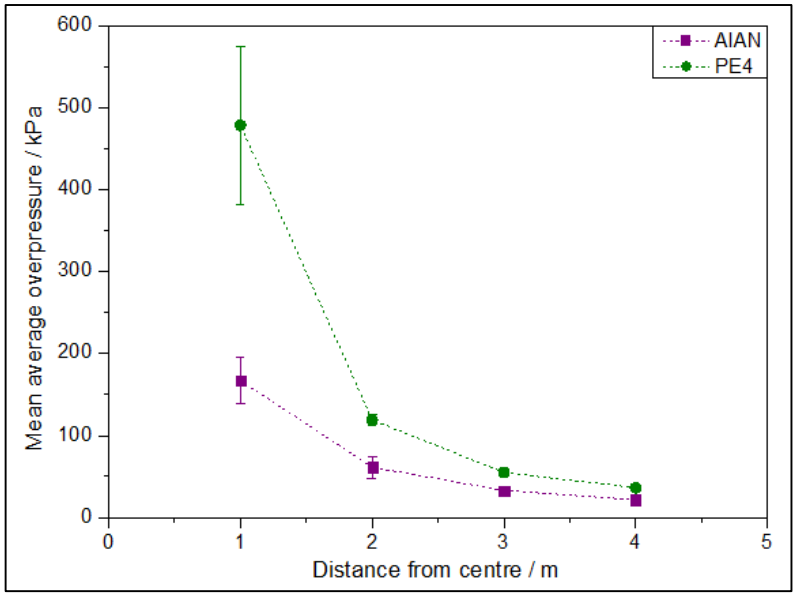

***Figure 4.30**: Mean average peak overpressures from repeated firings of 0.5 kg AlAN (purple) and PE4 (green) charges, measured at 1 m, 2 m, 3 m and 4 m. Peak overpressures from the 0.5 kg PE4 charges were higher than those of the AlAN charges (479 kPa and 167 kPa respectively). The decay of the positive overpressure at the 2 m, 3 m and 4 m distances showed similar responses (although still higher overpressures from the PE4).*

4.3.3 Fireball

The PE4 detonations were recorded using HSI techniques, the estimated radii of the observed fireballs per firing are shown in table 4.5 alongside the approximated fireball and smoke plume volumes. Volume estimates were made when the largest radii for the fireballs and smoke plumes were observed; at t = 40 ms and t = 350 ms, respectively, and both were assumed to have a spherical shape.

Firing No.	Fireball radius /m	Fireball volume /m^3	Smoke plume radius /m	Smoke plume volume /m^3
1	2.10	37.9	3.20	132
2	1.90	28.7	2.90	102
3	2.20	44.6	2.70	82.4
4	2.20	44.6	3.20	137
5	2.60	73.6	3.20	132
6	2.20	44.6	3.30	151

Table 4.5: *Estimated fireball and smoke cloud volumes based on HSI and GoPro footage of the 0.5 kg RDX based PE4 charge firings. All estimates are based on spherical volumes (3 sf).*

The average fireball size estimated for the 0.5 kg PE4 charges was ~45.7 m^3; the average smoke cloud was ~123 m^3. Figure 4.31, comprised of stills a-d shows some aspects of the organic explosive detonations and was representative of all the PE4 0.5 kg firings (a full set of stills can be found in appendix C). Figure 4.31a shows the initial detonation stage at t = 0.834 ms, followed by the irregular fireball expansion and blast-wave movement through the air (figure 4.31b). The third and fourth stills (figure 4.31c and d; 14.2 ms and 37.7 ms) show the growth of the fireball (with black soot areas) into a more spherical form and the closest residue sampling sites being engulfed by the smoke cloud.

Figure 4.31*: HSI stills of a representative 0.5 kg PE4 firing: a) at t = 0.834 ms; the initial energy release as heat and light.*

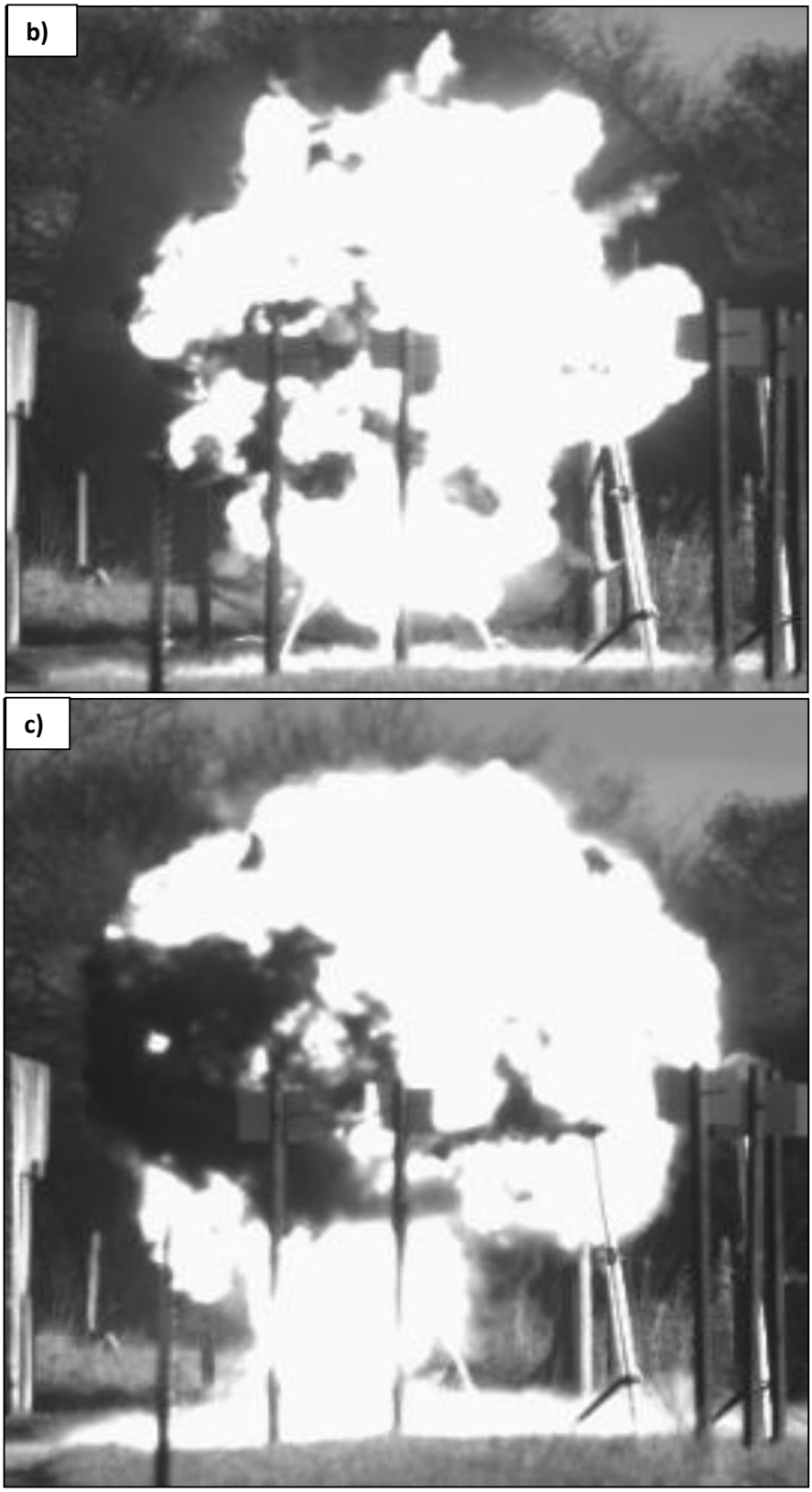

***Figure 4.31 cont'd**: HSI stills of a representative 0.5 kg PE4 firing: b) t = 2.17 ms; movement of blast wave, c) t = 14.2 ms; expansion of fireball, darker areas are soot regions*

***Figure 4.31 cont'd**: d) t = 37.7 ms; the fireball starts decaying into smoke which engulfs closest sites.*

Comparison between Fireballs and Post-blast Residues

The amount of RDX detected fluctuated within and outside of the observed fireball region (figure 4.32). From most firings the RDX mass detected at 1 m, (and therefore within the fireball), was lower than at 2 m (the edge of the fireball). An increase in the amount of RDX detected was also apparent further from the centre (4 m to 6 m) following some firings.

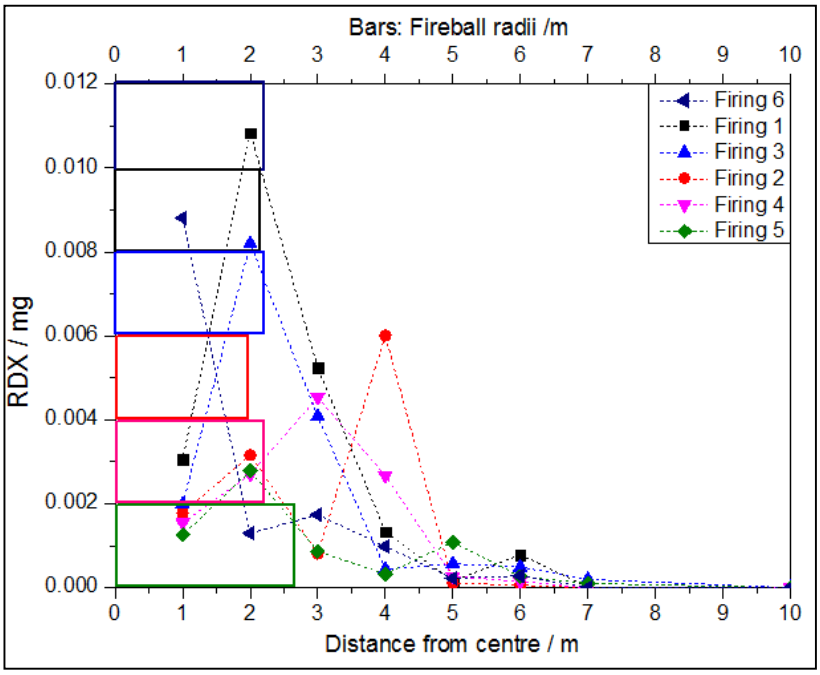

***Figure 4.32**: RDX amounts (scatter plots) from six repeated firings of PE4. The bars indicate the extent of the fireball (radius in metres) as observed through the HSI recordings for each detonation. Detected RDX masses fluctuated close to, and further from the detonation centre.*

Comparison of Fireballs between Explosive Charges

The average fireball volumes from the AlAN charges (~10.0 m^3) were smaller than those from the PE4 detonations (~45.7 m^3). Similarly, the AlAN smoke clouds (~39.1 m^3) were smaller in volume than from the PE4 (~123 m^3).

4.3.4 Meteorological Conditions

The effect of the smoke plume movement (as observed through the HSI) on the residue distribution was assessed by measuring meteorological conditions at the time of each PE4 firing. Table 4.6 shows the wind direction was mainly toward the north westerly direction for the majority of firings and the wind speed ranged between 2.6 m/s and 3.5 m/s. The temperature, barometric pressure and humidity were similar across the repeated firings.

Firing No.	Wind Speed / (m/s)	Wind Direction	Temperature /°C	Humidity /%	Pressure /mbar
1	2.6	W	13	56	1015
2	2.6	NNW	11	49	1013
3	2.7	NW	14	62	1013
4	3.2	NW	14	72	1005
5	3.5	NW	13	72	995
6	2.8	SWW	14	65	989

Table 4.6*: Meteorological conditions recorded at the time of each 0.5 kg PE4 firing.*

Comparison between Wind Direction and Post-blast Residues

Figure 4.33 shows the distribution of RDX after each firing in relation to the orientation (N, E, S or W) around the centre. The majority of RDX was detected in samples which were collected from plates that were in line with the wind direction during firing (principally in the north and west directions). Greater amounts were also detected in samples collected from north and west positioned sites at the further sampled distances (> 5 m). The precision of each measurement was high; indicated by the small error bars generated from triplicate analyses of each post-blast sample in figure 4.33 (the maximum standard deviation of the mean average mass from a triplicate analysis being in the region of 3.7 μg.

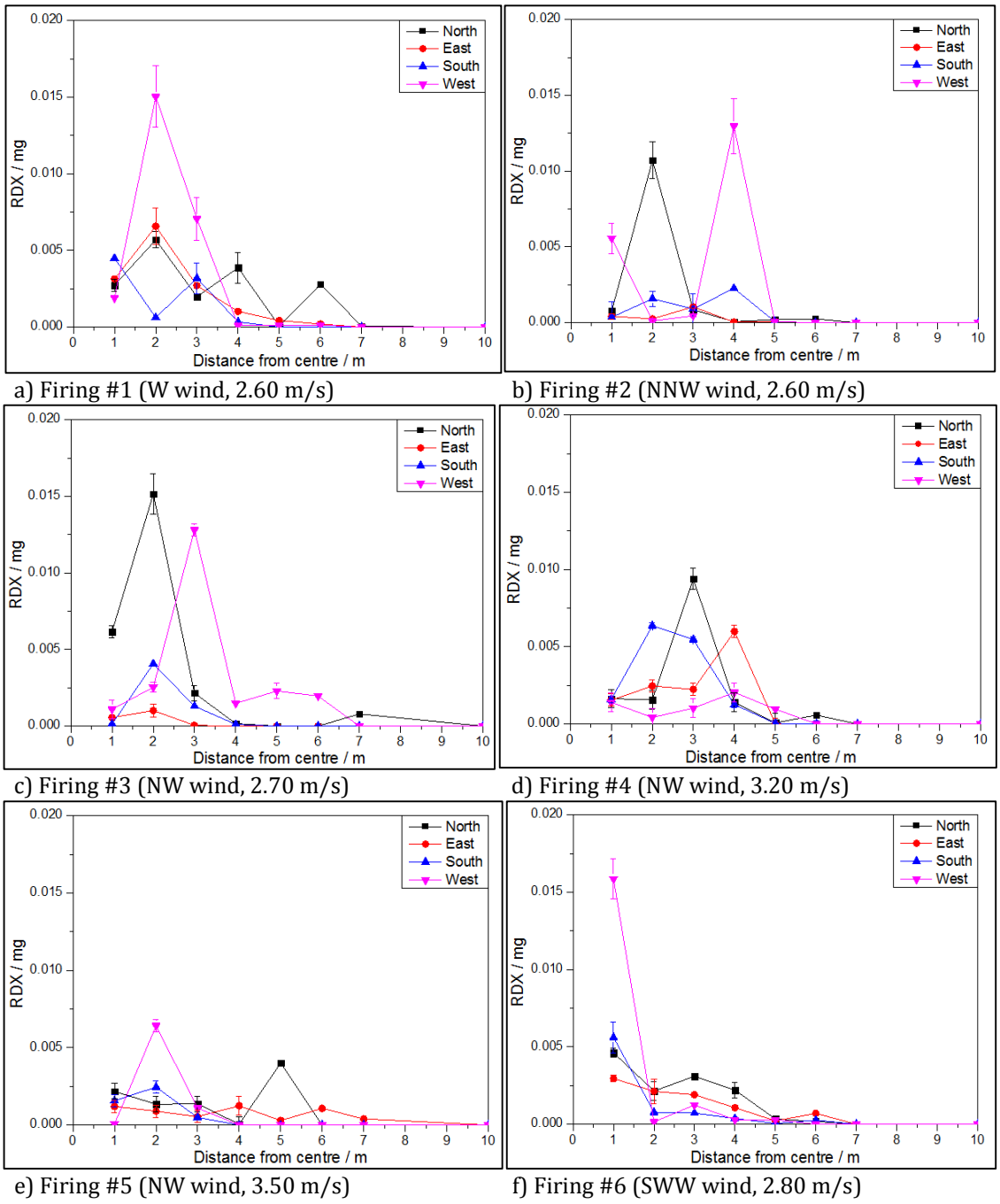

***Figure 4.33**: RDX mass distributions per sampled orientation around the charge centre. The wind was consistently towards the north/north-westerly directions. Lowest amounts were detected from sites in the southward direction.*

4.4 Results Summary

The results presented in this chapter are summarised in the following points and discussed in the following section.

- **Mass ranges**: The nitrate mass range was greater (0 mg to 14 mg) than ammonium (0 mg to 3 mg), which in turn was greater than RDX (0 μg to 20 μg) which was detected in greater quantities than aluminium (0 μg to 1 μg).

- **Radius**: The majority of the largest amounts of each inorganic analyte were detected within 6 m from the charge centre. The mass of RDX following the PE4 firings were higher within 4 m.

- **Theoretical trend comparisons**: With all data points included in the comparative analysis, neither the summed analyte, nor individual nitrate, ammonium, aluminium or RDX, experimentally determined mass distribution results followed the inverse square law distribution. However, by omitting the 1 m data, all analytes (apart from aluminium) corresponded to the theoretical model well, with varying degrees of linearity.

- **Trend:** The distribution trends were similar between the majority of repeated inorganic firings and nitrate and ammonium principally decreased with increasing distances from the charge. Conversely, aluminium was found in larger quantities at ~5 m from the centre. RDX mass fluctuated more than any inorganic analytes with the majority of firings producing higher mass deposits further than the closest sampled distance of 1 m.

- **Uncertainty**: Whilst the majority of repeated firings produced similar trends, the actual amounts of nitrate, ammonium and RDX detected were not comparable between firings. Excluding the measurements recorded from one anomalous firing, the amounts of aluminium detected were more consistent between firings. The accuracy of the inorganic measurements was unknown, however the detected organic measurements were thought to be only 25 % of the actual deposited amount. The precision of the measurements was high in all cases; the instrumental detector responses for the mass of residue within both the inorganic and organic samples were shown to be similar for triplicate injections.

- **Overpressure**: AlAN charges produced lower peak pressures than the PE4. No distinct correlation between blast overpressure and inorganic analyte distribution patterns was apparent. A lower amount of RDX was detected at 1 m where the peak

overpressure from the blast was the highest; where the blast overpressure decayed at 2 m, the RDX amount was higher there than at 1 m.

- **Fireball**: AlAN fireballs were spiky and particles were visible between the fireball and blast-wave; they were smaller than the PE4 fireballs which were darker (black soot regions) and less spheroidal. No particulate material was observed during the PE4 firings.

- **Fireball vs. residue:** Greater nitrate and ammonium amounts were detected from the closest sampling sites which were seen to be engulfed by the fireball. The aluminium was higher further from the centre at ~5 m, where the fireball was not observed to extend to. RDX was lower in the fireball region (1 m) than at the edge of the fireball region (2 m), but also fluctuated at further distances.

- **Wind vs. residue**: Detected nitrate and ammonium amounts were skewed with the wind direction following some firings. Aluminium was detected in lower amounts from upwind sites but was also higher from eastward sites which were not in line with the wind direction. Greater quantities of RDX were detected from downwind sites following firings.

4.5 Discussion

Detected Analyte Amounts

The finding of larger nitrate and ammonium analyte amounts (0 mg to 14 mg and 0 mg to 3 mg, respectively) compared to the organic residue (RDX; 0 µg to 20 µg) after the detonations can be explained by considering the velocity of detonation (VOD) of each of the explosive charges. The VOD is a factor thought to affect the formation of undetonated residues and explosives with a higher VOD (such as RDX; VOD ~8440 m/s) would have a thinner, and therefore faster moving, reaction zone which would cause a more efficient decomposition of the unreacted material, thus producing less undetonated material. The lower VOD for the ammonium nitrate based charges (VOD ~5000 m/s) is due to the composition being based on a fuel-oxidiser mixture rather than a unimolecular explosive; mixtures react slower as the oxidising component required for combustion is not present within the fuel molecule. Additionally, another reason for finding more inorganic residues may be the greater solubility of the analytes in their respective solvent (solubility of 0.2 kg AN in 1 m^3 of water at 20 °C) compared to the organic residue (solubility of 0.008 kg RDX in 1 m^3 of acetone at 25 °C)[2].

The finding of more inorganic residues compared to organic residues (figure 4.27) is consistent with findings from experimental work in the literature; studies using TNT and inorganic compositions found larger amounts of the inorganic residues (at μg levels) compared to the organic residues (at ng levels)[88], whilst others found binary compositions to leave more residues than organic military explosives[77]**.** The mass range of RDX detected in this study (0 μg to 20 μg) varied to that reported in the literature; being higher than that found in some studies, (0 ng to 76 ng[88]) and lower than that reported elsewhere (0 mg to 17 mg and 0 mg to 120 mg[80]).

The nitrate and ammonium mass ranges detected here (0 mg to 14 mg and 0 mg to 3 mg respectively), were greater than those reported from other studies (NO_3^-: 12 μg to 5 mg and 3 μg to 5.5 mg; NH_4^+: 26 μg to 161 μg and 3 μg to 366 μg[87]). The variations of concentrations from this study compared to those cited from the literature would be due to the differences in the methodological and analytical aspects between experiments; principally the use of different explosives (TNT[88], ammonium nitrate/sugar mixtures[87], mortars and grenades[178]), charge masses (454 kg[87,88]) and detection techniques (e.g. sampling from snow[178]).

Nitrate was recovered in greater quantities than ammonium (ratio of ~7:1; figure 4.14), and the relationship between the two analytes was not stoichiometric, which corresponded with findings from other studies[70,87,88]. The lower ammonium levels may have been due to measurement error during IC analysis; high concentrations of the ammonium cation are known to undergo suppression during suppressed conductivity detection[140]. A suppressor system is required in order to convert the detector into a solute-specific detector, without which the conductivity of the eluent and cations are measured. However, in doing so it is possible that the suppression of cations of higher concentrations also occurs[179]. Indication of this phenomenon was observed during ammonium calibration where the fit between the calibrant points was not highly linear but slightly curved in the higher concentration region (figure 3.9 in chapter 3); therefore the linear calibration (which fit the lower mass region well) was used instead. Whilst the potential error of the calibration fit and effect of the supressed conductivity detection system on the nitrate to ammonium ratio cannot be confirmed here, it does afford an explanation as to why the ratio between the two ions did not reflect the molar mass ratio of ~4:1.

The aluminium was added to the ammonium nitrate to increase the fuel content of the oxidiser-heavy formulation; a 10 % mass fraction of each charge was aluminium. The detected mass range in the post-blast samples (0 μg to 1 μg) was three orders of magnitude lower than that of the nitrate and ammonium (figure 4.14) and therefore did not correspond

to the lower proportion of aluminium added to the charges. The oxidation of aluminium occurring in the afterburning of each detonation would have generated aluminium oxide, however the ICP–AES metal analysis would not have distinguished between the Al_2O_3 formed due to afterburning and that due to the addition of elemental aluminium into water[152] and so would not be a reason for finding lower mass amounts. The finding of lower levels of aluminium concurs with findings of little or none of the fuel components in post-blast residues from previous studies[70,87,88].

The finding of overall low amounts of post-blast residues from the 0.5 kg charges highlights the importance of needing to know *where* to locate valuable trace residue evidence at post-blast scenes in order to allow the optimum samples to be collected.

Post-blast Residue Radii

The majority of the largest mass deposits of each inorganic and organic analyte were detected within six and four metres from the charge centres respectively (figures 4.5, 4.8, 4.12 and 4.26). The lowest mass deposits, and often no residues, were detected at the furthest sampled distance of 10 m from the charge centre. The limiting radius within which explosive residues could be found at a post-blast scene has been posited in the literature to be 60 m, the radius is based on an equation[57] which was developed from the results of metal fragment distributions[66]. Whilst the residue deposition at a distance of 60 m was not measured during these studies, it seems inconceivable that depositions would be made further than 60 m from these 0.5 kg charges. Therefore, the findings here support the concept of a theoretical limit; however a perimeter of 60 m to focus search/sampling techniques for residues seems too wide. The 6 m and 4 m radii established here correspond with the findings of previous experimental work where most residues were detected between 2 m and 5 m[68], within 10 m[75,79] or those which suggested a 15 m radii from around high order detonations which residue would be found in[77]. Based on these variations, the basis for the theoretical radius clearly requires evaluation which incorporates a consideration of the charge type and mass. The finding of smaller perimeters around which post-blast explosive residue can be found supports the current forensic practice of focusing search areas on the central region of the detonation area.

Distribution Trends

The majority of residue distribution patterns for all analytes generally showed a decrease in mass as a function of increasing distance from the charge centre (figures 4.5, 4.8, 4.12 and 4.26). No analyte distributions followed the inverse square law pattern posited in the literature[65] when including the data obtained from the samples at 1 m from the detonations (figures 4.3, 4.6 and 4.10). Excluding the 1 m data points however, and plotting the

experimental data against the inverse square law (given by 1/d^2, where d is the distance from the centre in m), the nitrate, ammonium and RDX demonstrated a linear fit to the theoretical model. Linearity was evaluated via the R^2 regression coefficient of determination which produced values of 0.9958, 0.8562 and 0.9286 for the nitrate, ammonium and RDX respectively (figures 4.4, 4.9, and 4.25). The exclusion of the 1 m data was deemed reasonable as this 'close-in' to the detonation, the measurements recorded at this point may have been anomalous.

Whilst not all experimental values were in complete accordance with the theoretical trend, in order to determine an exact inverse square law theoretical distribution, the original quantity of undetonated material to be dispersed would need to be known and with no (theoretical or experimental) way of establishing this, a correlation of 100 % accuracy is improbable. The comparisons calculated in this study therefore provide support for the distribution of some explosive-related analytes to follow an approximate inverse square law distribution upon their dispersal during detonation. No other experimental residue distribution studies in the published literature have demonstrated evidence for such a theory.

The experimental/theoretical comparisons discussed above were based on the averaged results of each analyte distribution from the 6 repeated firings of each charge type. The particular individual distribution trends following each firing (not averaged) varied depending on the target analyte. The inorganic nitrate and ammonium distributions from most repeated firings showed a consistent decrease in concentration with increasing distance (figures 4.5 and 4.8) and corresponded with the same trends reported in other studies[70,84,87]. However, following the organic firings the RDX trends fluctuated more so than any of the inorganic analytes overall, lower RDX amounts were detected at 1 m than at 2 m or 3 m, following which the residue amount decreased with increasing distance (with mass fluctuations still apparent at further distances following some firings) (figure 4.26). Such oscillating trends have been observed for organic post-blast residues in previous studies[60]. The variation between the distribution behaviour of the inorganic and organic analytes could be due to different detonation behaviour (i.e. how the undetonated residues are ejected from their origin) or variations in the stability of the analytes on closer positioned sampling sites (i.e. the potential thermal degradation of RDX by the fireball temperatures).

The notion of finding more residue material by mass further away from the centre than nearer to it[57] was supported more-so by the results of the aluminium trends, which were shown to not follow the inverse square law distribution, generating an R^2 value of 0.1959 when compared to the theoretical fit (figure 4.11). The aluminium distributions all exhibited

an increase in mass detected at five metres from the charge centre with the majority of the greatest aluminium amounts detected at this point (figure 4.12). This difference between the aluminium and AN distribution pattern signifies that studies which use taggants to establish explosive residue distributions[96] must verify the taggant molecule is bound to the explosive. The finding of higher mass deposits further from the centre has been explained as due to the angle and trajectory path of the residue particles following their ejection from the detonation[57]; if particles were to stop moving at a hypothetical hemisphere above the charge, material deposited within a particular segment on the ground covered between the two trajectory angles, would be more concentrated at further distances. This theory is supported by some of the findings of previous experimental work where larger residue mass deposits were at times recovered from mid-sampled distances as opposed to closer to the detonation centre[79]. Whilst the theory and experimental study cited are relevant to distribution of residue on the ground, they may also be applied to sampling sites perpendicular to it. If the residue particle trajectories from the theoretical hemisphere above the detonation were not directly linear to the ground below, but subtended between the two incident angles towards the ground, more particles would have deposited on plates further from the detonation centre (figure 4.34).

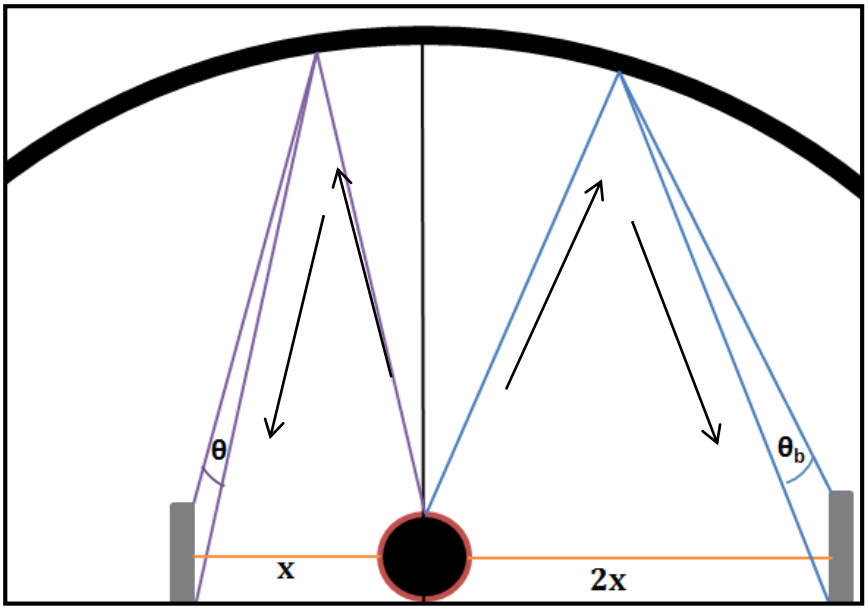

Figure 4.34*: Particle trajectory model which explains more residue mass deposition of further perpendicular sites than those closer to the centre. The central circle is the detonation area. The two grey rectangles represent sampling plates at x m and 2x m from the centre. The plate at 2x m from the detonation bisects more incident angles (ϑ_b) towards the ground than the plate at x m from the detonation.*

Clearly, the distribution patterns of different residue analytes differed by both increasing and decreasing with distance, and as this has been seen previously[88], attempts to apply only one exact theoretical construct to distribution trends of all post-blast residues is unsuitable. From a forensic perspective, the inconsistency in distribution trends amplifies the already complex task of locating trace evidence which cannot be visually identified with ease. Nevertheless based on these results, generally, the application of more sensitive analytical techniques to samples collected further from the central region of a detonation would be required in order to yield a beneficial explosive signal. Additionally, as the majority of the analytes followed an approximate inverse square law distribution, the practice of focusing residue collection near or in the central region of a detonation is supported here.

Uncertainty of Results

The quantity of all residues detected in the post-blast phase was very low, or trace, compared to the mass of the explosive charges fired. The accuracy of the measurements, i.e. the correctness of the recorded residue mass per sampled plate compared to the actual residue mass deposited on each plate, cannot be known. The amount of post-blast residue deposited during detonation would be impossible to measure exactly. It is therefore important to note that all mass ranges or absolute values detected and reported are *relative* to that deposited on the surrounding surfaces.

Indeed, this is of particular importance when stating maximum radii within which residues can be found following a firing – whilst the lowest amounts of undetonated residues, or none at all, were detected further than 6 m from the charge centres in most cases, there is no evidence that residues had not *deposited* further, just that they was not *detected* at further distances. This is augmented by the notion of instrumental detection limits; the signal produced by the analytical techniques was dependent on the instrument sensitivity to the target analyte with the LODs for ammonium, nitrate and RDX being 0.5 mg/L, 0.1 mg/L and 0.1 mg/L respectively. Therefore, any comments on nil detection or limiting radii of residue distribution are subject to these factors and hence only valid for the sampling and analysis procedures used during these experiments.

Through sampling recovery and extraction efficiency tests conducted with RDX, (details of which are in appendix A, section A.3) it was found that not all of the deposited explosive residue was collected from the sampling site, with ~ 65 % recovered through the swabbing; similar recovery rates have been reported elsewhere[126,180]. In addition, the extraction technique used incurred losses of the target analyte through the sonication, filtering and evaporation processes (average losses of ~60 %, 75 % and 87 % respectively). The estimated amount of RDX recovered following the sampling and extraction phases was

approximately 25 % based on these tests; therefore the reported amounts of the organic analyte could be only 25 % of the actual deposited amount. These efficiency tests however, were conducted by spiking known amounts of 'pre-blast' material onto surfaces, as opposed to post-blast residues, and may therefore not be an accurate reflection of the collection and extraction efficiency of the post-blast residues.

Furthermore, whilst the above discussion applies for the organic RDX residues detected, a 100 % efficient sampling and extraction of ammonium nitrate would also have been unlikely. Whilst it was not possible to assess the recovery rate of AN, the amounts reported in the results would be relative to the actual amount of AN deposited per sample site due to loss of material prior to confirmatory testing. Further to factors already discussed (such as equipment sensitivity, potential calibration errors, and sampling and extraction efficiencies), the uncertainty of measurements is further amplified by factors associated with random error which cannot be controlled for.

The uncertainty of each reported measurement would be based principally upon the variability of the measurement as established through repeated experiments, and the variability of the detector response during the various instrumental analyses, both of which were indicated where appropriate with the use of error bars.

The majority of repeated firings in this chapter produced similar residue distribution trends, however the actual amounts detected of each analyte were not comparable between firings. For example, the nitrate results in figure 4.3 showed the low reproducibility of measurements at 1 m to 5 m from the charge. Figure 4.5 demonstrated the variability was due to the random error between repeated firings as the general distribution trends were still consistent, just not the residue amounts. A study which repetitively fired ammonium nitrate based explosive charges three times under the same conditions, also found the levels of ammonium and nitrate varied between firings, yet the analyte distribution patterns were consistent[87]. Forensically, the findings signify the unique nature of each detonation event, reaffirming the concept that each bomb scene should be treated individually. Conversely, the aluminium, apart from the results from one firing, demonstrated highly agreeable amounts deposited at each sampled distance between repeated firings.

Whilst the accuracy and reproducibility of the measured mass deposits were variable (and more so indicative than highly accurate), the precision of each measurement was shown to be good, with the majority of the results from triplicate analyses of the samples generating similar detector responses (the error bars on the data plots were small and in majority of cases less than 10 % of the data point). This could not be confirmed however for the

aluminium, which could only be analysed once (the precision of the aluminium measurements were therefore unknown).

Any scientific experiment requires repeated measurements to be obtained (and further sampling efficiency tests to be conducted), the results here indicate that for experiments involving complex reactions such as detonations this is truer, although it is not necessarily practically feasible to do so. Indeed, with limited access to explosive ranges and explosive materials, few studies in the literature have repeated their experiments, focusing rather on conducting different firing trials during each opportunity instead, hence the six repeated firings makes this study unique in the literature. The requirement for experimental replicates may be overcome by combining the limited empirical datasets with numerical simulation techniques capable of generating multiple tests.

Potential Factors that Affect Distribution

Blast Over-pressure

The blast-pressures were measured in only one orientation (south-east) around charge. The blast-waves from spherical charges are known to produce spherical waves of similar pressures in all orientations[46,181] and due to this the overpressures measured at 1 m to 4 m from the detonations were presumed to be equivalent at all directions around the detonation. All detonations produced blast overpressure signals synonymous with theoretical concepts[28,45]; with an initial rapid rise in pressure, followed by pressure decay over the impulse time to a negative pressure region caused by the initial outward movement of air (figures 4.15 and 4.28). The pressures returned to ambient level when air had filled the 'void' caused by the inertial effect of the overpressure[44]. The AlAN charges produced lower peak overpressures (167 kPa) and slower moving blast-waves than the PE4 charges of equal mass (peak overpressure ~479 kPa) as expected; the energy release from RDX composition explosives is greater than that of AN-fuel mixtures[44,182]. The sensors positioned 1 m from the charge centres of the PE4 charges did not show the pressure level return to ambient. Close in (at 1 m) from the detonation of a 0.5 kg military composition charge, the pressure gauges can undergo thermal shock and this can manifest as a false negative shift in the data[183]. Whilst the sensor would not have been damaged by the peak overpressure, it would have taken longer than the recording time to recover due to the heat delivered to it.

The distribution of post-blast residue particles has been hypothesised as being due to the blast-wave movement, the positive overpressures of which could cause ejected residues to be pushed outward from the detonation centre[3,57]. For the inorganic detonations, the blast pressure decreased 1 m to 4 m from the charge centre as did the mass of the inorganic analytes at these measured distances (figure 4.16). No other correlation between the

overpressure and inorganic residue distribution pattern was apparent. Indeed, the blast-wave was observed to move ahead of the movement of potential particulate matter being ejected in front of the fireball during the AlAN detonations (figure 4.17b and 4.17c), which does not support the concept of particle movement being enhanced by detonation pressure. Other studies have also suggested the blast-wave does not aid the ejection of particulate material[70,87,88].

Conversely, the organic analyte distributions showed lower amounts of RDX at 1 m, where the blast overpressures were the highest. At 2 m the RDX mass was greater and the blast overpressure had decreased from 479 kPa to 119 kPa. At the following measured distances of 3 m and 4 m, both the overpressure and residue mass deposits decreased with increasing distance. If undetonated particles of RDX were spalled from the charge surface ahead of the shockwave and deposited onto surrounding plates at 1 m, it could be considered that the subsequent movement of the blast-wave through the plates at 1 m could have caused the decomposition of deposited particulates (hence causing lower amounts to be detected there). The particles on plates at 2 m were exposed to lower overpressures (119 kPa) and may have maintained their undecomposed state to subsequently be detected in greater quantities. If this were the case, this would explain the fluctuation of RDX close to the detonation centre, assuming the deposition of undetonated material occurred due to spallation from the charge surface. Nevertheless, the notion of the blast wave itself carrying or promoting the movement of the particles is unverified here. Furthermore, no literature to explain the effect of different pressure regimes on undetonated RDX particles is available to validate these suggestions at present. In order to fully assess the effect of the positive blast pressures on residue particle deposition it would be necessary to further understand the relationship between pressure and explosive residue decomposition, additionally the back of the sampling plates should be sampled in order to gauge the possible effect of the negative blast pressure on 'pulling' particles back in towards the detonation centre.

Fireball

Fireballs produced from both the AlAN and PE4 charges were spherical with unsmooth boundaries or surfaces. Each of the explosives was moulded into spherical charges; whilst the surface smoothness of each charge was not ascertained, it is very unlikely that completely smooth surfaces would have been produced. Hence, due to instabilities occurring on both a molecular and macro scale[51] the resulting fireballs would be expected to have irregular boundaries. The fireballs from the AlAN firings had a spiked appearance which was not observed in the PE4 fireballs; the addition of the aluminium to ammonium nitrate charges would have caused the metal particles to form filamentary jets protruding from the product gases which when ignited would appear as spikes due to the remnants of

particle jets[47]. Particulate material was also visible between the blast-wave and the fireball surface during the inorganic firings (figure 4.17), which was not clear during the organic firings (figure 4.31). This may have been evidence of the undetonated particulate matter moving away from the fireball to be deposited onto surrounding sampling sites, or the reaction of aluminium particles with atmospheric oxygen.

The overall volumes of the 0.5 kg AlAN fireballs were smaller (1.32 m radius) than the PE4 fireballs (2.20 m radius) produced from the same charge mass. Theoretical calculations of the fireball radius (equation 2.3)[3] are not applied here as they do not take into account the explosive type and each material clearly produced different fireball volumes. The larger volumes of gas from the PE4 charges were expected because theoretically more moles of gas are produced during the detonation of RDX compared to the detonation of AN (equations 1.1 and 1.2). The RDX fireballs were therefore observed to extend across further sample sites than those of the AlAN charges.

It has been suggested that any undecomposed explosive adhered to a surface close to the detonation centre may subsequently be engulfed in the fireball and decomposed due to exposure of the flame front[3,69]. The RDX amounts were lower in the fireball region (1 m) than at the edge of the fireball region (2 m), thus seemingly supporting this theory, however the amounts of RDX also fluctuated at further distances (3 m to 6 m) (figure 4.32) where the fireball was not seen to extend. Similarly, the quantity of aluminium detected peaked at 5 m, and therefore 3.5 m further than the observed extent of the fireball during the AlAN detonations (figure 4.20). Moreover, the highest nitrate and ammonium amounts were detected from the closest sampling sites (1 m) which were seen to be engulfed by the fireball (figures 4.18 and 4.19). The closest sampled distance in all cases was 1 m from the centre, it is unknown if sample sites closer than this (i.e. < 1 m) would have yielded lower quantities due to thermal decomposition.

The findings presented here neither strongly supported nor refuted the notion that lower amounts of residue may be found nearer the centre due to thermal degradation of undetonated residues by the fireball. The high speed recording of the detonations was conducted from only one angle around the charge centre and the fireball radius was assumed to be equal in the unobserved orientations but this may not have been the case. Contrary to the near symmetrical nature of blast overpressures from spherical charges[46], fireball dynamics are more sensitive to minor morphological variations[52,184]. In order to thoroughly assess any interaction between the fireball and sampling plates, and the relationship between the subsequent mass of residue detected upon them, it would be necessary to record detonation experiments from multiple angles around the charge centre.

Wind Direction

Light grey/white smoke plumes formed from the AlAN detonations because of the positive oxygen balance of the explosive charge and thus the more efficient oxidation of the fuel[11]. The dark grey/black smoke formed from the PE4 detonations was due to the negative oxygen balance of the explosive and thus the incomplete oxidation of the fuel components of the molecule, visible as carbon particles in the smoke cloud[11]. All smoke plumes were observed to move in line with the wind directions during firings.

From the majority of the repeated firings the amount of residue detected on similar distanced sampling sites in different orientations around the charge centre were not comparable, indicating some directional bias in the residue distribution, a finding which has also been identified and mentioned elsewhere[60,70]. The greatest quantities of each analyte from these experiments were recovered from sampling sites which were positioned downwind (figures 4.21, 4.22, 4.23, 4.33), indicating the movement of undetonated residues occurring in the smoke plume, which would be governed by the wind field. This hypothesis is reiterated elsewhere where the movement of residues has been explained as due to the acceleration of particles in the gas expansion with the final and predominant phase of movement determined by the wind[60]. The exact mechanism for how undetonated residue particles remain within the smoke plume is however unknown. This trend was less obvious for the aluminium though, which again was suggestive of it having a different dispersal mechanism.

The forensic implications of this finding would be to emphasise residue sampling in areas which are known to be downwind around a bomb scene. If CCTV footage of the area is available and the smoke plume movement was monitored within it, the areas where post-blast residues may have deposited (on surrounding surfaces for example) may be gauged in this way.

Summary

The results presented here and their comparison to theory and literature are subject to the conditions under which the experiments were conducted, principally that of small (0.5 kg) unconfined spherical charge systems which were detonated in an open field, the residues from which could only be sampled at discrete, limited points. No other openly available experiment has been conducted in such a 'controlled' manner. The findings here are therefore restricted to these scenarios and require development. In order to improve the accuracy of the measurements obtained, it would be necessary to establish a certain indication of residue loss through all experimental procedures and phases prior to the instrumental detection.

Nonetheless, key findings from this set of experiments highlight the variant nature of residue distribution based on the target analyte. Clear differences between the organic and inorganic residues were apparent; the ammonium and nitrate were more regularly dispersed generating more linear trends than the RDX, which fluctuated with increasing distance from the centre. Conversely, the aluminium was consistently deposited in greater mass further from the centre. The majority of the target analytes distributed approximately according to the proposed inverse square law (ammonium nitrate producing the strongest correlation and aluminium being the clear anomaly to this).

From these findings reported in this chapter it could be inferred that the factors which affect residue distribution also vary depending on the analyte. The inorganic residues seemed unaffected by the blast pressure and fireball, whereas RDX may have been affected by one or both of these. However, it could not be distinguished whether the distribution of RDX followed the trend of finding more material further away or more material depositing closer to the centre to be subsequently decomposed by the fireball/blast (thereby exhibiting a perceived maxima in mass at further sampled points). The variation between the ammonium nitrate and aluminium may also suggest that the mechanism by which different components of a mixed explosive charge disperse during detonation varies. The aluminium deposited further from the centre seemed to follow the residue trajectory model which considered the angles of particle movement, whereas ammonium nitrate seemed to distribute corresponding to a model closer to the inverse square law. Furthermore, the effect of wind direction on residue distribution was the most conclusive factor in all cases; it would not be unreasonable to deduce that the mechanism for residue distribution may therefore occur primarily dependent on the analyte type, and in a following phase be governed by the surrounding wind field irrespective of the analyte type.

CHAPTER 5: COMPLEMENTARY STUDIES WITH LARGER CHARGES

5.1 Introduction

This chapter contains results from complementary firings of larger charge masses; unconfined 1 kg and 2 kg of AlAN and PE7 (RDX-based) explosive compositions were fired at Porton Down, although only one firing of each of the larger charges was possible. Residue samples were collected from sampling plates positioned 0.75 m and 2 m from the ground at four different orientations and incremental distances up to 30 m from the detonation centres. Further to the unconfined larger charge masses, confined RDX-based charges (~1 kg) were fired inside of vehicles at the Kineton DEMSS firing range.

Inorganic residues (ammonium and nitrate) were analysed with IC; it was not possible to analyse for aluminium content from the inorganic firings in this series of tests. Organic residues were analysed with HPLC-MS. The results from the inorganic AlAN firings are presented first (section 5.2), followed by the unconfined organic (section 5.3) and confined firings (section 5.4); the post-blast residue amounts from each are compared to physical aspects of the detonation in order of their occurrence (the fireball volume and subsequent movement of the smoke plume). With no blast-pressure recording facilities available at either of these firing ranges, it was not possible to collect overpressure data. The results are also compared where appropriate to the findings from the smaller 0.5 kg charges from the previous chapter. The results are summarised (section 5.5) before being discussed in comparison to the literature (section 5.6).

5.2 Unconfined AlAN Firings

5.2.1 Inorganic Post-blast Residue Results

No nitrate or ammonium were detected in the control samples of blank DI water, blank swab samples, blank steel plate samples, or in blank DI water samples injected between test samples therefore any target analytes detected in each post-blast sample were attributed to the explosive residue in that sample.

The total residue amounts (i.e. the summed nitrate and ammonium masses) from all four sampled orientations around the charge centre are presented in comparison to the theoretically proposed inverse square law distribution in figure 5.1 for the 1 kg and 2 kg charge masses. The theoretical trend was initially calculated using the same totalled experimental value from the closest sampled distance of 3 m (15.3 mg and 70.4 mg for the 1 kg and 2 kg charges respectively).

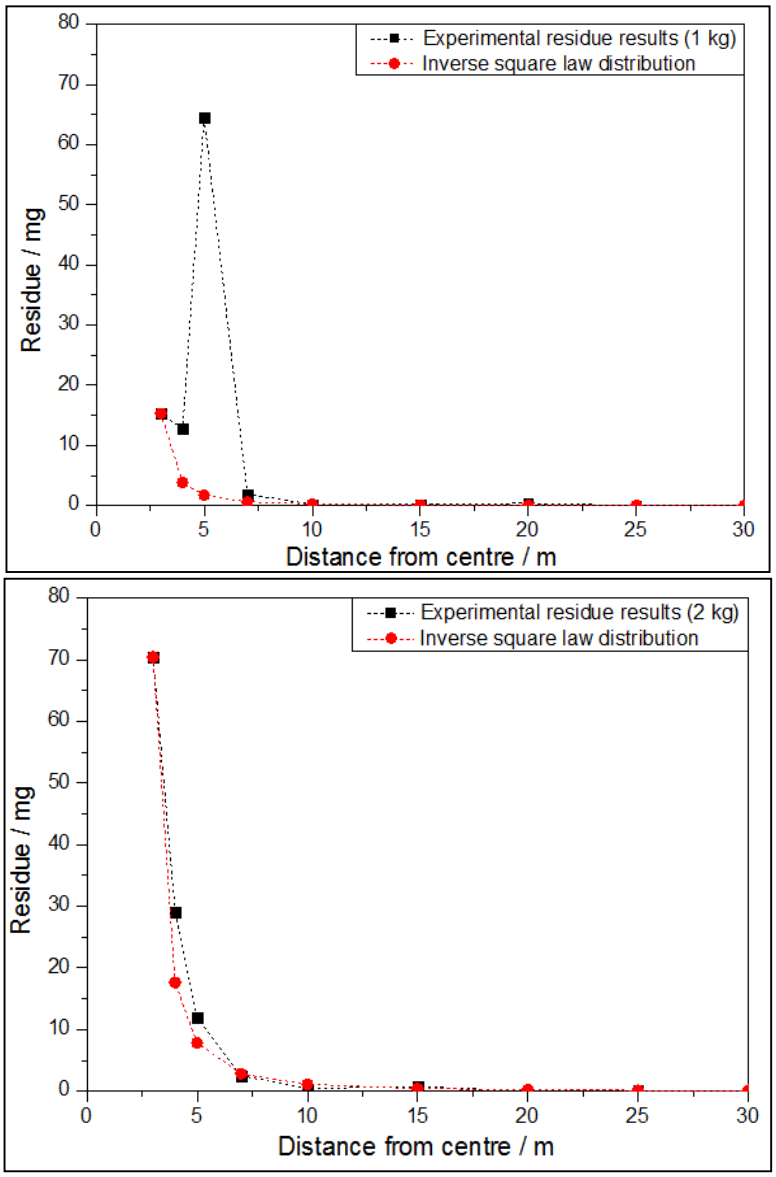

Figure 5.1*: Comparison of summed experimentally determined residues (nitrate and ammonium – in black) (all data points) against the theoretical inverse square law distributions (in red) for the detonation of the 1 kg (top) and 2 kg (bottom) AlAN firings.*

Comparison of the 1 kg firing to the theoretical trend showed the two plots differed; the experimental values at 4 m, 5 m and 7 m were greater (12.7 mg, 34.5 mg and 1.89 mg) than the theoretical ones (3.83 mg, 1.70 mg and 0.61 mg). The experimental and theoretical distributions from the 2 kg firing corresponded well, apart from at the 4 m and 5 m measured distances where the experimental values (29.0 mg and 12.0 mg) were greater than the respective theoretical ones (17.6 mg and 7.83 mg).

As done so in the previous chapter, by omitting the values obtained from the closest sampled point (in this case at 3 m from the centre; thought to skew the dataset due to their proximity to the detonation), the results were compared to the inverse square distribution by plotting against 1/d^2 (d being the distance from the centre in metres) in figure 5.2. In the case of the 1 kg firing results, the anomalous datum recorded from the 5 m point (64.5

mg; top of figure 5.1) was also omitted from the comparison in order to avoid skewing the comparison (figure 5.2).

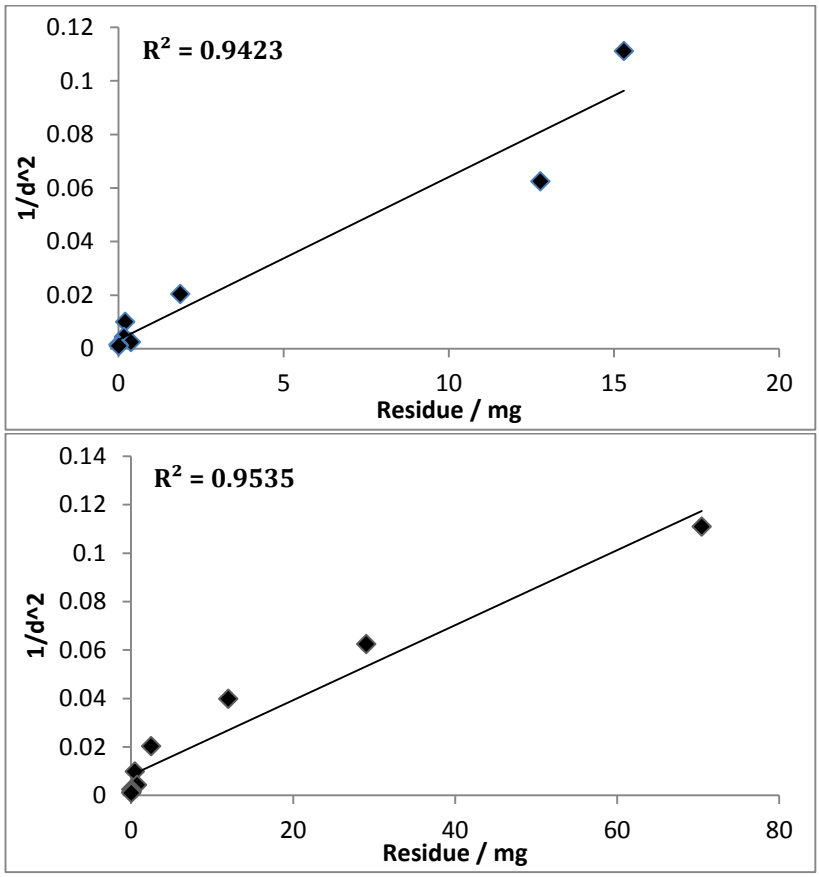

Figure 5.2: *The experimental data (without the anomalous datum from the 3 m sampling points) compared to the 1/d^2 theoretical inverse square law. In the case of both the 1 kg (top) and 2 kg (bottom) firings, a positive linear correlation was exhibited between the two.*

The R^2 values produced from each comparison (0.9423 and 0.9535 for the 1 and 2 kg AlAN firings respectively) demonstrated a high degree of linearity between the experimental and theoretical data.

Having compared the totalled residue values, the individual trends from each inorganic analyte were plotted to assess the distribution of each when compared against the theoretically proposed trend for each of the charge masses. As only one firing was possible per charge mass (and therefore the inclusion of the inconsistent result from the 1 kg firing would not affect averaged measurements), all measurements were included in subsequent comparisons.

Nitrate

The nitrate mass ranges detected following the 1 kg and 2 kg firings were 0 mg to 54 mg and 0 mg to 30 mg, respectively. The majority of the greater mass depositions were detected within 10 m around the detonation centre. Similarly to the summed trends depicted in

figure 5.1, the nitrate residues detected following the 1 kg AlAN firing did not follow the theoretical trend (figure 5.3).

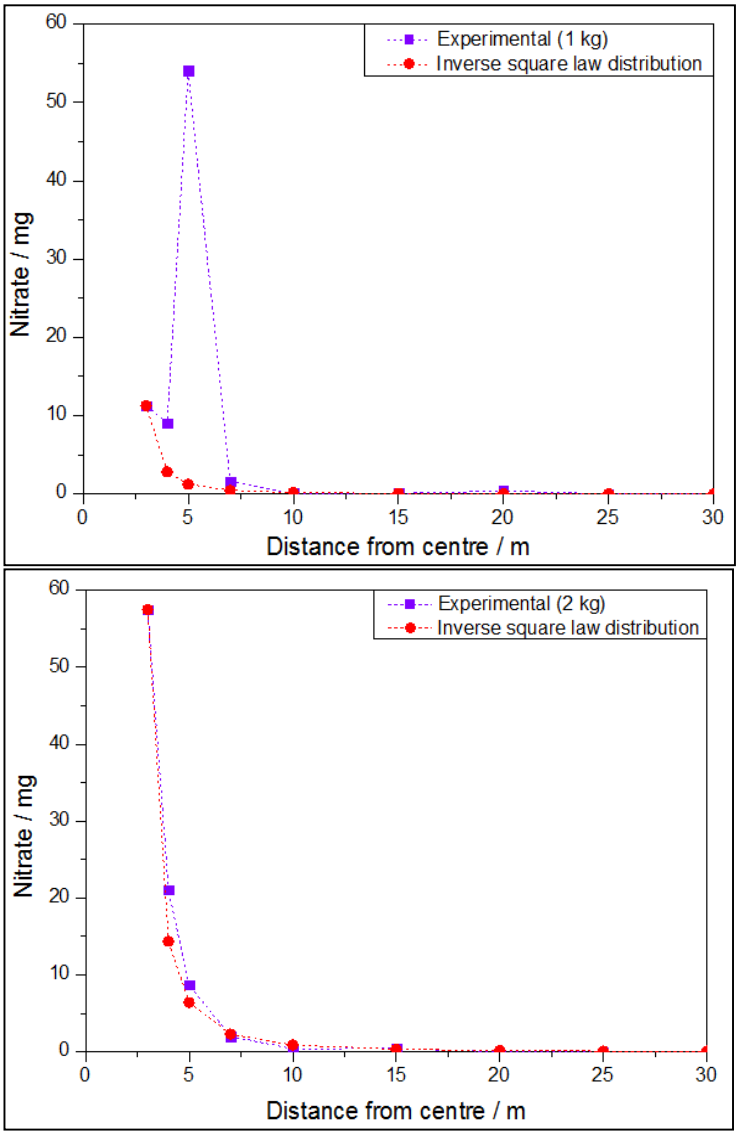

Figure 5.3: *Comparison of nitrate (purple) against theoretical inverse square distributions (red) for the detonation of the 1 kg (top) and 2 kg (bottom) AlAN firings.*

The experimentally determined nitrate recoveries were higher at 4 m and 5 m following the 1 kg and 2 kg firings compared to the theoretical values; the data did not appear to correspond exactly to the theoretical inverse square law, although the decreasing residue concentration trends were very similar, particularly following the 2 kg AlAN firing.

A comparison between the experimental data and '1/d^2' without the results from the points sampled at the closest distance of 3 m showed that due to the anomalous high mass of nitrate detected at 5 m following the 1 kg AlAN firing, the data did not follow the inverse square law distribution (R^2 of 0.1236; top of the figure 5.4). Conversely the data from the 2

kg firing showed the nitrate distribution corresponded well with the inverse square law distribution model (R^2 of 0.9388; bottom of figure 5.4).

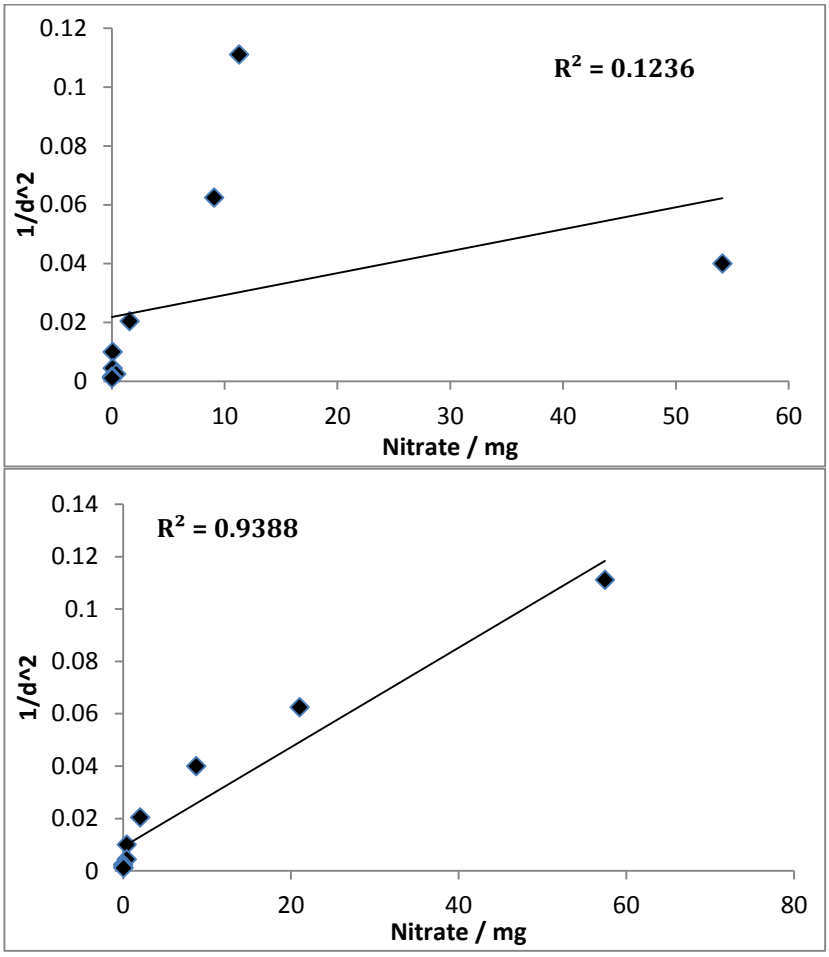

Figure 5.4: *Comparison of experimental data with 1/d^2 law (without the data from the 3 m sampling points) showing a better correlation following the 2 kg firing (bottom of figure; R^2 = 0.9388) than following the 1 kg firing (top of figure; R^2 = 0.1236).*

The results depicted in figure 5.3 and 5.4 were based on the summed values from both sampled heights (0.75 m and 2 m from the ground); in figure 5.5 the amounts detected from each sampled height around the detonation are presented in comparison to each other. Following the 1 kg firing, the nitrate deposited onto the 0.75 m high plates decreased with increasing distance from the centre. The amount of nitrate detected on the 2 m high sampling plates increased with increasing distance until 5 m, following which it decreased with increasing distance. The data point skewing the distributions following the 1 kg firing was from the 2 m high sampling plate positioned 5 m from the charge centre (top of figure 5.5).

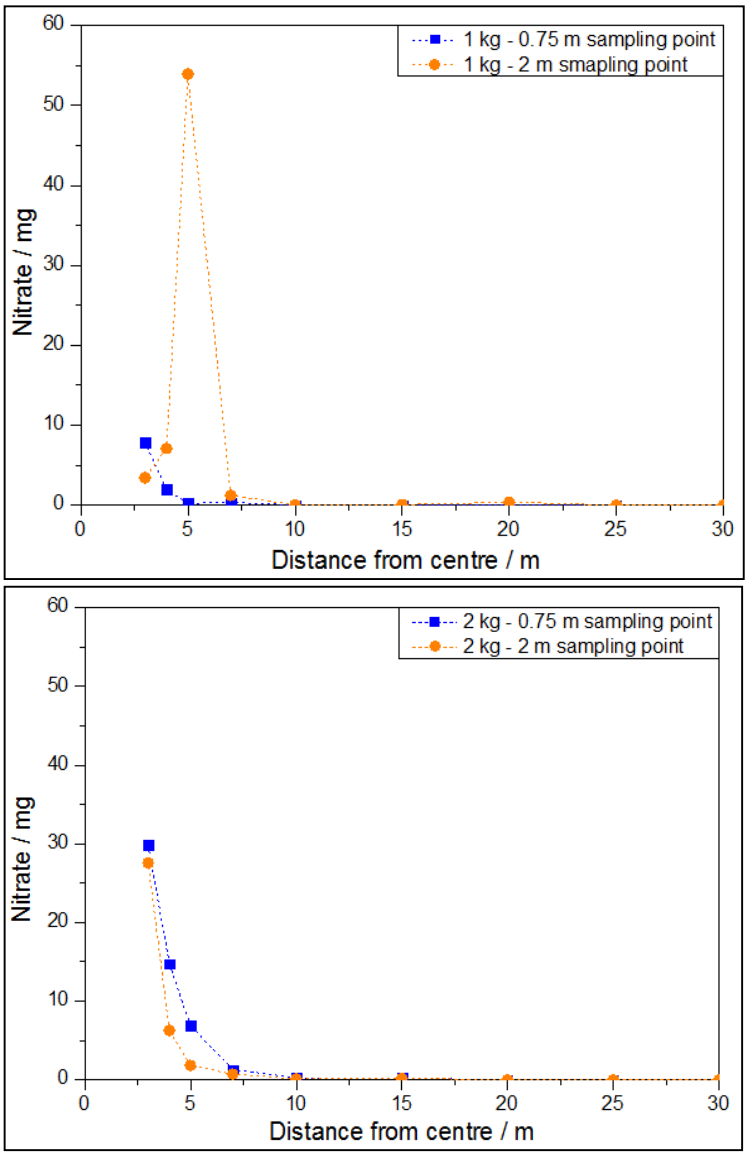

***Figure 5.5**: Variation between nitrate distribution based on sampling heights: top = 1 kg firing, bottom = 2 kg firing*

Following the 2 kg firing, similar distribution trends were exhibited from samples taken at both sampling heights, the actual nitrate amounts from the 0.75 m high sampling plates were higher (29.9 mg, 14.8 mg, 6.88 mg, and 1.31 mg) than those from the 2 m high sampled plates (27.6 mg, 6.27 mg, 1.82 mg and 0.70 mg) until 10 m from the detonation centre at which point the amounts were similar (bottom of figure 5.5).

Ammonium

The ammonium mass ranges detected from the 1 kg and 2 kg firings were; 0 mg to 8.50 mg and 0 mg to 6.86 mg, respectively. The majority of ammonium was detected within 10 m around the detonation centre. The ammonium distributions from both the 1 kg and 2 kg firings did not follow the theoretical inverse square law (when generated including the experimentally determined data point from 3 m; figure 5.6); the trend was dissimilar following the 1 kg firing, and whilst similar following the 2 kg firing, the experimental values

were higher at the 4 m, 5 m and 15 m sampled distances (8.00 mg, 3.28 mg and 0.33 mg) compared to those determined theoretically (3.24 mg, 1.44 mg and 0.08 mg) (bottom of figure 5.6).

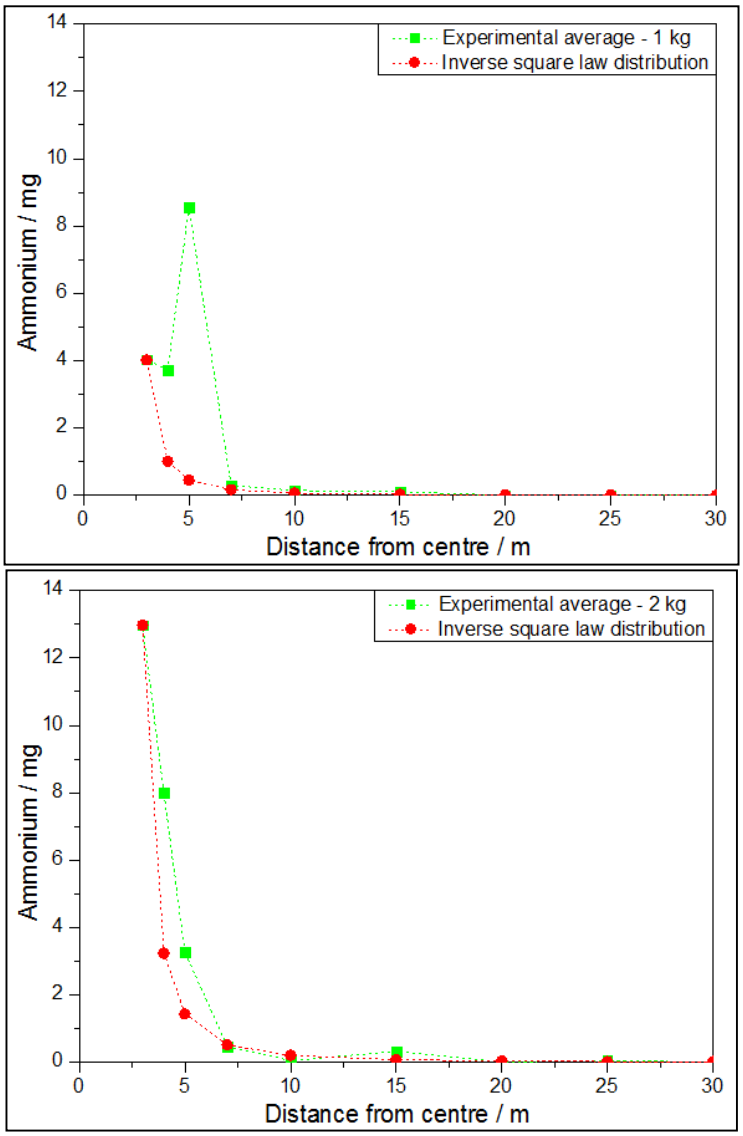

***Figure 5.6**: Comparison of ammonium (green) against the theoretical inverse square law distributions (red) for the detonation of the 1 kg (top) and 2 kg (bottom) AlAN firings.*

When plotted against the inverse square law equation (figure 5.7) and without the datum from the 3 m sampled points, the distributions correlated to a varying degree with the theoretical trend. The ammonium distributions following the 1 kg AlAN firing did not correspond well with the inverse square law (R^2 of 0.3808; top of figure 5.7). Conversely, following the 2 kg AlAN firing the data plot produced an R^2 of 0.9715, thereby indicating a better fit to the theoretical model (bottom of figure 5.7).

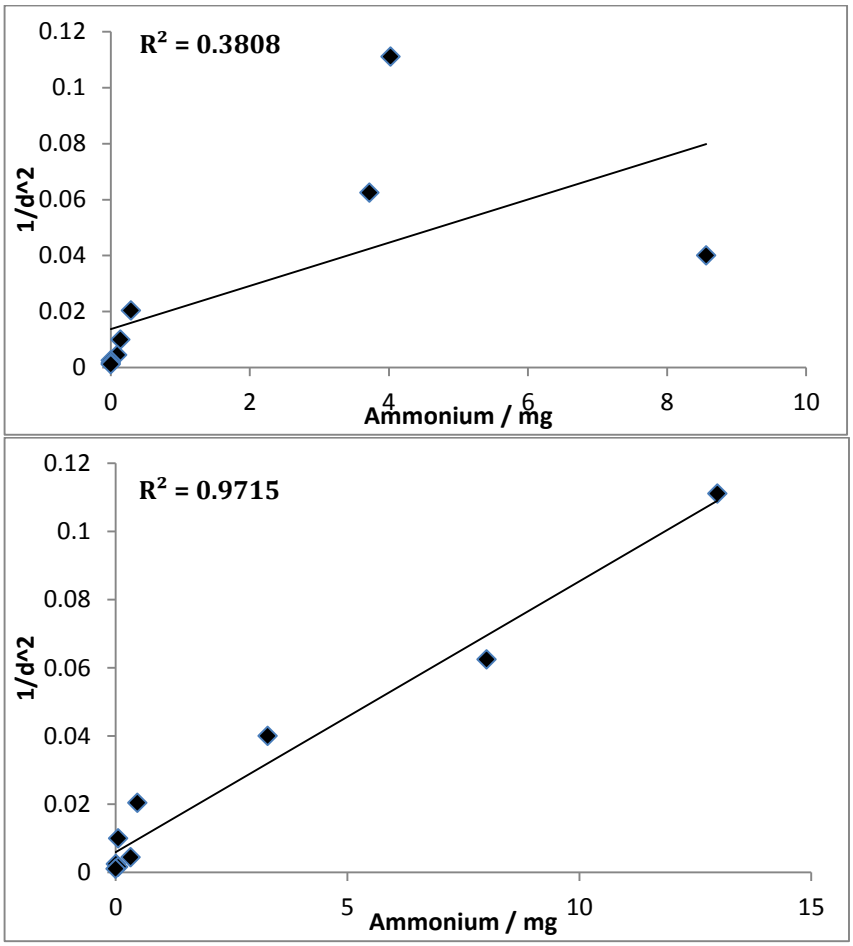

Figure 5.7: *Experimental data for ammonium plotted against theoretical inverse square law (1/d^2) without the data points from 3 m, showing a strong correlation for the data from the 2 kg firing (bottom of the figure) compared to that of the 1 kg firing (top of the figure).*

The results in figure 5.6 and 5.7 were based on the summed values from both sampled heights (0.75 m and 2 m high from the ground); figure 5.8 shows the amount of ammonium detected from each sampled height. Following the 1 kg AlAN firing, the majority of ammonium was detected from the sampling sites which were 2 m high from the ground, and therefore at the charge height (top of figure 5.8). Following the 2 kg firing, greater quantities of ammonium were detected from the sites which were lower down at 0.75 m from the ground (bottom of figure 5.8).

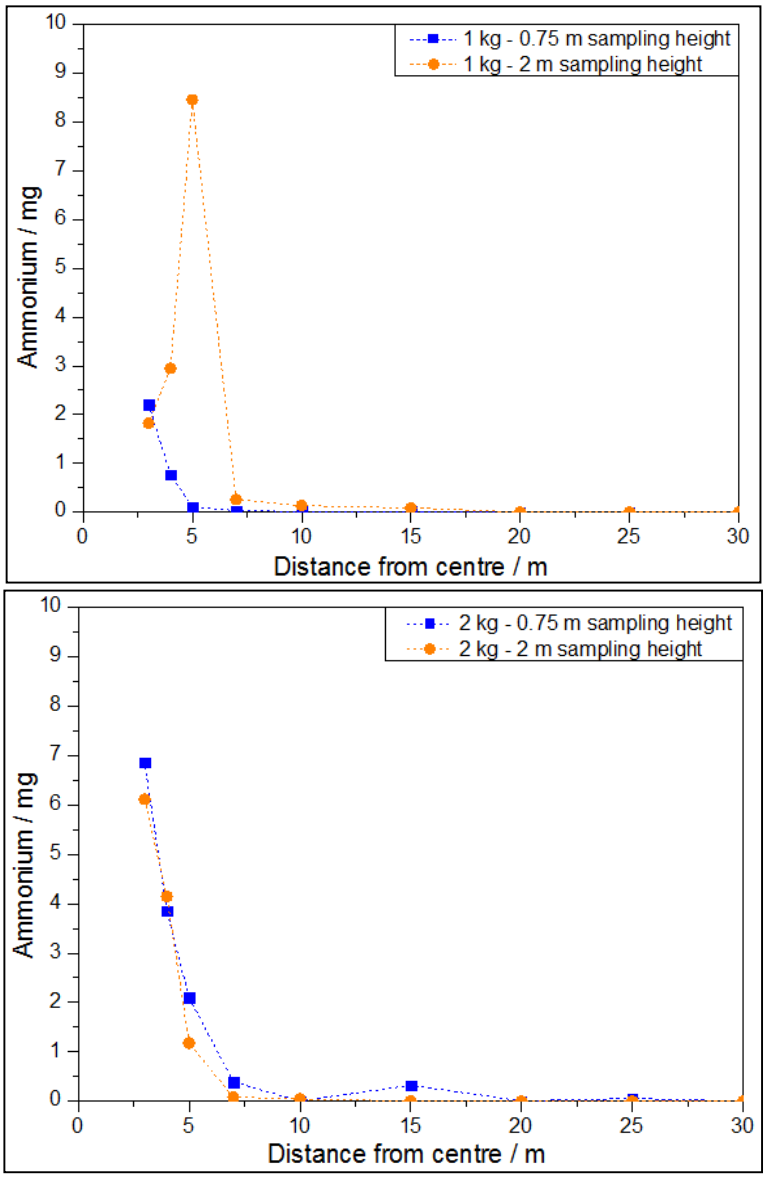

***Figure 5.8**: Variation between ammonium distribution based on sampling heights: top = 1 kg firing, bottom = 2 kg firing*

Comparison between Inorganic Analytes

Figure 5.9 shows a comparison between the total nitrate and ammonium amounts detected from the 1 kg and 2 kg AlAN charges. Both analytes depicted similar distribution trends to each other, clearly showing the ammonium and nitrate ions to be directly linked as undetonated ammonium nitrate. The greatest amounts of both ions were detected within a 10 m radius around the detonation centre (figure 5.9). Overall, the ammonium mass detected in the majority of samples (0 mg to 8.5 mg range) was lower than the corresponding nitrate mass range (0 mg to 54 mg), and a proximate stoichiometric relationship (molar mass ratio of ammonium:nitrate ~1:4) was observed between the two ions (here the actual ratio being 1:6).

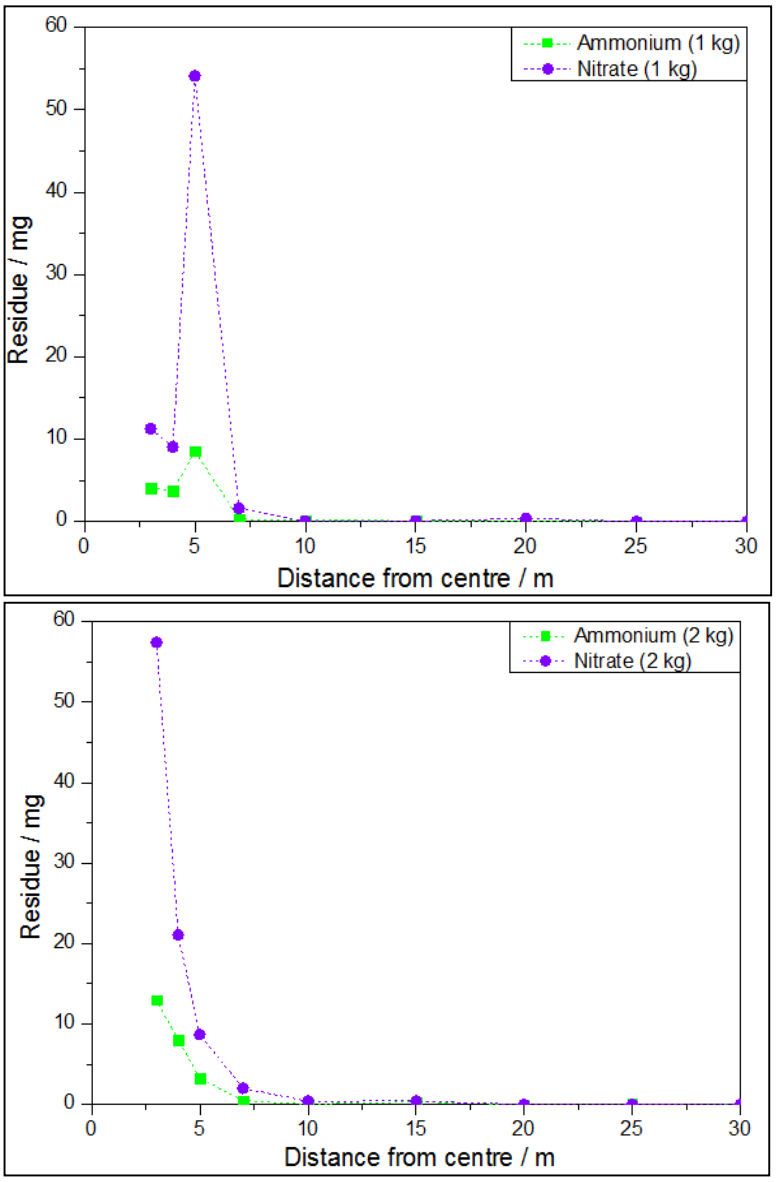

***Figure 5.9**: Direct comparison between nitrate and ammonium residues concentrations and trends from the 1 kg (top) and 2 kg (bottom) firings.*

No distinct variation was observed between the amount of each analyte detected and the charge mass fired (figure 5.9). However, compared to the 0.5 kg charges from the previous chapter (nitrate mass range; 0 mg to 14 mg, ammonium mass range; 0 mg to 3 mg), the amounts detected from these larger charge mass firings were approximately three times higher from the equivalent measured distances.

Having established the general residue distribution trends of the inorganic analytes, they were compared to the fireball and smoke plume movements.

5.2.2 Fireball

Representative stills from imaging footage of the AlAN firings were used to estimate the fireball volumes. A full set of high speed imaging (HSI) and GoPro footage stills can be seen in appendix C. Due to technical failures with the recording equipment the HSI footage of the

2 kg AlAN firing could not be retrieved. Table 5.1 shows the approximated fireball and smoke plume size based on radii observed through the HSI footage of the 1 kg AlAN detonation, the estimates are made when the largest radii of each were observed (at t = 35 ms and t = 250 ms respectively) in order to approximate the fireball extent in relation to the sampling sites. The volumes were calculated assuming a spherical volume for both the fireballs and smoke and for the 1 kg charge was estimated to be 268 m^3 and 382 m^3 respectively (table 5.1).

Charge mass /kg	Fireball radius /m	Fireball volume /m^3	Smoke plume radius /m	Smoke plume volume /m^3
1	4.00	268	4.50	382

Table 5.1*: Estimated fireball and smoke cloud sizes based on HSI footage of the 1 kg AlAN firing. All estimates are based on spherical volumes and given to 3 sig. figs.*

Representative stills of the 1 kg AlAN detonation showed the initial fireball shape (at t = 3.75 ms) was not spherical (figure 5.10a); the lower region of the fireball had a spiky surface. Potential particulate material being ejected from the detonation centre was visible at t = 10.3 and 35 ms (indicated by arrows in figures 5.10b and 5.10c respectively), where the fireball had grown more spheroidal and extended across sampling sites up to 4 m from the centre. The resulting smoke cloud was grey/white (figure 5.10d, seen at t = 258 ms).

Figure 5.10*: Stills from HSI footage of 1 kg AlAN firing (unconfined): a) t = 3.75 ms*

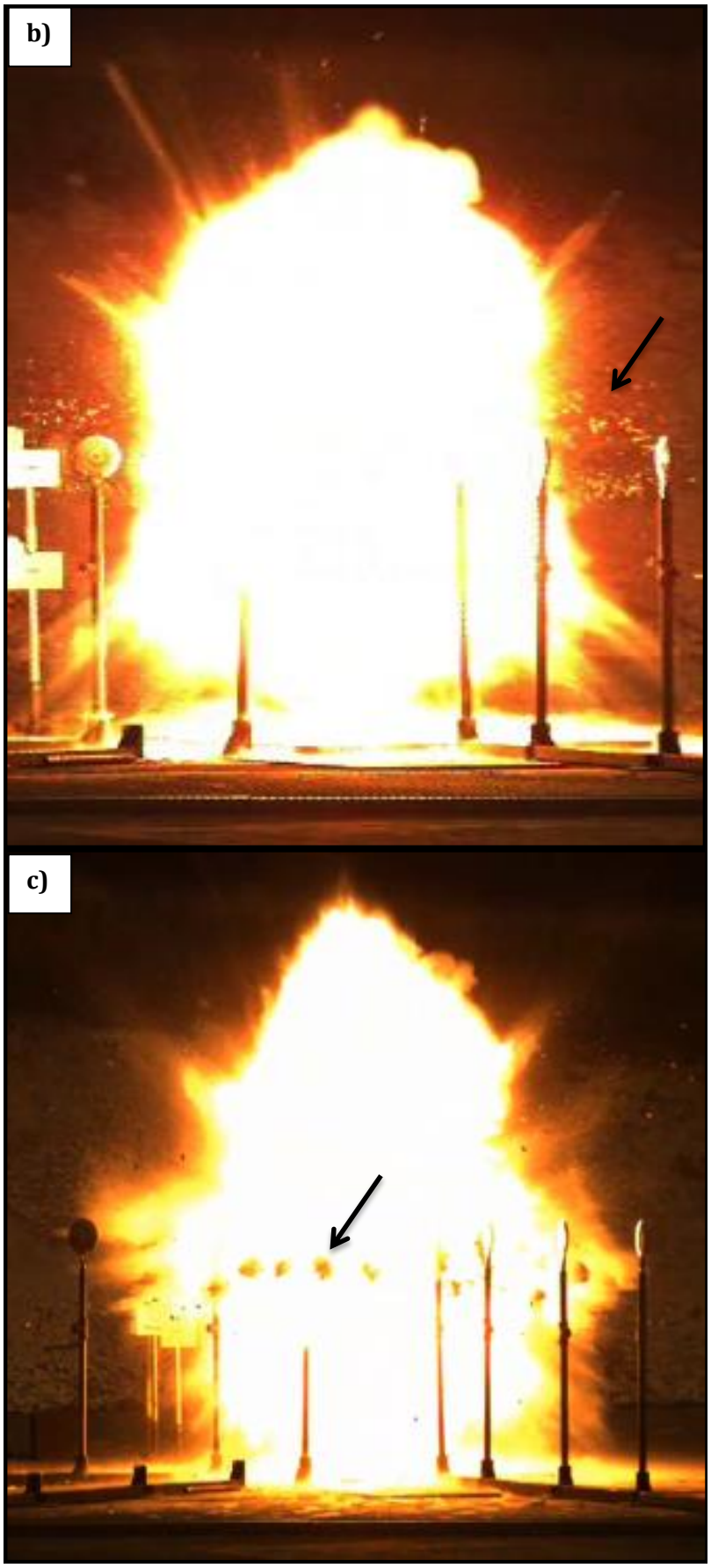

***Figure 5.10 cont'd**: b) t = 10.3 ms, c) t = 35.0 ms*

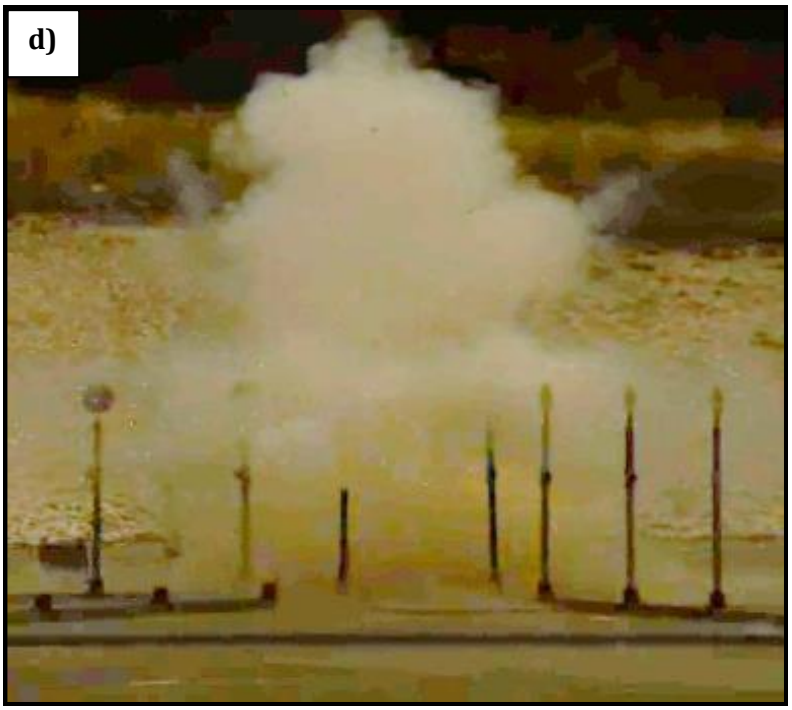

***Figure 5.10 cont'd**: d) t = 258 ms*

Comparison between Fireballs and Post-blast Residues

The fireball radius during the 1 kg AlAN firing was compared to the inorganic residue distributions (figure 5.11). The 2 m high sample sites (red and black plots in figure 5.11) which were within the fireball region (depicted by the blue bar in figure 5.11) yielded lower amounts of both nitrate and ammonium compared to at the edge of the fireball (5 m) where the detected analyte mass was higher. After 5 m the amounts of both analytes decreased (between 7 m and 30 m from the centre). The 0.75 m high sampling plates (left hand side in figure 5.11) did not exhibit the same trend; greater amounts of both inorganic analytes were recovered within the fireball region (3 m).

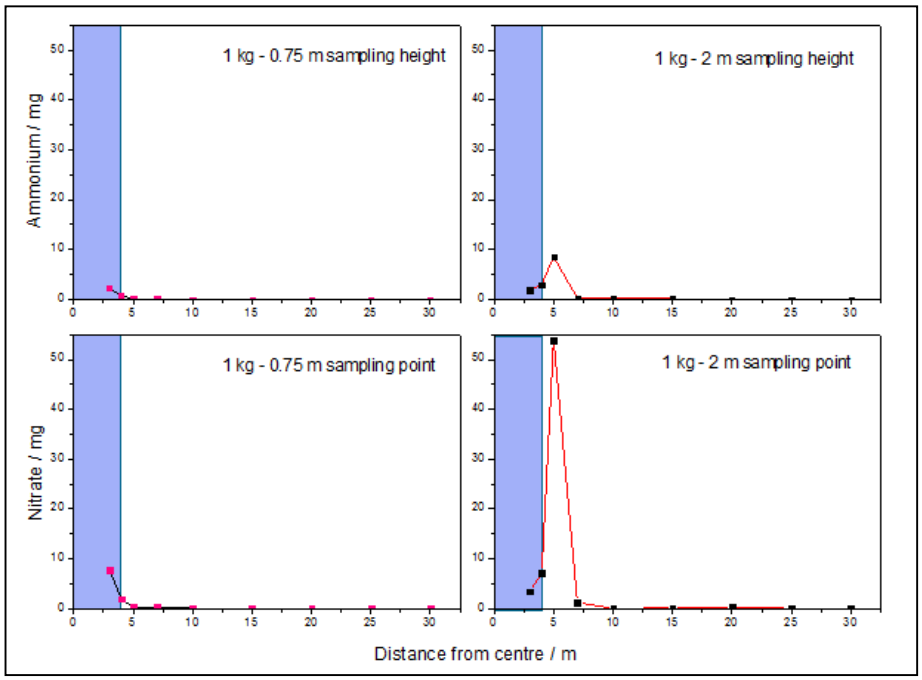

Figure 5.11: *NH_4^+ (top) and NO_3^- (bottom) distributions from 1 kg AlAN firing. Blue bar indicates fireball radius (m). 2m high plates yielded lower analyte concentrations within the fireball. 0.75 m high plates yielded highest concentrations within the fireball.*

5.2.3 Meteorological Conditions

The movement of the smoke cloud formed following the firing was observed and correlated with the meteorological conditions at the time of firing, details of which are presented in table 5.2. The wind direction was consistently toward the westerly and north-westerly directions throughout the firings; wind speed varied between 6 m/s and 7 m/s. The temperature, barometric pressure and humidity were similar between firings.

Charge mass /kg	Wind Speed / (m/s)	Wind Direction	Temperature /°C	Humidity /%	Pressure /mbar
1	6.00	N	19.0	39.0	1013
2	7.10	NW	24.0	47.0	1012

Table 5.2*: Meteorological conditions recorded at the time of each firing, for 1 kg and 2 kg charge masses. Measured with a Kestrel 3500 weather monitor.*

Comparison of Wind with Residue Distribution

Figures 5.12 – 5.15 show the residue distribution trends per orientation (north, east, south and west) around the charge centre following the 1 kg and 2 kg AlAN firings. Following the 1 kg firings the greatest quantities of nitrate (figure 5.12) and ammonium (figure 5.13) were recovered from sites which were in line with the general wind direction during firing (north and west), with the wind bias more obvious for the 2 m high sampling plates (right hand side plots of figures 5.12 and 5.13).

The precision of each measurement was evaluated by injecting all samples in triplicate; the maximum standard deviation of the mean averaged amounts detected per sample was approximately 5 mg for the nitrate ion and 2 mg for the ammonium ion. Both of these maxima were from outlier results (the 2 m high sampling sites positioned 5 m from the detonations), in all other cases the precision of each sample measurement was high (less than 5 % deviation) – indicated by the very small error bars on the plots.

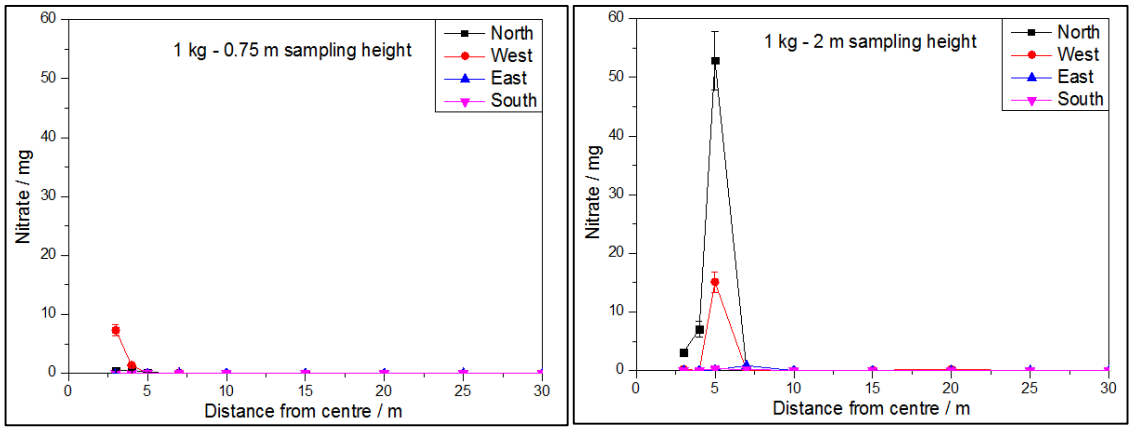

***Figure 5.12**: Nitrate recovery from 1 kg AlAN firing: left = 0.75 m high sites, right = 2 m high sites. Wind was 6 m/s towards north*

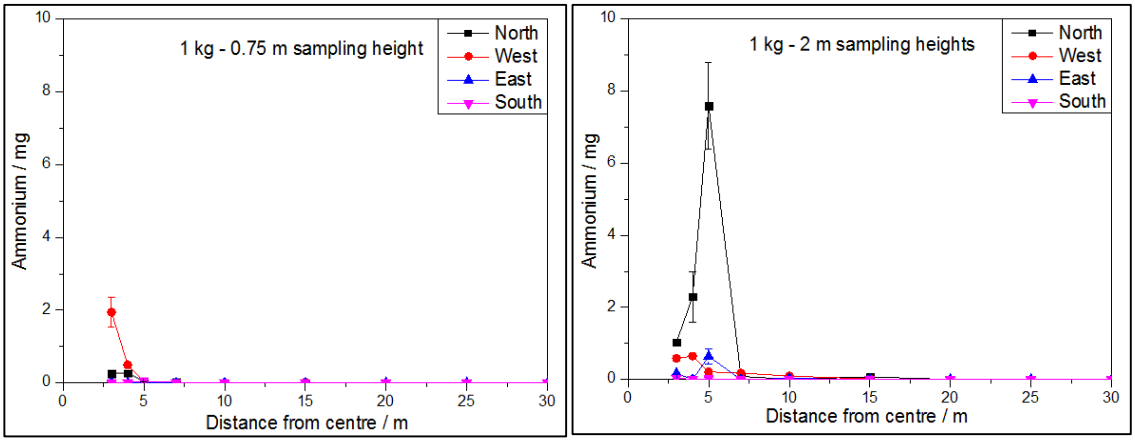

***Figure 5.13**: Ammonium recovery from 1 kg AlAN firing: left = 0.75 m high, right = 2 m high sites. Wind was 6 m/s towards north*

Following the 2 kg firings the greatest nitrate (figure 5.14) and ammonium (figure 5.15) amounts were again recovered from sites which were in line with the general wind direction during firing (north and west). No obvious wind bias between the two sampling heights (0.75 m and 2 m) was apparent following the 2 kg firing.

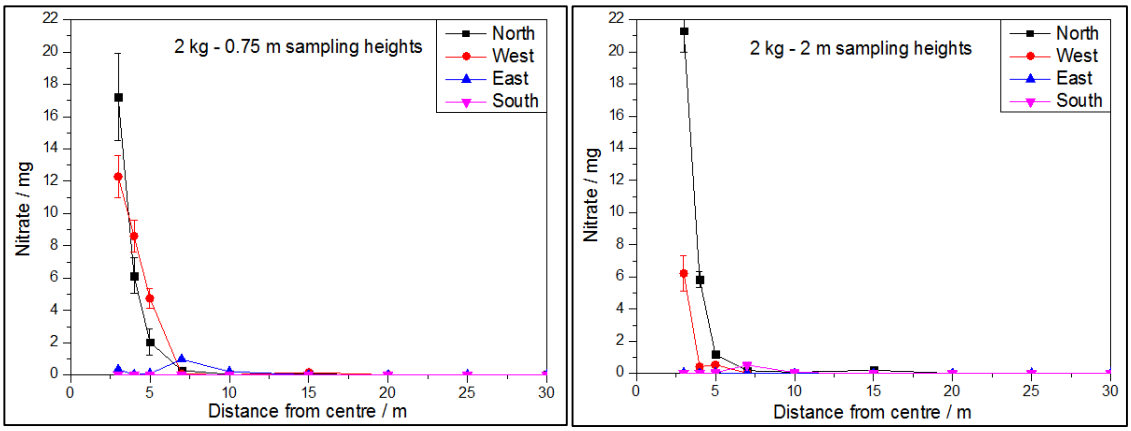

***Figure 5.14**: Nitrate recovery from 2 kg AlAN firing: left = 2 m high sites, right = 0.75 m high sites Wind was 7.1 m/s towards northwest*

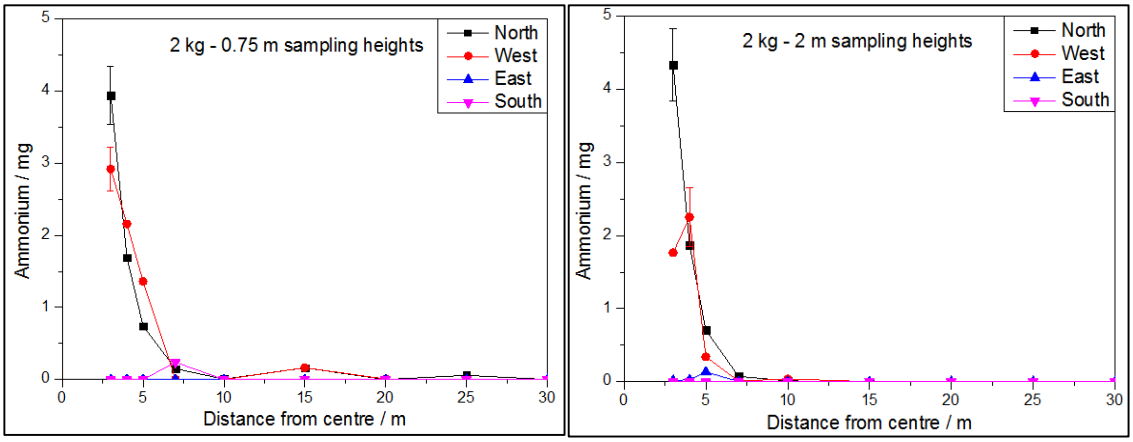

***Figure 5.15**: Ammonium recovery from 2 kg AlAN firing: left = 0.75 m high, right = 2 m high sites. Wind was 7.1 m/s towards northwest.*

Again, the precision of the results was tested by analysing each sample in triplicate. The majority of samples produced precise measurements (standard deviation of less than 5 %), with the major anomalies to this being the samples which contained the most residue (i.e. that from the 3 m sampling points) which had a maximum deviation about the mean average mass of approximately 4 mg for the nitrate and 1.5 mg for the ammonium.

5.3 Unconfined RDX Firings

5.3.1 Organic Post-blast Residue Results

No RDX was detected in the control samples of blank acetone or ACN, swab blanks or steel plate blanks, or in the blank ACN or water samples injected between test samples, therefore any RDX detected in each post-blast sample was attributed to the explosive residue in that sample. The RDX mass ranges detected in post-blast samples of the unconfined 1 kg and 2 kg PE7 charges were similar; between 0 µg and 37.5 µg, and 0 µg and 44.0 µg, respectively, and therefore greater than (approximately double) the mass range from unconfined 0.5 kg charges (0 µg to 20 µg) from the previous chapter. The majority of the largest amounts were detected within 15 m from the centre. The averaged RDX masses detected from the four sampled orientations, 3 m to 30 m from the centre decreased with increasing distance nonlinearly and appeared to vary from the theoretical inverse square distribution, when plotted including all data points and established using the experimental data points from 3 m following both the 1 and 2 kg PE7 firings (47.6 µg and 64.2 µg respectively) (figure 5.16).

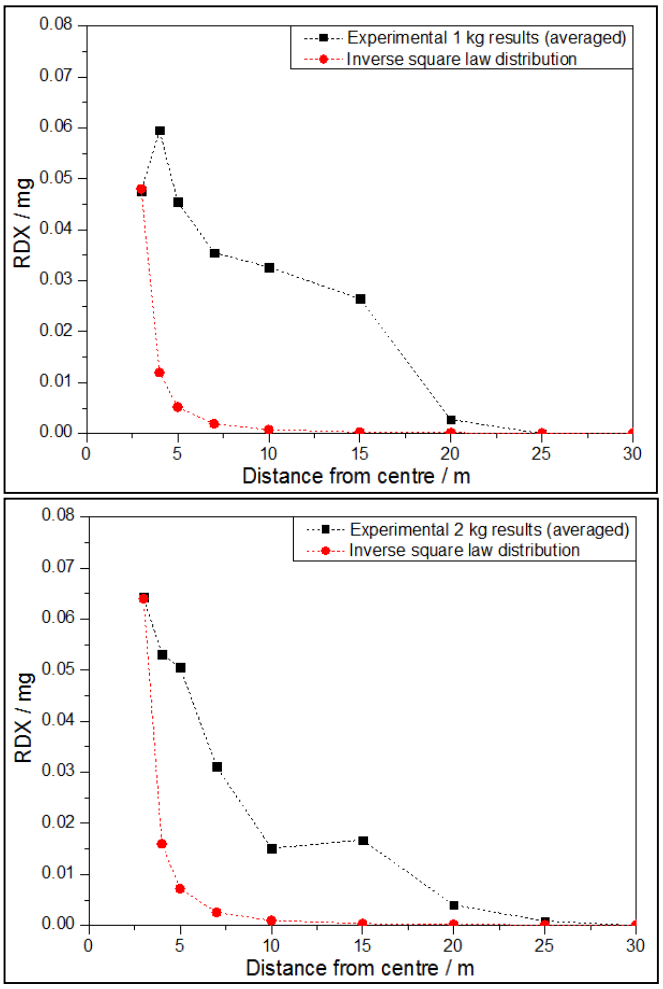

***Figure 5.16**: Comparison of experimental RDX (black) against the theoretical inverse square law distributions (red) for the detonation of the 1 kg (top) and 2 kg (bottom) PE7 charges.*

All experimental measurements between 4 m and 20 m from the detonation centre appeared greater than the theoretical values when plotted this way. No distinct differences were apparent between the trends of the two different charge masses (top and bottom of figure 5.16). When compared to the inverse square law distribution by plotting data points (without the values from the closest sampled distance of 3 m) against '1/d^2', the distribution trend was more linear following the 2 kg PE7 firing (R^2 of 0.8292) than the 1 kg firing (R^2 of 0.5498) (figure 5.17).

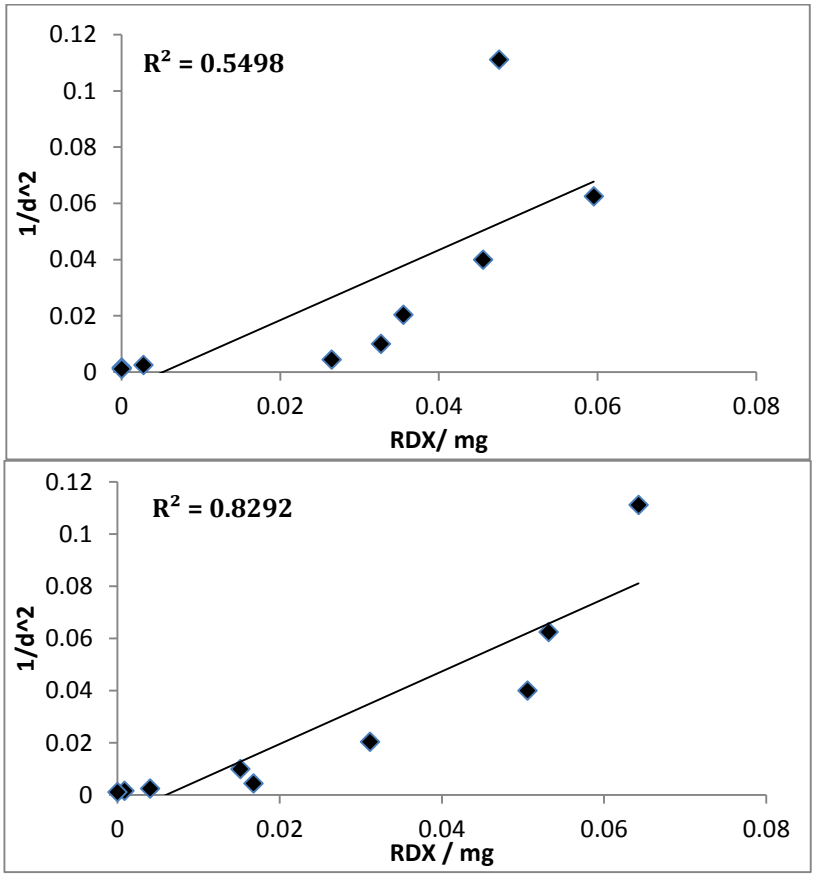

Figure 5.17: *RDX data vs. theoretical distribution trend (without data from the 3 m sampling point), now showing a better correlation following the 1 kg firing (top of figure) and even more so following the 2 kg firing (bottom of figure). R^2 values inset in figure.*

The results in figure 5.16 and 5.17 were based on summed values of residue recovered from two sampling heights (0.75 m and 2 m from the ground), which are presented separately in comparison to each other in figure 5.18. The amount of RDX detected upon the 2 m high sampling sites (orange plots in figure 5.18) was greater overall than those from the 0.75 m high samples (blue plots in figure 5.18), from both charge masses fired. The distribution trends from each sampling height were also similar; the detected mass of RDX in most cases was lower at the closest sampled distance of 3 m and then increased at ~4 m and 5 m, followed by a nonlinear decrease in mass up to 30 m from the detonations.

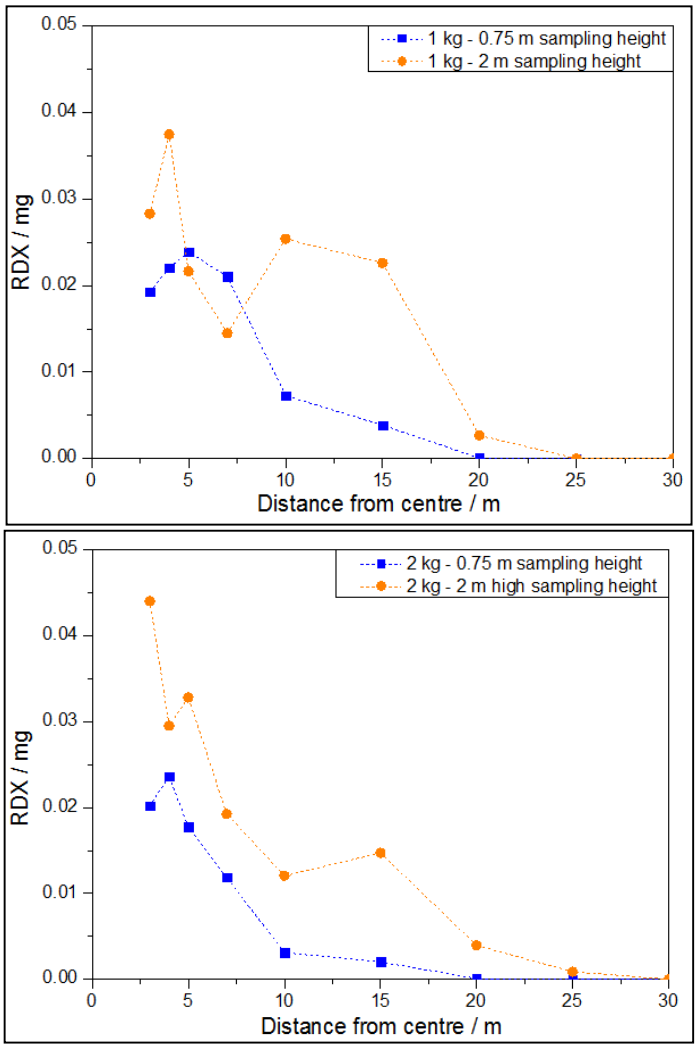

Figure 5.18: *Variation between RDX distribution based on sampling heights, (blue = 0.75 m high, orange = 2 m high): top = 1 kg firing, bottom = 2 kg firing.*

Comparison between Organic and Inorganic Analytes

As with the 0.5 kg charge firings reported in the previous chapter, in comparison to the inorganic analytes, the detected RDX mass range was the lowest from both the 1 kg and 2 kg charges (top and bottom of figure 5.19 respectively).

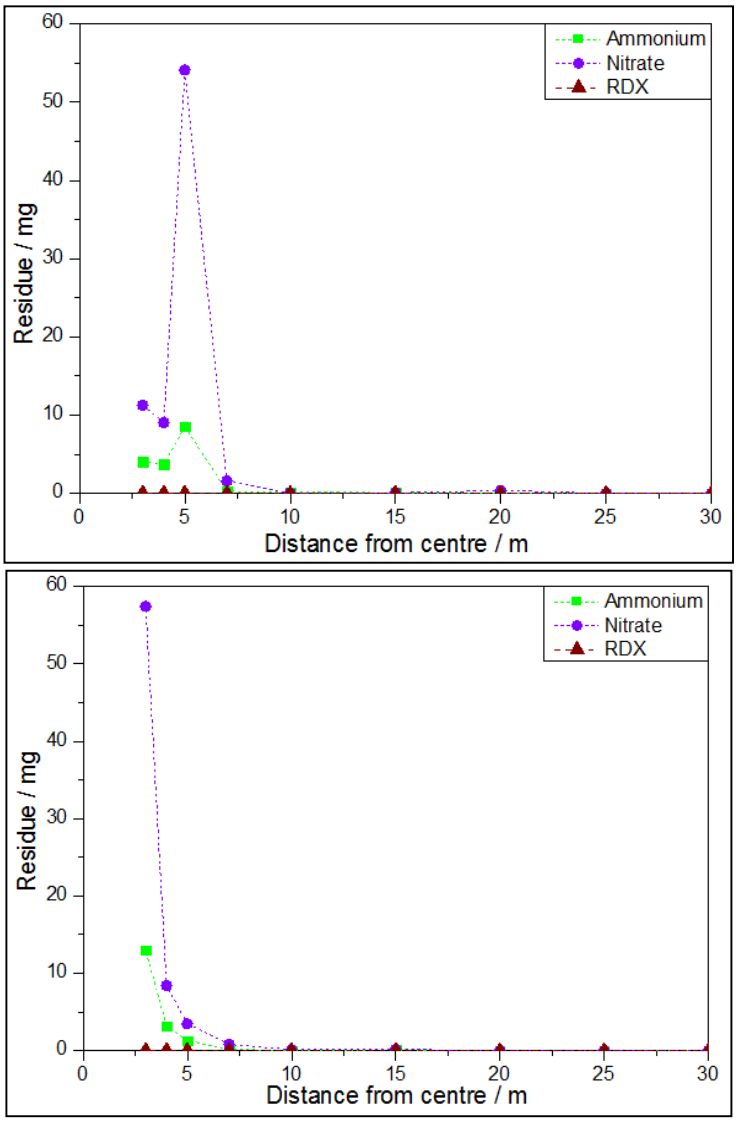

***Figure 5.19**: Comparison between inorganic and organic analytes from the 1 kg (top) and 2 kg (bottom) firings. The nitrate amounts (purple) were greater than the ammonium (green) which in turn was detected in greater amounts than the RDX (brown).*

Having established the general distribution trends of the RDX analyte from the detonation of both larger charge masses, the trends were compared to the fireball and smoke plume movements observed with HSI footage.

5.3.2 Fireball

The fireballs produced during the detonations of the 1 kg and 2 kg PE7 firings were recorded and their volumes estimated at the point when they were observed to have the largest radii. For the 1 kg charge, fireball volume estimates were made at t = 25 ms and smoke plume volume estimates at t = 210 ms; for the 2 kg charge, fireball volume estimates were made at t = 20 ms and the smoke cloud volume at t = 230 ms. Table 5.3 shows the approximated fireball and smoke plume volumes (which were calculated assuming a spherical shape for

both). The fireball and smoke cloud volumes estimated from the 1 kg PE7 charge were approximately half the size of those seen during the 2 kg charge detonation (table 5.3).

Charge/mass /kg	Fireball radius /m	Fireball volume /m^3	Smoke plume radius /m	Smoke plume volume /m^3
PE7/1 kg	5.30	624	5.50	697
PE7/2 kg	6.50	1150	7.00	1440

Table 5.3: *Estimated fireball and smoke cloud sizes based on HSI footage of the 1 kg and 2 kg RDX based (PE7) charge firings. All estimates are based on spherical volumes (3 sf).*

HSI stills from the 1 kg and 2 kg PE7 firings are seen in figures 5.20 (a – d) and 5.21 (a – d) respectively. A full set of both HSI stills and GoPro footage of the detonations can be seen in appendix C. The 1 kg PE7 charge did not have a spherical fireball initially (figure 5.20a) and the central rim around the fireball at t = 15.3 ms was surrounded by black smoke (figure 5.20b). At t = 36.0 ms (figure 5.20c) the fireball was larger and spheroidal, and by t = 200 ms (figure 5.20d) had decayed into a black smoke plume.

The 2 kg PE7 charge also did not have a spherical fireball initially (figure 5.21a) and as observed during the 1 kg firing, exhibited a black smoke ring around the central fireball rim (figure 5.21b; t = 3.5 ms). At t = 28.5 ms (figure 5.21c) the fireball was larger and extended across sampling plates 6 m from the charge centre. The resulting smoke cloud was dense black in the centre and had a grey plume above and around it (figure 5.21d).

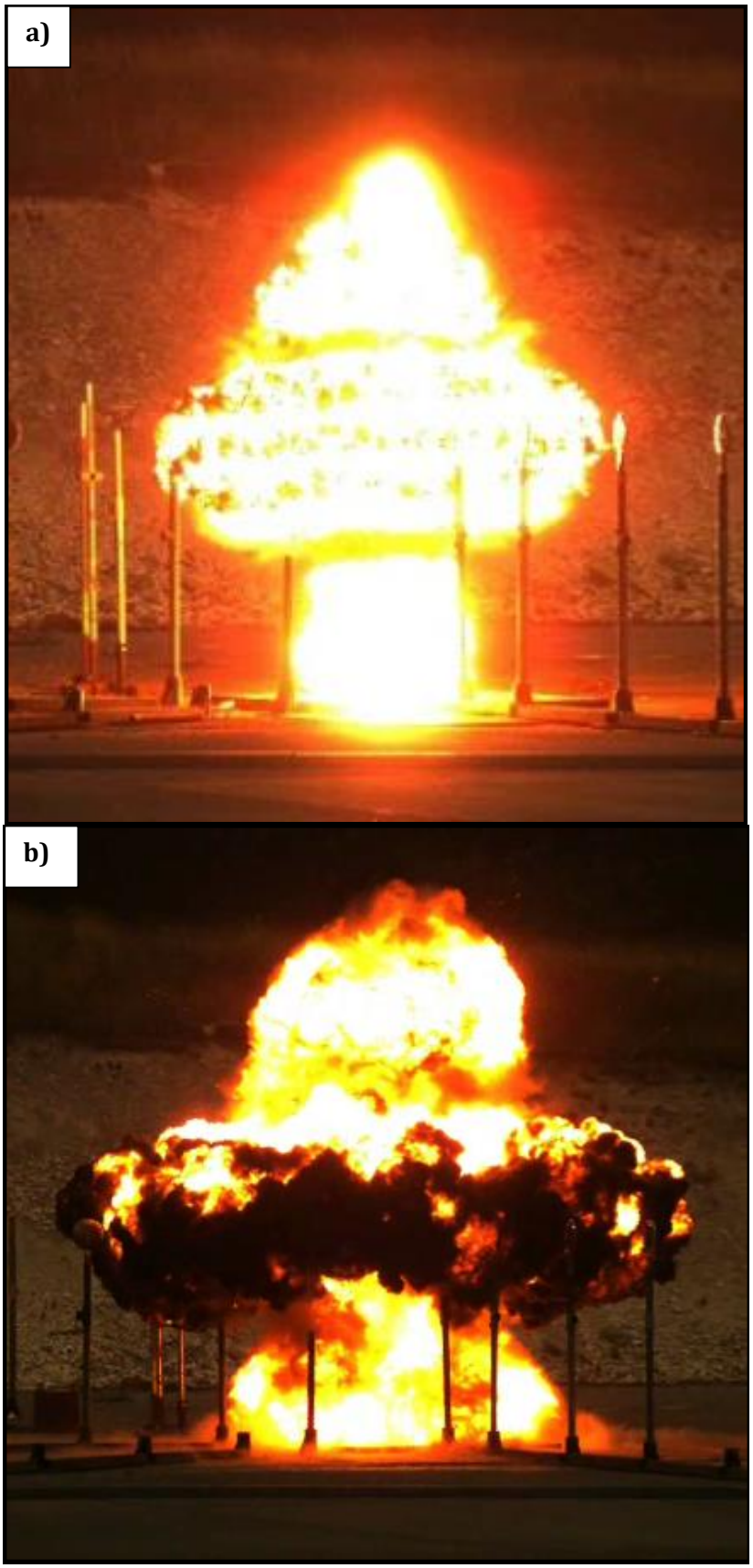

***Figure 5.20**: HSI stills of 1 kg PE7 detonation showing fireball morphology at a) t = 1.75 ms and b) t = 15.3 ms*

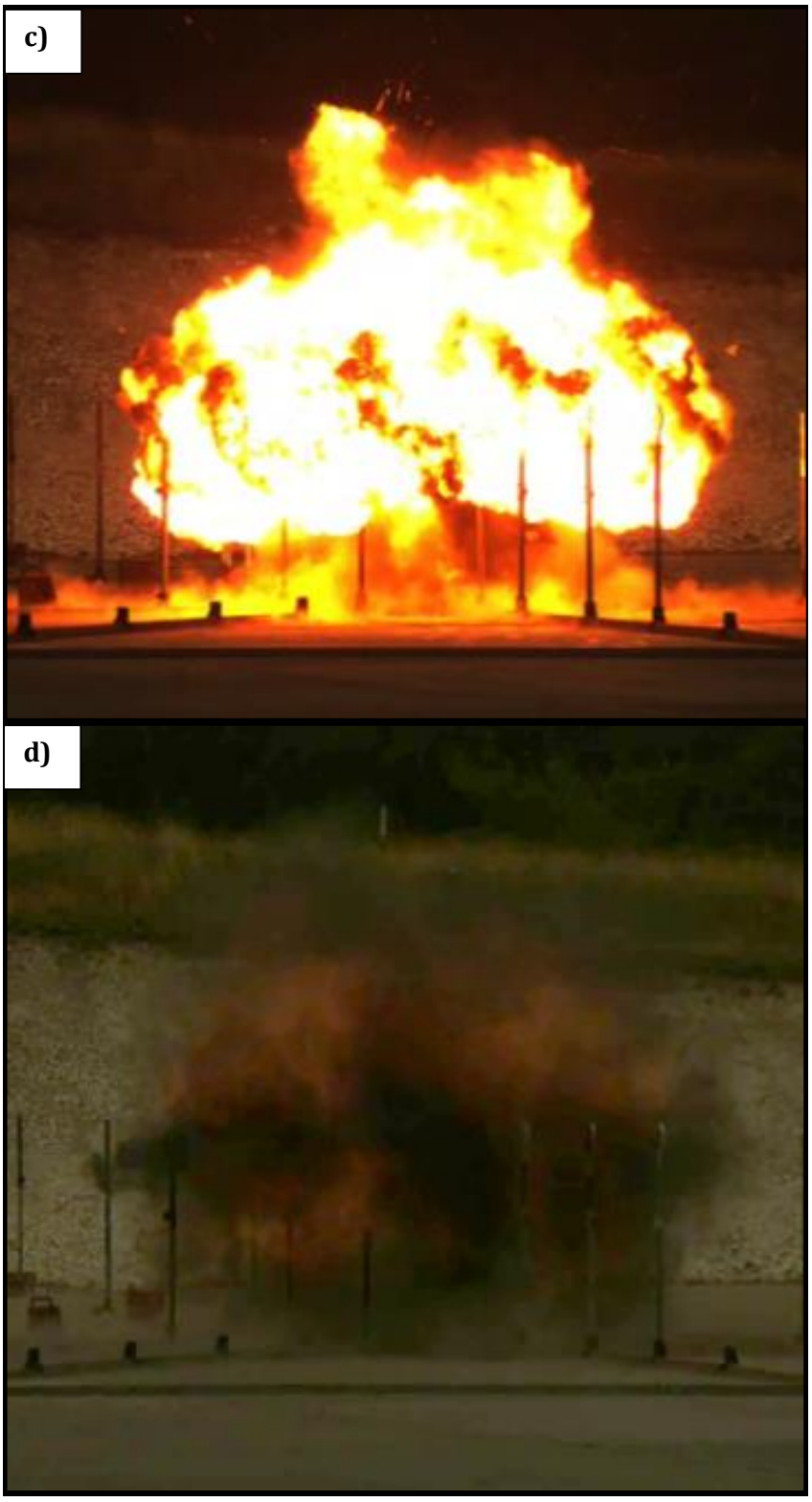

***Figure 5.20 cont'd**: c) t = 36.0 ms, d) t = 200 ms*

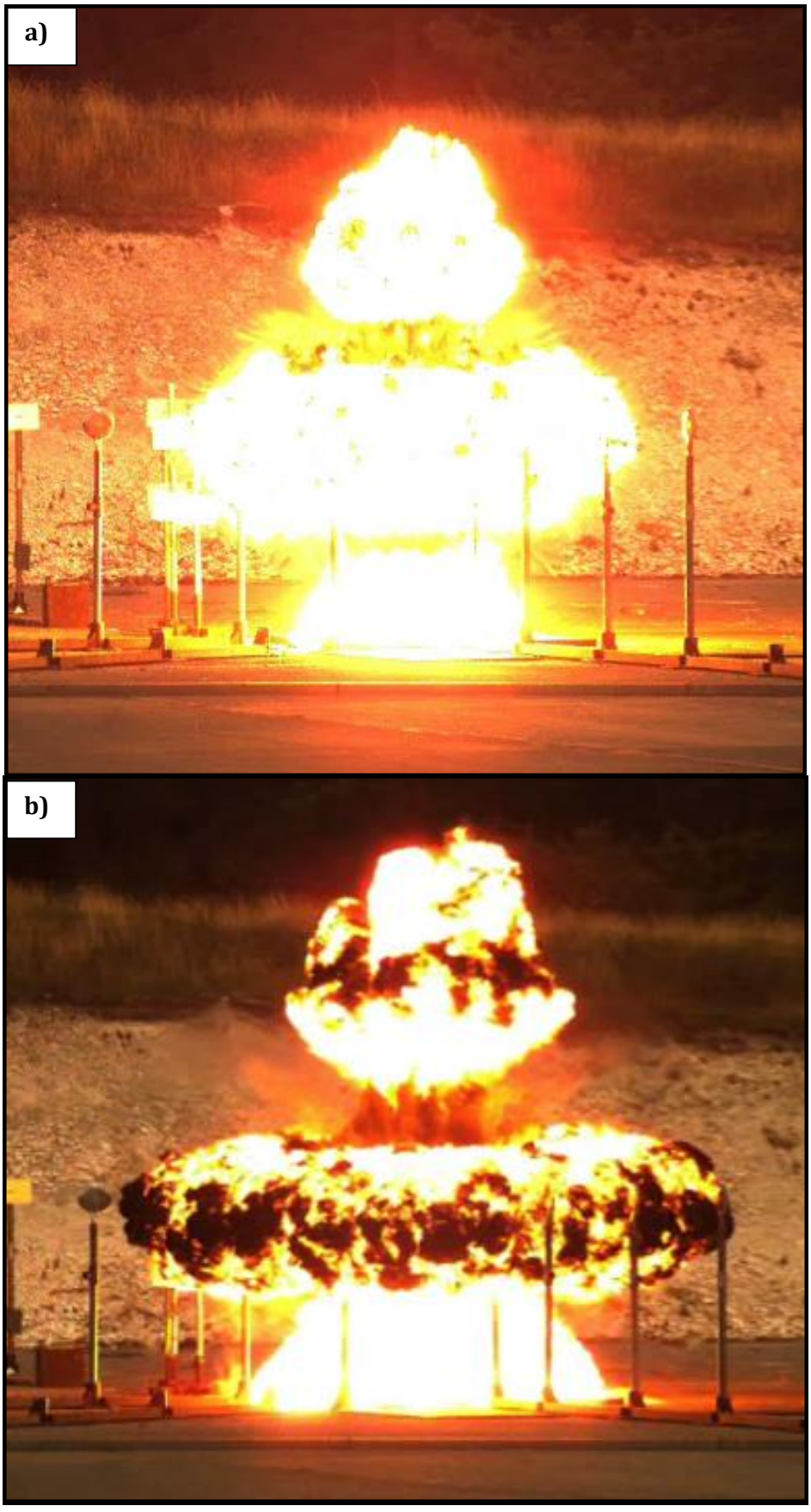

Figure 5.21*: HSI stills of 2 kg PE7 detonation showing fireball morphology at a) t = 1.75 ms, b) t = 3.50 ms*

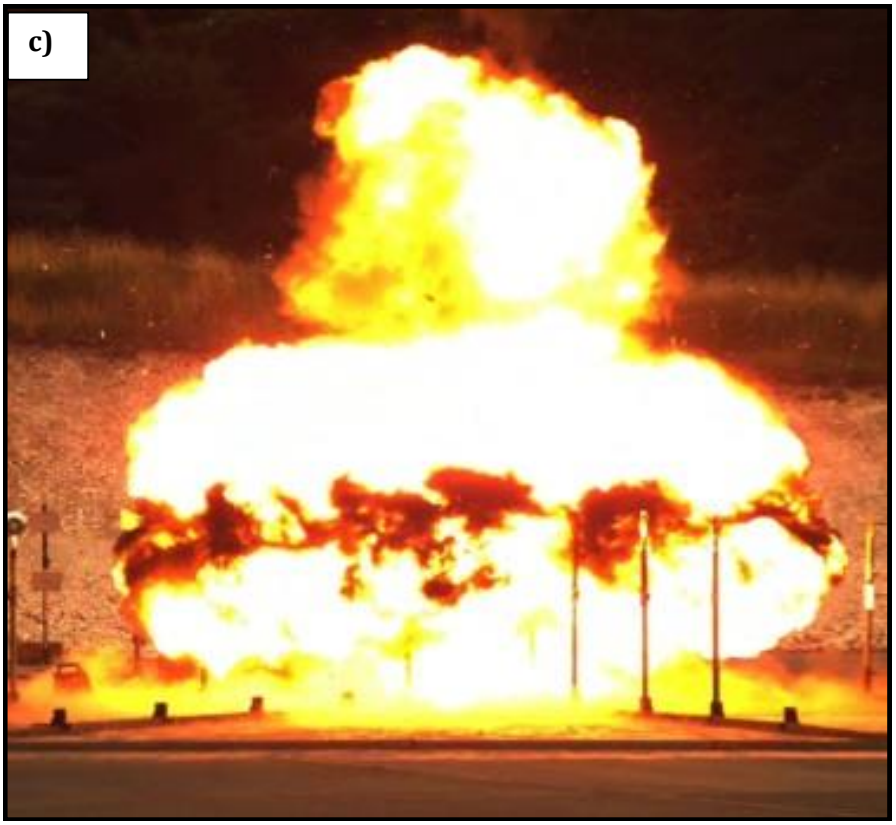

***Figure 5.21 cont'd**: c) t = 28.5, d) t = 243 ms*

Comparison between Fireball and Post-blast Residue

Following the 1 kg and 2 kg PE7 firings, the amount of RDX recovered from sampling plates fluctuated within and outside the area of the observed fireball (similarly to the results of the 0.5 kg RDX composition firings in the previous chapter). From the 1 kg firing (black and red plots in figure 5.22), greater quantities were detected on plates which were slightly further from the fireball centre than those in it, after which the mass of RDX decreased with increasing distance.

Following the 2 kg firing, the plates which were 0.75 m from the ground (blue plot in figure 5.22) showed the same trend; the plate closest to the detonation (and therefore most exposed to the fireball temperatures) yielded lower RDX mass than from the plate at the next sampled distance. The 2 m high plates sampled following the 2 kg firing (pink plot in figure 5.22) produced a seemingly anomalous result whereby the greatest mass of RDX was recovered from the sampling plate which was within the observed fireball region.

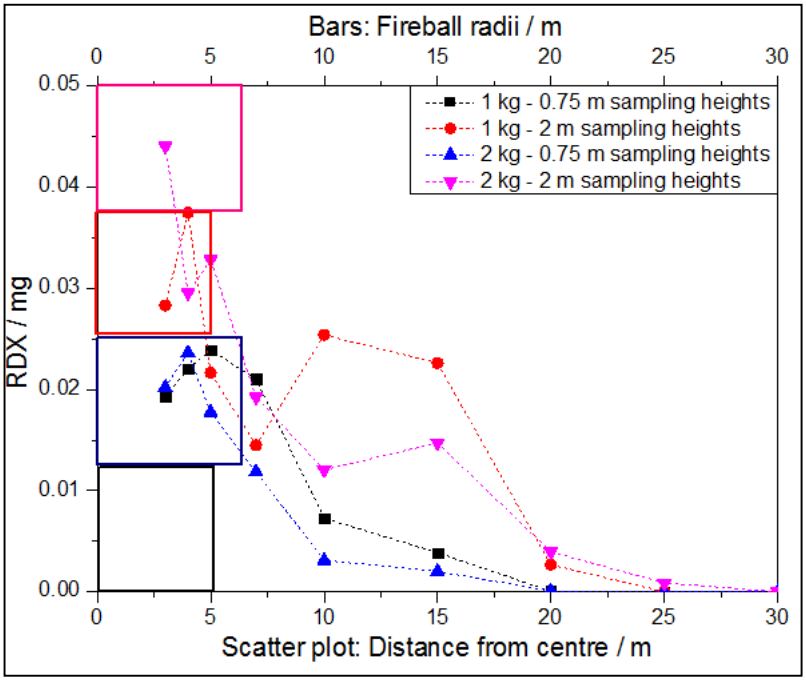

Figure 5.22: *RDX distributions (scatter plots) from 1 kg and 2 kg PE7 firings. The bars indicate the extent of the fireball (radius in metres) from each firing as observed through the HSI recordings. The RDX amounts fluctuated within and outside of the fireball region. The majority of the closest sampled sites, and therefore those exposed to the highest fireball temperatures, had lower RDX quantities on them than those at subsequent sampled distances. The only anomaly to this trend was the 2 m high sampling site, positioned 3 m from the centre, following the 2 kg firing.*

Comparison of Fireballs between Explosive Charges

Comparisons here are made between firings from which it was possible to collect HSI recording data. Table 5.4 shows the collated data regarding fireball and smoke cloud volumes from this chapter and from the previous chapter (where 0.5 kg charges were detonated).

Charge mass/kg	Fireball radius /m	Fireball volume /m^3	Smoke cloud volume / m^3
AlAN/0.5 kg	1.32 (mean)	~10.0 (mean)	~39.1 (mean)
AlAN/1 kg	4.00	268	382
AlAN/2 kg	---	---	---
PE4/0.5 kg	2.2 (mean)	~45.7 (mean)	~123 (mean)
PE7/1 kg	5.30	624	697
PE7/2 kg	6.50	1150	1440

Table 5.4*: Estimated fireball and smoke cloud volumes from all firings as observed through HSI footage*

All RDX based charges produced larger fireballs and smoke clouds than their corresponding AlAN charges (table 5.4). For RDX based charges, between the different charge masses fired, the 2 kg charge produced a larger fireball and smoke cloud than the 1 kg charge (~double in volume), which produced a larger volume fireball and smoke cloud than the average 0.5 kg firings (again, ~double in volume). For the AlAN charges, it was not possible to get size estimates from the 2 kg firing; but the 1 kg firing generated a larger fireball and smoke cloud than the average 0.5 kg firings.

All observed larger charge mass firings produced initially non-spherical fireballs, followed by their growth into more spheroidal fireballs which in the case of the PE7 charges were surrounded with a black carbon soot rim and resulted in black and dark grey smoke clouds. This was not the case for the 1 kg and 2 kg AlAN firings from which the fireballs had 'spiky' edges and the ejection of apparent particulate matter was visible and the resulting smoke clouds where light grey. The fireball morphologies from the larger charge masses were inconsistent to those of the 0.5 kg firings from the previous chapter; the fireballs from which were more spheroidal than seen here.

5.3.3 Meteorological Conditions

The movement of the smoke cloud formed following the firing was observed and correlated with the meteorological conditions at the time of firing, details of which are presented in table 5.5. The wind direction was consistently toward the north and north-westerly direction during both firings. The temperature, barometric pressure and humidity were similar between firings.

Charge mass /kg	Wind Speed / (m/s)	Wind Direction	Temperature /°C	Humidity /%	Pressure /mbar
PE7/1 kg	6.0	NW	21	74	995
PE7/2 kg	7.0	N	22	74	1013

***Table 5.5**: Meteorological conditions recorded at the time of each firing, for 1 kg and 2 kg organic charge masses. Measured with a Kestrel 3500 weather monitor at firing point.*

Comparison of Wind with Residue Distribution

Figures 5.23 and 5.24 show the comparison between the RDX detected at different orientations around the detonation centre following the 1 kg and 2 kg PE7 firings. Whilst the amounts fluctuated from the 0.75 m high (left of figure 5.23) and 2 m high (right of figure 5.23) sampling sites in all orientations, the majority of the greatest RDX amounts were detected from sites which were in line with the wind direction (north and west; black and red plots in figure 5.23). The bias of residue distribution in the downwind orientation was not obvious following the 2 kg PE7 firing (figure 5.24).

The precision of the obtained measurements was high; the standard deviation of the mean average result based on triplicate injections of each sample into the HPLC-MS showed little deviation (maximum of 7 µg variation).

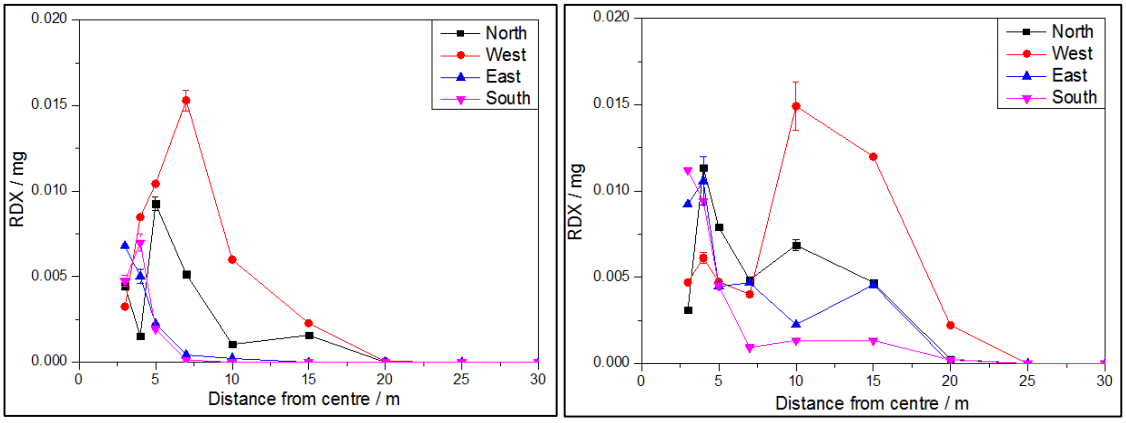

***Figure 5.23**: RDX recovery from 1 kg PE7 firing: left =0.75 m high sites, right = 2 m high sites*

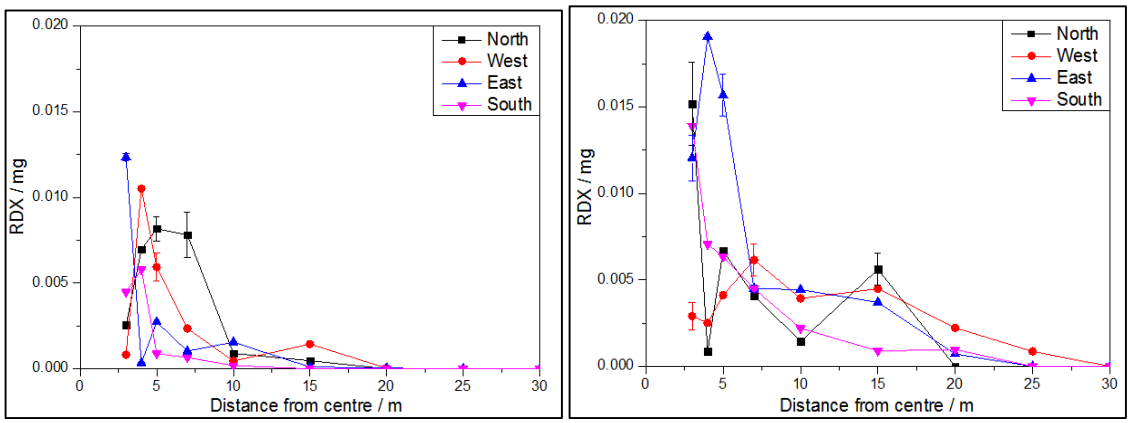

***Figure 5.24**: RDX recovery from 2 kg PE7 firing: left =0.75 m high sites, right = 2 m high sites*

5.4 Confined RDX Firings

Six vehicle firings with an RDX composition contained within each were attempted; however only four functioned efficiently, the results from the successful firings are presented here. The reason for the malfunction of two firings was unknown.

5.4.1 Organic Post-blast Residue Results

No RDX was detected in the control samples of blank acetone or ACN, swab or steel plate blanks, or from control samples of the vehicles which were swabbed prior to the firings. Samples could only be collected at one height (2 m from the ground) around the vehicles. The mass range of RDX detected from post-blast samples was 0 µg to 330 µg (higher than the range from the unconfined 1 kg and 2 kg firings; 0 µg to 37.5 µg, and 0 µg to 44.0 µg; and the unconfined 0.5 kg firings; 0 µg to 20.0 µg). The greatest quantities of RDX were detected within 10 m from the detonation centres.

The mass of RDX (averaged across the four repeated firings) detected from all four sampled orientations, 3 m to 30 m around the charge centre varied from the theoretical inverse square law distribution pattern, which was generated using the experimental value from 3 m (167 µg) (figure 5.25). The experimental results did not decrease linearly with increasing distance from the centre but initially increased from 3 m to 4 m. This initial increase in mass on the closer sampled distances, followed by a decrease in RDX mass was similar to that found following the unconfined 0.5 kg and 1 kg RDX composition firings.

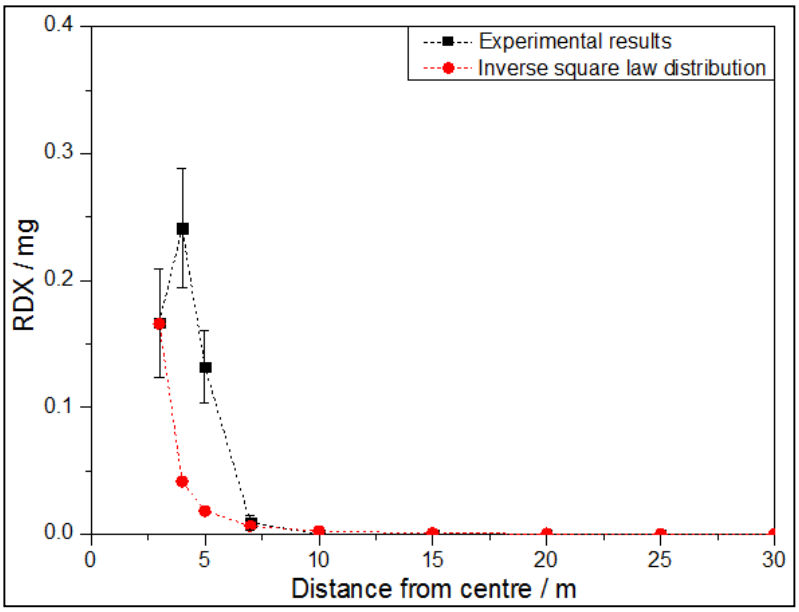

***Figure 5.25**: Averaged RDX amounts from 1 kg RDX-based confined firings in vehicles (in black) compared to the theoretical inverse square law distribution pattern (in red). Values for each distance were totals from all four sampled orientations. The error bars represent standard deviations of the average from four repeated firings.*

As found previously, the closest sampled point from the detonation often produces an anomalous result and therefore the comparison was also conducted without this datum. Figure 5.26 shows there was a high degree of linearity between the experimental and inverse square distribution (R^2 of 0.9351).

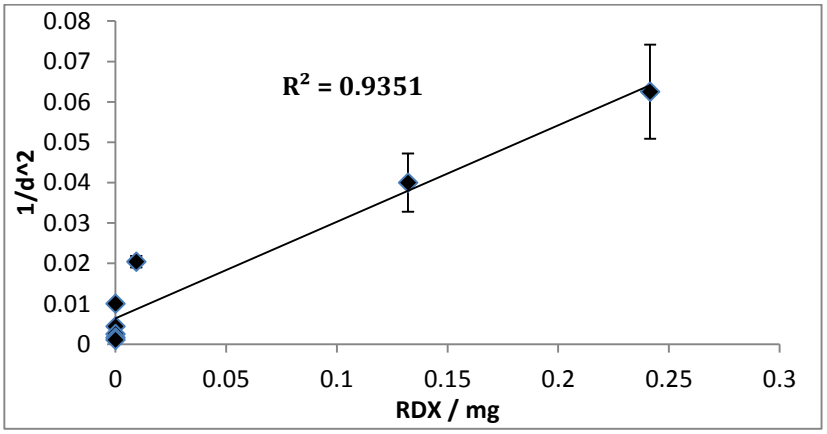

***Figure 5.26:** RDX mass detected in samples following confined firings of ~1 kg charges plotted against the theoretical distribution (without anomalous data from the 3 m sampling points). The correlation between the two was strong with an R^2 of 0.9351.*

The error bars in figures 5.25 and 5.26 represented the standard deviation of the mean average mass of RDX detected at each sampled point from the four repeated vehicle firings. Figure 5.27 shows the RDX distribution patterns from each individual firing. Similar trends were apparent between firings 1 and 3; from both of which lower amounts were detected at 3 m than 4 m, however firings 2 and 4 did not exhibit this, and the RDX mass decreased

more linearly. Whilst two different trends were clear, no methodological variations were apparent between the firings.

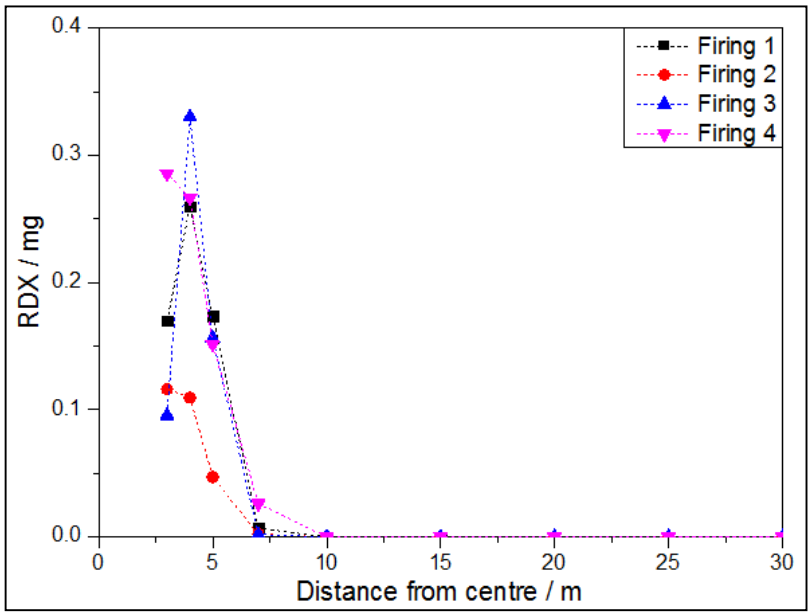

***Figure 5.27**: RDX concentrations from each confined vehicle firing. Each value is the totalled amount from four sampled orientations around the centre. Firings 1 and 3 had similar distribution trends as did firings 2 and 4.*

Samples collected from Vehicles

Samples were also collected from the vehicles following firings; whilst all vehicles were damaged, most had retained their structure, although all glass and much panelling was ejected out and formed a debris field around each vehicle. The same areas of the cars were sampled following each firing; the amounts of RDX detected at each point are presented in table 5.6 and figure 5.28 depicts the areas sampled for explosive residue. The area of each car surface sampled was consistent with the 200 mm x 300 mm metal sampling plates positioned around the detonations.

Sampled area		Firing 1	Firing 2	Firing 3	Firing 4	Mean	S.D.
1	**Bonnet**	6.36	7.56	4.78	6.35	**6.26**	1.14
2	**Boot**	0.599	2.55	3.94	1.53	**2.15**	1.43
3	**Dashboard**	11.2	4.93	17.4	22.0	**13.9**	7.43
4	**Centre**	56.8	28.4	39.8	16.0	**35.3**	17.3
5	**Roof**	64.9	38.7	40.2	95.9	**59.9**	26.8

***Table 5.6**: RDX concentrations (/µg) (3 sig.fig.) retrieved from sampling the cars following each detonation. Samples were extracted in the same manner as those retrieved from steel sampling plates.*

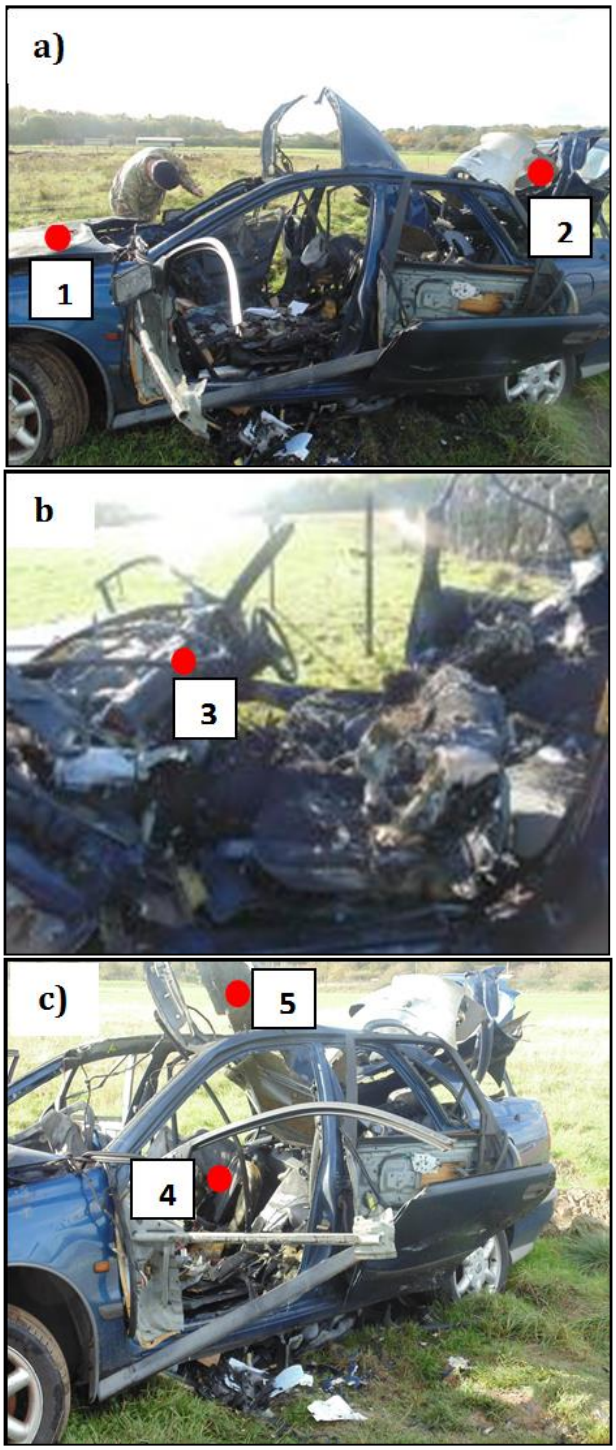

Figure 5.28: *Sampled areas (red markers) of vehicles following detonation. a) markers 1 and 2 correspond to the outer bonnet and boot; b) marker 3 corresponds to dashboard; c) markers 4 and 5 correspond to the area of the charge placement and the inner roof.*

The amount of RDX detected on the cars themselves ranged between 0 μg and 96 μg (lower than that of the sampling sites surrounding the car; 0 μg to 330 μg). The largest amounts were detected in samples from the roof of the car, above the charge placement (average mass of ~60.0 μg). The second largest amounts were from the central area in the car near the charge itself, and the fewest residues were detected on the boot of the cars.

Comparison between Unconfined and Confined Firings

Figure 5.29 shows the RDX distribution trends between the unconfined and confined 1 kg charges were similar; both showing lower amounts detected at the closest sampled distance of 3 m, followed by greater amounts detected at the next sampled distance of 4 m, after which, with increasing distance from the centre, all residue amounts decreased. The actual masses detected following the confined firings (red plot in figure 5.29) were higher between 3 m and 5 m; the masses detected following the unconfined firings (black plot in figure 5.29) were higher between 7 m and 15 m. Between 20 m and 30 m both firing types yielded similar RDX amounts from the sampling sites.

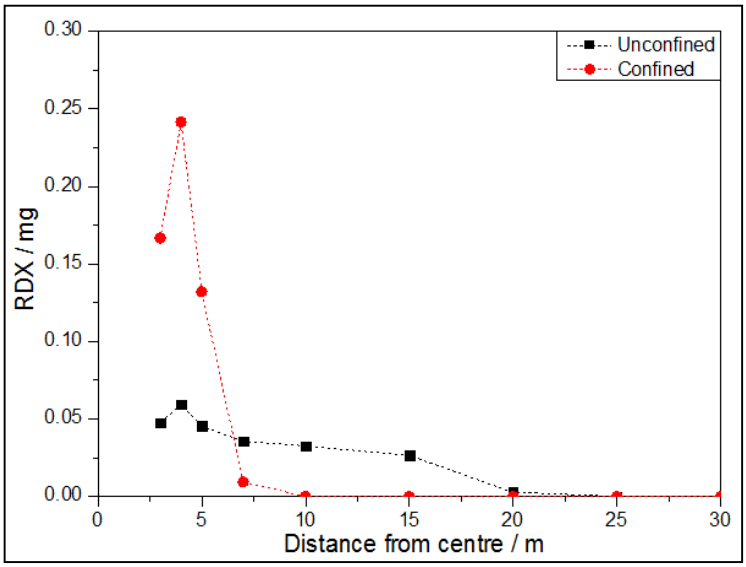

***Figure 5.29**: Comparison between averaged quantities of RDX detected around the detonation centre of the 1 kg unconfined firing of PE7 (black) and the 1 kg RDX-based detonations confined in vehicles (red).*

5.4.2 Fireball

No HSI recording facilities were available at the Kineton DEMSS range where the vehicle confined charges were fired therefore the fireball dynamics of the confined firings could not be gauged with the resolution of the cameras used previously. The detonations were captured with GoPro cameras and stills from one vehicle firing (which are representative of all firings) are depicted in figure 5.30 (another set of firing stills depicting similar observations can be found in appendix C). Based on these images it was not possible to estimate the fireball or smoke cloud volumes. However, clearly within 1 second (figure 5.30b) the smoke plume had engulfed the area surrounding, and was rising above, the vehicle. In the following 1.5 seconds (figure 5.30c and 5.30d) the plume density decreased and was moving towards the east, in line with the dominant wind direction during firing. All samples plates however were observed to be engulfed by the smoke cloud. The smoke plumes formed were larger than those from the unconfined 1 kg RDX-based charges.

***Figure 5.30**: Stills of car bomb from real time video footage of firing number 1 between 0.00 and 2.50 seconds. a) t = 0.00 s shows the car prior to firing; b) at t = 1.00 s the charge has been fired and the smoke plume encompasses the area surrounding the car; c) and d), at t = 1.80 and 2.50 s respectively the smoke plume dispersed and moved in line with the wind direction towards the east.*

5.4.3 Meteorological Conditions

The movement of the smoke cloud formed following the firing was observed and correlated with the meteorological conditions at the time of firing, details of which are presented in table 5.7. The wind direction was mainly towards the north or south-eastward for most firings and the wind velocity between 4 m/s and 9 m/s. The temperature, humidity and barometric pressure were similar across repeated firings.

Firing No.	Wind Speed / (m/s)	Wind Direction	Temperature /°C	Humidity /%	Pressure /mbar
1	7.00	E	9.00	72.0	1015
2*	13.5	NE	11.0	45.0	1017
3	5.00	E/SE	13.0	61.0	1014
4	4.90	NE	16.0	48.0	1013
5*	11.0	NE	16.0	57.0	1010
6	8.50	SE	14.0	49.0	1011

***Table 5.7**: Meteorological conditions at the time of each firing (* - firing malfunction)*

Figure 5.31 displays the residue distribution from the four successful firings in relation to the sampled orientations around the centre. Following every vehicle firing, the greatest quantities of RDX were recovered from sample sites which in line with the wind direction at the time of firing.

The precision of each obtained measurement was high; the instrumental response to the mass of RDX within each post-blast sample was consistent between triplicate injections (maximum standard deviation of a mean average mass being 4 µg).

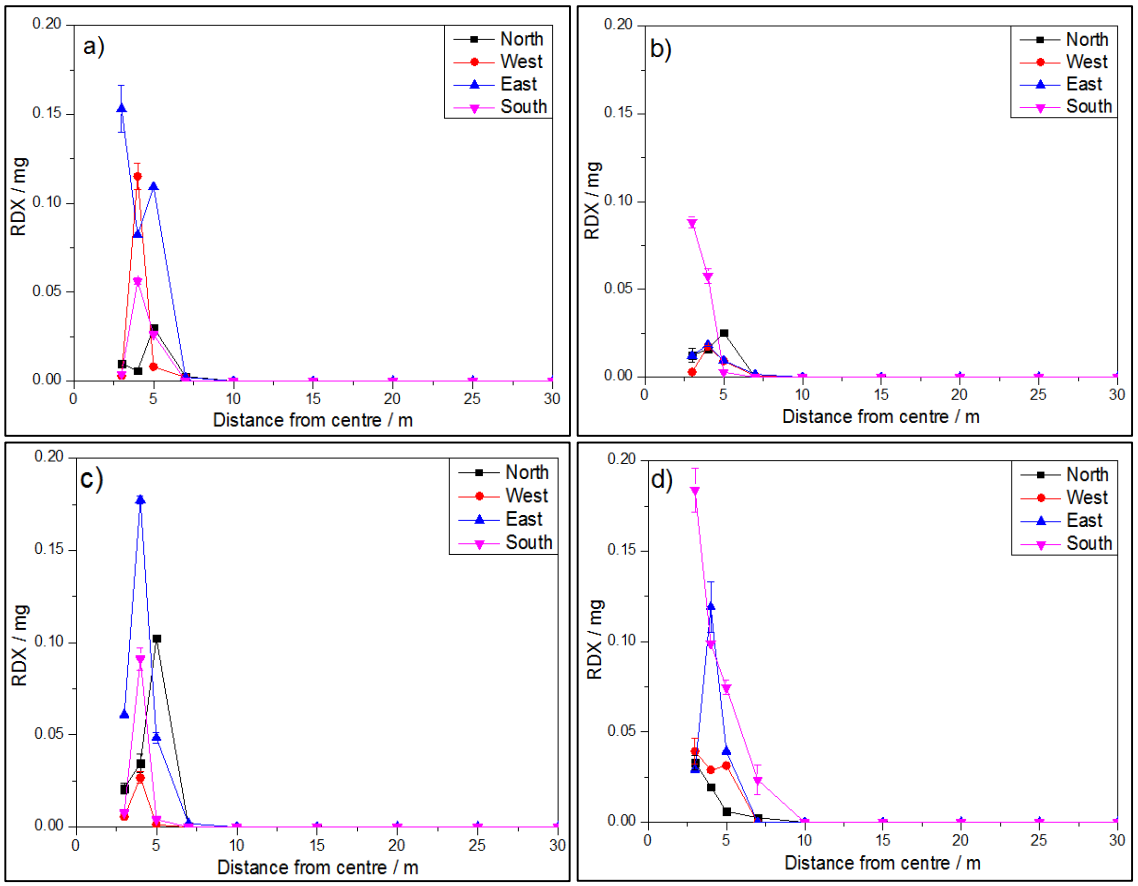

***Figure 5.31**: RDX distributions per sampling orientation from each vehicle firing. a) firing 1 (eastward wind), b) firing 3 (east/south-eastward wind), c) firing 4 (north-eastward wind), d) firing 6 (south-eastward wind).*

5.5 Results Summary

The results presented in this chapter are summarised in the following points and discussed in the following section.

- **Mass ranges:** Nitrate mass ranges from the 1 kg and 2 kg firings (0 mg to 54.0 mg, and 0 mg to 30.0 mg respectively) were overall higher than the corresponding ammonium mass ranges (0 mg to 8.50 mg and 0 mg to 6.86 mg). The amounts recovered following the larger charge firings were approximately three times greater than those from the 0.5 kg charges from chapter 4. The overall RDX mass range detected from the 1 kg and 2 kg PE7 charges was lower (0 µg to 44.0 µg) than the corresponding inorganic analytes and the corresponding confined organic firings (0 µg to 330 µg), but greater than that of the 0.5 kg charges from chapter 4 (0

μg to 20 μg). From the vehicles themselves, a lower concentration range was recovered (0 μg to 96 μg) than from sampling sites.

- **Radius**: The majority of the higher concentrations of each inorganic analyte were detected within 10 m from the charge centre (a greater radius than the 6 m established from the 0.5 kg charges). The largest quantities of RDX were detected within 15 m from the charge centre from the unconfined charges and 10 m from the confined charges (both greater than the 4 m radius of the 0.5 kg charges).
- **Theoretical trend comparisons**: When plotted without the data point from the closest sampled sites to the charge centre (at 3 m), the inorganic analytes distribution showed a positive correlation with the inverse square law model (particularly following the 2 kg firings). The RDX distribution did not conform as strongly with the theoretical fit (again the 2 kg firing produced a distribution of better linearity than the 1 kg firing). The confined RDX charge firing generated the strongest correlation with the model out of all organic analyte distributions.
- **Trend:** The amount of detected residue principally decreased with increasing distance from the charge but not linearly. RDX amounts fluctuated more than the inorganic analytes. Variations between the two different sampled site heights were apparent; 2 m high sites yielded higher residue amounts following the organic firings, but this was not the case for the inorganic firings.
- **Uncertainty:** The repeated confined vehicle firings produced similar distribution trends in most cases but actual amounts of RDX were inconsistent between comparable sites from different firings. Similarly to the previous chapter, the reported measurements from all firings had high precision; however, the error associated with them, and therefore the accuracy of the measurements, could not be determined without repeat firings.
- **Fireball:** Fireballs were not spherical (as those observed from the 0.5 kg charges reported in chapter 4), but elongated and had consistent morphologies between the two different explosive types and charge masses. Particulate material ejected from the fireball was observed from the AlAN firing, but not from the PE7 firings. PE7 produced black smoke; the plumes from the AlAN charges were light grey. PE7 charges produced larger fireballs and smoke clouds than AlAN charges. The 2 kg charges produced larger fireballs than the 1 kg charges which in turn were larger than the 0.5 kg charges from chapter 4 (by ~double). The confined 1 kg RDX firings produced more smoke than the corresponding unconfined 1 kg firing.

- **Fireball v. residue:** The relationship between the inorganic analyte distributions and the fireball sizes varied: inorganic analyte amounts were lower from 2 m high sampling plates which were engulfed by the fireball; this was not the case from the 0.75 m sampling heights upon which residue decreased with increasing distance. The RDX quantities from sampling sites engulfed by the fireball were from some sites lower and others higher – no consistent trend was observed.
- **Wind v residue:** The majority of nitrate and ammonium detected were skewed in line with the wind direction following firings (more-so for the 2 m high sampling sites). Greater quantities of RDX were detected from downwind sites following both the unconfined and confined firings, but the bias was not strong in all cases.

5.6 Discussion

Detected Analyte Amounts

As with the 0.5 kg charges of the previous chapter, following the unconfined AlAN firings the nitrate mass range (overall range of 0 mg to 54.0 mg) was greater than that of the ammonium (overall range of 0 mg to 8.50 mg) (figure 5.9), which in turn was higher than the RDX (0 μg to 44.0 μg). The explanation for these findings between the different analytes are as reported in chapter 4 and are explained in section 4.5, so are not recounted here.

When comparing the amounts of detected inorganic analytes from the different charge masses, more nitrate was recovered following the detonation of the 1 kg AlAN charge (up to 54.0 mg) compared to the 2 kg charge (up to 30.0 mg). Similarly, the amount of ammonium was higher from the 1 kg charge (up to 8.50 mg) than the 2 kg (up to 6.86 mg). The overall amounts detected of each analyte were approximately three times greater than that detected from the 0.5 kg charges in chapter 4. However, in the case of both inorganic analytes, the upper extent of the mass range detected following the 1 kg firing was determined by including an outlier result from the samples taken at 5 m (figures 5.5 and 5.8). If this upper value in each case is discounted, the variation in analyte amounts due to explosive charge mass demonstrates the opposite trend; the nitrate and ammonium mass ranges from the 1 kg charge become 0 mg to 7.83 mg and 0 mg to 2.20 mg respectively; both of which are smaller than the respective mass ranges from the 2 kg firings for each analyte. The inorganic analyte mass ranges from the 1 kg firing, without the anomalous data points, were also consistent with that detected following the 0.5 kg AlAN charges in chapter 4 (nitrate; 0 mg to 14 mg and ammonium; 0 mg to 3 mg).

The relationship between the nitrate and ammonium ions detected in post-blast residues collected from the larger charge mass firings was close to stoichiometric and variations

from an exact stoichiometric relationship may have been due to different extraction efficiencies of each individual ion.

The recovery of overall greater amounts of explosive residue from the larger 2 kg charges is reasonable if it is accepted that residue survives at the charge surface and it is considered that the amount of undetonated residues produced would be proportional to the surface area of the charges (which would be greater for the 2 kg charges). More than double the amount of residue was detected in samples following the 2 kg firing which contradicts theories stating that larger charge masses would produce fewer undetonated residues relative to their mass and volume compared to smaller charge masses[3] and that charges with larger diameters would have higher VODs[42,57,60] and thereby produce fewer residues. The finding of larger charges producing more residue is however consistent with other experimental studies[76,84] in the literature.

Conversely, the RDX mass ranges from the 1 kg and 2 kg charges were similar (up to 37.5 μg and up to 44. 0 μg respectively) and no such variation due to charge mass was found. However, compared to the 0.5 kg charges from chapter 4 (mass range of 0 μg to 20 μg) the larger charge masses produced more undetonated residue. The reason behind the variation from the inorganic firings, and lack thereof from the 1 kg and 2 kg organic explosive firings, is unknown. The inconsistency of the results emphasises the discrete nature of each material and the variability in the amount of undetonated material which can be produced.

When comparing the masses recovered from the unconfined 1 kg organic firings (0 μg to 37.5 μg) to those from the ~1 kg confined vehicle firings (0 μg to 330 μg), clearly, more undetonated residue was detected on sampling plates following the latter, particularly at distances sampled closer to the centre (figure 5.29). A greater mass range (0 μg to 96 μg) was also detected from the vehicles themselves. This counters theory which states fewer residues may be found from confined firings as encasement increases the pressures and temperature during the explosion, which would cause greater decomposition of further material[54]. No experimental work is available in the literature which directly assesses the amount of undetonated residue produced from confined and unconfined charges and so the results presented here cannot be compared.

Post-blast Residue Radii

The majority of residues of each inorganic analyte were detected within 10 m (figure 5.9) from the charge centre (greater than the 6 m radius from the 0.5 kg charges). The greatest quantities of RDX were detected within 15 m (figure 5.18) from the charge centre following both the unconfined and confined vehicle firings (greater than the 4 m radius from the 0.5 kg charges). The reason for the larger limiting radii following the larger charge masses is

unknown. It could be reasoned that the particles ejected from the 1 kg and 2 kg detonations would be moving with higher kinetic energy than those from the 0.5 kg charges due to the greater energy imparted to them. However if this were the case a distinction between the radii within which residues were detected from the 1 kg and 2 kg charges would also have been apparent.

Nonetheless, the optimum radii within which to locate residues found here concurs with findings from previous studies which have suggested radii of 10 metres[75,79] and 15 metres[77]. As found in the previous chapter, the results demonstrate that the posited limiting radius[57] of 60 m is too large.

Distribution Trends

Comparably to the trends found from the 0.5 kg firings in the previous chapter, in general the amount of residue detected decreased with increasing distance from the charge centre with varying degrees of linearity. When all data points were included in the comparison of the distribution trends to the theoretical inverse square law distribution, no strong correlation between the experimental and hypothetical plots were observed. However, when omitting the first datum value obtained from 3 m around the detonations, the inorganic analytes comparisons showed a positive correlation with the inverse square model (figures 5.4 and 5.7). A greater degree of linearity was exhibited for the distributions following the 2 kg firing, compared to the 1 kg. The RDX distributions from the unconfined organic firings did not correlate as well with the inverse square law model (figures 5.17), yet the distributions from the confined organic firings did (figures 5.26).

As explained in the previous chapter, in order to generate an exact and equivalent comparison it would be necessary to know the original amount of undetonated residue that was to be distributed from the detonation point. Overall, the evidence to support the notion that residue distribution during and following detonation events follows a mathematical law[3,57] is somewhat supported here (less convincingly than found in the previous chapter).

Whilst the amounts of RDX recovered from sampling sites around the confined and unconfined 1 kg organic firings varied, the resulting distribution patterns were similar (figure 5.29). This suggests that whilst the majority of experiments conducted in this research were based on unconfined systems, the application of the results to confined systems, and therefore more forensically valid scenarios, may be valid. Furthermore, if the distribution trends are similar, the mechanism for residue formation may not be affected by the boundary layer of the explosive charge where it is hypothesised that undetonated

residues survive[57]. No experimental work is available in the literature which directly compares the undetonated residue trends produced from confined and unconfined charges.

When considering the summed residues from both sampled heights (0.75 m and 2 m from the ground) at each measured distance, besides an increase in mass of both ammonium and nitrate at 5 m following the 1 kg charge (figure 5.9), all other measurements (from both the inorganic and organic firings) demonstrated a decrease in residue mass as a function of increasing distance from the charge centre (figures 5.5, 5.8 and 5.18), corresponding with experimental findings in the literature[70,84] and countering theoretical concepts of being able to detect higher residue mass quantities at much greater distances from the centre[57].

With regard to the sampling height, following the organic firings (both the 1 kg and 2 kg charge masses), the majority of samples collected from the 2 m high sampling sites were found to have greater amounts of RDX on them than those positioned at 0.75 m from the ground (figure 5.18). The results from the inorganic firings were not as distinct; following the 1 kg firing, most 2 m high sampling sites were found to have more ammonium and nitrate on them; following the 2 kg firing the 0.75 m high sample sites had more residues on them (figures 5.5 and 5.8). Whilst multi-increment sampling in terms of incremental distances horizontally from the charge centre has been incorporated into previous experimental studies, few have included multi-incremental sites in terms of their height from the ground and no theoretical notions to explain the effect of post-blast explosive residue sampling height are detailed thoroughly in the literature, which makes direct data comparisons between the sampling height parameter harder still.

Studies which have used two different sampling heights (car doors and signposts positioned 1.8 m from the ground) around a detonation (which was 0.76 m from the ground) have reported smaller amounts of residue recovered from the lower sampling sites and variations in the residue distribution patterns between the two different sampling heights used. Residue quantities were found to increase unexpectedly with increasing distance from the centre from the lower positioned sampling sites, whilst decreasing with increasing distance from the higher positioned sampling sites[70,88]. Whilst this phenomenon was not observed here (as all residue amounts ultimately decreased with increasing distance) the finding of lower quantities from the lower positioned (0.75 m high) sampling sites is supported here by the majority of the results.

Inconsistencies in the results regarding the sampling height potentially indicate the effect of an undetermined factor which affects residue deposition at different heights relative to the charge height, such as the wind current; the wind velocity may move at a lower relative

velocity on the ground due to friction and turbulence that occurs as air moves over the ground[72] which may have affected residue deposition and caused fewer residues to be deposited on sampling sites which were nearer the ground. From a forensic perspective the findings principally show that the height of the sampling site, as well as the distance, may have an effect on the quantity of explosive residue and predominantly sites which are at the detonation height (if the source height can be established) may be focused on primarily at a bomb scene.

Uncertainty of Results

The results from repeated firings reported in chapter 4 signified the importance of collecting repeated measurements from detonation trials. However, it was practically impossible to do this for the unconfined 1 kg and 2 kg firings conducted at Porton Down due to the limited amount of explosive material available and range time. The reproducibility of the measurements recorded from these firings is therefore unknown and this severely limits the application of the data; the implications of which are suggestive at best. Further repeated testing is ideally required to verify the data obtained.

The repeated confined vehicle firings produced differing distribution trends; two of the repeated firings showed a consistent decrease in the concentration of RDX detected in samples with increasing distance from the centre, whilst two other repeated firings showed lower concentrations at the closest sampled distance of 3 m than at 4 m where the concentrations were higher and then subsequently followed by a more linear decrease (figure 5.27). Further to the differences in the distribution trends between the repeated firings, in most cases the actual amounts of RDX detected were not consistent between comparable sites from different firings either (figure 5.27) and in this respect were therefore consistent with the results from repeated firings reported in the previous chapter. The lack of consistency between the repeated firings reinforces the requirements of further experimental work coupled with potential numerical simulation techniques in order to normalise any apparent data trends.

The accuracy of the data (in terms of the correctness of the stated values compared to the actual amount of post-blast residue deposited on each sampling plate) cannot be known. As explained in the discussion in chapter 4, this can be estimated at best via sampling and extraction tests; based on such tests (presented in Appendix A for RDX), the data regarding residue mass per sample was estimated to be approximately 25 % of the actual amount. An equivalent percentage for aluminised ammonium nitrate was unverified and therefore the accuracy of the inorganic data was not known. Despite this, it could be argued that as all of the sampling and extractions were consistently conducted for all samples, the error

associated with each measurement would be also be consistent across the dataset and the reported amounts therefore relative to the amount of residue actually deposited.

Whilst accuracy and reproducibility of the results were not high, the precision was found to be so. Each sample was injected in triplicate and the instrumental response for the majority of the repeated analyses was similar, indicating high precision of the measurement of the mass of material detected in each sample.

Potential Factors that Affect Distribution

Fireball

The fireballs observed during the 1 kg and 2 kg firings of both AlAN and PE7 were not spherical as observed during the 0.5 kg firings presented in chapter 4. The larger charges were moulded into near spherical shapes, as opposed to spherical moulds for the 0.5 kg charges; the slight variation in the morphology of the charge prior to detonation would have caused the resulting gas evolved to be shaped differently (figures 5.10a, 5.20a and 5.21a). Further instabilities caused by the non-spherical charges would have manifested during the rise of buoyant detonation gases and as air was drawn into the centre of the plume, a vortex ring formed at the edge of the fireball (figures 5.20b and 5.21b) caused by the turbulent vortices curling downwards in a toroidal shape[53].

Material being ejected from the fireball was clearly visible during the 1 kg AlAN firing (figure 5.10b and 5.10c) and was not as apparent during the PE7 firings (figures 5.20 and 5.21). As binary charges such as AlAN are likely to produce more undetonated material[10,57] the visible particulate material may have been related to the explosive residue. Within the same rim around the fireball where particulate material was observed during the AlAN firing, the PE7 firings exhibited the vortex rings; if any particulate material was indeed ejected from the PE7 firings, it may have gone unnoticed due to the presence of the high temperature curling gas plumes in that area. Alternatively, the use of a better resolution imaging tool might show particle movement from all detonations.

The estimated measurements of the 2 kg AlAN charge fireballs or the confined charges could not be obtained and so cannot be included in the analysis. The estimated radii of the 1 kg PE7 fireballs (5.3 m) were greater than those of the AlAN firings (4 m; table 5.4) as expected (based on molar ratios of gas produced from the two different explosive types). The 2 kg charges produced larger fireballs and smoke plumes (almost double) compared to the 1 kg charges, which in turn were larger (by approximately double) than the 0.5 kg charges fired in the previous chapter). This trend would be expected as larger charge masses would

evolve more gas. However, the approximations were made from only one camera angle around the charge centre and are therefore estimates.

As no high speed imaging capability was available at the Kineton DEMSS range, the confined firings were not recorded at the same resolution. Therefore the fireballs were not observed and their estimated volumes were unknown. The inclusion of the ammonium phosphate fire retardant to the charges used in the confined vehicle firings would have also suppressed fireball formation[185,186]. This could be an alternative explanation for why the confined firings produced unexpectedly higher residue concentrations than the respective unconfined RDX-composition firings. The inclusion of the ammonium phosphate in the confined composition charges would also explain why the smoke plumes formed during these organic firings were light grey instead of the typical darker grey/black smoke cloud expected of oxygen deficient military explosives.

The relationship between the size of the fireball and the residue distribution trends following the firings of the larger charge masses was variable. Lower quantities of both ammonium and nitrate were recovered from the 2 m high sampling sites which were observed to be within the region of the fireball (figure 5.11); thus seemingly supporting theories which state closer surfaces will harbour fewer undetonated residues due to their exposure to high temperature flame fronts and the subsequent decomposition of any explosive residue material on them[3,44,69]. In contrast, both nitrate and ammonium detected on the 0.75 m high sampling sites did not exhibit this trend and instead decreased with increasing distance; the greatest amounts being recovered from the 3 m distance sites which also appeared to be engulfed by the fireball. The reason for the variation could be because the 2 m high sample sites may have been exposed to higher temperatures as the rim of the fireball was greatest at 2 m from the ground (the height the AlAN charge was positioned) (figure 5.10c). If so, this would suggest the fireball shape and extent to be an important factor to consider when attempting to recover post-blast explosive residues from surrounding surfaces.

Following the 1 and 2 kg PE7 firings, the amounts of RDX recovered from sampling plates fluctuated within and outside the area of the observed fireball (figure 5.22). The majority of sample site at the closest measured distance (3 m) yielded lower RDX quanitities than those at the next measured distance (4 m); the temperature closer to the centre of the fireball would be higher, thus further corroborating the theory that residue on the sites closest to the detonation centre would undergo thermal degradation. Nevertheless, with inconsistent and variable trends observed, the comparison between the fireball extent and the trend in residue distribution requires further testing. No other study has attempted to correlate the

two phenomena and therefore based on data here the relationship between the two is speculative for the larger charge masses fired (but was more convincing for the 0.5 kg firings from the previous chapter).

The high speed recording of the detonations was conducted from only one angle around the charge centre and the fireball radius was assumed to be equal in the unobserved orientations but this may not have been the case. In order to thoroughly assess any interaction between the fireball and sampling plates, and the relationship between the subsequent residue masses detected upon them, it would be necessary to record experiments from multiple angles around the charge centre and repeat the firings numerous times as individual detonations have been shown to produce varying results to each other.

Wind Direction

As observed from the experiments in chapter 4 the AlAN detonations formed light grey/white smoke plumes whereas the RDX–based PE7 charges produced black/grey smoke plumes due to the varying oxygen content (positive and negative oxygen balances respectively[11]) of each of the charge types. Following each firing the smoke plumes were observed to move constantly in line with the wind direction.

The majority of nitrate and ammonium residue amounts were skewed strongly in line with the wind direction following firings, particularly on those sites which were higher from the ground (2 m high) (figures 5.12–5.15). Noticeably higher quantities of RDX were also detected from downwind sites following both the unconfined (figure 5.22) and confined 1 kg (figure 5.31) firings. This finding from the firings of larger charge masses corroborates the directional biases observed in chapter 4 from smaller charger masses as well as previous literature[60,70] which comments on the mechanism of residue dispersal occurring, at least in part, in the smoke cloud and depended therefore on the wind direction. This validates the importance of ascertaining knowledge of the environmental conditions if at an outdoors bomb scene, or the potential movement of the smoke plume (to higher floors/vents/ceilings for example) if at an indoor bomb scene in order to retrieve trace residue evidence from optimal sampling locations.

Summary

The studies presented here supplement those conducted in the previous chapter; variables such as the charge mass, sampling height and confinement could be tested, although only one firing of the unconfined charges was possible and limited visual recordings of the detonations, and no blast pressure data or aluminium content data, could be obtained. Nonetheless, the key findings from the studies in this chapter indicate that, as with the results of the 0.5 kg charges reported in chapter 4, some support for the theoretical inverse square law distribution model was found (particularly for the inorganic data), but it is not possible to fit one theoretical distribution model to residue distribution of all different explosive analytes. Rather, the general trend of finding decreasing residue concentrations with increasing distance applies in most cases (from both unconfined and confined detonations).

The residue distribution trends did not vary greatly based on the different charge masses tested so far (0.5 kg, 1 kg and 2 kg); apart from one anomalously high result, the majority of ammonium nitrate residue decreased with increasing distance. The RDX compositions generated more fluctuating concentrations with increasing distance, but overall also decreased with increasing distances from the detonation centres. This supports the current forensic practice of focusing explosive residue collection on central regions of the detonation centre. Most texts discuss the sampling of residues on the ground (or in the crater area if one is apparent[8,55]); findings here relating to the sampling height indicate that sites which are actually higher from the ground may yield higher amounts of residue. In order to test this theory residues should be collected from sites which are positioned higher than the charge height.

The effects of the fireball on residue distribution patterns have not been supported in their entirety here, with varying results produced. However, evidence for the wind direction being a principal factor which affects the distribution patterns has been provided. This further supports the notion that the residue dispersal mechanism occurs, at least partly, during the movement of the smoke plume formed after firing, whilst compounding the need for forensic investigators to focus residue sampling efforts on downwind sampling sites if possible. In order to strengthen the validity of the results produced thus far, clearly further experiments would be required and as these are not necessarily practicably feasible, computational efforts applied to the limited empirical data sets produced from experimental studies would consolidate the findings and their implications greatly. This may then allow a protocol for forensic analysis based on these results to be generated which may provide empirical evidence for current forensic practice.

CHAPTER 6: MORPHOLOGICAL AND CHEMICAL ASSESSMENT OF POST-BLAST PARTICLES AND SIMULATION STUDIES OF PARTICLE DISTRIBUTION

6.1 Introduction

If computational modelling of residue distribution were possible, it would be necessary to know not only the factors which might affect the distribution patterns (such as the wind field surrounding the detonation) but also the physical appearance of the residue particles as they move through the air. Given the possibility of recovering organic and inorganic post-blast explosive residues from swabbed samples, which were verified with the use of HPLC-MS and IC respectively, the physical nature of the residues themselves were therefore also investigated. Scanning electron microscopy (SEM) stubs were positioned on sampling poles around the detonation centres of the AlAN and RDX-based firings. The particles on the stubs were analysed with SEM-EDS for their morphology and elemental composition, and Raman spectroscopy, MeV secondary ion mass spectrometry (MeV SIMS) and particle induced X-ray emission (PIXE) techniques were also used to characterise the detected particles.

The morphological and chemical characteristics of the particles from the AlAN charge firings are presented first (section 6.2), followed by that of the RDX-based charges (section 6.3); both of which are compared to the morphology and chemical signatures of the 'pre-blast' material for comparison. The information obtained from the particle analyses is used as input data into the simulation experiments of post-blast particle residue distribution, the results of which are presented following the particle studies (section 6.4). The experimental and numerical simulation data generated are compared and discussed (section 6.5).

6.2 Aluminised Ammonium Nitrate Particles

6.2.1 Morphology and Elemental Composition

6.2.1.1 Pre-blast Particles

The AN prills were spherical, approximately 3 mm in diameter (figure 6.1a) and consisted of agglomerated particles (figure 6.1b). Once ground and mixed with aluminium the particles were no longer spherical but irregularly shaped; diameters of individual particles varied between 30 μm and 1300 μm in diameter (figure 6.1c shows a ground AlAN particle ~210 μm in diameter).

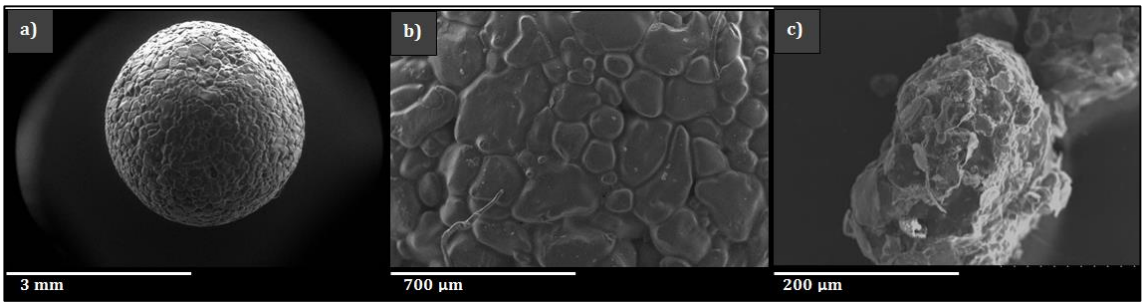

***Figure 6.1**: SEM images pre-blast particles: a) whole ammonium nitrate, b) close-up of prill, c) aluminised ammonium nitrate particle.*

The material present on the surface of the irregularly shaped particles (indicated by lighter coloured areas in the micrograph in figure 6.1c) was attributed to flakes of aluminium; whilst this was not conclusively proved, the lighter shaded material did not appear on the AN particles prior to being ground.

The EDS spectrum of the whole ammonium nitrate prill produced atomic percentages of 36.7 % and 63.3 % for nitrogen and oxygen (ratio of 2:3.4), respectively (figure 6.2); approximately corresponding to the theoretical ratio of nitrogen to oxygen (2:3) in AN (NH_4NO_3).

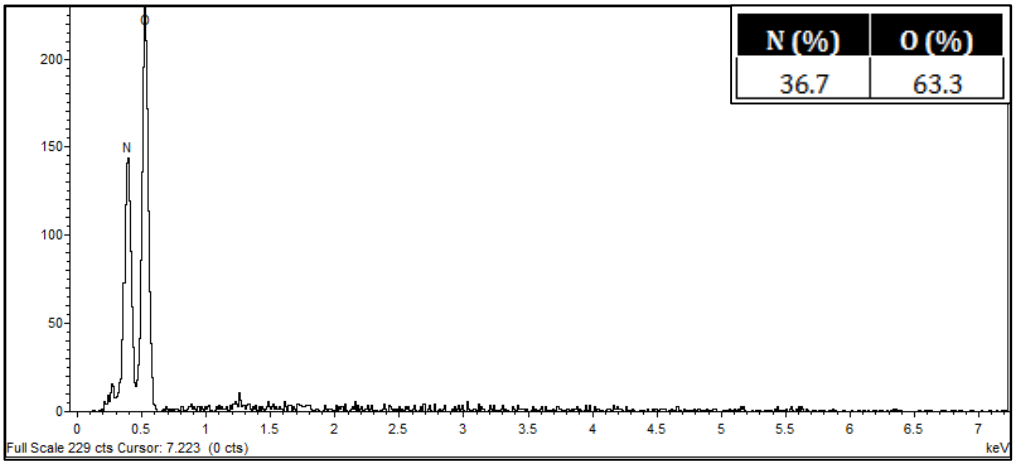

***Figure 6.2**: EDS spectrum of AN prill prior to grinding. The ratio of nitrogen to oxygen was consistent with the theoretical ratio (2:3). Atomic % are inset in the figure.*

The EDS spectra collected from multiple ground and mixed particles (AlAN particles) exhibited similar atomic percentages for nitrogen and oxygen (~18.5 % and ~19 % respectively) and ~50 % for aluminium, a representative spectrum of which is shown in figure 6.3.

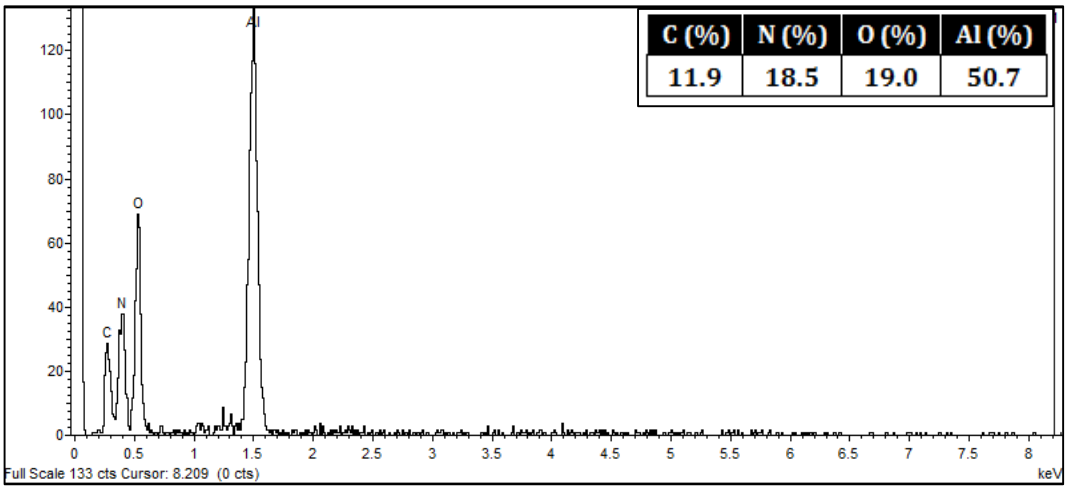

Figure 6.3: *Representative EDS spectrum of AlAN particles (AN particles ground and mixed with aluminium). Atomic % are inset in the figure. The ratio of N:O (1:1) was inconsistent with the theoretical ratio (2:3).*

The ratio of nitrogen to oxygen in the ground particles was almost 1:1, unlike the theoretical ratio (2:3) detected from the unground material in prill form (figure 6.2). The variation from the theoretical ratio may have been due to carbon, without which the normalised atomic percentages of N, O and Al were 21.0 %, 21.5 % and 57.5 % respectively. The high aluminium signal (~58 atomic %) varied from the theoretical amount of ~22 % (based on a 10 % aluminium mass fraction in the 0.5 kg AlAN charge compositions).

The provenance of carbon was likely to be from the adhesive disc placed onto the SEM stub as no carbon was present in the inorganic AlAN particles. The EDS result of the 'blank' stub surface with no particles (figure 6.4) showed the presence of carbon (~84 %) and oxygen (~16 %). The quantity of oxygen detected in any pre or post-blast particles would also therefore have been unreliable.

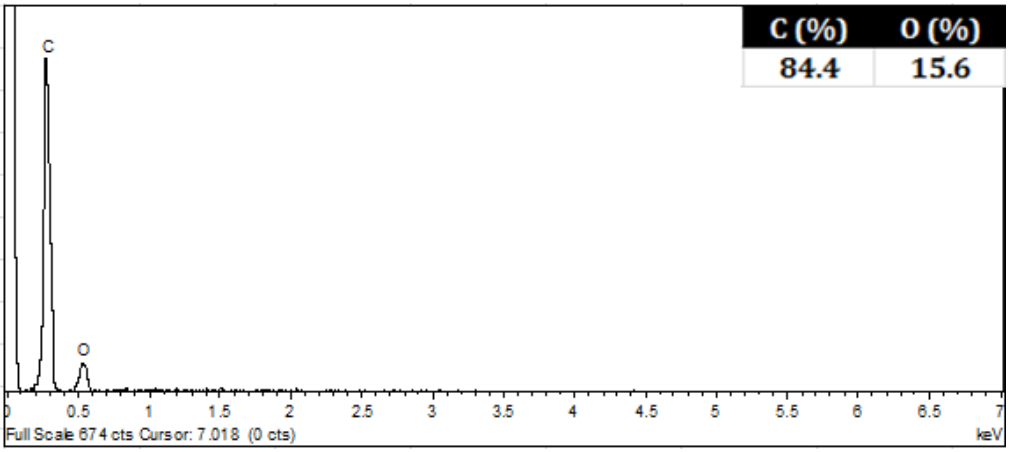

Figure 6.4*: EDS of blank stub surface – only carbon and oxygen were detected (atomic % inset).*

6.2.1.2 Post-blast Particles

The results presented here apply to stubs which were collected following the firings of the 0.5 kg, 1 kg and 2 kg AlAN charges. Particles were not homogeneously deposited across any of the stub surfaces; in order to locate particles, the surface of the stubs was systematically scanned. Whilst a variety of particles were seen, only those with elemental compositions containing N, O and Al were ascribed to be post-blast explosive residues and focused on for this analysis. The morphology and elemental compositions of residue particles were grouped into distance 'bins' of '1 m', '2 m to 3 m', '4 m to 7 m' and '>7 m'; these groupings were chosen as similar particles were observed within each.

Particles observed at 1 m

The morphology of particles found on stubs retrieved 1 m from the detonation centres of AlAN charge firings varied from that of the pre-blast material; SEM images of representative particles are shown in figure 6.5.

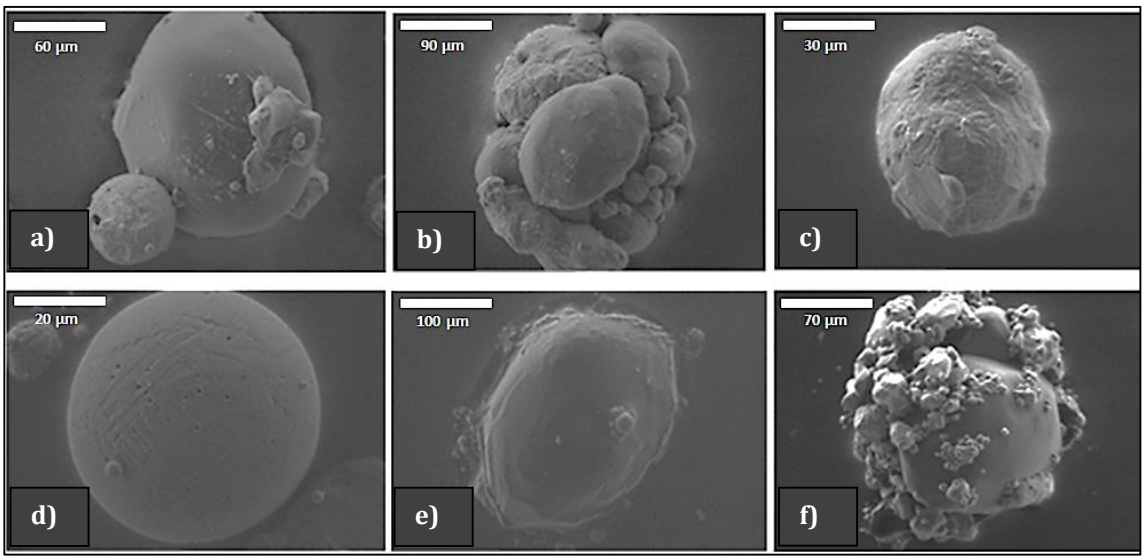

Figure 6.5*: SEM images of particles observed on stubs retrieved 1 m from the detonations of AlAN charges.*

The post-blast particle sizes ranged between 30 µm and 120 µm in diameter on average and were therefore smaller overall than the pre-blast particles (which were 30 µm to 1300 µm in diameter). Particles were spheroidal with generally smooth surfaces; where surface features were apparent, they consisted of smaller (10 µm to 80 µm) spheroidal particles upon the main particle surface as seen in figure 6.5. No features ascribed to be aluminium flakes, as exhibited on the pre-blast AlAN particles (figure 6.1c), were observed.

The EDS results of the particles in figure 6.5 are presented in table 6.1. Carbon from the adhesive disc was detected in every case, therefore the EDS results presented are the normalised data calculated without the carbon signal. The atomic percentages of the

detected elements (N, O and Al) varied between the particles; no consistent signal in terms of elemental atomic percentages was detected and no individual particles exhibited the same elemental ratios to that of the pre-blast material. The averaged elemental ratios of particles 1 m from the detonation were however more consistent with the pre-blast material (table 6.1).

Particle (fig. 6.5)	N (%)	O (%)	Al (%)
a	41.0	47.4	11.6
b	29.1	8.59	62.3
c	8.44	13.5	78.0
d	3.54	33.8	62.7
e	30.2	36.5	33.2
f	48.8	24.2	27.0
Average	**26.8 ± 17.7**	**27.3 ± 14.7**	**45.8 ± 25.6**
Pre-blast	**21.0**	**21.5**	**57.5**

Table 6.1: *Atomic % of elements detected from EDS analysis of particles recovered 1 m from the charge centre of AlAN firings (3 sf.) The averaged elemental ratios were consistent to the pre-blast particles.*

As well as the spheroidal particles, flattened deposits were also found on the stubs collected 1 m from the detonation centres (figure 6.6).

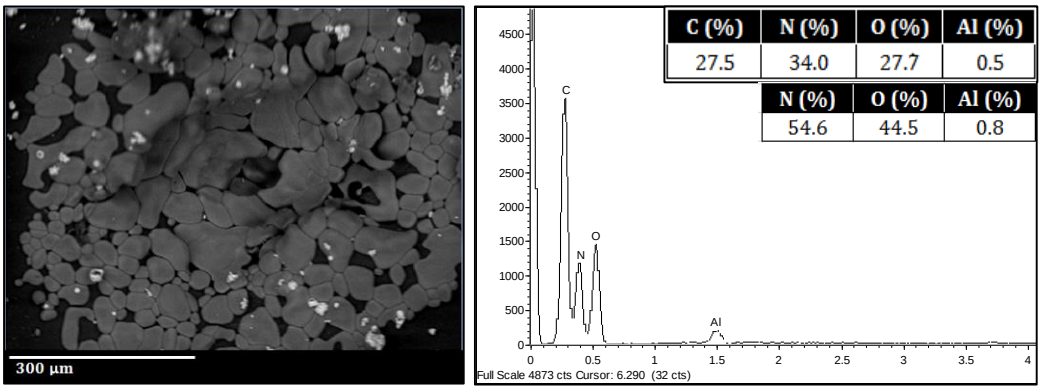

Figure 6.6*: left: SEM image of smeared particles seen on stubs collected 1 m from the centre. Right: EDS spectrum of smeared particles (atomic % inset). Normalised data calcualted without the carbon for N, O and Al were 54.6 %, 44.5 % and 0.80 %.*

These broader depositions (> 300 µm) were larger than the individual particles observed in figure 6.5 (the largest of which were ~120 µm) but were themselves made up of agglomerated flattened particles and flecks of aluminium (indicated by the lighter regions in the SEM image in figure 6.6). The EDS analysis of the darker regions of these flattened depositions showed the nitrogen content (~34 %) was higher than that detected in both the pre-blast material and post-blast spheroidal particles; whereas the aluminium content within them (0.8 %) was lower than that in either.

Particles observed at 2 m to 3 m

The morphologies of post-blast residue particles did not vary greatly at 2 and 3 m from the detonations compared to those at 1 m; spheroidal particles with smooth surfaces were predominantly observed (representative particles seen in figure 6.7). Particles resembling the consolidated particles of the AN prill were also seen (figure 6.7e). Faceting of particles was also observed (figure 6.7d and f).

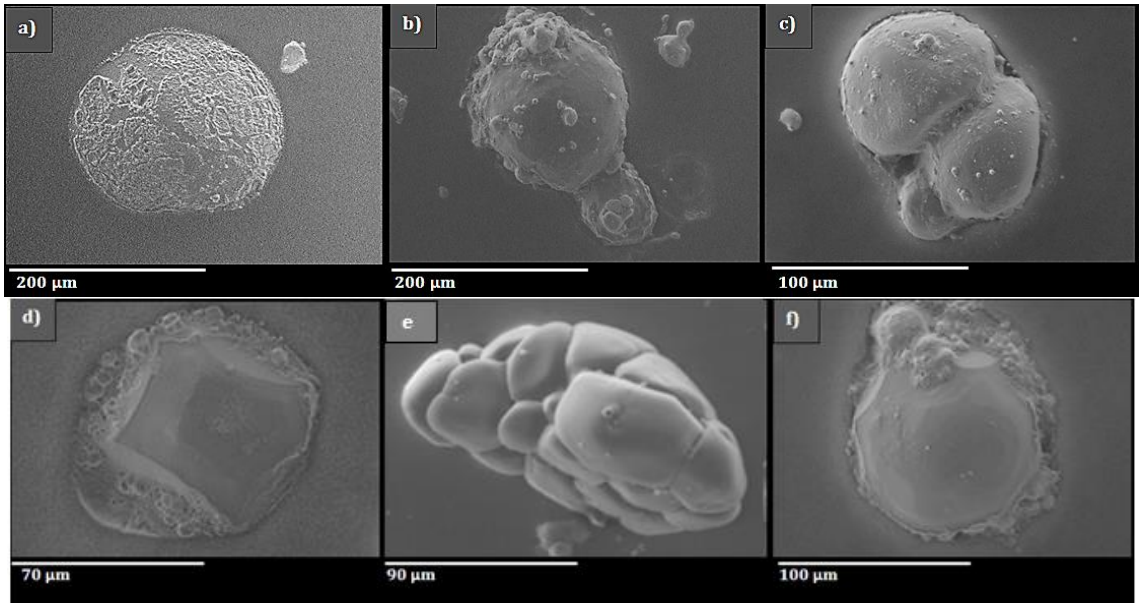

Figure 6.7: *SEM images representative of particles observed on stubs retrieved 2 m and 3 m from the detonations of AlAN charges.*

The particle size range (30 µm to 210 µm in diameter) however, was greater than that found for particles at 1 m. The elemental compositions of the particles displayed (calculated without the carbon) are shown in table 6.2; like the particles observed at 1 m, no consistent signal in terms of the elemental ratios detected between particles was found and no particles exhibited the elemental ratios of the pre-blast material. The averaged elemental signal from the particles at 2 m and 3 m was also inconsistent with the pre-blast material. Qualitatively, fewer particles were observed on stubs 2 m and 3 m from the detonations than those at 1 m.

Particle (fig.6.7)	N (%)	O (%)	Al (%)
a	40.5	51.6	7.95
b	11.0	18.3	70.7
c	25.9	36.2	37.9
d	45.0	32.7	22.3
e	32.9	60.1	7.07
f	11.9	60.1	28.0
Average	**27.9 ± 14.3**	**43.1 ± 16.9**	**29.0 ± 23.6**
Pre-blast	**21.0**	**21.5**	**57.5**

Table 6.2*: Atomic % of elements (normalised) detected from EDS analysis of particles recovered 2 m and 3 m from the detonation centres of AlAN charges (3 sf.)*

At the 2 m and 3 m distances, as well as the individual spheroidal particles, clustered residue depositions were also found impacted upon stubs; these were larger (up to 1000 μm in diameter; figure 6.8) than other particles ascribed to be post-blast residue, including the smeared, flattened depositions observed on stubs at 1 m distances (cf. figure 6.6).

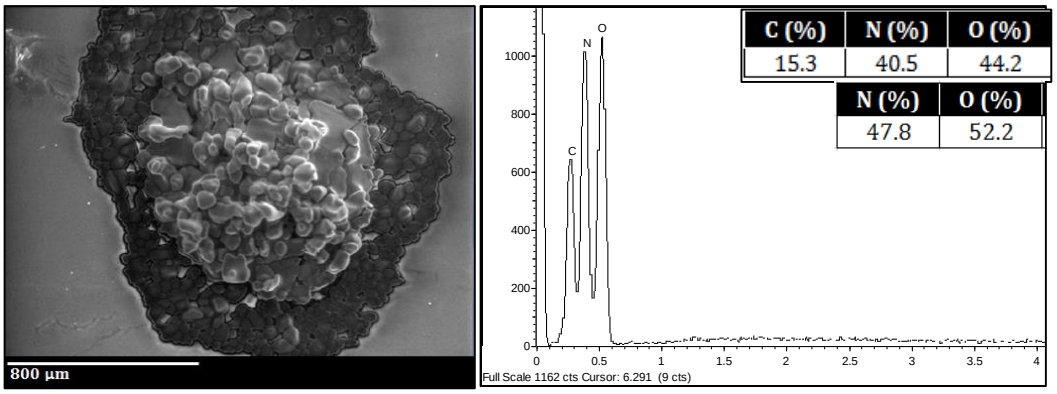

***Figure 6.8**: SEM image (left) of representative agglomerated particle mound seen on stubs retrieved 2 m and 3 m from detonation centres. Corresponding EDS spectrum with atomic % (right). Without carbon, the normalised counts for N and O were 47.8 % and 52.2 %.*

Figure 6.8 shows the agglomerated residue particles and the corresponding EDS spectrum with only C, N and O detected (the atomic percentages of which are inset in figure 6.8). The nitrogen to oxygen ratio was ~1:1, comparable to that of the pre-blast AlAN particles but dissimilar to the theoretical ratio (2:3). The morphology of the particles in the centre of the agglomeration (of which individual sizes were between 20 μm and 120 μm) was similar to that of the individual particles of the AN prill (figure 6.1a and 6.1b). Around the edge of the deposition (darker region in figure 6.8) the particles were flattened on the stub surface similarly to the flattened depositions observed on stubs which were 1 m from the detonations (figure 6.6).

Particles observed at 4 m to 7 m

The majority of residue on stubs positioned 4 m to 7 m from the detonation centres principally consisted of an aggregated mass of individual particles. Individual particles ranged in size between 10 μm to 150 μm, the clusters were up to 500 μm in diameter (figure 6.9). No smeared or flattened residue particles were found on stubs at these distances as were observed at the 1 m and 2 m to 3 m distances.

Table 6.3 displays the atomic percentages of elements detected from each particle displayed in figure 6.9 (which were calculated by discounting the carbon content and normalising the data). The elemental ratios varied between the different observed particles and were inconsistent with the pre-blast material. The averaged elemental atomic percentages of particles found between 4 m and 7 m was also inconsistent to that of the pre-blast particles.

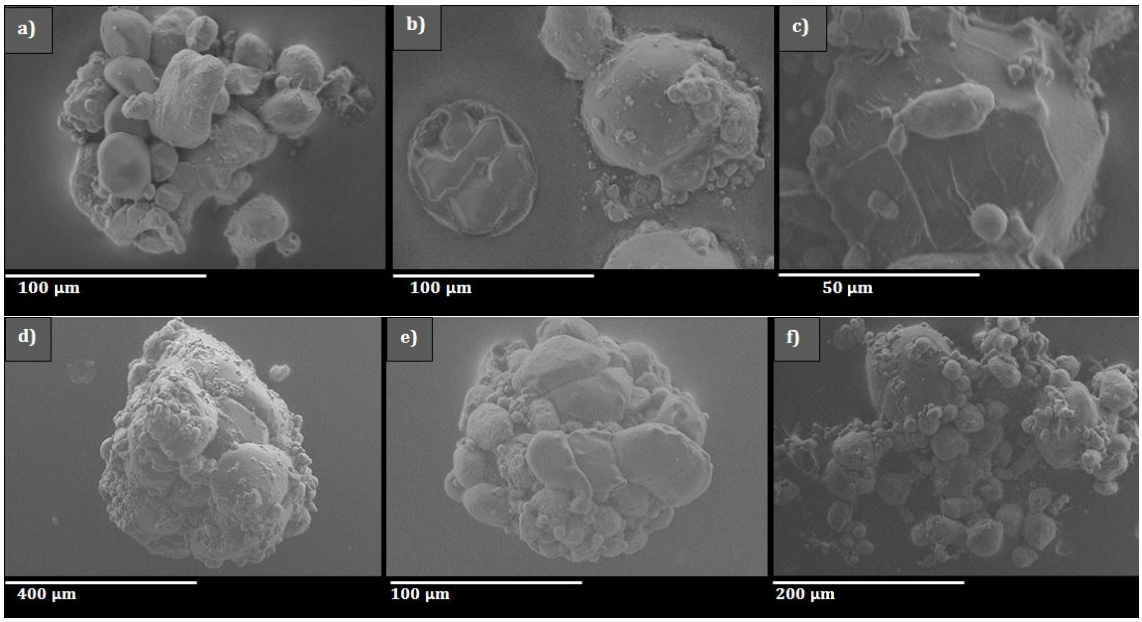

Figure 6.9: *SEM images representative of particles observed on stubs retrieved 4 m to 7 m from the detonations of AlAN charges.*

Particle (fig 6.9)	N (%)	O (%)	Al (%)
a	33.1	39.2	27.6
b	13.4	62.3	24.4
c	22.4	58.1	19.5
d	9.05	45.2	45.7
e	6.23	37.7	56.1
f	5.36	30.9	63.7
Average	**14.9 ± 11**	**45.6 ± 12.3**	**39.5 ± 8.3**
Pre-blast	**21.0**	**21.5**	**57.5**

Table 6.3*: Atomic % (normalised data) of elements detected from EDS analysis of particles recovered 4m to 7 m from the charge centre of AlAN firings (3 sf.)*

Qualitatively, fewer particles were identified on stub surfaces which were 4 m to 7 m from the detonation centres than those which were positioned 1 m to 3 m from it.

Particles observed at > 7 m

Following the detonations of all AlAN charges (0.5 kg, 1 kg and 2 kg), no particles, of any type, were found on stubs which were positioned further than 7 m from the detonations, in any of the four sampled orientations around the centre.

6.2.2 Chemical Identity

The EDS analyses indicated the presence of explosive residue related material based on the elemental compositions of the particles, however, in order to elucidate their chemical identity, particles were analysed with Raman spectroscopy.

The background Raman spectrum of the carbon discs (with no particles on) is shown in figure 6.10. Two prominent broad bands at ~1324 cm^{-1} and ~1586 cm^{-1} were characteristic of the carbon filled acrylic adhesive discs.

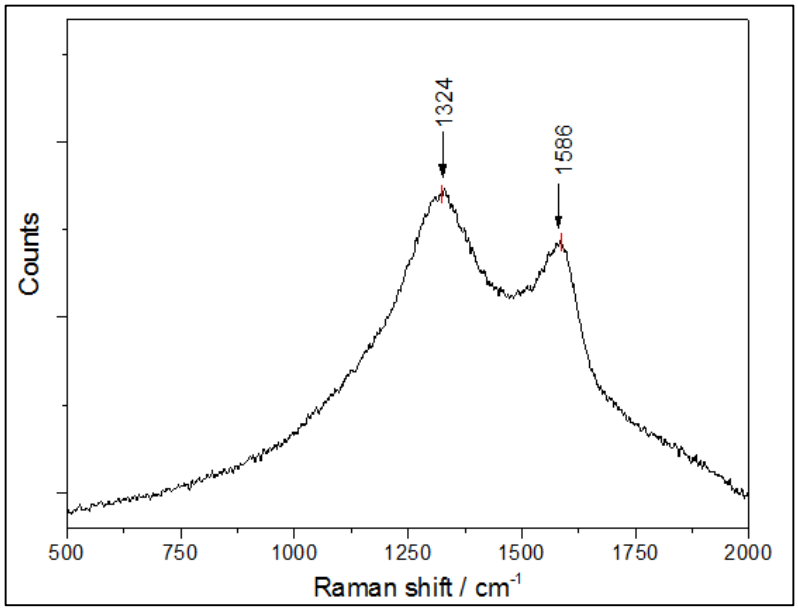

***Figure 6.10**: Background spectrum of carbon discs on SEM stubs. Collected with a 785 nm laser (5 % power, 3 accumulations, 10 second exposure time).*

Pre-blast Particle Identity

The Raman spectrum of the pre-blast AN provided a chemical fingerprint of the material (figure 6.11); the features corresponding to the labelled bands are shown in table 6.4.

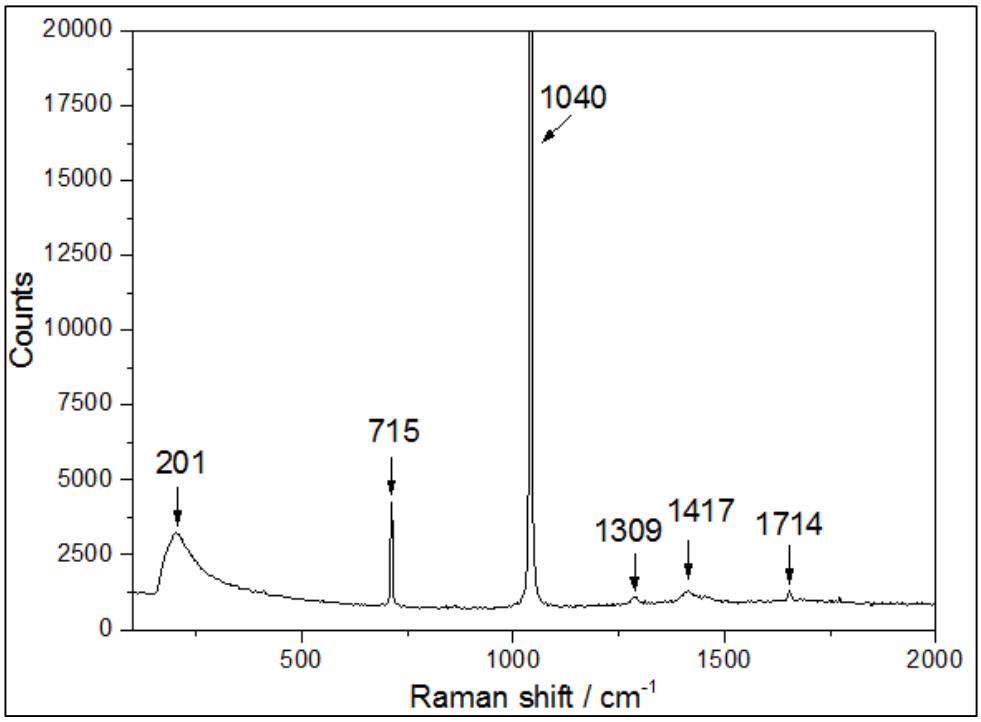

***Figure 6.11**: Raman spectrum of AlAN particles, collected over 5 accumulations of 10 second exposure times using a 785 nm laser at 5 % power*

Raman shift /cm^{-1}	Feature[165,167]
~200	Lattice vibrations of the NO_3^- and NH_4^+ ions
~715	In-plane bending vibrations of the NO_3^- ion
~1040	Symmetric stretching vibration of the NO_3^- ion
~1300	Weaker bands due to symmetric N-O stretches
~1400	Stretching vibration of NO_3^-
~1700	Unassigned in reference

***Table 6.4**: Chemical feature of Raman bands detected from pre-blast AlAN particles.*

Post-blast Particle Identity

It was not possible to locate the exact particles which were observed through the SEM when using the Raman microscope; based on the size estimations and macroscopic features of particles observed on stubs positioned at different distances from the detonations similar particles were focused upon for analysis. Figure 6.12 shows a characteristic image viewed through the Raman microscope used to identify and focus upon particles.

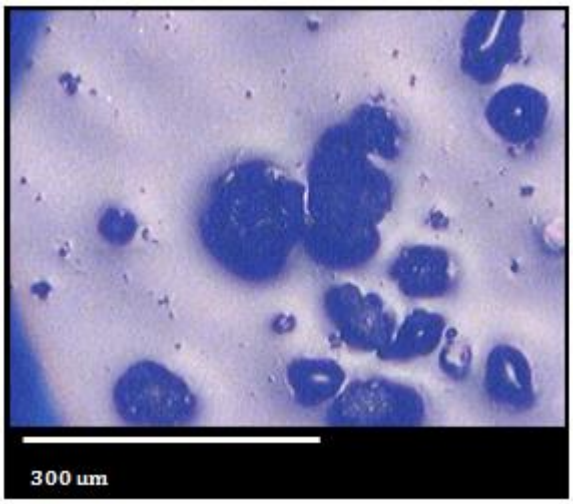

Figure 6.12: *Characteristic Raman micrograph of particles used to identify particles from which spectra were collected using Raman spectroscopy.*

Representative Raman spectra of particles found at 1 m, 2 m to 3 m, and 4 m to 7 m from the detonations (figure 6.13) all exhibited similar spectra to the pre-blast material. The intensity of the bands varied; particles closer (1 m to 3 m) to the detonation centre (red and blue spectra in figure 6.13) exhibited weaker signals relative to particles on stubs positioned 4 m to 7 m (green and pink spectra in figure 6.13) from the centre.

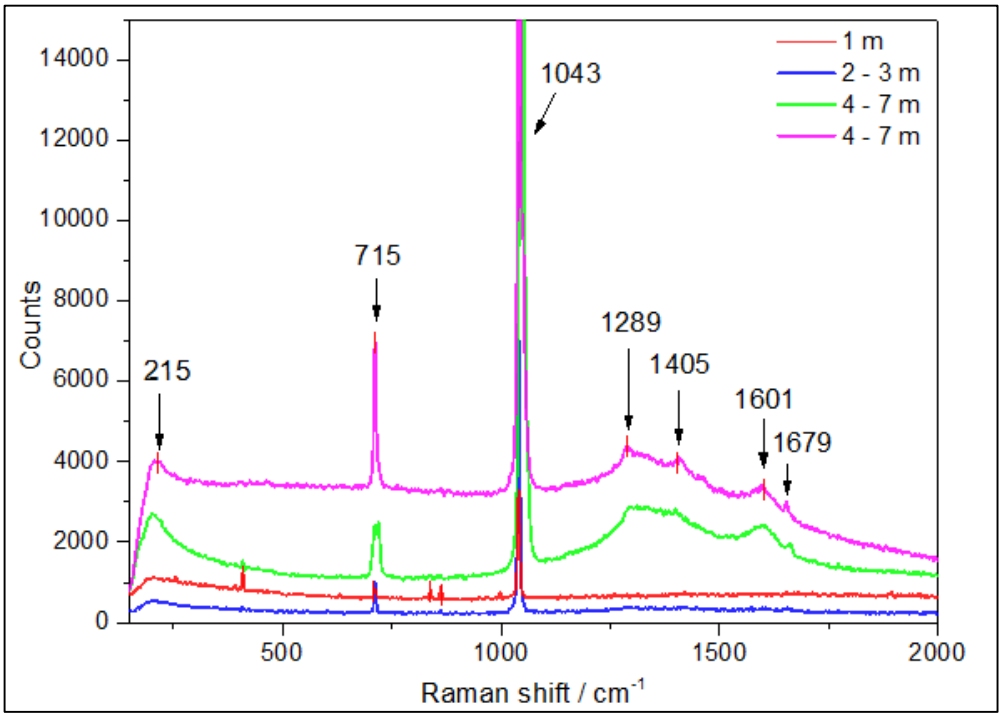

Figure 6.13*: Representative Raman spectra of AlAN particles positioned 1 m (red spectrum), 2 m to 3 m (blue spectrum), and 4 m to 7 m (green and pink spectra) from the detonation centres of AlAN charges. Spectra collected over 5 accumulations of 10 second exposure using a 785 nm laser at 5 % power.*

The Raman bands present in the pre-blast AN were compared to those in the post-blast particles (table 6.5); spectra collected from particles found 4 m to 7 m from the detonations were consistent with the pre-blast material in that all of the same Raman bands were present in all spectra at similar intensities. The particles found on stubs recovered 1 m to 3 m from the detonations had the dominant Raman bands at ~200 cm^{-1}, ~715 cm^{-1} and 1040 cm^{-1} but exhibited the broad peaks between 1290 cm^{-1} and 1750 cm^{-1} at lower relative intensities.

Raman shift region /cm^{-1}	Feature	1 m (red)	2–3 m (blue)	4–7 m (green)	4–7 m (pink)
~201	Lattice vibrations of NO_3^- and NH_4^+ ions	✓	✓	✓	✓
~715	In-plane bending vibrations of NO_3^- ion	✓	✓	✓	✓
~1040	Symmetric stretching vibration of NO_3^- ion.	✓	✓	✓	✓
~1300	Medium intensity bands due to symmetric N-O stretching	weak	weak	✓	✓
~1400	Stretching vibration of NO_3^-	weak	weak	✓	✓

Table 6.5*: Comparison of presence of Raman bands in spectra obtained from particles found at 1 m, 2 m to 3 m and 4 m to 7 m from the detonation centres.*

6.2.3 AlAN Particle Summary

Charge mass variation: No variation was observed in terms of particle morphology, size or elemental composition between the different AlAN charge masses (0.5 kg, 1 kg and 2 kg) fired; such that the particles could be grouped in distances ('1 m', '2 m to 3 m' and '4 m to 7 m') based on their morphological appearance regardless of the mass of the charge fired from which they were collected. No particles were observed on any stubs further than 7 m from any charge mass fired; corresponding well with the 6 m and 10 m radii within which inorganic residues were detected from sampling plates following detonations of 0.5 kg and larger charge masses fired in chapters 4 and 5 respectively.

Shapes: Some post-blast particles somewhat resembled the pre-blast AN material, having agglomerated structures. At 1 m from the detonations the majority of particles were spheroidal with smooth surfaces; however deposits which appeared to be molten at the time of impact (flattened particles) were also seen (figure 6.6). At 2 m to 3 m, particles had similar spheroidal and smooth surfaced morphologies and agglomerated depositions consistent with high velocity impact were also observed (figure 6.8). No such particles were observed further than 3 m from the detonations, instead residues found 4 m to 7 m were principally clusters of individual particles.

Sizes: The ground pre-blast particles were 30 μm to 1300 μm in diameter. At 1 m the size range of individual particles was 30 μm to 120 μm, smeared depositions were larger (> 300 μm). Individual particles at 2 m to 3 m were larger (30 μm to 210 μm), with the flattened deposits being up to 1000 μm in diameter. Individual particles at 4 m to 7 m were between 10 μm to 150 μm, but the clusters were up 500 μm in diameter.

Chemical analysis: Post-blast residues contained the same elemental compositions as the pre-blast material, but the ratio between detected elements varied between the pre- and post-blast particles as well as between individual post-blast particles. This was the case for all particles observed on stubs from all distances. Little (0.5 %) or no aluminium was detected in the smeared/flattened depositions found at 1 m to 3 m. Despite not being able to target specific particles with Raman analysis, the Raman spectra obtained of post-blast particles were consistent with the chemical fingerprint of ammonium nitrate. Particles detected further from the detonation (4 m to 7 m) were generally larger and produced Raman bands of greater intensity than those closer to it (1 m to 3 m).

Quantification of particles: Figure 6.14 shows a typical surface from a stub positioned 1 m from the detonations and demonstrates why it was not possible to count every particle observed on each stub surface.

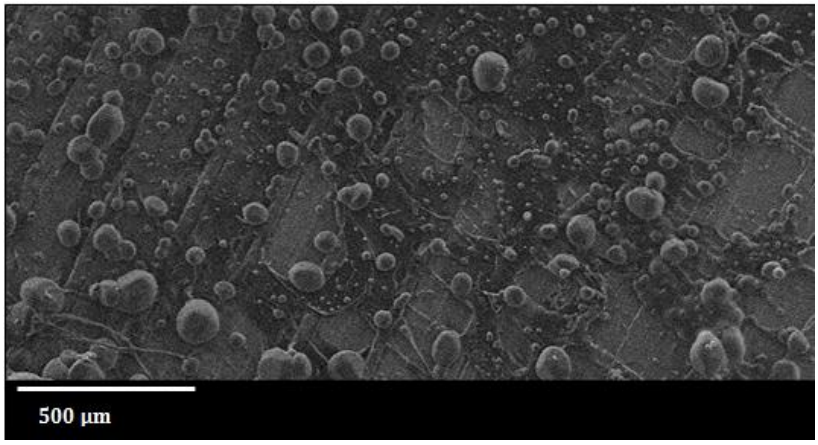

Figure 6.14*: SEM image of stub surface collected from 1 m of AlAN detonation. Particle deposition was heterogeneous and it was not possible to count all individual particles.*

As the particle deposition was not homogeneous across the stub surfaces, estimates of particle counts based on smaller areas would have been inaccurate. Qualitatively, more particles were observed on stubs which were closer to the detonations (as was the case for the inorganic residue distribution results reported in chapters 4 and 5). However, no bias was found in the amount of particulate material observed on stubs from different orientations around the charge centres based on qualitative observations.

6.3 RDX Particles

6.3.1 Morphology and Elemental Composition

6.3.1.1 Pre-blast Particles

The undetonated, or pre–blast, RDX-based compositions consisted of individually discernible particles amassed together (figure 6.15a). The EDS spectrum (figure 6.15b) contained only carbon, nitrogen and oxygen; the representative atomic percentages of each, collected from multiple particles, are inset in figure 6.14b. The theoretical ratio of the carbon, nitrogen and oxygen in RDX (3:6:6) was not reflected in the EDS spectrum of the compositions; whilst the nitrogen to oxygen ratio (~1:1) was analogous to the theoretical N:O ratio, the carbon signal was twice as high. This may have been due to detection of carbon from the adhesive stub or from the organic binder in the compositions which may also have affected the oxygen quantification.

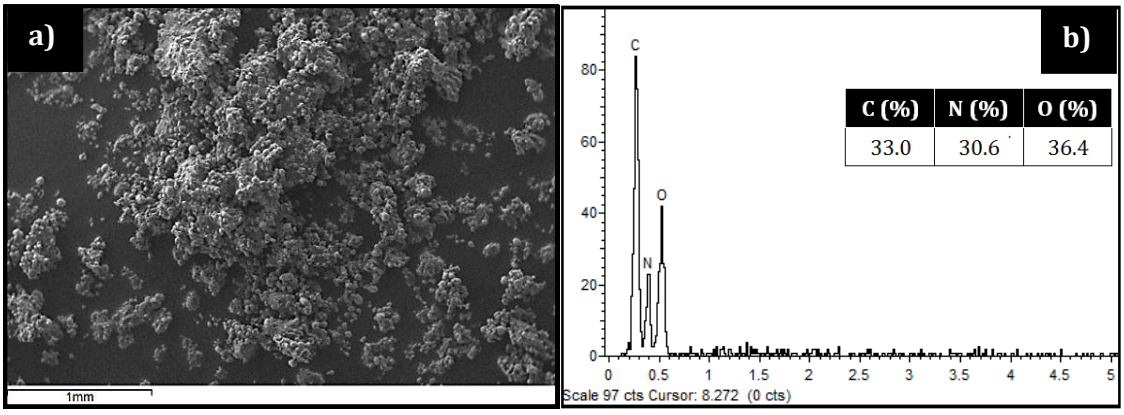

Figure 6.15*: Left: SEM image of RDX composition particles (pre-blast) (100 x magnification). Right: EDS spectrum of RDX composition showing elemental composition of C, N and O. The spectrum is representative of multiple particles analysed via EDS.*

6.3.1.2 Post-blast Particles from Unconfined Firings

The results presented here apply to particles on stubs which were collected following the firings of the 0.5 kg, 1 kg and 2 kg PE4 and PE7 (RDX-based composition) charges. Numerous particle types were present on the stub surfaces (particularly on those retrieved 1 m from the detonations). Particles were not homogeneously deposited across any of the stub surfaces; in order to locate particles, the stubs were systematically scanned across the surface. Particles which exhibited elemental compositions similar to the pre-blast material (containing only C, N and O) were focused on for this analysis as markers for explosive residue. The morphology and elemental compositions of post-blast explosive residue particles were grouped into distance 'bins' of '1 m', '2 m to 3 m', '4 m to 5 m' and '> 5 m'; these groupings were chosen as similar particles were observed within each.

Particles observed at 1 m

The morphological appearances of particles thought to be post-blast RDX-composition residues on stubs positioned 1 m from the detonations were inconsistent with those of the pre-blast material. The post-blast particles were not agglomerated clusters but rather individual particles which ranged between 10 μm to 70 μm in diameter (figure 6.16). The shape of the particles was also dissimilar to those of the pre-blast material; post-blast particles exhibited greater irregularity with folded and curled forms. Few were observed to have spheroidal forms (as seen in figure 6.16 b).

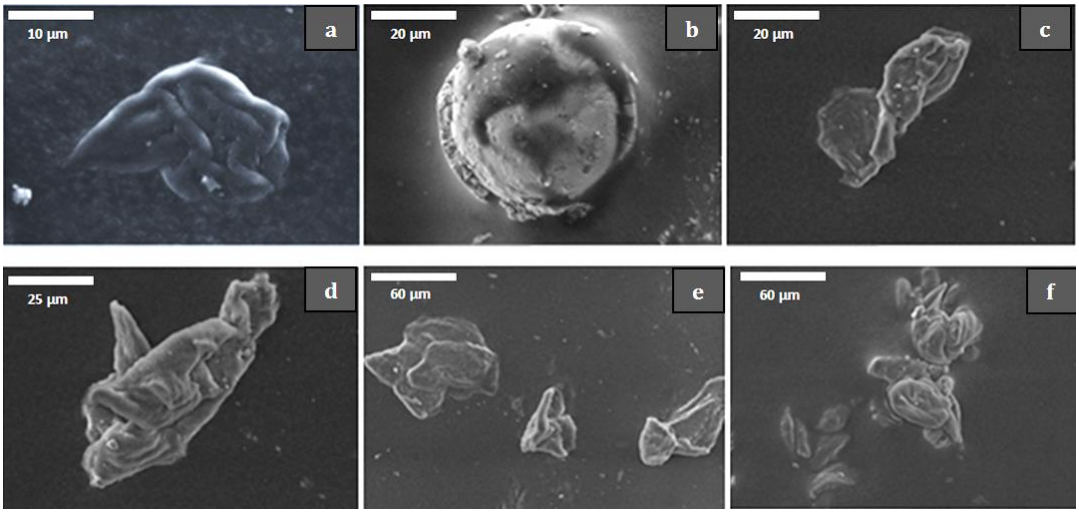

Figure 6.16: *SEM images of post-blast particles observed on stubs collected 1 m from the RDX-based detonations. Curled particles (10 μm to 70 μm diameter) were principally found.*

The elemental compositions of the particles were consistent with the raw material in that, overall, the only elements detected were C, N and O. However, the atomic percentages varied from that of the pre-blast material; the carbon content of each particle was higher and the nitrogen signals produced were lower (table 6.6). The averaged oxygen content was similar to that of the pre-blast material, however due to the presence of oxygen in the stub surfaces this was not a reliable quantification of it in the particles. Particles from which nitrogen was not detected were also observed on the stubs; those which had morphologies consistent with those containing nitrogen were included in the analysis (figure 6.16a and table 6.6).

Particle (fig. 6.16)	C (%)	N (%)	O (%)
a	43.5	0.00	56.5
b	74.3	6.20	19.5
c	73.0	0.80	26.2
d	47.6	9.78	42.6
e	59.7	13.8	26.5
f	71.1	1.06	26.8
Average	**61.5 ± 13.5**	**5.27 ± 5.6**	**33.0 ± 13.8**
Pre-blast	**33.0**	**30.6**	**36.4**

Table 6.6*: Atomic % of elements detected via EDS of particles in figure 6.16 (3 s.f.) compared to the elemental composition of the raw material. Averaged percentages were also inconsistent.*

Particles observed at 2 m to 3 m

Particles upon stubs retrieved 2 m and 3 m from the detonations had shapes consistent with those detected at 1 m; the particles were irregular, non-spherical, with curved and folded edges (figure 6.17). However, the particle size range (20 μm to 100 μm in diameter) was greater than that found for particles at 1 m (which ranged between 10 μm to 70 μm). Qualitatively, fewer particles were observed on stubs 2 m and 3 m from the detonation than those at 1 m.

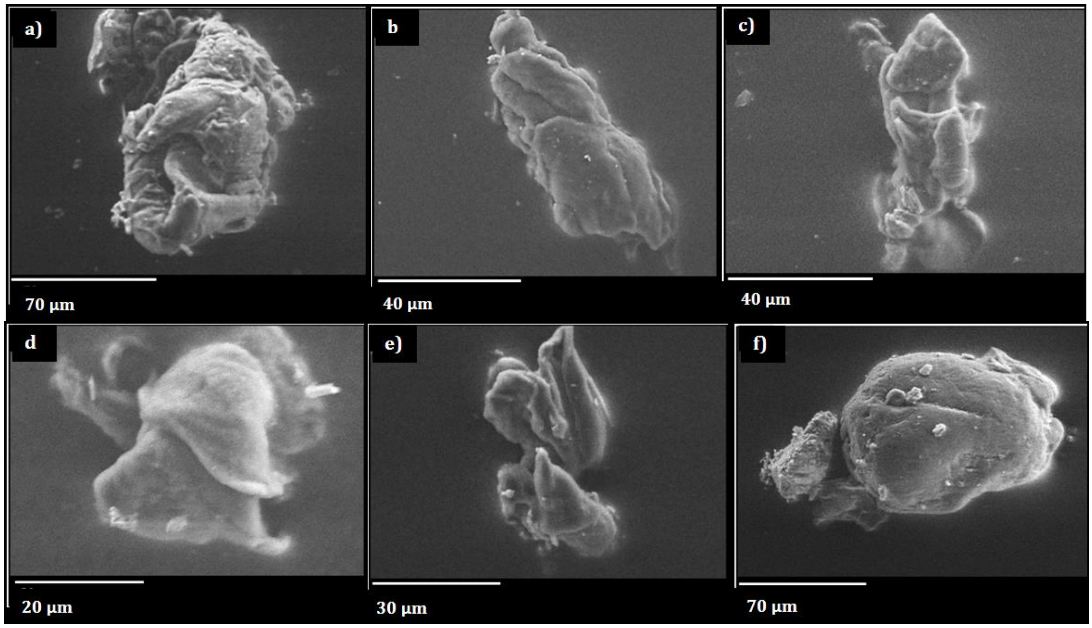

Figure 6.17: *SEM images of post-blast particles found on stubs retrieved from 2 m and 3 m from the charge centre of the RDX-based firings. Particle sizes ranged between 20 μm to 100 μm.*

The elemental compositions of the particles on figure 6.17 are shown in table 6.7; similarly to the pre-blast particles they contained only carbon, nitrogen and oxygen. However, the elemental ratios varied between particles, likewise to those detected at 1 m. The carbon content was higher than in the pre-blast material and comparable to the levels detected in particles found at 1 m. The nitrogen signals were weaker than those detected in the pre-blast material but more intense than those detected in particles found at 1 m. The range of oxygen signals was comparable to both the pre-blast and 1 m particles.

Particle (fig. 6.17)	C (%)	N (%)	O (%)
a	43.0	10.5	46.5
b	61.2	12.0	26.8
c	44.3	8.20	47.5
d	57.8	16.1	26.1
e	60.2	13.3	26.5
f	62.9	11.2	25.9
Average	**54.9 ± 8.8**	**11.9 ± 2.6**	**33.2 ± 10.7**
Pre-blast	**33.0**	**30.6**	**36.4**

Table 6.7*: Atomic % of elements detected from EDS analysis of particles a–f from figure 6.17 (3 s.f.) recovered 2 m and 3 m from the centre, compared to that of the pre-blast particles.*

Particles observed at 4 m to 5 m

At distances of 4 m and 5 m, no particles resembling those seen at the 1 m to 3 m distances were observed. Particles were spherical and spheroidal and overall smaller (5 µm to 40 µm in diameter) than those found on the closer positioned stubs (representative particles are seen in figure 6.18). Qualitatively, fewer particles were detected on the stubs at 4 m and 5 m than those closer (1 m to 3 m) to the detonations.

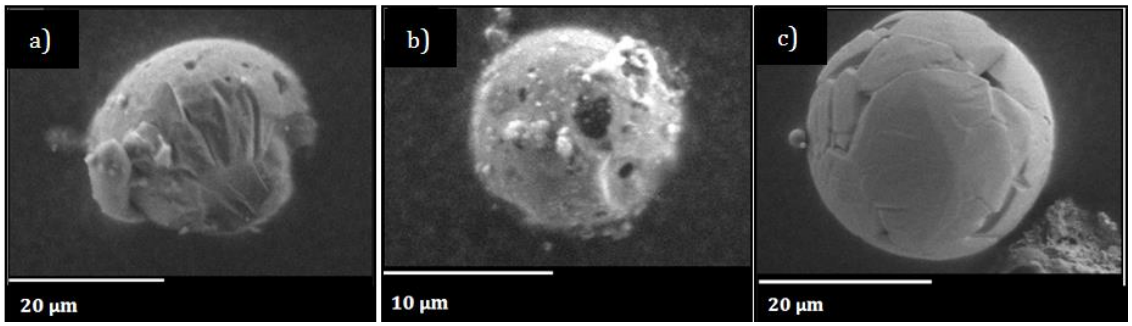

Figure 6.18: *SEM images of post-blast particles found on stubs retrieved from 4 m and 5 m from the charge centre of RDX composition firings. Particle sizes ranged between 5 µm and 40 µm.*

The elemental compositions of the particles displayed are seen in table 6.8. Whilst the averaged atomic percentages of elements varied to that of the pre-blast material, the intensity of the carbon and oxygen signals were comparable to those of particles detected 1 m to 3 m from the detonations (the carbon being approximately double than that detected in the pre-blast material). The nitrogen intensities were lower than those detected in the particles recovered at 2 m and 3 m (cf. table 6.7) and similar to nitrogen quantities detected in some of the particles found at 1 m (cf. table 6.6). The provenance of the aluminium from particle b in figure 6.18 was unknown.

Particle (fig. 6.18)	C (%)	N (%)	O (%)	Al (%)
a	70.4	2.10	27.5	0.00
b	55.4	4.40	39.1	1.10
c	62.0	0.60	37.4	0.00
Average	**62.6 ± 7.5**	**2.37 ± 1.9**	**34.7 ± 6.3**	**0.367 ± 0.6**
Pre blast	**33.0**	**30.6**	**36.4**	**0**

Table 6.8: *Atomic % of elements detected from EDS analysis of particles a–f in figure 6.18 (3 sf.) recovered 4 m and 5 m from the charge centres of RDX composition firings. The averaged atomic % varied from that of the pre-blast particles.*

Particles observed > 5 m

No particles (of any type) were observed on stubs retrieved further than 5 m, in any orientation, around the detonations of the 0.5 kg, 1 kg and 2 kg RDX based compositions.

6.3.1.3 Post-blast Particles from Confined Firings

The results presented thus far have been based on stubs collected from around unconfined charge detonations. SEM stubs were also positioned around the confined vehicle firings containing ~1 kg of an RDX explosive composition. The particles seen were similar in morphology and size to those from the unconfined firings at 1 m to 3 m; however no particles were detected on any stubs at 4 m or 5 m distances.

6.3.2 Chemical Identity

Pre-blast Particle Identity

A representative Raman spectrum of the RDX-based compositions is shown in figure 6.19 and provides a chemical fingerprint for the detection of RDX in the post-blast residues.

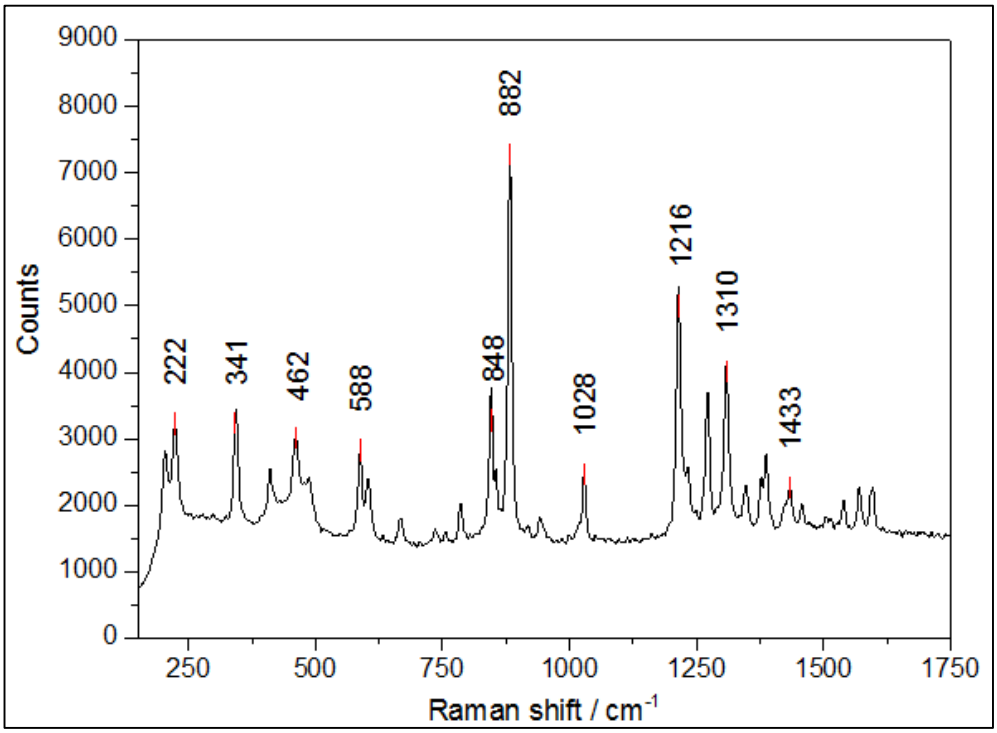

***Figure 6.19**: Raman spectrum of RDX composition (pre-blast). Measured with 785 nm laser at 5 % power, over 5 accumulations of 10 second exposure time.*

Raman shift /cm^{-1}	Feature[187]
882	Symmetric ring-breathing mode ions
~1000	ring stretching and N–O deformation
~1216	CH_2 scissoring and N–N stretch vibration
~1310	CH_2 wagging
~1430	NO_2 symmetric stretching vibration

***Table 6.9**: Chemical features of Raman bands detected from pre-blast RDX composition particles.*

A representative MeV secondary ionisation mass (MeV SIMS) spectrum of the RDX compositions is shown in figure 6.20; the most intense peak at *m/z* 221.8 was consistent with the molecular mass of RDX (~222 Da).

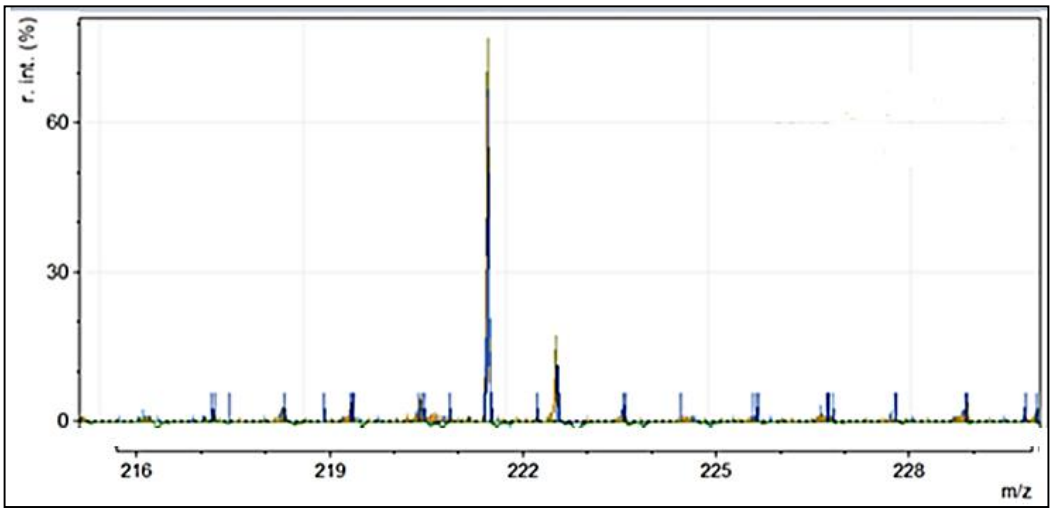

***Figure 6.20**: MeV SIMS spectrum of RDX composition particles; major peak at m/z 221.8 corresponded to molecular mass of RDX.*

Post-blast Particle Identity

Whilst elemental compositions similar to that of the pre-blast material have been used as a diagnostic measure for the presence of explosive residue particles, in order to obtain information regarding the chemical identity of the particles, spectroscopic and spectrometric techniques were employed.

Using the Raman microscope, it was possible to identify post-blast AlAN particles which were observed through the SEM with relative ease; this was not the case for the post-blast RDX particles which due to their smaller size (maximum 100 μm diameter particles were observed) could not be located amongst other particulate matter present on the stub surface. Therefore, Raman spectroscopic analysis was not successful. A scanning electron microscope – structural chemical analyser (SEM-SCA), which provided the resolution of the SEM alongside the capability for compositional analysis via Raman spectroscopy, was also attempted. Particles observed on the stubs were located with the SEM capability and the machine mode then switched to obtain the Raman spectrum. However, no valid spectra (i.e. no Raman signal) was obtained using this technique. Sample degradation due to the heating from the laser (which was set between 0.1 % and 0.5 % power) or misalignment of the laser with the SEM electron beam may have been causes for the non-signal. In order to counter potential heating effects from the laser, analysis was repeated with a cold-stage; however, the results were still inconclusive and no spectra were obtained. The potential misalignment of the laser with the crosshairs was also assessed by obtaining spectra at multiple micron distances around visible particles; nonetheless, no Raman spectra were generated and the analysis was unsuccessful.

Whilst Raman and SEM-SCA were ineffective, the stub surfaces were mapped using PIXE and MeV SIMS techniques; allowing particles of similar shapes and sizes to the ascribed post-blast residues to be recognised on the surfaces (figure 6.21).

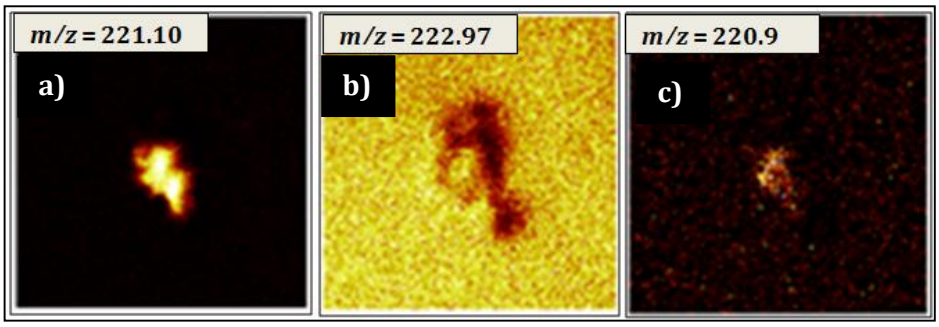

Figure 6.21: *Negative ion image maps of stub surfaces – particles of 10 µm to 100 µm in diameter were identifiable. Analysis with MeV SIMS found ions at m/z 220 to m/z 223 for the presented particles.*

Whilst the exact particles visible through SEM analyses could not be discerned, particles between 10 µm to 100 µm were targeted for further analysis with MeV SIMS. Figure 6.21 shows that the molecular masses of some particles observed with the negative ion image maps (*m/z* ratios inset in figure 6.21) were consistent with the molecular mass of RDX. A mass spectrum representative of that obtained from these types of particles is seen in figure 6.22 (green spectra); peaks related to the molecular signal of RDX (*m/z* 222) were present (orange spectra in figure 6.22); however peaks from the background (blue in figure 6.22) also arose in this range. Compared to the MeV SIMS spectrum of the pre-blast material (cf. figure 6.20) both exhibited intense peaks of *m/z* ~222.

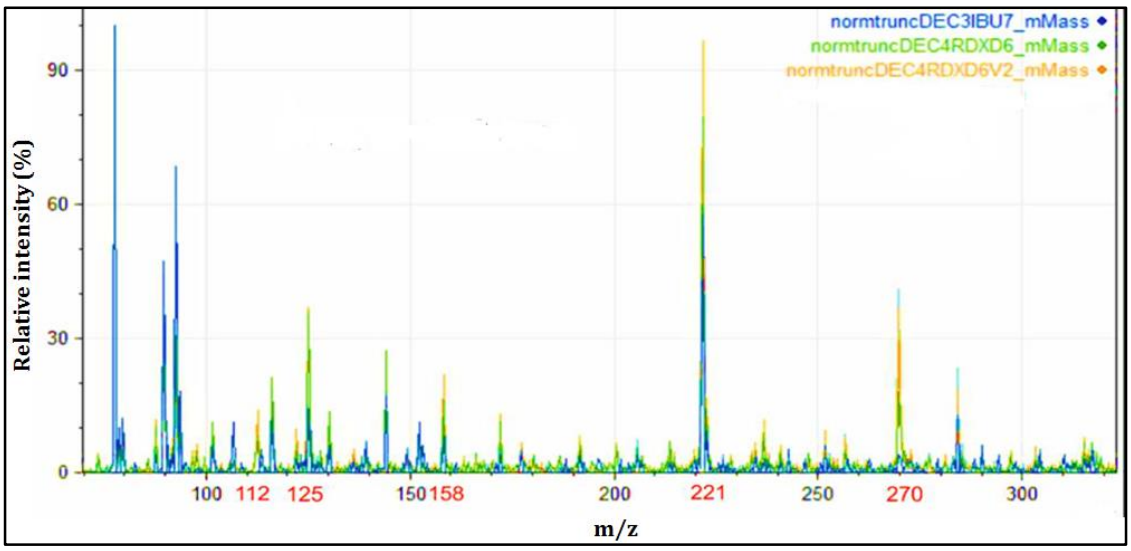

Figure 6.22: *MeV SIMS analysis (negative mode) of particles visible on stubs collected following RDX detonations. The blue spectrum is of the background (stub surface). Green and orange spectra are representative of particles on stubs collected between 1m and 3 m, and further than 3 m, respectively. The labels within the spectra are codes of the sample names and analysis dates.*

Peaks at *m/z* 74 (figure 6.22) had the highest relative intensity and were present across all sampled points of the stub surfaces. The *m/z* 74 peak was attributed to poly-dimethyl-siloxane (PDMS) $(C_2H_6OSi)_n$, a constituent of the double sided adhesive carbon discs which were adhered to the SEM stubs. The presence of the PDMS made spectral analysis more complex via ambient pressure MeV SIMS; attempts to elucidate the chemical identities of particles observed on stubs were therefore inconclusive. The indications of the presence of explosive residue were provided by the detection of a comparable molecular mass from the particles (peak at *m/z* 222) and the absence of intense peaks below *m/z* 100 in the sample; these suggested the presence of RDX, however the veracity of these results to conclusively prove the presence of undetonated particles of RDX was uncertain due to the background signal also generating peaks at *m/z* 222.

6.3.3 RDX Particle Summary

Charge mass variation: Similarly to the AlAN particles, no variation was observed in terms of particle morphology, size or elemental composition between the different RDX composition charge masses (0.5 kg, 1 kg and 2 kg) fired; such that the particles were grouped based on their morphological appearance regardless of the charge mass detonations from which they were collected. The groupings were similar to those from the AlAN particle studies ('1 m', '2 m to 3 m' and '4 m to 5 m'). No particles were observed on any stubs further than 5 m (a shorter range than the 7 m of the AlAN particles). The 5 m range corresponded well with the 4 m and 10 m radii within which residues were detected from the 0.5 kg and larger charge masses fired in chapters 4 and 5.

Shapes: The pre-blast material appeared as agglomerated particles clumped together due to the binder in the RDX compositions. The post-blast particles did not resemble the pre-blast composition; no clumped particles were observed and the majority of individual particles were smooth edged shards with folded and curved morphologies. This was the case for particles found on stubs 1 m to 3 m from the detonations with very few spherical particles found within these distances. At 4 m and 5 m however these particles were not found, only spheroidal particles were detected. The RDX residue morphology differed greatly to that of the AlAN post-blast particles; no agglomerated residues or flattened residue deposits were observed following the organic firings.

Sizes: The size range of individual particles in the pre-blast compositions was estimated to be 10 μm to 250 μm. At 1 m the size range of individual particles was 10 μm to 70 μm, at 2 m to 3 m particles were on average 20 μm to 100 μm in diameter. Individual particles at 4

m to 5 m were between 5 μm to 40 μm. The RDX particles were consistently smaller than the AlAN post-blast particles at each of the grouped distances.

Chemical analysis: The N:O ratio in the pre-blast material was consistent with the theoretical ratio (1:1), the atomic percentage of carbon was higher; due to either the binder or carbon disc on the stub. The elemental composition of the post-blast particles was the same as the pre-blast material; however the ratios between elements were inconsistent. The nitrogen signals were weaker at 1 m than at 2 m to 3 m (the particles at 2 m to 3 m were larger and hence may have generated a stronger N signal). At 4 m and 5 m the atomic percentages of N in particles were similar to those at 1 m (the size range of particles were also similar; 10 μm to 70 μm at 1 m and 5 μm to 40 μm at 4 m and 5 m). It was not possible to conclusively identify the particles ascribed to be post-blast residue as definitely related to the explosive charge; the only indication of which was from the generation of similar *m/z* values between the particles and RDX (~222 Da).

Quantification of particles: It was not possible to count the number of particles on each stub surface and therefore generative a quantitative measurement of particle distribution as a function of distance from the charge centre. As the particle deposition was not homogeneous across the stub surfaces, estimates of particle counts based on smaller areas would have been inaccurate. Qualitatively, more particles were observed on stubs which were closer to the detonations than those further away and no bias was seen in the amount of particulate material observed on stubs from different orientations around the charge centres. This finding did not concur with the RDX residue distribution patterns (which fluctuated with distance) found in chapters 4 and 5. Overall fewer particles were observed following the RDX composition detonations than from corresponding stubs collected following the AlAN firings.

6.4 Simulation Studies

The simulation experiment results presented here were based on computations which modelled the distribution of particulate post-blast residues from a 0.5 kg spherical explosive charge detonation (full methodological details can be found in chapter 3, section 3.6). The simulations assessed particle distribution at both the height of the explosive charge (2 m from the ground) and lower down at the ground level. Two different heights were chosen as experimental studies (in chapter 5) indicated variations occurring due to the residue sampling height. The movement of the residues during the simulations was predominantly determined by the surrounding wind field (velocity and direction), as

experimental findings (in chapters 4 and 5) indicated the wind to be a dominant influential factor in the residue dispersal mechanism.

Physical aspects of the particles to be simulated were partially determined by the results of the particle studies presented above in this chapter. The sizes of particles detected through the experimental studies varied, therefore the distribution of representative particles (of 10 μm, 50 μm, 100 μm and 200 μm in diameter; and therefore similar to particle sizes seen from the experiments) were simulated. As the shape of the post-blast particles observed through experiments also varied widely, a spherical form was simulated in these preliminary experiments. The density of the post-blast AlAN and RDX compositions found on SEM stubs was unknown; in order to model particle movement the density of the simulated particles was assumed to be as water (~998 kg/m^3) for simplicity. The initial position of the simulated post-blast particles was a spherical shell on the surface of the charge (synonymous to the theory that the residues survive from the charge surfaces as well as for reasons of simplicity).

In order to compare the simulation results to corresponding experimental data, experiments with 0.5 kg AlAN charges were conducted; AlAN was chosen as it was found to produce more undetonated residues than the organic charges (chapter 4 and 5 results). Residue samples and stubs were collected from 2 m high sampling sites (as done so in chapter 4) but also from plates positioned at ground level at every sampling pole. Estimates of particles counts on stubs were made in order to compare the results to the numerical simulation data generated. A series of sampling poles were also positioned in line with the wind direction (the sampling pole layout is detailed in chapter 3, section 3.2.2) and the wind velocity and direction at the time of firing (NW, ~2.8 m/s) were inputted into the simulation experiments.

The simulation outputs were a visual sequence of particle movement (to be compared to the HSI footage of detonations) and simulated particle plots of the number of different sized particles distributed around the detonations (to be compared to estimated particle counts from the SEM stubs and residue depositions on larger plates around the charges).

6.4.1 Imaging Comparisons

The HSI recordings of the 0.5 kg AlAN charges were qualitatively compared with the simulated detonation videos between t = 0.3 ms to t = 2900 ms (figure 6.23).

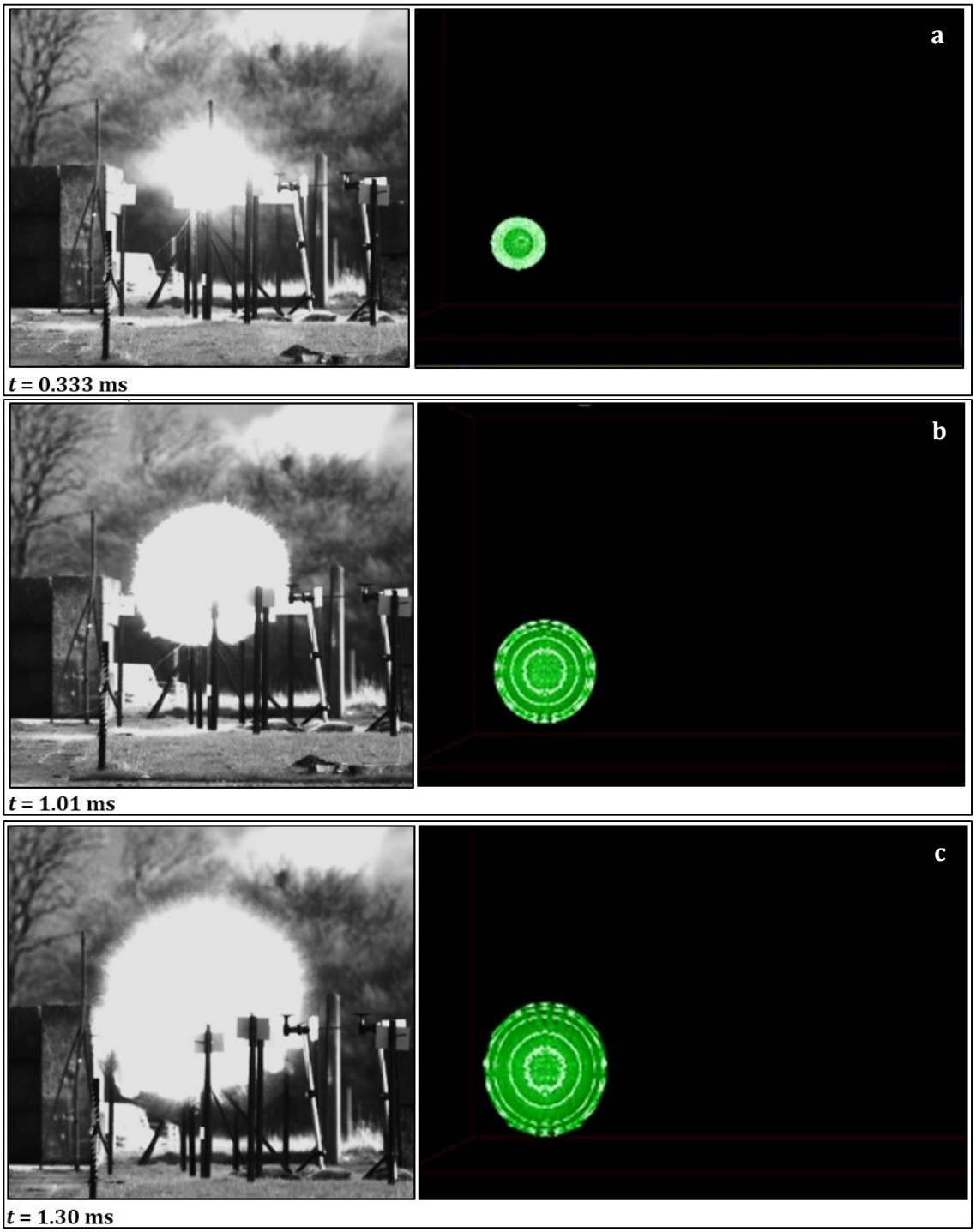

***Figure 6.23**: High speed imaging stills vs. simulated detonation at t = 0.333 ms (a), 1.01 ms (b) and 1.30 ms (c).*

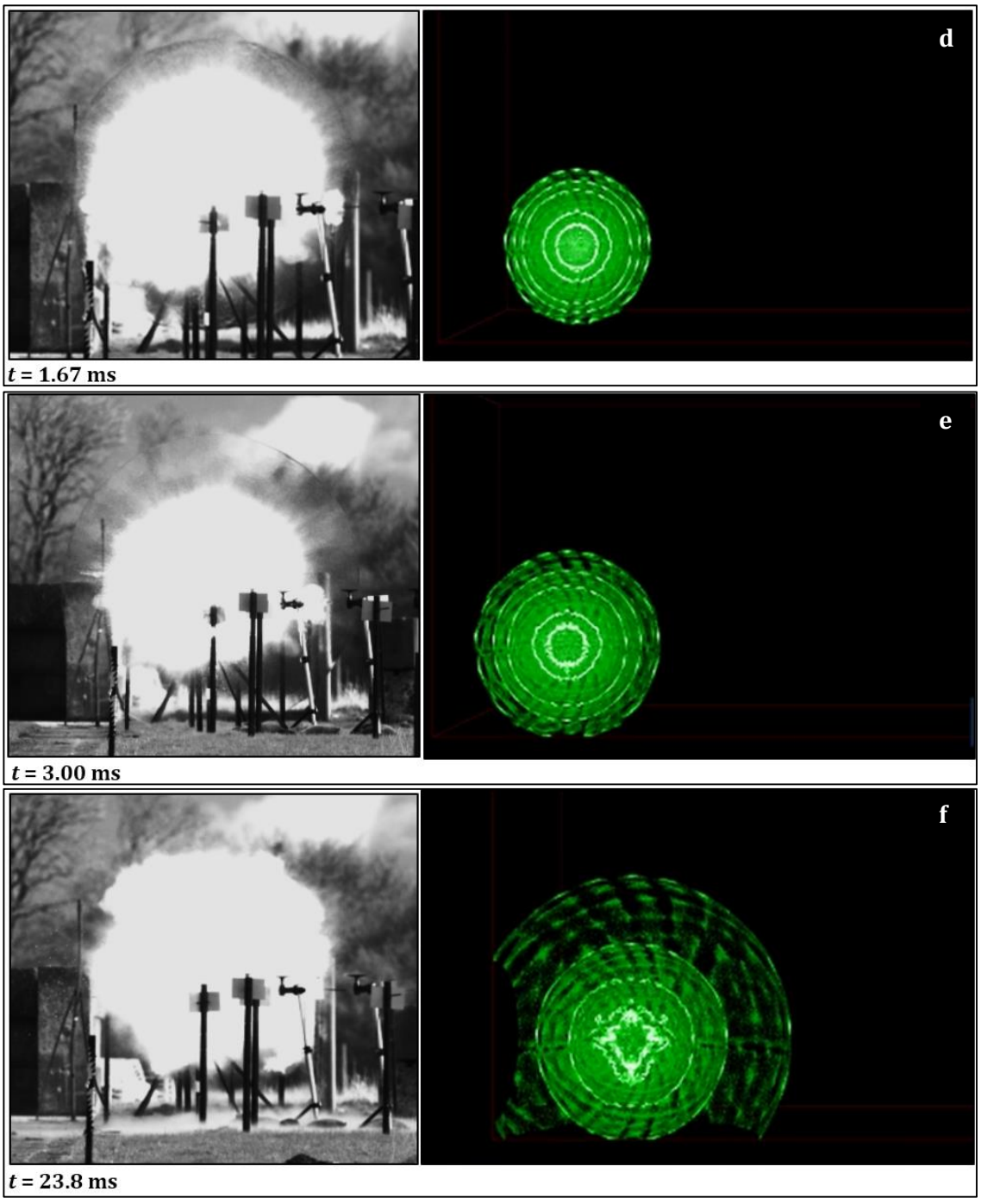

***Figure 6.23 cont'd**: HSI stills vs. simulated detonation at t = 1.67 ms (d), 3.00 ms (e) and 23.8 ms (f).*

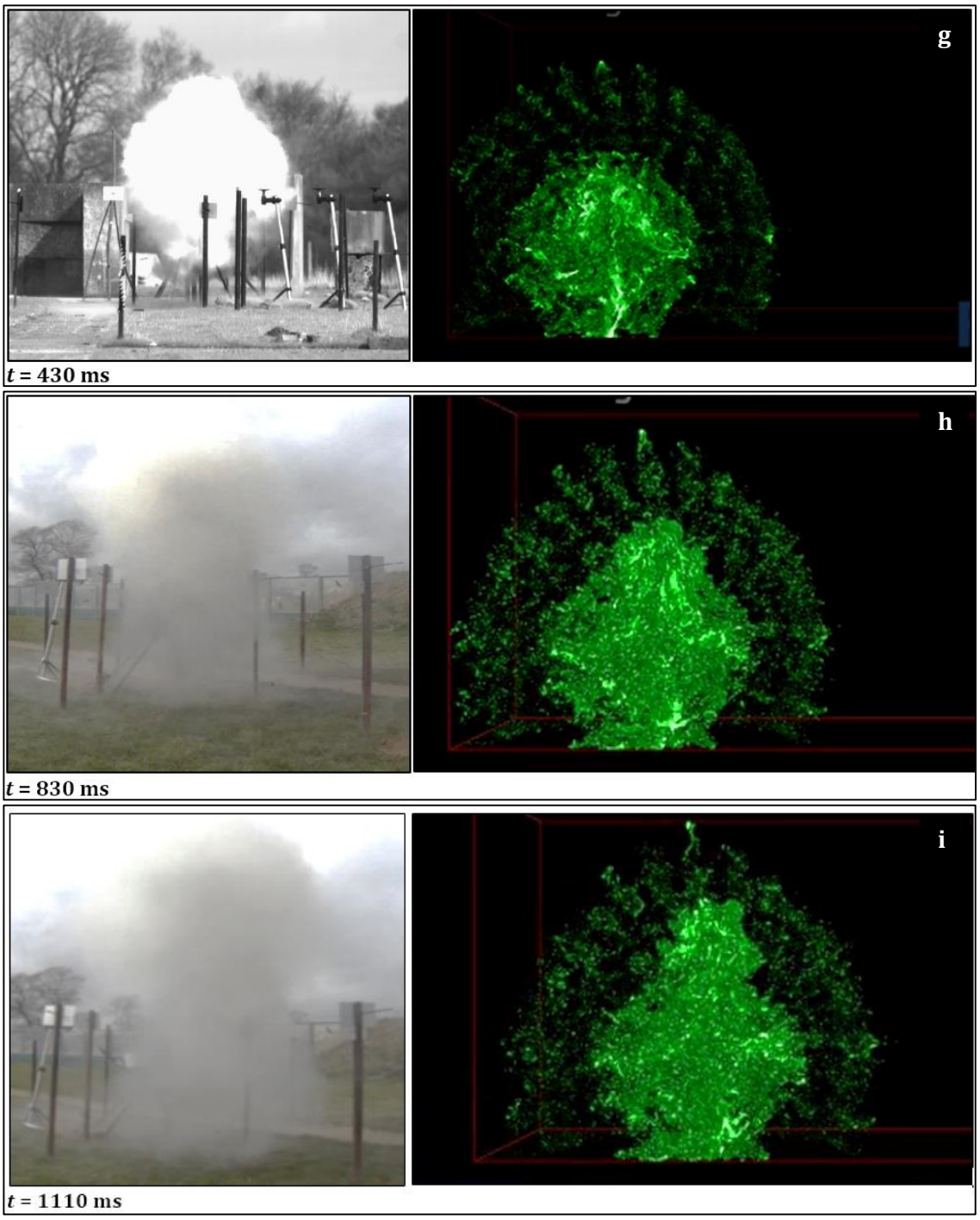

***Figure 6.23 cont'd**: HSI and GoPro footage stills vs. simulated detonation at t = 430 ms (g), 830 ms (h) and 1101 ms (i). (GoPRo footage was used in the comparisons at later stages as the HSI was not recorded up to those later time frames.*

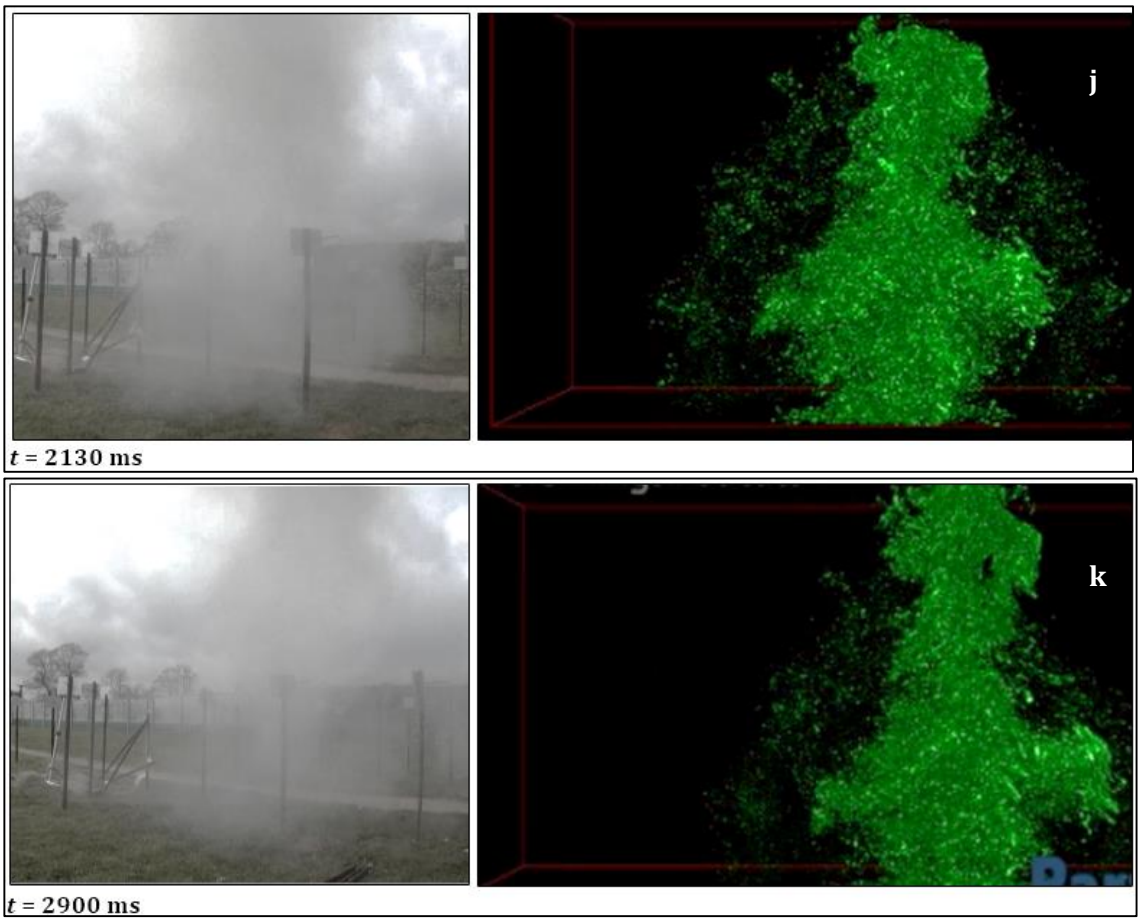

***Figure 6.23 cont'd**: GoPro footage stills vs. simulated detonation at t = 2130 ms (j) and 2900 ms (k). The frames between the two techniques correspond well with each other showing smoke and particle movement in line with the wind direction*

The simulated particle distribution during detonation corresponded well to the HSI stills of a 0.5 kg AlAN firing at each of the time frames; as the experimental conditions (charge mass, shape, position, wind velocity and direction) were inputted directly into the simulation, the correlation between the two imaging methods was reasonable. Frames a – f (t = 0.333 ms to 23.8 ms) reflected step 1 of the simulation where the initial detonation phase occurred and no wind effects were included. Frames g – k (t = 430 ms to 2900 ms) showed the second phase of the detonation (including wind effects) and was compared to HSI and GoPro footage stills. The smoke plume (seen in the left of figure 6.23 h – k) moved in line with the wind direction during firings (towards the north-west) as did the simulated particles (seen on the right of frames in figure 6.23 h – k).

Qualitatively, the movement of particles was agreeable between simulated and actual firings. A comparison between the numerical data generated from the experiments and simulations was then assessed.

6.4.2 Residue Distribution Trends

Residue sampling plates were positioned at the charge height (2 m high) and at the ground level in six orientations around the detonation centre; these were the compass points used in previous experiments (N, E, S and W) and also in the NW and SW directions as the wind moved in these orientations near the time of firing (predominantly moving in the NW orientation). The summed ammonium and nitrate quantities from the ground level and charge height distributions are presented in figures 6.24 and 6.25, respectively.

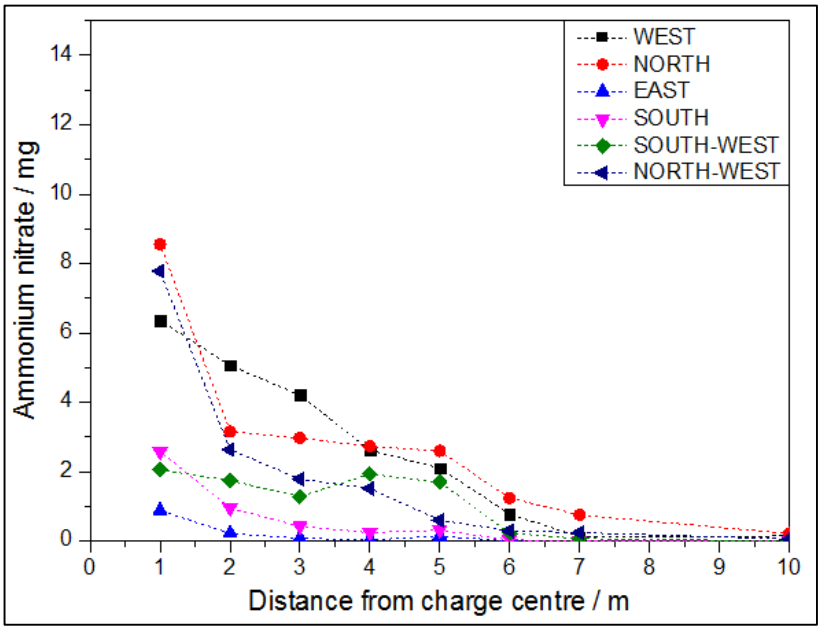

***Figure 6.24**: Ground level distributions of ammonium nitrate residues collected from sampling plates around 0.5 kg firing of AlAN*

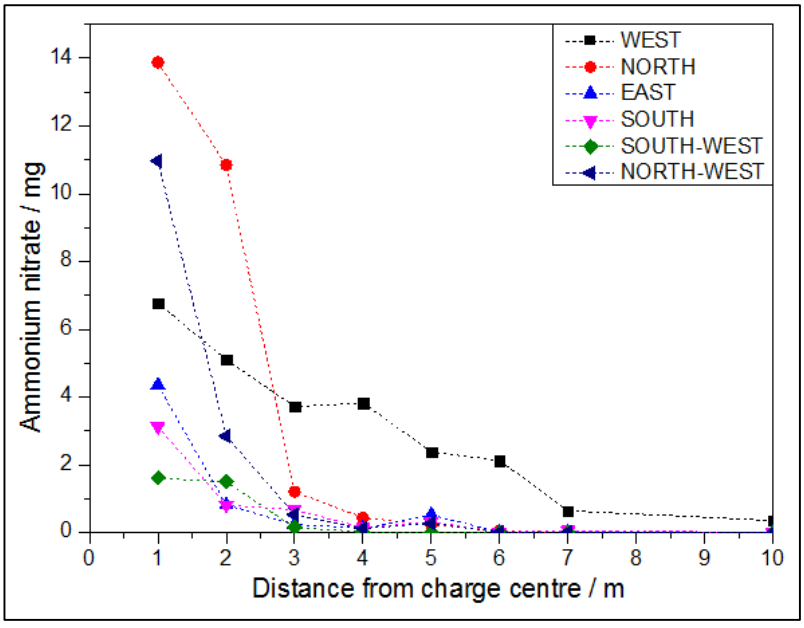

***Figure 6.25**: At charge height (2 m high) distributions of ammonium nitrate residues collected from sampling plates around 0.5 kg firing of AlAN*

Overall, more residue was recovered from sampling sites 2 m from the ground as opposed to at ground level, and from orientations which were in line with the wind direction. The distribution trend of decreasing ammonium and nitrate amounts with increasing distance from the centre was consistent with that seen from previous 0.5 kg firings of AlAN (chapter 4), as was the mass range of the detected analytes. The simulations could only generate data regarding the number of different sized particles at different points and therefore residue mass data could not be compared effectively. If the number of particles equating to an amount in mass (i.e. 1 mg) was known, it may have been possible to semi-quantitatively compare the two data sets, however this was not the case; furthermore as the residue recovery rate was not 100 % efficient it would be relative amounts which could be compared. It was not possible to count the number of particles upon every stub surface collected from the previous AlAN and RDX composition particle studies (sections 6.2 and 6.3 of this chapter), however, given that the simulation experiments produced particle count data, the particles upon the SEM stubs (which were morphologically and chemically similar to those found during the AlAN particle studies in section 6.2) were counted by systematically scanning the stubs collected following the detonations used for the simulation comparisons (this was only feasible for one set of stubs (48) collected following one firing.

6.4.3 Particle Counts: Experiment vs. Simulation

The number and sizes (diameter) of particles was recorded for each scanned stub surface. The relative deposition (in log-scale), for the different particle sizes counted on stubs (in size grouping of '< 49 μm', '50 μm to 99 μm', '100 μm to 149 μm' and '150 μm to > 200 μm') collected from the ground level were compared to the simulated particle distribution plots (also in log-scale) in figures 6.26 and 6.27 respectively. The detonation centre of each plot was at the co-ordinates 0, 0.

The experimental results showed that smaller particles (< 100 μm) were generally more concentrated on the ground in the central detonation region, whereas those which were larger (> 100 μm) distributed to further sampling sites on the ground (figure 6.26). This coincided with the simulated particle plots which clearly showed larger particles distributed to further distances than smaller ones (figure 6.27).

From the 2 m high sampling experiments, more particles were found on all stubs compared to respective ground positioned stubs, similarly to the particle distribution on the ground, larger particles moved further from the detonation than smaller ones which were concentrated near the detonation. The particle distribution bias with the wind direction was more obvious with the samples collected from 2 m high than those at ground level (figure

6.28). The experimental results corresponded well with the simulated data which also showed the same trend with particle distribution (figure 6.29).

Simulated number of particles to start with were ~2 million (the number of residue particles to be dispersed during real experiments is unknown so a comparison on quantities between the two methods would not be useful).

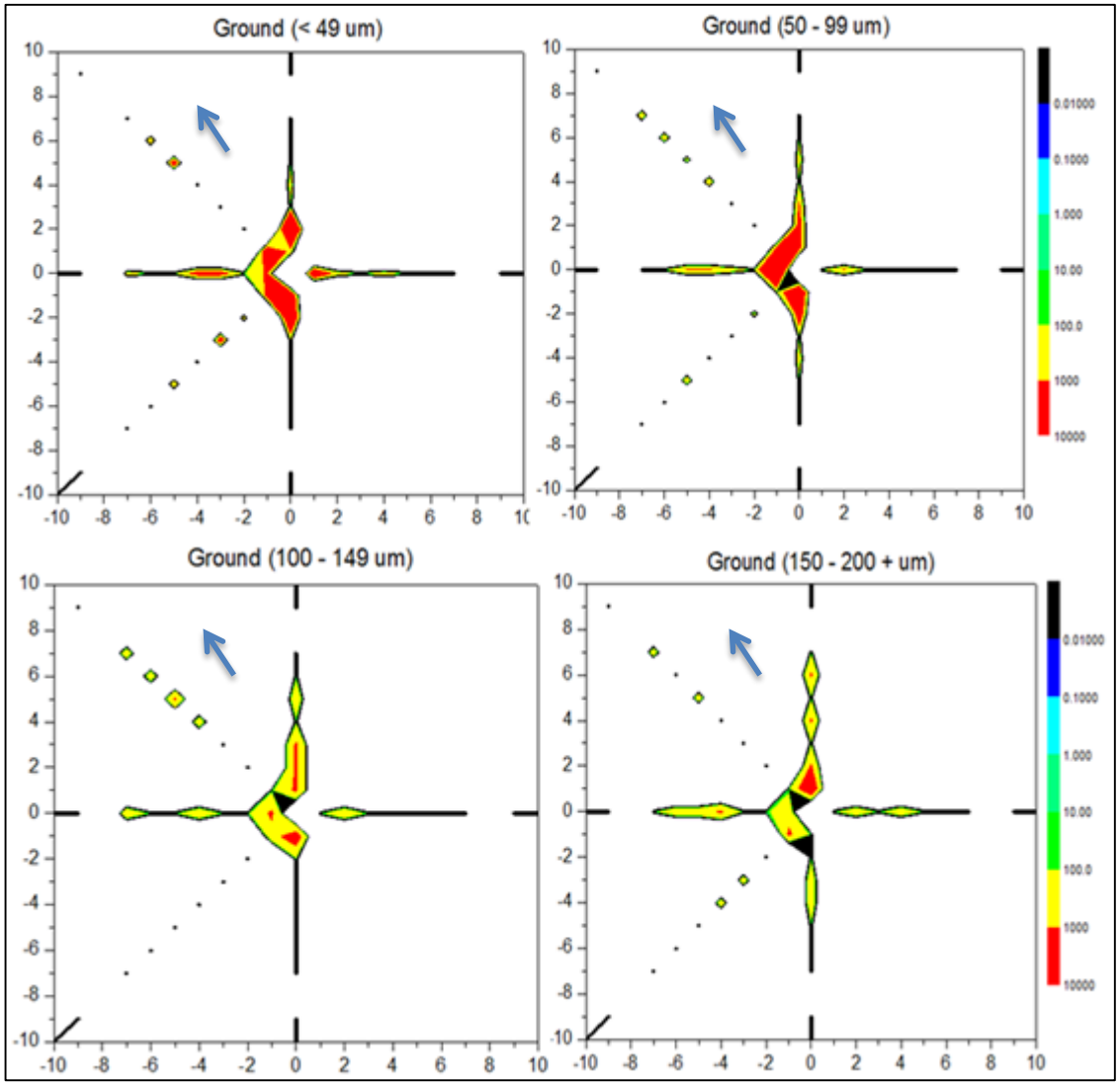

***Figure 6.26**: Experimental results – contour plots of particle counts (log-scale) from ground level positioned stubs around the detonation centre of 0.5 kg AlAN charge. (0, 0 is the detonation centre). Smaller particles were more concentrated near the detonation centre than larger ones. The data points are clearly limited to those which could be measured experimentally. The blue arrows indicate the wind direction (NW) at the time of firing.*

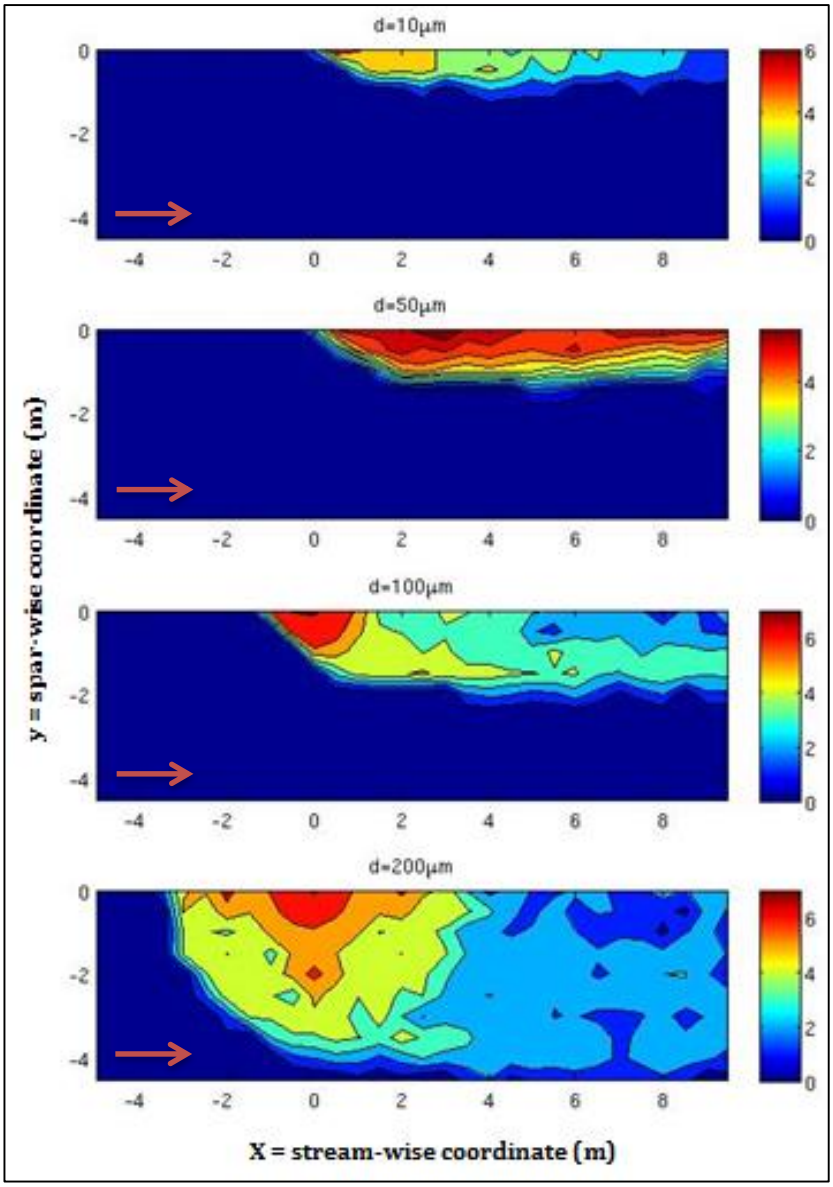

***Figure 6.27**: Contour plots of the number of particles (log-scale) passing through plates on the ground at different positions. d = particle diameter. The origin of the explosion is at (0,0) and x is in the stream-wise (wind) direction. The numbers on the colour-bars are the exponent (e^x) of the data. The plots are a section of the detonation area which covers the wind direction; the point at (8,0) is towards north. The red arrows indicate simulated wind direction (N/NW).*

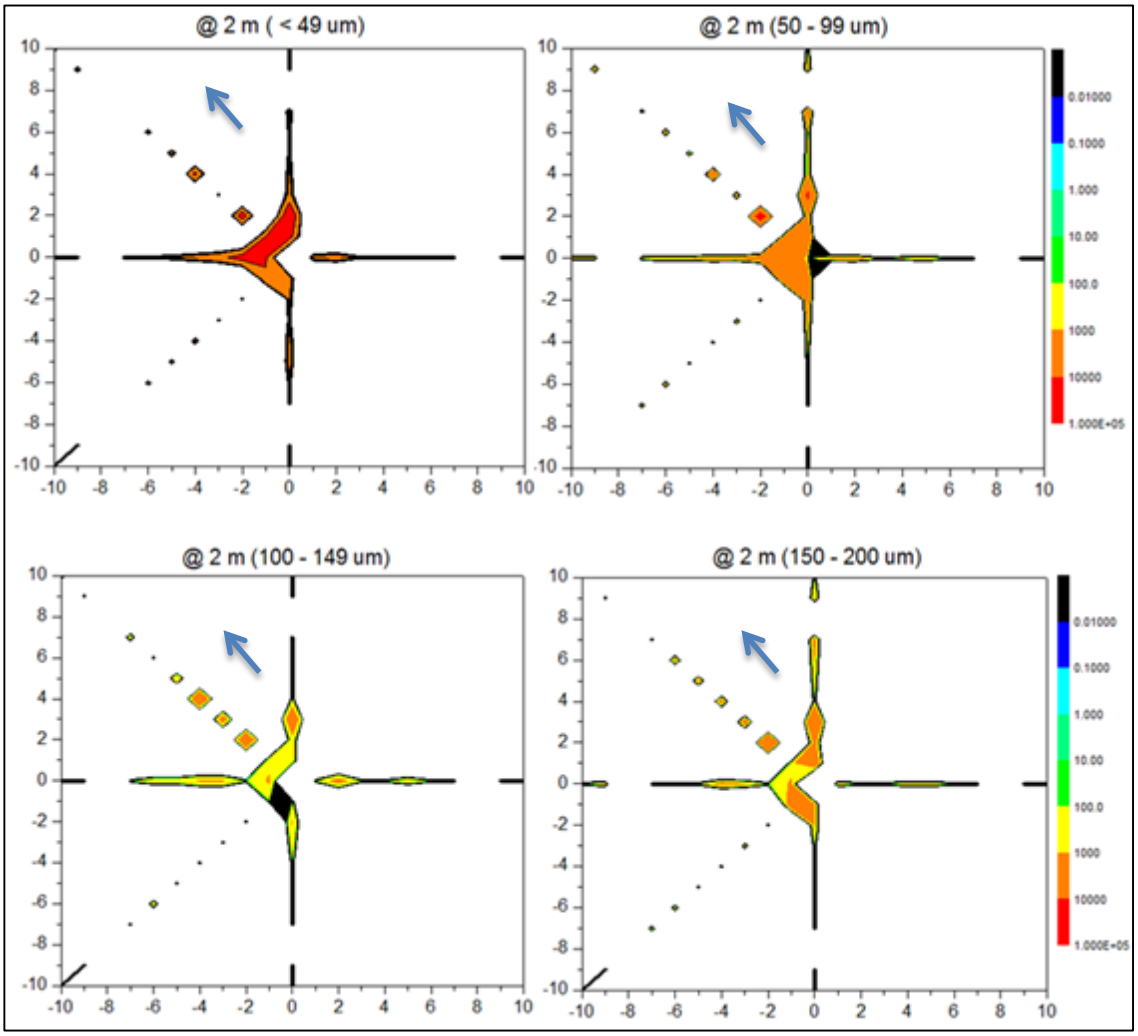

Figure 6.28: *Experimental results – contour plots of particle counts (log-scale) from 2 m high positioned stubs around the detonation centre of 0.5 kg AlAN charge. (0, 0 is the detonation centre). Smaller particles were more concentrated near the detonation centre than larger ones which moved further from it. Distribution biases with wind direction were more apparent for the 2 m high sampled particles than those on the ground. The blue arrows indicate the wind direction (NW) at the time of firing.*

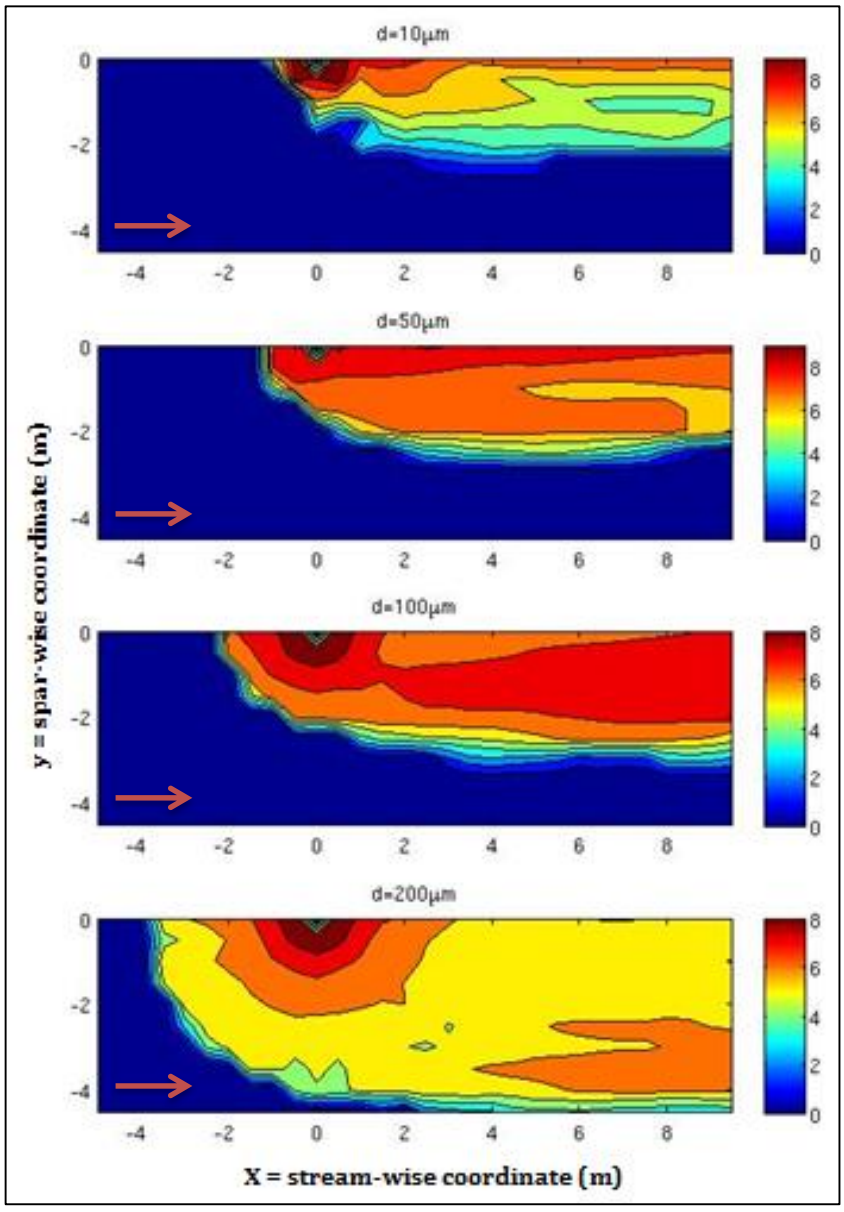

Figure 6.29*: Contour plots of the number of particles (log-scale) passing through plates 2 m from the ground at different positions. d = particle diameter. The origin of the explosion is at (0,0) and x is in the stream-wise (wind) direction. The numbers on the colour-bars are the exponent (e^x) of the data. The plots are a section of the detonation area which covers the wind direction; the point at (8,0) is towards north. The red arrows indicate simulated wind direction (N/NW).*

6.4.4 Simulation Summary

Imaging comparisons: The imaging of the 0.5 kg detonation compared well qualitatively between the simulation and high-speed imaging techniques used. Each simulated detonation time frame corresponded well with what was observed experimentally and both showed the movement of particles in-line with the wind direction.

Residue concentration comparisons: The simulations could not generate residue mass data and therefore residue amounts (in mg) were not comparable to the simulated particle distributions. If it was assumed that the residue amounts were proportional to the number of particles, the trends between the two, i.e. decreasing residue mass and decreasing number of particles observed as a function of increasing distance from the centre, were comparable.

Particle count comparisons: Experimental and numerical trends were similar for the distributions on the ground at the charge height of 2 m. Smaller particles in both cases were concentrated closer to the detonation centres whereas larger particles were more widespread; this was the case for both the ground level sampling sites and those at 2 m high. The amount of particulate material deposited at 2 m was greater than that on the ground (in both the experimental and simulated cases); furthermore the 2 m high distributions were biased with the wind direction more noticeably than the ground level distributions. Simulations were clearly capable of sampling at numerous points; much more so than only the discrete sampling possible in reality, demonstrated by the relatively sparse contour plots of particle distribution generated experimentally. However, only one segment (one half) of the detonation area could be produced as an output within the time-frame of this project, as the simulation run times and costs were great.

6.5 Discussion

Differences in particles based on charge mass fired

In chapters 4 and 5, higher residue concentrations were detected from the 2 kg charges than 1 kg charges, which in turn produced higher concentrations than the 0.5 kg charges. Qualitatively, the observed number of particles on stubs collected from firings did not exhibit the same trend. No variation in morphology, size or elemental composition of particles was observed on stubs collected from the same distances and orientations fired from different charge masses (0.5 kg, 1 kg and 2 kg) of both the AlAN and RDX compositions. Similar particles were also observed at different distance for both explosives (at 1 m, 2 m to 3 m and 4 m to 7 m for AlAN particles and at 1 m, 2 m to 3 m and 4 m to 5 m for RDX particles). The apparent similarities observed between the particles detected following different charge mass detonations may be due to the small sample size collected for analysis; had it been possible to collect sample for particulate analysis at many more additional points, discrepancies between different charge masses may have been noticeable, or conversely, the similarity between the particles found from different charge mass firings may be confirmed. Furthermore, no inconsistencies were observed between the particles collected from the unconfined and confined RDX composition firings; smaller

residue particles have been found following the firing of confined pyrotechnic compositions[54] however this was not the case for the confined explosive particles.

Radii within which particles were found

No particles were observed on any stubs further than 7 m from the inorganic firings or 5 m from the organic firings, demonstrating that the presence of particles was due to the detonation and not just ambient conditions. The smaller radius from the organic firings corresponded with the smaller radii (4 m and 10 m from 0.5 kg and larger charge masses respectively) within which explosive residues were detected from the swabbed sampling plates surrounding the detonations (chapters 4 and 5). Additionally, a previous study also found the majority of visible post-blast organic residue particles within 5 m from the charge detonations with little or no material further from 5 m[68]. This finding supports the concept of organic residues detection limits being closer to the detonation than inorganic residues which move further from it.

The variation in detection radii between the explosive types may be due to the amount of residue produced from each explosive detonation; the lower VOD AlAN charges have been shown to produce higher quantities of post-blast residue, which may subsequently have a more widespread distribution, as opposed to the fewer residues found to be produced from the organic charges. The particle detection radii found here complement the swabbed residue studies in previous chapters and perpetuate the concept that the 60 m limiting radius[57,70] within which residues may be found is too large for smaller charge masses. Forensic sampling procedures of such smaller charge masses should be focused within 10 m from the detonation centres.

Post-blast particle morphology

The post-blast residue particles found following the different explosive type detonations varied in their morphology; the AlAN particles sometimes resembled the undetonated material (having agglomerated structures) and the majority of particles were smooth surfaced and spheroidal. In contrast, the post-blast particles from the RDX compositions did not resemble the pre-blast material and were predominantly smooth-edged, shard like particles with folded and curved features. No other published study has commented on such morphological variations based on explosive type; the implications of which on post-blast forensic investigation are considerable, particularly if microscopic examination of material can provide initial explosive identification.

The reason why different explosive types produced post-blast particles of varying morphology is unknown; the cause may be related to the mechanism by which the residues are formed and if this is the case, this suggests that explosive residue formation may not be

governed by one theory but vary based on the explosive type; thus reiterating the conclusions from the previous chapters. The post-blast AlAN particles may have retained their agglomerated, pre-blast material like structure if they had been spalled from the charge surface and moved away from the detonation prior to being affected by higher reaction temperatures. In contrast, the organic residues may not be spalled from the charge surface but exist for an unknown reason during the reactions within which time they are affected somewhat by the reaction temperatures (potentially why they have such different morphology from the pre-blast material) but not to the extent where the particles decompose into product gases.

The particle morphologies also varied with distance from each material. Flattened deposits of AlAN were also observed at 1 m to 3 m. The particle features were synonymous to molten material which had impacted on a surface (at 1 m; figure 6.6) and then cooled through the air to deposit as a partially solidified mound of particles (2 m to 3 m deposits; figure 6.8). If the residues move through the air as molten material, they would have been heated (potentially by the fireball or the shockwave[60,68]) either prior to or after ejection from the charge. The initial melting and/or vaporisation of residue particles and their subsequent solidification during dispersion has been reiterated elsewhere[115,116]. Alternatively, the material may have deposited as a solid material impacting the sampling surface at high velocity; which would suggest that not all particles ejected from the charge moved with the same velocity (as not all deposits observed at 1 m to 3 m were flattened), thus contradicting theories which state they do[57].

Further than 4 m from the detonations, the AlAN residues were clusters of individual particles, whereas the RDX residues were spheroidal particles which had not been seen closer to the centre; spherical particles following RDX composition firings have also been found elsewhere[84], but the distance at which they were found was not commented on. The finding of clustered inorganic particles and spherical RDX particles further corroborates the notion that the formation mechanism of post-blast residues from different explosive types is dissimilar. Organic material moving in molten form (which for an unknown reason had not decomposed during the reactions) would solidify upon cooling and be deposited as spherical or spheroidal particles at greater distances[81]. The higher mass, larger or clumped inorganic particles spalled from a charge surface would move with higher kinetic energies to further distances[68], while smaller inorganic particles spalled from a charge surface would be moving with high velocity (potentially accelerated by the shockwave[68]) and appear as flattened deposits closer to the centre upon impact with a sampling surface (seemingly appearing as due to molten residue deposition). No particles suggested the finding of higher

concentrations of aluminium further from the detonation, as was the case for the aluminium analyte residue distributions (cf. chapter 4).

Post-blast particle sizes

The size of post-blast AlAN particles was consistently larger at each of the sampled distances compared to the organic residue particles (table 6.10), the finding of which was reasonable as the average particle size of the pre-blast inorganic material was larger (30 μm to 1300 μm) than the organic material (10 μm to 250 μm).

Distance	AlAN particle size range	Distance	RDX particle size range
Pre-blast	30 μm to 1300 μm	Pre-blast	10 μm to 250 μm
1 m	Individual: 30 μm to 120 μm Flattened: >300 μm	1 m	10 μm to 70 μm
2 m to 3 m	Individual: 30 μm to 210 μm Flattened: ~1000 μm	2 m to 3 m	20 μm to 100 μm
4 m to 7 m	Individual: 10 μm to 150 μm Flattened: ~500 μm	4 m to 5 m	5 μm to 40 μm

Table 6.10*: Particle sizes of post-blast residues detected at different distances from detonations of AlAN and RDX compositions.*

Finding larger particles of inorganic residues correlates with the finding of greater inorganic residue amounts from the swabbed sampling plates (chapters 4 and 5) compared to the organic charges. The size of post-blast particulate material from high order detonations is not specified in the literature, these original results would enhance post-blast forensic practice; the finding of particular sized particles, coupled with their morphology, may indicate the explosive type used in a bombing incident.

Post-blast particle chemical identity

The inorganic and organic post-blast particles contained the same elemental compositions as their respective original explosive charges. The atomic percentage ratios of the elements detected with EDS analysis however were inconsistent to the pre-blast material and in the majority of cases the ratios were also inconsistent between individual particles for both explosive types. EDS is only a semi-quantitative technique if used without standards[188], additionally, the presence of carbon in the adhesive discs would have skewed the elemental ratios generated in both the inorganic and organic particles; convolution of the nitrogen and carbon peaks in the spectra may have produced unresolved signals which affected the intensity of the nitrogen peak and the elemental ratios. Therefore elemental composition was only indicative of post-blast residue.

The observed inorganic particles were confirmed as undetonated post-blast AlAN residues via Raman spectroscopy; the spectra of the post-blast particles being consistent with the characteristic chemical fingerprint of the undetonated material. Larger particles (detected 4 m to 7 m from the detonations) produced greater signals for each characteristic Raman

band than the smaller particles observed, from which the signal intensity was so much lower, not all characteristic bands were clearly apparent (figure 6.13). No other published study which has assessed the chemical signature of post-blast AlAN residues was found for comparison. The results here have determined that the particles seen on stubs give the chemical signature of undetonated material (i.e. the provenance of the cation and anion peaks in the ion chromatograms of inorganic residues are the spheroidal post-blast particles found here).

However, specific particles observed through the SEM could not be found for Raman analysis due to the lower resolution of the microscope. It is unlikely that the spectra were obtained from other particles which may have been upon the stub as targeted particles had the same sizes and shapes as post-blast particles seen via SEM. Similarly, it was not possible to identify the exact post-blast organic particles seen from SEM analysis to focus further analysis on. Whilst attempts with Raman spectroscopy did not work, PIXE and MeV SIMS mapping techniques allowed similar shaped and sized particles to be found for targeting mass spectrometric analysis on, the results of which suggested the presence of molecules with the molecular weight of ~222 Da (that of RDX) (figures 6.21 and 6.22). However, the background spectrum of the stub surface also produced peaks in this *m/z* region; the rheological properties of the adhesive on the stub surface may have caused it to coat the particles deposited upon it; thus potentially obscuring the RDX signal and preventing the definitive verification of the undetonated material.

The only other study to comment on the appearance of post-blast RDX residues stated them to be spherical[84], but no other morphological details or chemical information ascertaining their chemical identity was provided. The results presented here are therefore the most substantial indication of the provenance of the chromatographic peaks produced via HPLC for example, which demonstrate the presence of undetonated RDX. In order to verify the findings it would be necessary to apply an analytical tool capable of elucidating structural information about the particles.

Quantification of particles

More particles were observed on stubs collected following the AlAN firings than those following the RDX composition firings, reflecting the concept that more residues are produced from lower VOD (AN) charges compared to higher VOD (RDX) ones[7,57]. Qualitatively, fewer particles were observed on stubs which were further from the centre following the detonations of both explosive types. For the AlAN firings, this trend was similar to that of the decreasing ammonium and nitrate concentrations found from swabbed sampling plates around the detonations in chapters 4 and 5. Conversely, no inorganic particles were found to have higher aluminium content with increasing distance from the

detonation centre, as was found for the aluminium analyte distributions from the swabbed sample sites in chapter 4. This finding of fewer organic post-blast particles further from the detonation did not concur with the RDX residue distribution patterns from chapters 4 and 5 (which fluctuated with distance), however as the particle counts were based on small (~1 cm^2) SEM stubs a direct comparison between the trends would be unbalanced.

The vast number of particles on some stubs (particularly those at 1 m following the inorganic firings) made it impossible to count all particles on every stub and to do so would require particle counting software such as that available for gunshot residue (GSR) particles[189]. Such software cannot yet be applied to particles consisting of light elements and has been developed to work only for the accurate quantification of gun ammunition residues. Without counting the number of particles observed on stubs, qualitative assessments did not indicate that the number of particles was skewed with the wind direction at the time of firing. No other published literature which has quantified post-blast explosive residue particles (as opposed to concentrations) at different distances around detonations was found for comparison. However, in order to directly compare with the simulation experiment results, particles on stubs collected following some firings were counted.

Simulation vs. experiment

The simulations represented the movement of particles in the same way as that observed experimentally (figure 6.23), indicating reliability in the simulation data generated. Both the experimental and simulation experiments also found more particles deposited 2 m from the ground than at ground level; thus supporting findings from chapter 5 of higher residue concentrations on sampling plates at the charge height compared to beneath it. The simulation results complemented the experimental findings from AlAN firings of higher quantities of smaller particles nearer the detonation centre and the more widespread distribution of larger particles (figures 6.26–6.29). This finding further demonstrates the capability of simulation techniques to inform residue distribution patterns consistently.

The experimental data showed that particle distribution was biased with the wind direction more-so for the 2 m high samples, the simulated data showed the particle distribution was skewed with wind direction from both sampled heights. No other known study has investigated the comparison between simulation and experiment relating to post-blast particle residue distribution. The attempts made here are subject to limitations; principally, the experimental data set collected was clearly sparse compared to the number of data points generated by simulation. A like-for-like comparison between the two methods (and therefore model validation) would require further experimental data which may not be practically feasible to collect. Additionally the experimental analysis method was subject to

errors; due to the limited resolution of microscopes, any particles less than 10 μm would not have been seen and therefore excluded from quantification. Furthermore human error in counting particles, though systematically, may have generated inaccurate particle counts. Nonetheless, despite experimental limitations, as a first approximation the modelling was capable of predicting similar results.

The heterogeneous nature of post-blast particle deposition has been commented on previously[60], however the method by which the irregularity of dispersed particles was established in that particular study (from 1 m^2 surfaces) was not explained. Here, the particle deposition was not homogeneous across the stub surfaces and therefore estimates of particle counts based on smaller areas of the stubs, which could be used to calculate approximate particle deposition on a 200 mm x 300 mm sampling plate for example, would have been inaccurate. Had the depositions been less random, potentially it would have been possible to approximate the number of particles which may have equated to a concentration value (in mg/L) which would have substantiated the experimental data greatly by allowing comparison between simulated distribution data and experimental residue concentration plots. The assumption of homogeneous particle deposition at 'sampled' points was therefore a limitation of the model.

Further modelling limitations included the cost and time required to generate the data plots – the distribution around only half of the detonation area could be computed within the time frame of this project and ongoing comparisons are required to address the effectiveness of combining computational and experimental techniques. Additionally, the simulation data produced was subject to other uncertainty and inherent errors in the model; one of the principle issues is related to the uncertainty of the initial and boundary conditions of the cells in the computational domain which had to be assumed. In order to understand these conditions better, ideally, the entire wind field surrounding the experimental site would need to be known (not just at the 2 m charge height as was measured), as well as the details of the detonation within the explosives (which is currently not understood). Since this was impossible an approximation of these conditions was needed, therefore the random nature of the wind field and the explosive events were not represented exactly.

Furthermore, the particles used in the simulation did not necessarily have the same density as the explosive residue (which was unknown) and the particle density would have affected the particle flow during simulation; the shape of simulated particles was spherical and as demonstrated by the experimental results this was not always the case. The current comparison may also have been affected by the fact that different materials were used (the simulations used TNT equivalents whereas the experimental charges were AlAN). Also, as the initial amount of residue to be distributed was unknown (and impossible to know) the

amount of particles distributed in the simulation and the experiments could not match. Only relative values of particle deposition can therefore be compared.

Nevertheless, this study has provided a basis upon which further comparisons between CFD simulation techniques and experiments which feature several identical parameters can be developed. These should include methods to estimate the residue particle size distribution and an assessment of the homogeneity assumption used for the calculation of the particle numbers on the plates and a verification of the material models used. In doing so, it may become possible to determine distributions from experimentally untestable explosive charges such as peroxide–based compositions.

Summary

The particle studies have demonstrated the ability to recover post-blast condensed phase explosive residues which are indicative of an explosive type. The findings also support the general results of the residue concentration studies of previous chapters. The combination of computational and experimental techniques applied to assess residue distribution appears encouraging based on both qualitative and quantitative comparisons, and whilst both require further development, the effectiveness of the application of simulation techniques to modelling the distribution of explosive reside has been established. Consequently, it will be possible to develop the combination of experiment and simulation for forensic bomb-scene uses. Experiments should incorporate more sampling points; the wind field should be accurately measured at numerous points around the detonation and the density of the post-blast particles should be investigated experimentally. The models should be refined to include different particle shapes and explosive charges whilst assessing the variation in results as a function of assumed initial and boundary conditions in order to understand the impact of these factors on the generated datasets. By doing so it may be possible to develop a model capable of establishing residue distribution trends from multiple detonation scenarios, which would definitely be a complementary and useful tool for post-blast scene investigation.

CHAPTER 7: SUMMARY AND CONCLUSIONS

7.1 Summary

The aim of this research was to develop the empirical data set regarding the spatial distribution of post-blast explosive residues in order to better inform forensic sampling procedures for residues at post-blast crime scenes. By conducting the following experiments it has been possible to determine the residue distribution trends from AlAN and RDX composition charges.

- **Chapter 4: Detonations of spherical 0.5 kg AlAN and PE4 charges**

The residue distribution trends varied depending on the target analyte being assessed and the inorganic analytes followed the theoretically proposed inverse square law distribution model. AN distributed more regularly than other analytes and exhibited a nonlinear decrease in concentration with increasing distance from the centre. The distribution did not appear to be strongly affected by the fireball temperatures or blast pressures close-in to the detonation centre. Aluminium was found in higher concentrations further from the detonation centre, indicating its dispersal mechanism varied to that of the AN. It is possible that the aluminium distributes at a slightly later stage during the detonation than the AN (as it's reaction occurs after the primary detonation reactions) and this may cause the dispersal mechanism to differ. RDX concentrations fluctuated with distance and depositions on closer sampling sites may have been degraded in the fireball or blast overpressures. The wind direction was found to skew all analyte distributions around the detonation centres which suggested that in the latter detonation phases the residue dispersal mechanism was occurring in the smoke plume. The majority of post-blast residues were detected within 6 m and 4 m from the inorganic and organic detonations respectively.

- **Chapter 5: Detonation of with (near) spherical 1 kg and 2 kg charges of AlAN and PE7, and detonations of RDX-compositions confined in vehicles**

Findings from these studies corroborated those from the previous chapter which indicated the residue distribution trends varied depending on the detected analyte. Whilst the majority of residues decreased in concentration with increasing distance from the detonations, again the AN exhibited a more linear decrease (and better correlation with the inverse square law distribution) whilst the RDX fluctuated in concentration. The evidence for a distribution pattern based on the inverse square law was presented, however it was not as strong here in every case, compared to that found in chapter 4. The effect of the fireball temperatures potentially degrading residues deposited closer to the detonation was not confirmed through these tests. However the effect of the wind skewing the residue

distributions was apparent and confirmed the notion of residue dispersal occurring in the smoke plume. No distinct variation was observed between results of different charge masses. The higher sampling sites sampled around the detonations yielded greater quantities of explosive residue than those positioned below the detonation height. The majority of post-blast residues were detected within radii of 10 m and 15 m from the inorganic and organic detonations respectively.

- **Chapter 6: Condensed phase particles and simulation experiments of distribution**

Whilst it was not possible to quantify the number of particles observed on the SEM stubs used to collect condensed particles, qualitatively, the number of particles observed closer to the detonations was higher than on stubs further from it. Some of the post-blast AlAN particles morphologically resembled the pre-blast material particles. The post-blast particles ascribed to be RDX did not resemble the pre-blast material. The variations may indicate the difference in the formation or survival of explosive particles during detonation. The particles also varied in their size between the two different explosive types and also with increasing distance from the detonations. The variations found with the particle sizes and shapes meant that the particle distributions could not be simulated with ease based on the experimental data. Rather the distribution of spherical particles of a set density was modelled around a detonation at ground level and charge height sampling points. The simulation results complemented the experimental distribution data well; both found that larger particles distributed to greater distances than smaller particles which were more concentrated closer to the centre. No particles were observed on sites which were positioned further than 7 m and 5 m from the AlAN and RDX detonations respectively.

Forensic bomb scene investigation protocol for locating trace explosive residues

As is already known, and has been found in this research, the collection and analysis of explosive residue is not completely efficient. In order to collect the optimum samples, the research results summarised above can be used as a basis to generate a protocol for locating trace explosive resides at crime scenes where a high order detonation has taken place.

The principle points are:

- To not focus solely on the crater area or central detonation area on the ground; higher quantities of residue can be found on perpendicular sites which are slightly further from the immediate centre and can offer less complex samples.
- If the charge height can be established, residue sampling should be focused above it (to avoid potential fireball and/or blast-wave degradation effects).
- If CCTV of the area and the time of the explosion event is available (or the approximate wind direction is known), this should be used to ascertain the movement of the smoke plume following the firing and therefore potential residue deposition sites.
- Search perimeters should be within a 10 m radius from the central detonation area, if one can be identified.

7.2 Key Conclusions and Contributions to the Field

No other published study has investigated the spatial distribution of post-blast explosive residues from 0.5 kg, 1 kg and 2 kg AlAN and RDX composition charges. The findings here have validated current forensic practice of sampling for explosive residues near the central region of a detonation via the generation of empirical evidence. Additionally it has been found that different residue analytes produce different distribution trends, thus signifying that the dispersion mechanisms or factors which affect distribution vary depending on the analyte. This new knowledge augments the unique nature of each explosive material and contradicts the application of one theoretical distribution model to all residue distribution patterns, such as the inverse square law which was found to be consistently valid here only for the inorganic analytes. No other experimental study has found such support for a mathematical model.

The radius within which explosive residues may be detected during forensic investigations of up to ~2 kg detonations has also been established as approximately ten metres for both the inorganic and organic charges fired. No other study has determined such approximate perimeters for smaller explosive charge masses using perpendicular sampling sites; previous tests used only very large charge masses (over 400 kg). The findings here indicate theoretical sixty meter perimeters are too extensive for smaller bomb scenes, and they signify again that general theoretical constructs cannot be applied to all explosive charge types and detonations of different charge masses. Conversely, the use of the wind direction to determine principal residue movement (as determined through this research) may be applied to all explosive types and charges.

The appearance of the post-blast condensed phase particles found following the detonations varied between the two explosive types used. The novel method applied here of using SEM stubs to collect residues was successful. No previously published literature has found or explained such morphological variations between particles and this information could be used to identify the explosive material used based on microscopic assessments prior to chemical analysis. Furthermore the finding of such various particles had implications on the simulation experiments which as a result needed to be simplified to model only spherical particles of a set density for simplicity.

Despite the variation from exact experimental replication, the simulation and experimental results were in good agreement. The successful ability to couple experimental and numerical simulations of residue distributions has been demonstrated here. Whilst particle distribution models exist, no comparative work has been conducted previously to assess the validity of the models against experimental data – this study has commenced such validation processes. Development in this area would allow estimates of the dispersion of explosives and other analytes (such as radiological material) from explosive releases to be authenticated. The limited database which establishes the residue distribution patterns in the literature has been successfully developed through this research. As the findings presented here are relevant to only these experiments, further work is required in order to establish their impact on not only the knowledge base in detonation phenomenon but also the forensic investigation thereof.

7.3 Future Research Areas

The experiments conducted during this research were as controlled as possible with the outdoor firing of mainly unconfined spherical charges. Whilst the results also seemed to apply for the confined systems which were tested here, further work should be done to verify the application of the findings to more forensically valid scenarios. Experiments which incorporate the detonation of different charge shapes and varying levels and types of confinement (including indoors) should be conducted. Furthermore, variables such as the sampling height, (with a focus on heights above the detonation centre) should be tested in order to fully develop the literature upon which post-blast scene residue collection is based.

As the different explosives produced varying results, further explosive types should be tested in order to ascertain whether variations between different explosive analyte distribution trends and particle morphologies occur between chemicals. Here, the mechanisms of residue formation and dispersal were suggested to vary depending on the explosive types (military or binary compositions), but it is unknown how. Studies which focus on the actual formation, or survival, of explosive residues may allow the dispersal

mechanisms to be determined and subsequently enhance the forensic scene investigation practices.

The effect of blast phenomena (blast-wave, fireball dynamics and smoke plume movement) on residue distribution need to be verified. It is currently unknown whether the fluctuating distribution patterns of some explosive analytes (e.g. RDX) are due to the dispersal mechanism of the residue or possible degradation effects from the blast-wave overpressure or fireball temperatures. Whilst controlled studies of thermal and blast effects on explosive molecules are conducted, those which address the effects on post-blast residues are lacking.

Further experiments elucidating the physical and chemical nature of post-blast condensed phase residues from different explosive types are required in order to potentially enhance understanding of the residue formation process. The application of more robust analytical techniques to the chemical identification of the condensed phase particles would allow their structural identity to be determined more conclusively. If morphological variations were significantly characteristic of an explosive material the particles may be used as primary identification of the explosive used at a bomb scene.

The work proposed may not be practically feasible to test experimentally given the methodological constraints and costs of using explosives and test firing facilities. The coupling of modelling and experiment capabilities developed here should be extended to fully validate the models used, thereby potentially precluding the need for complex experimental work. Accordingly, it will be possible to enhance the scientific underpinning of post-blast scene investigation. Furthermore, the combination of experimental and computational techniques in examining the spatial distribution of particulate materials during detonation events has clear, considerable applications on the movement of material during and following 'dirty bomb' events. Within this field it would be imperative to understand particle movement not only from a forensic perspective (in order to sample for residues), but also environmentally, in order to counter negative effects in the surrounding environment, and understand how many of the surrounding population may have been affected by released chemical, biological, radiological or nuclear matter.

The outlined future research areas are not exhaustive but provide recognisable avenues for the development of the research presented herein. The current use of explosive devices in terrorist attacks, both nationally and internationally, necessitates research in counter-proliferation of explosive weapons first and foremost. However, with the continued threat and use of such devices, the importance of research within the post-blast domain cannot be emphasised enough.

References

1. Strobel, R. 'Chapter 5: Recovery of Material from a Scene of an Explosion and its Subsequent Forensic Laboratory Examination', in *Forensic Investiation of Explosions* (Ed. Beveridge, A.) Taylor and Francis Ltd., Salisbury, (1998) pp. 101–133.
2. Zitrin, S. & Yinon, J. *Modern Methods and Applications in Analysis of Explosives*. Wiley and Sons, Ltd. Chichester, (1996) pp. 163 – 240.
3. Yallop, H. J. *Explosion Investigation*. Forensic Science Society and Scottish Academic Press Ltd, Edinburgh, (1980) pp. 21 – 89.
4. Zonderman, J. *Beyond the Crime Lab: The New Science of Investigation*. 2nd edition, Wiley and Sons, New York, (1998) pp. 45-75.
5. Lane, B. *The Encyclopaedia of Forensic Science*. Headline Book Publishing, London, (1992) (Accessed online 2014).
6. Nickell, J. and Fischer, J. F. *Crime Science: Methods of Forensic Detection*. Lexington: University Press of Kentucky, Kentucky, (1999) pp. 219 – 246.
7. Abdul-Karim, N., Blackman, C. S., Gill, P. P., Wingstedt, E. M. M. & Reif, B. A. P. 'Post-Blast Explosive Residue – A Review of Formation and Dispersion Theories and Experimental Research'. *Royal Society of Chemstry Advances,* Manuscipt Accepted. (2014).
8. Technical Working Group on Crime Scene Investigation. *A Guide for Explosion and Bombing Scene Investigation*. National Institute of Justice and US Department of Justice Report, Washington D.C., (2000).
9. Hoffman, C. M., & Byall, E. B. 'Identification of Explosive Residues in Bomb Scene Investigations'. *Journal of Forensic Sciences,* **19,** (1974) pp. 54–63.
10. Lancaster, S. L., Marshall, M. & Oxley, J. C. 'Laboratory Analysis of Explosion Debris', in *Wiley Encyclclopaedia of Forensic Science.* (Eds. Jamieson, A. & Moenssens, A.) Wiley and Sons, Ltd., New York, (2009) pp. 1028–1060.
11. Akhavan, J. *The Chemistry of Explosives*. 3rd edition, Royal Society of Chemistry, Cambridge, (2004) pp. 27 – 112.
12. Meyer, R., Kohler, J. & Homburg, A. *Explosives*. 6th edition, Wiley-VCH, Wenheim, (2007) pp. 68 – 167.
13. Kubota, N. *Propellants and Explosives: Thermochemical Aspects of Combustion*. 2nd edition, Wiley-VCH, Weinheim, (2007) pp. 7 – 33.
14. Department of the Army Headquarters United States Army Materiel Command, *Engineering Design Handbook Explosives, Explosives Series: Explosive Trains*. AMC Pamphlet No. 706-179, (1974).
15. Merriam R. *US Army Ordnance Research and Development in World War II A Review*. Merriam Press, Bennington, (1988).
16. McPartland, R. M. 'Chapter 15: Terrorism Tradecraft II: Case Studies - Past, Present and Future', in *Principles of Emergency Management: Hazard Specific Issues and Mitigation Strategies*, (Ed. Fagel, M. J.), CRC Press, Taylor and Francis Group, Boca Raton (2011) pp. 345 – 363.

17. Bowden, F. P. & Yoffe, Y. D. *Initiation and Growth of Explosion in Liquids and Solids,* Cambridge Univeristy Press, Cambridge, (1985) pp. 14 – 96.

18. Field, J. E. 'Hot Spot Ignition Mechanisms for Explosives'. *Journal of the American Chemical Society*, **25,** (1992), pp. 489–496.

19. Bdzil, J. B. & Stewart, D. S. 'The Dynamics of Detonation in Explosive Systems'. *Annual Review of Fluid Mechancics,* **39,** (2007), pp. 263–292.

20. Tarver, C. M. 'Multiple Roles of Highly Vibrationally Excited Molecules in the Reaction Zones of Detonation Waves'. *Journal of Physical Chemistry A,* **5639,** (1997), pp. 4845–4851.

21. Dlott, D. D. 'Ultrafast Spectroscopy of Shock Waves in Molecular Materials', *Annual Review of Physical Chemistry,* **50,** (1999), pp. 251–278.

22. Dlott, D. D. 'New Developments in the Physical Chemistry of Shock Compression'. *Annual Review of Physical Chemistry.* **62,** (2011), pp. 575–597.

23. Moore, D. J., Funk, D. J. & McGrane, S. D. 'Chapter 13: At the Confluence of Experiment and Simulation: Ultrafast Laser Spectroscopic Studies of Shock Compressed Energetic Materials', in *Chemistry at Extreme Conditions,* (Ed. Manaa, M. R.) Elsevier, Amsterdam, (2005), pp. 369-393.

24. Kuklja, M. M. 'Thermal Decomposition of Solid Cyclotrimethylene Trinitramine', *Journal of Physical Chemistry B,* **105,** (2001), pp. 10159–10162.

25. Botcher, T. R. & Wight, C. A. 'Explosive Thermal Decomposition Mechanism of RDX'. *Journal of Physical Chemistry,* **98,** (1994), pp. 5441–5444.

26. Chakraborty, D., Muller, R. P., Dasgupta, S. & Goddard, W. A. 'The Mechanism for Unimolecular Decomposition of RDX (1,3,5-Trinitro-1,3,5-triazine), an *ab Initio* Study', *Journal of Physical Chemistry A,* **104,** (2000), pp. 2261–2272.

27. Wu, C. J. & Fried, L. E. 'First-Principles Study of High Explosive Decomposition Energetics', in *Eleventh International Detonation Symposium: Proceedings - August 31-September 4, 1998, Snowmass Conference Center, Snowmass Village, Colorado,* Office of Naval Research, (1998). pp. 490-498.

28. Kinney, G. F. & Graham, K. J. *Explosive Shocks in Air*. Springer-Verlag, New York, (1985). pp. 3-99.

29. Bibhu, M. 'Physics of Explosion Hazards', in *Forensic Investigation of Explosions* (Ed. Beveridge, A.) Taylor and Francis Ltd., Salisbury, (1998), pp. 15–45.

30. Gross, K. C. *Phenomenological Model for Infrared Emmissions from High Explosive Detonation Fireballs*, PhD Thesis, Department of the Air Force Air University, Air Force Institute of Technology, Ohio, (2007).

31. Chaturvedia, S. & Davea, P. N. 'Review on Thermal Decomposition of Ammonium Nitrate', *Journal of Energetic Materials,* **31,** (2013), pp. 1–26.

32. Brower, K. R., Oxley, J. C. & Tewari, M. 'Evidence for Homolytic Decomposition of Ammonium Nitrate at High Temperature'. *Journal of Physical Chemistry,* **93,** (1989), pp. 4029–4033.

33. Owens, F. J. & Sharma, J. 'X-ray Photoelectron Spectroscopy and Paramagnetic Resonance Evidence for Shock-Induced Intramolecular Bond Breaking in Some Energetic Solids. *Journal of Applied Physics,* **51,** (1980), pp. 1494 – 1497.

34. Kamlet, M. & Jacobs, S. 'Chemistry of Detonations'. *Journal of Chemical Physics,* **43,** (1968), pp. 23–25.

35. Balakrishnan, K. & Menon, S. 'On the Role of Ambient Reactive Particles in the Mixing and Afterburn behind Explosive Blast Waves'. *Combustion Science and Technology,* **182,** (2010), pp. 186–214.

36. Kim, C., Moon, J., Lai, M. & Im, K. 'Afterburning of TNT Explosive Products in Air with Aluminum Particles', *46th AIAA Aerospace Sciences Meeting and Exhibit, 7 – 10 January 2008, Reno, Nevada,* (2008) paper 2008 – 1029.

37. Keshavarz, M. H. 'A Simple Theoretical Prediction of Detonation Velocities of Non-ideal Explosives only from Elemental Composition', in *New Research on Hazardous Materials,* (Ed. Warey, P. B.), Nova Science Publishers, USA, (2006), pp. 255-257.

38. Maranda, A. 'Research on the Process of Detonation of Explosive Mixtures of the Oxidizer Fuel Type Containing Aluminium Powder', *Propellants, Explosives, Pyrotechnics,* **15,** (1990), pp. 161–165.

39. Paszula, J., Trzciński, W. A. & Sprzatczak, K. 'Detonation Performance of Aluminium – Ammonium Nitrate Explosives'. *Central European Journal of Energetic Materials,* **5,** (2008), pp. 3 – 11.

40. Trzciński, W. A., Cudziło, S. & Paszula, J. 'Studies of Free Field and Confined Explosions of Aluminium Enriched RDX Compositions', *Propellants, Explosives, Pyrotechnics,* **32,** (2007), pp. 502–508.

41. Cooper, P. W. & Kurowski, S. R. *Introduction to the Technology of Explosives,*. Wiley-VCH, Weinheim, (1996) pp. 57 – 82.

42. Cooper, P. W. 'Introduction to Detonation Physics', in *Explosive Effects and Applications* (Eds. Zukas, J. A. & Walters, W. P.) Springer-Verlag, New York, (1998), pp. 115 – 136.

43. Davis, W. C. 'Shock Waves, Rarefaction Waves, Equations of State', in *Explosive Effects and Applications*. (Eds. Zukas, J. A. & Walters, W. P.) Springer-Verlag, New York, (1998), pp. 64–71.

44. Beveridge, A. *Forensic Investigations of Explosions*. Taylor and Francis, Ltd., Salisbury, (1998) pp. 16 – 139.

45. Freidlander, F. G. 'The Diffraction of Sound Pulses. I. Diffraction by a Semi-Infinite Plate', *Proceedings of the Royal Society of London A,* **186,** (1946), pp. 322–344.

46. Brode, H. L. 'Blast Wave from a Spherical Charge'. *Physics of Fluids,* **2,** (1959), pp. 217 – 229.

47. Frost, D. L., Zarei, Z. & Zhang, F. 'Instability of Combustion Products Interface from Detonation of Heterogeneous Explosives'. *Proceedings of the 20th International Colloquium on the Dynamics of Explosions and Reaction Systems, July 31 – August 5*, *Montreal, Quebec,* (2005).

48. Anisimov, S. I., Zeldovich, Y. B., Inogamov, M. A. & Ivanov, M. F. 'The Taylor Instability of Contact Boundary between Expanding Detonation Products and a Surrounding Gas', in *Shock waves, Explosions, and Detonations*, American Institute of Aeronautics and Astronautics, Inc., New York, (1983), pp. 218-227.

49. Anisimov, S. I. & Zeldovich, Y. B. 'Rayleigh-Taylor Instability of Boundary between Detonation Products and Gas in Spherical Explosion'. *Pis'ma Zh. Eksp. Teor. Fiz.* **3,** (1977), pp. 1081-1084.

50. Kuhl, A. L. 'Spherical Mixing Layers in Explosions,' in *Dynamics of Exothermicity: In Honor of Antoni Kazimierz Oppenheim,* (Ed. Bowen, J. R.), Gordon and Breach, New York, (1996), pp. 291-323.

51. Taylor, G. I. 'The Instability of Liquid Surfaces when Accelerated in a Direction Perpendicular to their Planes'. *Proceedings of the Royal Society of London, Series A, Mathematical, Physical and Engineering Sciences,* **201**, (1950), pp. 192 – 196.

52. Balakrishnan, K. & Menon, S. 'On Turbulent Chemical Explosions into Dilute Aluminum Particle Clouds', *Combustion Theory and Modelling* 14, (2010), pp. 583–617.

53. Onufriev, A. T. 'Theory of the Motion of a Vortex Ring Under Gravity. Rise of the Cloud from a Nuclear Explosion', *Journal of Applied Mechanics and Technical Physics,* **8,** (1967), pp. 3–15.

54. Vermeij, E., Duvalois, W., Webb, R. & Koeberg, M. 'Morphology and Composition of Pyrotechnic Residues Formed at Different Levels of Confinement', *Forensic Science International,* **186,** (2009), pp. 68–74.

55. Thurman, J. T. *Practical Bomb Scene Investigation*. CRC Press, Boca Raton (2006) pp. 117 – 278.

56. J. Yinon & Zitrin, S. *The Analysis of Explosives*. Pergamon Press, Oxford (1981) pp. 216 – 263.

57. Kelleher, J. D. 'Explosives Residue: Origin and Distribution', *Forensic Science Communications*, **4**, Issued online by the US Department of Justice Federal Bureau of Investigation (2002).

58. Davis, W. 'High Explosives: The Interaction of Chemistry and Mechanics'. *Los Alamos Science,* **2**, (1981), pp. 48–75.

59. Van der Steen, A. C. & Kodde, H. H. 'Detonation Velocities of the Non-Ideal Explosive Ammonium Nitrate'. *Propellants, Explosives, Pyrotechnics,* **15,** (1990), pp. 58–61.

60. Ulbrich, P. & Varga, R. 'Some Experience with Trace Analysis of Post-Explosion Residues', *Academic and Applied Research in Military Science*, **3,** (2004), pp. 633–646.

61. Di Baldassare, G., Ripani, L. & Silvestrini, M. 'Esplosioni: Utilizzo di Modelli per la Previsione Degli Effetti e per L'investigazione', *Quaderni. Di Sci. Tec.,* **4**, (2005), pp. 3–28.

62. Jones, G. E., Kennedy, J. E. and Bertholf, L. D. 'Ballistics Calculations of R. W. Gurney', *American Journal of Physics,* **48,** (1980), pp. 264–269.

63. Gurney, R. W. *The Initial Velocities of Fragments from Bombs, Shell, Grenades,* Aberdeen Proving Ground Ballistics Research Laboratory Report No. 405 41. (1943).

64. Kennedy, J. E. *Gurney Energy of Explosives: Estimation of the Velocity and Impulse Imparted to Driven Metal,* Sandia National Laboratories Report SC-RR-70-90 Albequerque, New Mexico, (1970).

65. Zaker, T. A. *Fragment and Debris Hazards*, Technical Paper No. 12, Deparment of Defence Explosive Safety Board, Washngton D. C. (1975).

66. Bishop, R. H. *Maximum Missile Ranges from Cased Explosive Charges*. Report SC-4205 (TR), Sandia Corporation Albequerque, New Mexico, (1958).

67. Baker, W.E., Kulesz, J.J., Ricker, R.E., Westine, P.S., Parr, V.B., Vargas, L.M. and Mosely, P.K. *Workbook for Estimating Effects of Accidental Explosions in Propellant Ground Handling and Transport Systems*, Lewis Research Centre, NASA, San Antonio, (1978).

68. Kolla, P. & Sprunkel, A. 'Identification of Dynamite Explosives in Post Explosion Residues'. *Journal of Forensic Sciences*, **40,** (1995), pp. 406–411.

69. Noon, R. *Engineering Analysis of Fires and Explosions*. CRC Press, Boca Raton (1995) pp. 173 – 195.

70. Cullum, H., Lowe, A., Marshall, M. & Hubbard, P. 'Physical and Chemical Evidence Remaining after the Explosion of Large Improvised Bombs. Part 2: Firings of Calcium Ammonium Nitrate/Sugar Mixtures'. *Journal of Forensic Sciences,* **45,** (2000), pp. 333–48.

71. Baker, W. E., Cox, P. A., Westine, P. S., Kulesz, J. J. & Strehlow, R. A. 'Chapter 2: Free Field Explosions and their Characteristics', in *Explosion Hazards and Evaluation,* (Ed. Kauffman, C. W.), Elsevier, Amsterdam, (1983), pp. 106–218.

72. McKinnon, G. *Fire Protection Handbook,* National Fire Protection Association, Quincy, MA (1981).

73. Jenkins, T. F., Hewitt, A. D., Walsh, M. E., Ranney, T. A., Ramsey, C. A., Grant, C. L. & Bjella, K. L. 'Representative Sampling for Energetic Compounds at Military Training Ranges'. *Environmental Forensics*, **6,** (2005), pp. 45–55.

74. Brannon, J. M., Jenkins, T. F., Parker, L. V., Deliman, P., Gerald, J. A., Ruiz, C., Porter, B. & Davis, W. M. *Procedures for Determining Integrity of UXO and Explosives Soil Contamination at Firing Ranges*, US Army Corps Engineers, Engineering Research and Development Centre, Report No. TR-00-4 (2000).

75. Walsh, M. E., Collins, C. M., Racine, C. H., Jenkins, T. F., Gelvin, A. B. & Ranney, T. A. *Sampling for Explosives Residues at Fort Greely, Alaska: Reconnaissance Visit July 2000*. US Army Corps of Engineers, Cold Regions Research and Engineering Laboratory Technical Report TR-01-15 (2001).

76. Pennington, J.C., Silverblatt, B., Poe, K., Hayes, C.A. & Yost, S. 'Explosive Residues From Low Order Detonations of Heavy Artillery and Mortar Rounds', *Soil and Sediment Contamination: An International Journal,* **17,** (2008), pp. 533–546.

77. Penningon, J. C., Hayes, C. A., Yost, S., Crutcher, T. A., Berry, T. A., Clarke, J. U. & Bishop, M. J. 'Explosive Residues from Blow in Place Detonations of Artillery Munitions', *Soil and Sediment Contamination: An International Journal,* **17,** (2008), pp. 163–180.

78. Lewis, J. Thiboutot, S., Ampleman, G., Brochu, S., Brousseau, P., Pennington, J. C. & Ranney, T. *Open Detonation of Military Munitions on Snow: An Investigation of the Quantities of Energetic Materials Produced*. Report No. 3 ERDC TR-03-2, Vicksburg, MS: US Army Engineer research and Development Centre, Environmental Laboratory, (2003).

79. Jenkins, T. F., Ranney, T. A., Miyares, P. H., Collins, N. H. & Hewitt, A. D. *Use of Surface Snow Sampling to Estmate the Quantity of Explosive Residues Resuting from Landmine Detonations*, US Army Corps of Engineers ERDC/CREEL Report No. TR-00-12, (2000).

80. Hewitt, A. D., Jenkins, T. F., Walsh, M. E., Walsh, M. R. & Taylor, S. 'RDX and TNT Residues from Live-fire and Blow-in-place Detonations', *Chemosphere,* **61,** (2005), pp. 888–894.

81. Taylor, S., Hewitt, A., Lever, J., Hayes, C., Perovich, L., Thorne, P. & Daghlian, C. 'TNT Particle Size Distributions from Detonated 155-mm Howitzer Rounds', *Chemosphere,* **55,** (2004), pp. 357–67.

82. Borusiewicz, R., Zadora, G. & Zieba-Palus, J. 'Chemical Analysis of Post Explosion Samples obtained as a Result of Model Field Experiments', *Talanta,* **116,** (2013) pp. 630–636.

83. Jenkins, T. F., Pennington, J. C., Ranney, T. A., Berry, T, E., Miyares, P. H., Walsh, M. E., Hewitt, A. D., Perron, N. M., Parker, L. V., Hayes, C. A. & Wahlgren, E. G. *Characterization of Explosives Contamination at Military Firing Ranges,* ERDC Report: TR-01-5, US Army Corps of Engineers, (2001).

84. Taylor, S., Campbell, E., Perovich, L., Lever, J. & Pennington, J. 'Characteristics of Composition B Particles from Blow-in-Place Detonations'. *Chemosphere,* **65,** (2006), pp. 1405–1413.

85. Wingstedt, E. M. M., Fossum, H. E. & Pettersson Reif, B. A. *Simulation of Bomb Residue Deposition Following the Oslo Bombing July 22, 2011,* FFI Rapport 2012/01836, ISBN 978-82-464-2176-6. (2012).

86. Pennington, J. C., Jenkins, T. F., Ampleman, G., Thiboutot, S., Brannon, J. M., Hewitt, A. D., Lewis, J., Brochu, S., Diaz, E., Walsh, M. R., Walsh, M. E., Taylor, S., Lynch, J. C., Clausen, J., Ranney, T. A., Ramsey, T. A., Hayes, C. A., Grant, C. L., Collins, C. M., Bigl, S. R., Yost, S. & Dontsova, K. *Distribution and Fate of Energetics on DoD Test and Training Ranges: Final Report*, Engineer Research and Development Center (2006).

87. Phillips, S., Lowe, A., Marshall, M., Hubbard, P., Burmeister, S. G. & Williams, D. R. 'Physical and Chemical Evidence Remaining after the Explosion of Large Improvised Bombs. Part 1: Firings of Ammonium Nitrate/sugar and Urea Nitrate', *Journal of Forensic Sciences,* **45,** (2000), pp. 324–32.

88. Monsfield, A. M., Marshall, M., Walker, C. L. & Hubbard, P. 'Physical and Chemical Evidence Remaining After the Explosion of Large Improvised Bombs . Part 3 : Firings of Calcium Carbonate Ammonium Nitrate/Sugar'. *Journal of Forensic Sciences,* **46,** (2001), pp. 535–548.

89. Committee on Marking, Rendering Inert, and Licensing of Explosive Materials, *Marking, Rendering Inert, and Licensing of Explosive Materials Interim Report*, Board on Chemical Sciences and Technology, Commission on Physical Sciences, Mathematics, and Applications, National Research Council, National Academy Press, Washington, D.C., (1997).

90. Office of Technology Assessment, *Taggants in Explosives*, Government Printing Office, Washington D.C., (1980).

91. Rouhi, M. A., *Government, Industry Efforts Yield Array of Tools To Combat Terrorism,* Chemical & Engineering News, July 24, pp. 10–19 and How One Chemist's Outrage Sparked a Counterterrorism Invention, Chemical &Engineering News, July 24, pp. 13, (1995).

92. US Department of the Treasury and the Bureau of Alcohol, Tobacco and Firearms (ATF), *Progress Report: Study of Marketing, Rendering Inert and Licensing of Explosives Materials, in International Explosives Symposium, F*airfax *Virginia, September 18–22, 1995.* (1995).

93. Scharer, J. 'Switzerland's Explosives Identification Program' in *Proceedings of the International Explosives. Symposium,* Government Printing Office, (1995).

94. Mayersak, R. J., *A Technical Approach to Marking Explosives, Propellants and Precursor Chemicals*, Naval Surface Warfare Center, Indian Head Div Md Ordnance Environmental Support Office, (1998).

95. National Research Council, *Containing the Threat from Illegal Bombings: An Integrated National Strategy for Marking, Tagging, Rendering Inert, and Licensing Explosives and Their Precursors*, The National Academies Press, Washington, D. C. (1998).

96. Kirkendall, T., Baker, J., Barnes, J. H., Lewis, C. & Wheeler, M. 'Lanthanide Taggants for Characterizing the Explosive Blast Radius of Homemade Explosive Mixtures', in *Pittcon,* Philadelphia, USA, (2013).

97. Ngo, T., Mendis, P., Gupta, A. & Ramsay, J. 'Blast Loading and Blast Effects on Structures: An Overview'. *Electronic Journal of Structural Engineering,* **7,** (2007), pp. 76–91.

98. Bloom, S. G. *Models for Close-In, Atomspheric Dispersion, Explosive Releases, and Particle Deposition*. (1993) Oak Ridge National Laboratory ORNL/TM-12452

99. Deaves, D. M. & Hebden, C R. *Aspects of Dispersion Following an Explosive Release*. Atkind Process Report: ADMLC/2004/3, (2004).

100. Ayer, J. E. Ayer, J.E., Clark, A.T., Loysen, P., Ballinger, M.Y., Mishima, J., Owczarski, P.C., Gregory, W.S. & Nichols, B.D. *Nuclear Fuel Cycle Facility Accident Analysis Handbook*. Office of Nuclear Material Safety and Safeguards, (1988).

101. Williams, M. D., Brown, M. J., Singh, B. & Boswell, D. *QUIC-PLUME Theory Guide,* Report: LA-UR-04-0561. (2004).

102. Gowardhan, A., Brown, M., Williams, M. & Pardyjak, E. 'Evaluation of the QUIC Urban Dispersion Model using the Salt Lake City URBAN 2000 Tracer Experiment Data – IOP 10' in *Sixth Symposium on the Urban Environment, 29th January – 2nd February, Atlanta* (2006).

103. Williams, M. D., Brown, M. J., Boswell, D., Singh, B. & Pardyjak, E. 'Testing of the QUIC-PLUME Model with Wind-Tunnel Measurement for a High-Rise Building', in *Fifth AMS Urban Environment Conference, 23rd – 26th August, Los Alamos, New Mexico* (2004).

104. Zhang, F., Frost, D.L., Thibault, P.A. & Murray, S. B. 'Explosive Dispersal of Solid Particles'. *Shock Waves,* **10,** (2001), pp. 431–443.

105. Lanovets, V.S., Levich, V.A., Rogov, N.K., Tunik, Yu.V. & Shamshev, K. N. 'Dispersion of the Detonation Products of a Condensed Explosive with Solid Inclusions'. *Fiz. Goreniya i Vzryva,* **29,** (1992), pp. 88–92.

106. Walter, H. 'Handling "Dirty Bomb"-Scenarios with the Lagrangian Particle Model Lasair', *Hrvat. Meteorološki Časopis,* **43,** (2008), pp. 230–234.

107. Il'in, V. V., Rybakov, A.P. & Kozlov, V. V. 'Mathematical Model of Dispersion of Explosive Products During the Exit of Oblique Denotation Wave on the Free', Investigated in Russia (English), (2006), pp. 1538–1545.

108. Fossum, H. E., Reif, B. A. P., Tutkun, M. & Gjesdal, T. 'On the Use of Computational Fluid Dynamics to Investigate Aerosol Dispersion in an Industrial Environment: A Case Study'. *Boundary-Layer Meteorology.* **144,** (2012), pp. 21–40.

109. Wingstedt, E. & Reif, B. A. P. *Numerical Simulations of Particle Dispersion in an Urban Area*. Norwegian Defence Research Establishment Report. FFI-rapport 2012/00266, (2012).

110. Vermette, J. 'General Protocols at the Scene of an Explosion' in *Forensic Investigation of Explosions* (Ed. Beveridge, A.) Taylor and Francis, Ltd., Salisbury, (1998), pp. 75–101.

111. White, P.C. *Crime Scene to Court: The Essentials of Forensic Science*. 2nd edition. Royal Society of Chemistry, Cambridge, (2004) (Accessed online 2014).

112. Jackson, A. & Jackson, J. M. *Forensic Science*. 2nd edition, Pearson Education Limited, Harlow, (2008) pp. 326 – 342.

113. Thatcher, P. & Kelleher, J. *The Practice of Crime Scene Investigation*. CRC Press, Boca Raton, (2004) pp. 297 – 310.

114. Technical Support Working Group. *Trace Explosives Materials Field Guide: Best Collection Practices*. Government Printing Office (2012).

115. Kosanke, K. L., Dujay, R. C. & Kosanke, B. 'Characterization of Pyrotechnic Reaction Residue Particles by SEM/EDS', *Journal of Forensic Sciences,* **48,** (2003), pp. 531–537.

116. Kosanke, K. L., Dujay, R. C. & Kosanke, B. J. 'Pyrotechnic Reaction Residue Particle Analysis', *Journal of Forensic Sciences,* **51,** (2006), pp. 296–302.

117. Kosanke, K. L., Dujay, R. C. & Kosanke, B. J. 'Applications for Pyrotechnic Reaction Residue Particle Analysis'. *International Association of Microanalysis,* **4,** (2003), pp. 1–8.

118. Phillips, S. A. 'Pyrotechnic Residues Analysis – Detection and Analysis of Characteristic Particles by Scanning Electron Microscopy/Energy Dispersive Spectroscopy, *Science and Justice,* **41,** (2001), pp. 73–80.

119. National Fire Protection Association. *Guide for Fire and Explosion Investigations*. Quincy, MA. (2011).

120. Crowson, C., Cullum, H., Wiley, R. & Lowe, A. 'A Survey of High Explosive Traces in Public Places'. *Journal of Forensic Sciences,* **41,** (1996) pp. 980-989.

121. Cullum, H. E., McGavigan, C., Uttley, C. Z., Stroud, M. A. & Warren, D. C. 'A Second Survey of High Explosives Traces in Public Places', *Journal of Forensic Sciences,* **49,** (2004), pp. 684–90.

122. Saferstein, R. 'Chapter 15: Forensic Investigation of Explosion', in *Criminalistics. An Introduction to Forensic Science.* 10th edition, (Ed. Saferstein, R.), Prentice Hall, Harlow, (2011), pp. 399-417.

123. DeTata, D. A, Collins, P. A & McKinley, A. J. 'A Comparison of Common Swabbing Materials for the Recovery of Organic and Inorganic Explosive Residues', *Journal of Forensic Sciences,* **58,** (2013), pp. 757–63.

124. Song-Im, N., Benson, S. & Lennard, C. 'Establishing a Universal Swabbing and Clean-up Protocol for the Combined Recovery of Organic and Inorganic Explosive Residues', *Forensic Science International.* **223,** (2012), pp. 136–147.

125. Waddell, R., Dale, D. E., Monagle, M. & Smith, S. A. 'Determination of Nitroaromatic and Nitramine Explosives from a PTFE Wipe using Thermal Desorption-gas Chromatography with Electron-capture Detection', *Journal of Chromatography A,* **1062,** (2005), pp. 125–131.

126. Thompson, R.Q., D.D. Fetterolf, M.L. & Miller, R. F. M. 'Aqueous Recovery from Cotton Swabs of Organic Explosives Residue Followed by Solid Phase Extraction', *Journal of Forensic Sciences.* **44,** (1999), pp. 795–804.

127. Song-im, N., Benson, S. & Lennard, C. 'Evaluation of Different Sampling Media for Their Potential use as a Combined Swab for the Collection of both Organic and Inorganic Explosive Residues', *Forensic Science International.* **222,** (2012), pp. 102–110.

128. Twibell, J.D., Home, J.M., Smalldon, K.W., Higgs, D.G & Hayes, T. S. 'Assessment of Solvents for the Recovery of Nitroglycerine from Hands using Cotton Swabs', *Journal of Forensic Sciences,* **27,** (1982) pp. 792–800.

129. Oxley, J. C., Marshall, M. & Lancaster, S. 'Chapter 2: Principles and Issues in Forensic Science', in *Forensic Chemistry Handbook,* (Ed. Kobilinksy, L. F.) Wiley and Sons, Hoboken, (2012) pp. 24-38.

130. Lloyd, J. B. F. 'Clean-up Procedures for the Examination of Swabs for Explosives Traces by High-Performance Liquid Chromatography with Electrochemical Detection at a Pendant Mercury Drop Electrode', *Journal of Chromatography,* **261,** (1983), pp. 391–406.

131. Twibell, J. D., Wright, T., Sanger, D. G., Bramley, R. K., Lloyd, J. B. F., & Downs, N. S. 'The Efficient Extraction of Some Common Organic Explosives from Hand Swabs for Analysis by Gas Liquid and Thin-Layer Chromatography', *Journal of Forensic Sciences,* **29,** (1984), pp. 277–283.

132. Staymates, J. L., Grandner, J. & Gillen, G. 'Fabrication of Adhesive Coated Swabs for Improved Swipe-based Particle Collection Efficiency', *Analytical Methods*, **3,** (2011), pp. 2056-2060.

133. Byall, E. B. 'Explosives Report 1998 – 2001: Detection and Characterisation of Explosives and Explosive Residue: A Review', *13th INTERPOL Forensic Science Symposium,* October 16th – 19th, Lyon, France, (2001).

134. Klapec, D. J. & Czarnopys, G. 'Analysis and Detection of Explosive Residues. Review: 2010 to 2013', *17th Interpol International Forensic Science. Management Symposium.* (Ed. Daéid, N. N.) (2013), pp. 280–435.

135. Ogata, Y., Wada, Y., Katsuyama, K. & Ma, G.-C. 'Photographic Measurement of the Detonation Velocity of Explosives by High-speed Camera and its Comparison with Other Methods', in *10th Symposium (International) on Detonation*, *July 1995, Pasadena, California,* US Naval Ordnance Laboratory, Office of Naval Research, (1995).

136. Sultanoff, M. 'Some Philosophical Aspects of High-Speed Photographic Instrumentation', *Society of Motion Picture and Television Engineers*, **71**, (1962), pp. 411-416.

137. Tyrrell, E., Dicinoski. G. W., Hilder, E. F., Shellie, R. A., Breadmore, M. C., Pohl, C. A., Haddad, P. R. 'Coupled Reversed-Phase and Ion Chromatographic System for the Simultaneous Identification of Inorganic and Organic Explosives', *Journal of Chromatography A*, **1218**, (2011) pp. 3007-3012.

138. Ahmad, U. K., Tze, O. S., Ghazali, M. F., Hooi, Y. W. & Abdullah, M. K. 'Analysis of Anionic Post-Blast Residues of Low Explosives from Soil Samples of Forensic Interest', *Malaysian Journal of Analytical Sciences,* **15,** (2011), pp. 213–226.

139. Sarazin, C., Delaunay, N., Varenne, A., Vial, J., Costanza, C., Eudes, V., Minet, J. J. & Gareil, P. 'Identification and Determination of Inorganic Anions in Real Extracts from Pre- and Post-blast Residues by Capillary Electrophoresis', *Journal of Chromatography A*, **1217,** (2010), pp. 6971–6978.

140. Johns, C., Shellie, R. A., Potter, O. G., O'Reilly, J. W., Hutchinson, J. P. & Guijt, R. M. 'Identification of Homemade Inorganic Explosives by Ion Chromatographic Analysis of Post-blast Residues', *Journal of Chromatography A,* **1182,** (2008), pp. 205–214.

141. Johns, C., Hutchinson, J. P., Breadmore, M. C., Guijt, R. M., Hilder, E. F., Dicinoski, G. W. and Haddad, P. R. 'Profiling the chemical composition of explosives', *Chemistry in Australia,* **76,** (2009), pp. 30-34.

142. Hutchinson, J. P., Evenhuis, C. J., Johns, C., Kazarian, A., Breadmore, M. C., Macka, M., Hilder, E. F., Guijt, R. M., Dicinoski, G. W. & Haddad, P. R. 'Identification of Inorganic Improvised Explosive Devices by Analysis of Pstblast Residues using Portable Capillary Electrophoresis Instrumentation and Indirect Photometric Detection with a Light-Emitting Diode', *Analytical Chemistry,* **79,** (2007), pp. 7005–13.

143. Dicinoski, G. W., Shellie, R. A. & Haddad, P. R. 'Forensic Identification of Inorganic Explosives by Ion Chromatography', *Analytical Letters,* **39,** (2006), pp. 639–657.

144. Barron, L. & Gilchrist, E. 'Ion Chromatography-Mass Spectrometry: A Review of Recent Technologies and Applications in Forensic and Environmental Explosives Analysis', *Analytica Chimica Acta,* **806**, (2014), pp. 27-54.

145. Henderson, I. K. & Saari-Nordhaus, R. 'Analysis of commercial explosives by single-column ion chromatography', *Journal of Chromatography,* **149**, (1992), pp. 149-154.

146. Burns, D. T., Lewis, R. J. & Bridges, J. 'Systematic approach to the identification of water-gel explosives'. *Analytica Chimica Acta,* **375**, (1998), pp. 255-260.

147. Reutter, D. J., Buechele, R. C. & Rudolph, T. 'Ion chromatography in Bombing Investigations', *Analytical Chemistry,* **55**, (1983), pp. 1468 – 1472.

148. Green. M. J. No Title. *LC Mag,* **894**, (1985).

149. McCord, B. R., Hargadon, K. A., Hall, K. E. & Burmeister, S. G. 'Forensic Analysis of Explosives Using Ion Chromatographic Methods', *Analytica Chimica Acta***, 288,** (1994), pp. 43 – 56.

150. Bender, E. C. 'Chapter 11: Analysis of Low Explosives', in *Forensic Investigation of Explosions,* (Ed. Beveridge, A.) Taylor and Francis, Salisbury, (1998), pp. 343-387.

151. Kasamatsu, M., Sugita, R., Suzuki, S. & Suzuki, Y. 'Forensic Discrimination of Match Heads by Elemental Analysis with Inductively Coupled Plasma-Atomic Emission Spectrometry', *Journal of Forensic Sciences,* **50***,* (2005), pp. 883-886.

152. Martin, T. D., Brockhoff, C. A., Creed, J. T. & Long, S. E. 'Method 200.7 Determination of Metals and Trace Elements in Water and Wastes by Inductively Coupled Plasma-Atomic Emission Spectrometry', in *Methods for the Determination of Metals in Environmental Samples,* Environmental Monitoring Systems Laboratory, Office of Resaerch and Development, US Environmental Protection Agency, Ohio, (1994).

153. Boss, C. B. & Fredeen, K. J. *Concepts, Instrumentation and Techniques in Inductively Coupled Plasma Optical Emission Spectrometry*, 3rd edtion, Perkin Elmer Corporation, USA (2004).

154. US Environmental Protection Agency, *Method 8330A: Nitroaromatics and Nitramines by High Performance Liquid Chromatography (HPLC),* Report SW-846, (2007).

155. US Department of Health and Human Services, *Toxicological Profile for RDX,* Agency for Toxic Substance and Disease Registry Report (2010), pp. 127 -142.

156. De Hoffman, E. & Stroobant, V. *Mass Spectrometry Principles and Applications*. 3rd edition, Wiley and Sons, Ltd, Sussex, (2007).

157. Gapeev, A., Sigman, M., Yinon, J. & Wiley, J. 'Liquid Chromatography/Mass Spectrometric Analysis of Explosives:RDX Adduct Ions', *Rapid Communications in Mass Spectrometry.* **17,** (2003), pp. 943–948.

158. Casetta, B. & Garofolo, F. 'Characterisation of Explosives by Liquid Chromatography/Mass Spectrometry and Liquid Chromatography/Tandem Mass Spectrometry Using Electrospray Ionisation and Parent-Ion Scanning Techniques', *Organic Mass Spectrometry,* **29,** (1994), pp. 517–525.

159. Beller, H. R. & Tiemeier, T. 'Use of Liquid Chromatography/Tandem Mass Spectrometry to Detect Distinctive Indicators of *in situ* RDX Transformation in

Contaminated Groundwater', *Environmental Science and Technology,* **36**, (2002), pp. 2060-2066.

160. Yinon, J., McClellan, J. E. & Yost, R. A. 'Electrspray Ionisation Tandem Mass Spectrometry Collision Induced Dissociation Study of Explosives in an Ion Trap Mass Spectrometer', *Rapid Communications in Mass Spectrometry,* 11, (1997), pp. 1961–1970.

161. Evans, C. S., Sleeman, R., Luke, J. & Keely, B. J. 'A Rapid and Efficient Mass Spectrometric Method for the Analysis of Explosives', *Rapid Communications in Mass Spectrometry*, **16**, (2002), pp.1883-1891.

162. Wu. Z., Hendrickson, C. L., Rodgers, R. P. & Marshall, A. G. 'Compositional Analysis of Military Explosives by Electrospray Ionization Fourier Transform Negative Ion Cyclotron Resonance Mass Spectrometry', *Analytical Chemistry*, **74**, (2002) pp.1879-1883.

163. Brozek,-Mucha, Z. & Jankowicz, A. 'Evaluation of the Possibility of Differentiation between Various Types of Ammunition by Means of GSR Examination with SEM-EDX Method', *Forensic Science International,* **123,** (2001), pp. 39–47.

164. Hanke, L. D. 'Scanning Electron Microscopy (SEM)', in *Handbook of Analytical Methods for Materials,* Materials Evaluation and Engineering Inc. (2001) pp. 35-39.

165. Ali, E. M. A., Edwards, H. G. M. & Scowen, I. J. 'Spectroscopy and Security Applications: The Detection of Explosives and Precursors on Clothing', *Journal of Raman Spectroscopy*, **40**, (2009), pp. 2009-2014.

166. Raman RNX Systems, *Identification of Explosives*, Application Note Number 101, Kaiser Optical Systems Inc. New Orleans, USA. (2001).

167. Ghosh, M., Wang, L. & Asher, S. A. 'Deep-Ultraviolet Resonance Raman Excitation Profiles of NH_4NO_3, PETN, TNT, HMX, and RDX', *Applied Spectroscopy,* **66,** (2012), pp. 1013 –1021.

168. Lane, D. W. & Wicks, D. C. 'PIXE, A New Technique for the Trace Element Analysis of High Explosives', *Nuclear Instruments and Methods in Physics Research Section B*, **161,** (2000), pp. 792-796.

169. Johansson, S. A. E., Campbell, J. L. & Malmqvist, K. G. *Particle Induced X-ray Emission Spectroscopy (PIXE)*. Wiley, Chichester (1995) pp. 1 – 92.

170. Tellez, H., Vadillo, J. M. & Laserna, J. J. 'Secondary Ion Mass Spectrometry of Powdered Explosive Compounds for Forensic Evidence Analysis', *Rapid Communication in Mass Spectrometry,* **26,** (2012), pp. 1203-1207.

171. Mahoney, C. M., Fahey, A. J., Steffens, K. L., Benner, B. A. & Lareau, R. T. 'Characterization of Composition C4 Explosives using Time-of-flight Secondary Ion Mass Spectrometry and X-ray Photoelectron Spectroscopy', *Analytical Chemistry,* **82**, (2010), pp. 7237 – 7248.

172. Versteeg, H. K. & Malalasekera, W. *Introduction to Computational Fluid Dynamics: The Finite Volume Method*. Pearson Hall, Harlow, (2007) pp. 1 – 102.

173. Hewitt, A. D., Jenkins, T. F., Walsh, M. E., Walsh, M. R., Bigl, S. R. & Ramsey, C. A.*Protocols for Collection of Surface Soil Samples at Military Training and Testing*

Ranges for the Characterization of Energetic Munitions Constituents. US Army Corps of Engineers, ERDC/CRREL Report No. TR-07-1055, (2007).

174. Walsh, M. R., Collins, C. M. & Hewitt, A. D. *Energetic Residues from Blow-in-Place Detonation of 60-mm and 120-mm Fuzed High-Explosive Mortar Cartridges*. US Army Corps of Engineers, ERDC/CRREL Report No. TR-08-19, (2008).

175. Abdul-Karim, N., Morgan, R., Binions, R., Temple, T., Harrison, K. 'Spatial Distribution of Post-Blast RDX Residue: Forensic Implications', *Journal of Forensic Sciences*, **58**, (2012), pp. 365-371.

176. Cooper, P. W. 'Comments on TNT Equivalence', in *20th International Pyrotechnic Seminar. July 25–29, Colorado Springs, CO*, (1994), pp. 215–226.

177. Whartona, R. K., Formby, S. A. & Merrifield, R. 'Airblast TNT Equivalence for a Range of Commercial Blasting Explosives', *Journal of Hazardous Materials,* **79,** (2000), pp. 31–39.

178. Hewitt, A.D., Jenkins, T. F., Ramsey, C. A., Bjella, K. L., Ranney, T. A. & Perron, N. M. *Estimating Energetic Residue Loading on Military Artillery Ranges*. US Army Corps of Engineers, ERDC/CRREL Report No. TR-05-7, (2005).

179. Weiss, J. *Conductivity Detection in Cation Chromatography - Pros and Cons of Suppression*. Dionex Environmental Report, June 2011 (2011).

180. Lloyd, J. B. F. & King, R. M. 'One Pot Processing of Swabs for Organic Explosives and Firearms Residue Traces', *Journal of Forensic Sciences,* **35,** (1990), pp. 956–959.

181. Berry, F. J., Butler, D. S. & Holt, M. 'The Early Development of Spherical Blast from a Particular Charge', *Proceedings of the Royal Society A*, **227,** (1955), pp. 258–270.

182. Dobratz, B. M. & Crawford, P. C. *LLNL Explosives Handbook: Properties of Explosives and Explosives Stimulants,*. Lawrence Livermore National Laboratory, University of California, (1985) pp. 2 – 39.

183. Walter, P. L. *Measuring Static Overpressures in Air Blast Environments*. Technical Note, PCB Piezotronics, (2009).

184. Kuhl, A.L., Bell, J.B., Beckner, V.E., Balakrishnan, K. & Aspden, A.J. 'Spherical Combustion Clouds in Explosions', *Shock Waves*, **23** (2013) pp. 233-249.

185. Green, J. 'A Review of Phosphorus-Containing Flame Retardants', *Journal of Fire Sciences,* **10,** (1992), pp. 470–487.

186. Levan, S. L. 'Chemistry of Fire Retardancy', *Advances in Chemistry.* **207,** (1984), pp. 531–574.

187. Akhavan, J. 'Analysis of High-explosive Samples by Fourier Transform Raman Spectroscopy', *Spectrochimica Acta,* **47A,** (1991), pp. 1247–1250.

188. Willis, R. D., Blanchard, F. T. & Conner, T. L. *Guidelines for the Application of SEM/EDX Analytical Techniques to Particulate Matter Samples*. US Environmental Protection Agency Report No. 600/R-02/070, (2002).

189. Oxford Instruments*, INCA GSR Gunshot Residue,* Technical Brochure, Oxford Instruments Plc. (Accessed online 2014).

Appendix A: RDX Method Development

A.1: RDX Direct Infusion Results: MS^1 and MS^2 experiments

Hydrochloric acid (HCl) was used as a source of chlorine for chloride adducts formation with RDX. Adduct formation was also attempted with chloroform and methylene chloride as well as with ammonium chloride. For these experiments HCl produced the most intense signal for both adduct ions ($[M+^{35}Cl]^-$ and $[M+^{37}Cl]^-$) during these tests and therefore all samples were spiked with 0.1 % HCl.

An MS^1 spectrum (*m/z* range 150 to 500 shown in figure A.1) shows the expected adduct ions, $[M+^{35}Cl]^-$ and $[M+^{37}Cl]^-$ with *m/z* 257 and *m/z* 259 respectively, were not the most abundant due to the sensitivity of the molecule to fragmentation. The most abundant ion had *m/z* 197.82 corresponding to $[C_3H_6N_4O_4+^{37}Cl]^-$, with the ion at *m/z* 160.88 corresponding to the $[C_3H_6N_5O_3]^-$ ion (loss of ^{37}Cl) from the ion at *m/z* 197.82 (figure A.1). Collision energies between 10 and 55 were tested, nonetheless the spectra were dominated by the ion at *m/z* 197.82, with both $[M+^{35}Cl]^-$ and $[M+^{37}Cl]^-$ adduct ions present at relative abundances of 40 % and 12 % respectively (figure A.1). Adduct ions at *m/z* 295.75 and *m/z* 297.75 corresponding to $[M+2^{35}Cl]^-$ and $[M+2^{37}Cl]^-$ adducts had lower relative abundances of 8 % and 10 % respectively. The ion at *m/z* 478.58 may correspond to $2[M+^{35}Cl]^-$ ion.

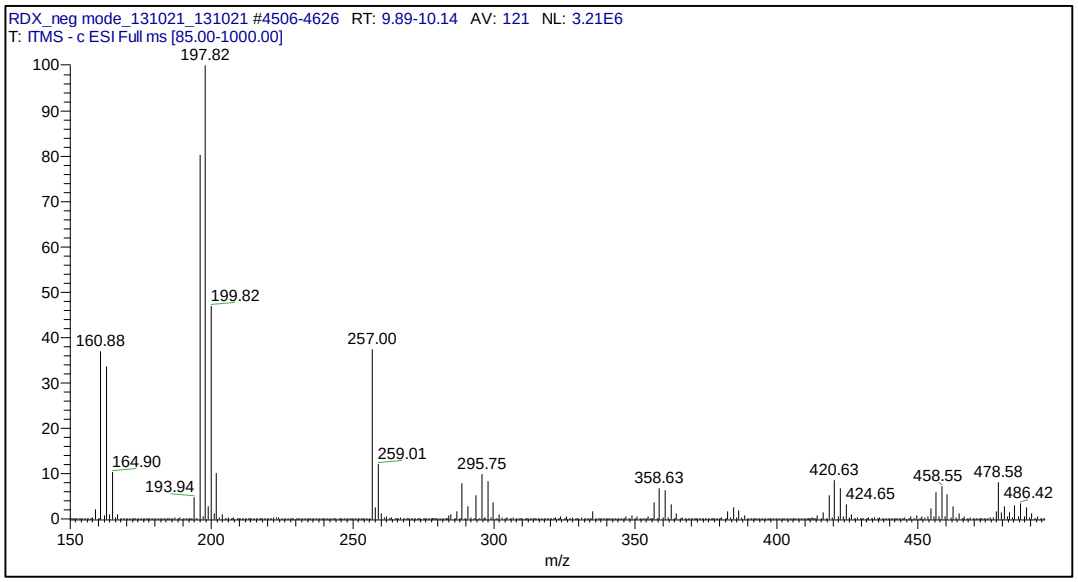

Figure A.1*: Full MS scan of 5 mg/L RDX in ACN (+ 0.1 % HCl). Scan was run in negative mode with spray voltage of ~5 kV, capillary temperature of 275 °C, m/z range of 100 to m/z 700 and data collected in centroid mode. Signal = 3.21 x10⁶.*

MS² experiments: Collision of ion *m/z* 257

MS² experiments on the precursor ion $[M+^{35}Cl]^-$ (*m/z* 257.44) produced fragment ions of *m/z* 226.98 and *m/z* 198.00 (figure A.2) corresponding to $[M+^{35}Cl–30]^-$ and to $[C_3H_6N_5O_3+^{37}Cl]^-$, respectively.

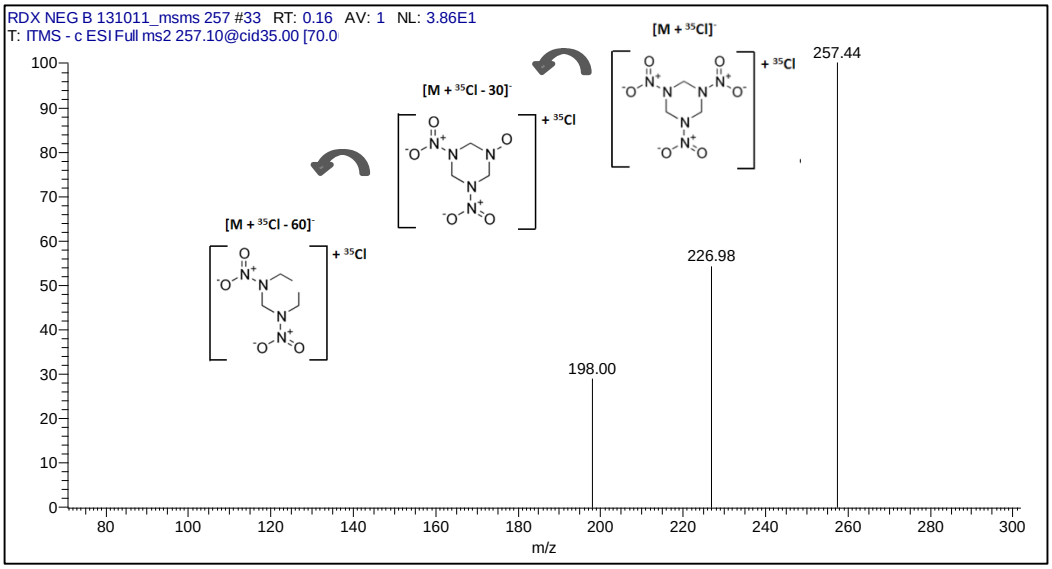

Figure A.2: *MS² spectrum of m/z 257 ion with product ions at m/z 226.98 and m/z 198.00. Spectrum collected with collision energy of 35.0, isolation widths of 2.00, and consisting of 3 averaged micro-scans each of maximum injection time of 200 ms.*

MS² experiments on the precursor ion $[M+^{35}Cl]^-$ (*m/z* 257. 44) also produced product ions at *m/z* 162.88 and *m/z* 92.89 (figure A.3), corresponding to $[M–60]^-$ and $[M–129]^-$.

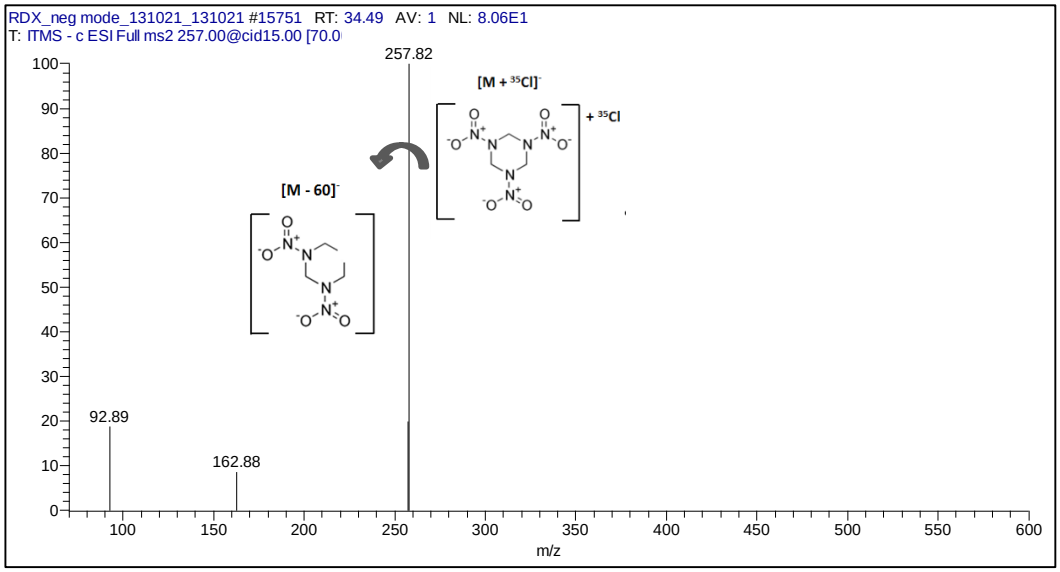

Figure A.3: *MS² spectrum of m/z 257 ion with product ions at m/z 162.88 and m/z 92.89. Spectrum collected with collision energy of 10.0, isolation widths of 2.00, and consisting of 3 averaged micro-scans each of maximum injection time of 200 ms.*

MS² experiments: Collision of ion *m/z* 197.8

MS² experiments on the ion with *m/z* 197.8 produced a fragment ion at *m/z* 162.74 corresponding to the $[M - 60]^-$ (figure A.4).

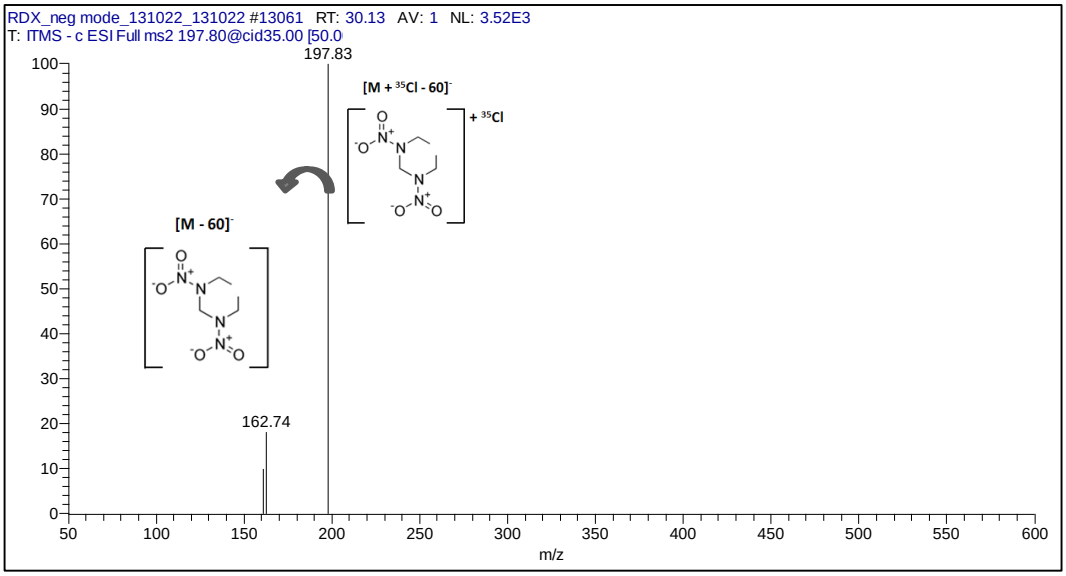

Figure A.4: *MS² spectrum of m/z 197.8 ion with product ion at m/z 162.74. Spectrum collected with collision energy of 35.0, isolation widths of 2.00, and consisting of 3 averaged micro-scans each of maximum injection time of 200 ms.*

A.2: RDX Limit of Detection

Figure A.5 shows the chromatogram for the injection of 0.1 mg/L of RDX. The detection limit is the smallest quantity of analyte that yields a signal that can be distinguished from the background noise (generally a signal equal to three times the background noise). It should be noted that the minimum quantity is not enough to obtain peak resolutions of sufficient quality for characterisation and detection purposes. Therefore any samples containing less than 0.1 mg/L would not have been quantified.

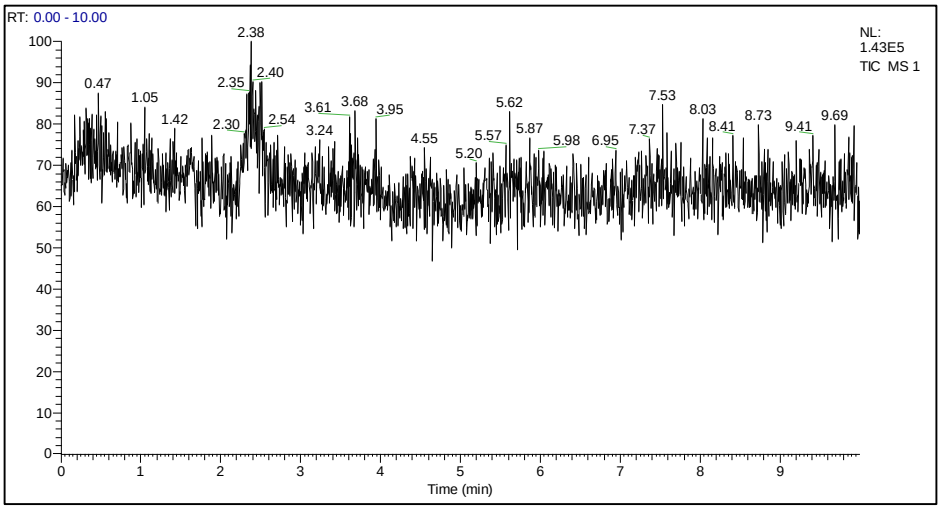

Figure A.5: *Chromatogram of 0.1 mg/L injection of RDX standard on column. The limit of detection was established at 0.1 mg/L (peak above noise at RT: 2.38 minutes).*

A.3: RDX Recovery Efficiency Tests

Method

The efficiency of the swabbing and extraction methods was evaluated by conducting the following tests:

- **Swabbing efficiency**: swabbing efficiency was assessed by spiking 1 cm^3 known concentrations of RDX (100 mg/L, 500 mg/L and 1000 mg/L RDX in ACN) onto the centre of clean plates with a pipette. The ACN was allowed to dry and the remaining residue swabbed with 5 cm^3 acetone moistened sterile cotton balls. The swabs were placed into new glass vials labelled with the number of the recovery test and sealed with the plastic cap before extracting as described in section 3.4.1. The swabbing recovery tests were repeated in triplicate.

- **Extraction efficiency**: the extraction efficiency was assessed by spiking 1 cm^3 of known concentrations of RDX (100 mg/L, 500 mg/L and 1000 mg/L RDX in ACN) onto sterile cotton swabs. The cotton swabs were held individually in glass vials. To each vial 5 cm^3 of acetone was added using a pipette, the swabs were pounded with the pipettes and the extract filtered through the disposable syringes into a new set of glass vials, 5 cm^3 of acetone was again added to each swab and the procedure repeated, the resulting extract syringed into the new vial and allowed to evaporate. Once dry, 1.5 cm^3 of ACN was added to each of the vials and the samples pipetted into labelled chromatography vials. The extraction recovery tests were repeated in triplicate.

- **Filtering efficiency**: the loss of RDX as part of the filtering procedure was assessed by spiking acetone solvent with known amounts of RDX (100 mg/L, 500 mg/L and 1000 mg/L RDX in ACN) and filtering the samples through 0.2 µm nylon filters attached to disposable syringes and analysing the filtrate. The filtration recovery tests were repeated in triplicate.

- **Evaporation efficiency**: to evaluate the loss of RDX as part of the evaporation procedure 5 cm^3 of acetone was spiked with 1 cm^3 of the known RDX concentration solutions (100 mg/L, 500 mg/L and 1000 mg/L). Following evaporation of the acetone, 1.5 cm^3 of ACN was added to each of the vials and the resulting samples pipetted into chromatography vials. The procedure was conducted in triplicate.

All recovery test samples were made with 0.1 % HCl (volume fraction) and analysed with the same HPLC-MS system conditions as described in chapter 3, section 3.4.4.2.

Results

Figures A.6–A.9 show the RDX recoveries from the different recovery tests.

Swabbing efficiency: (figure A.6)

- The overall average recovery rate of RDX was between ~50 % – ~60 % for all deposited concentrations of RDX.
- Three repeat experiments of the same concentration were conducted; the standard deviations of recovery between the repeated tests were 12 % (1000 mg/L depositions), 4.16 % (500 mg/L depositions), and 10.6 % (100 mg/L depositions).

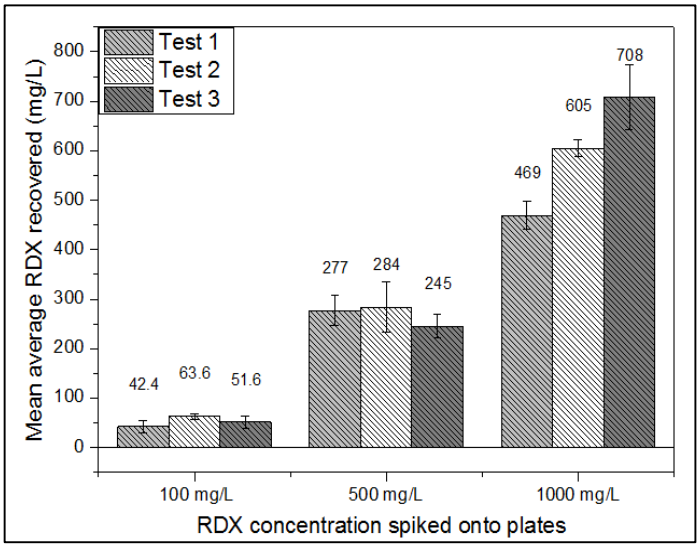

Figure A.6*: Recovered concentrations of RDX from plates spiked with 100, 500 and 1000 mg/L RDX (3 sf.) From three triplicate test of each standard concentration, the average recoveries were 52.5, 286 and 594 mg/L respectively. Error bars on each measurement are based on triplicate injections of each sample.*

Extraction efficiency: (figure A.7)

- Similar amounts were recovered from the swabs compared to the steel plates ~ 60 % recovery overall) – averages of 61.0, 302 and 597 mg/L were recovered for the 100, 500 and 1000 mg/L deposited, respectively.
- Three repeat experiments of the each concentration were conducted; the standard deviations of recovery between the repeated tests were 17 % (100 mg/L depositions), 17 % (500 mg/L depositions) and 13.3 % (1000 mg/L depositions).

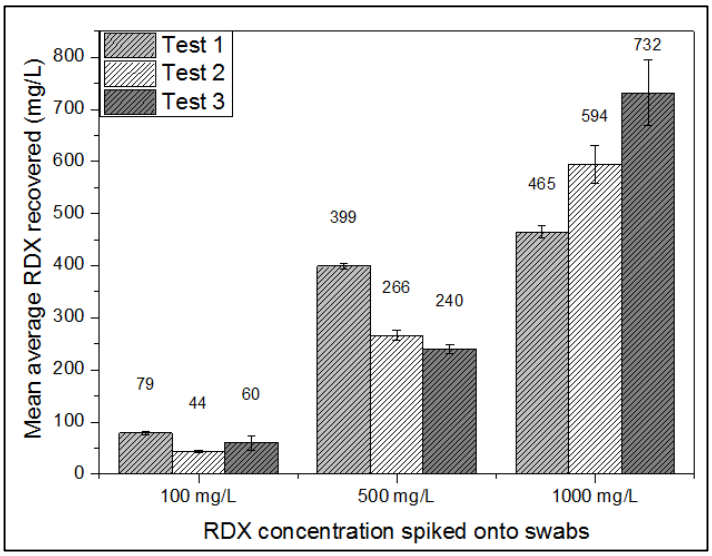

Figure A.7: *Recovered concentrations of RDX from swabs spiked with 100, 500 and 1000 mg/L RDX. From three triplicate tests of each standard concentration, the average recoveries were 61.0, 302, 597 mg/L respectively. Error bars on each measurement are based on triplicate injections of each sample.*

Filtering efficiency: (figure A.8)

- The average recovery from 100, 500 and 1000 mg/L spikes was 74.5, 389 and 788 mg/L, respectively, and therefore approximately between 75 % and 78 %.

- Three repeat experiments of the each concentration were conducted; the standard deviations of recovery between the repeated tests were 9 % (100 mg/L depositions), 4 % (500 mg/L depositions) and 6 % (1000 mg/L depositions).

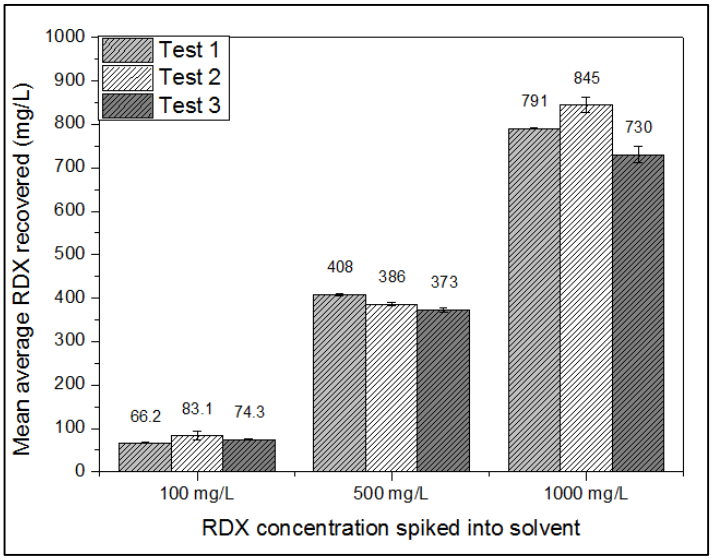

Figure A.8*: Recovered concentrations of RDX from solvent spiked with 100, 500 and 1000 mg/L RDX and then filtered and analysed. From three triplicate tests of each standard* concentration, the average recoveries were 74.5, 389 and 788 mg/L respectively. Error bars on each measurement are based on triplicate injections of each sample.

Evaporation efficiency: (figure A.9)

- The recovery rates were higher (approximately between 83 % and 95 %) than other recovery tests; mean average RDX concentrations recovered from spiking 100, 500 and 1000 mg/L were 83.6, 425 and 904 mg/L, respectively.

- Three repeat experiments of the each concentration were conducted; the standard deviations of recovery between the repeated tests were 4 % (100 mg/L depositions), 4 % (500 mg/L depositions) and 3 % (1000 mg/L depositions).

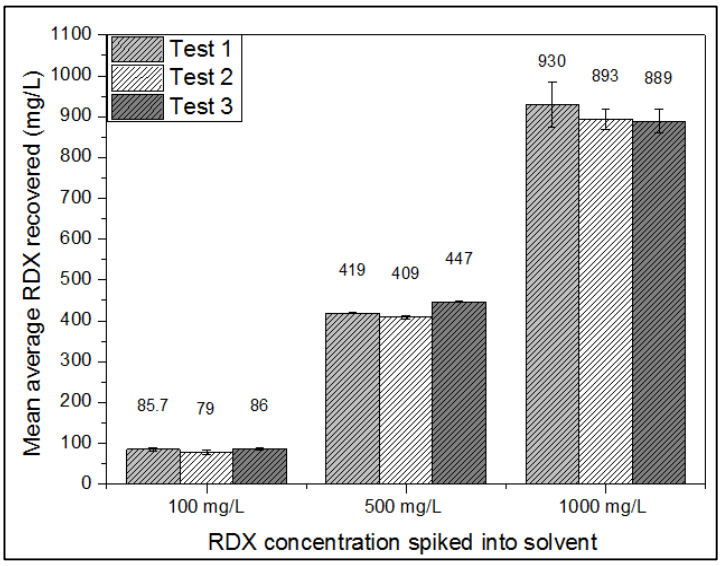

Figure A.9*: Recovered concentrations of RDX from solvent spiked with 100, 500 and 1000 mg/L RDX which was then evaporated. From three triplicate tests of each standard concentration, the average recoveries were 83.6, 525 and 904 mg/L respectively. Error bars on each measurement are based on triplicate injections of each sample*

Appendix B: Blast Over-pressure Tables

0.5 kg AlAN Charges

Firing No.	Arrival time /ms	Positive duration /ms	Impulse area	Peak over-pressure /kPa
1	0.934	1.25	31.5	173
2	1.15	1.37	35.5	116
3	0.969	1.40	23.5	167
4	0.859	1.36	41.0	195
5	1.08	1.36	40.8	161
6	0.895	1.11	41.5	192
Mean	**0.981**	**1.31**	**35.6**	**167**
S.D.	0.112	0.110	7.13	28.6

Table B.1*: Sensor 1 (0.5 kg AlAN)*

Firing No.	Arrival time /ms	Positive duration /ms	Impulse area	Peak over-pressure /kPa
1	3.42	1.71	22.5	44.4
2	3.50	1.52	22.9	44.4
3	2.95	1.89	32.5	67.1
4	2.88	1.78	35.2	71.6
5	3.21	1.67	29.9	64.6
6	2.92	1.63	36.5	75.9
Mean	**3.15**	**1.7**	**29.9**	**61.3**
S.D.	0.27	0.116	6.04	13.7

Table B.2*: Sensor 2 (0.5 kg AlAN)*

Firing No.	Arrival time /ms	Positive duration /ms	Impulse area	Peak over-pressure /kPa
1	5.57	1.92	21.3	33.7
2	6.11	1.67	14.3	23.8
3	5.49	2.00	21.6	33.4
4	5.35	1.63	22.4	35.5
5	5.71	1.82	19.3	32.2
6	5.39	1.85	23.7	38.1
Mean	**5.60**	**1.82**	**20.4**	**32.8**
S.D.	0.28	0.130	3.33	4.86

Table B.3*: Sensor 3 (0.5 kg AlAN)*

Firing No.	Arrival time /ms	Positive duration /ms	Impulse area	Peak over-pressure /kPa
1	8.37	2.03	17.3	21.6
2	8.99	1.91	11.6	16.4
3	8.26	2.04	17.5	22.3
4	8.15	2.05	18.1	22.7
5	8.47	2.13	15.5	21.1
6	8.11	1.99	19.8	24.2
Mean	**8.39**	**2.03**	**16.6**	**21.4**
S.D.	0.322	0.0663	2.83	2.66

Table B.4*: Sensor 4 (0.5 kg AlAN)*

0.5 kg PE4 Charges

Firing No.	Arrival time /ms	Positive duration /ms	Impulse area	Peak over-pressure /kPa
1	0.517	0.763	81.0	366
2	0.408	0.872	52.1	366
3	0.481	1.06	54.2	533
4	0.553	1.20	64.3	461
5	0.444	0.876	79.6	560
6	0.481	1.24	57.9	590
Mean	**0.481**	**1.00**	**64.9**	**479**
S.D.	0.0513	0.194	12.7	97.6

Table B.5: *Sensor 1*

Firing No.	Arrival time /ms	Positive duration /ms	Impulse area	Peak over-pressure /kPa
1	2.26	1.53	52.6	117
2	2.15	1.60	53.3	108
3	2.30	1.56	53.2	126
4	2.30	1.60	51.9	120
5	2.22	1.53	52.8	123
6	2.41	1.56	53.8	119
Mean	**2.27**	**1.56**	**52.9**	**119**
S.D.	0.0876	0.0314	0.657	6.18

Table B.6: *Sensor 2*

Firing No.	Arrival time /ms	Positive duration /ms	Impulse area	Peak over-pressure /kPa
1	4.59	1.96	36.2	54.1
2	4.52	1.99	38.9	54.2
3	4.52	1.88	38.8	55.5
4	4.55	1.93	38.7	53.5
5	4.41	2.03	38.2	55.5
6	4.62	1.78	38.5	57.1
Mean	**4.54**	**1.93**	**38.2**	**55.0**
S.D.	0.0729	0.0889	1.02	1.31

Table B.7: *Sensor 3*

Firing No.	Arrival time /ms	Positive duration /ms	Impulse area	Peak over-pressure /kPa
1	7.20	2.04	28.3	34.7
2	7.06	2.25	30.4	37.3
3	7.09	2.22	30.0	36.0
4	7.09	2.25	30.0	35.3
5	6.98	2.26	30.2	36.9
6	7.13	2.21	30.4	36.7
Mean	**7.09**	**2.21**	**29.9**	**36.2**
S.D.	0.0731	0.0831	0.796	1.00

Table B.8: *Sensor 4*

Appendix C: Imaging

AlAN Firings

Figure C.1 displays GoPro video footage stills (a-f) of firing number 3 of the 0.5 kg AlAN charges and is representative of all 0.5 kg firings. Figure C.1a shows the point between triggering the detonation and the development of the fireball, during which the charge was intact upon the firing pole and the ground directly below a white/grey colour. The still was captured at *t* = '0.00' based on the GoPro footage which did not yield the real-time accuracy of HSI.

Figure C.1*: GoPro recording stills of a 0.5 kg AlAN charge showing the growth and movement of the smoke cloud following detonation between '0' and 2.13 seconds.*

Figure C.2 shows representative stills from the 0.5 kg AlAN firing HSI footage.

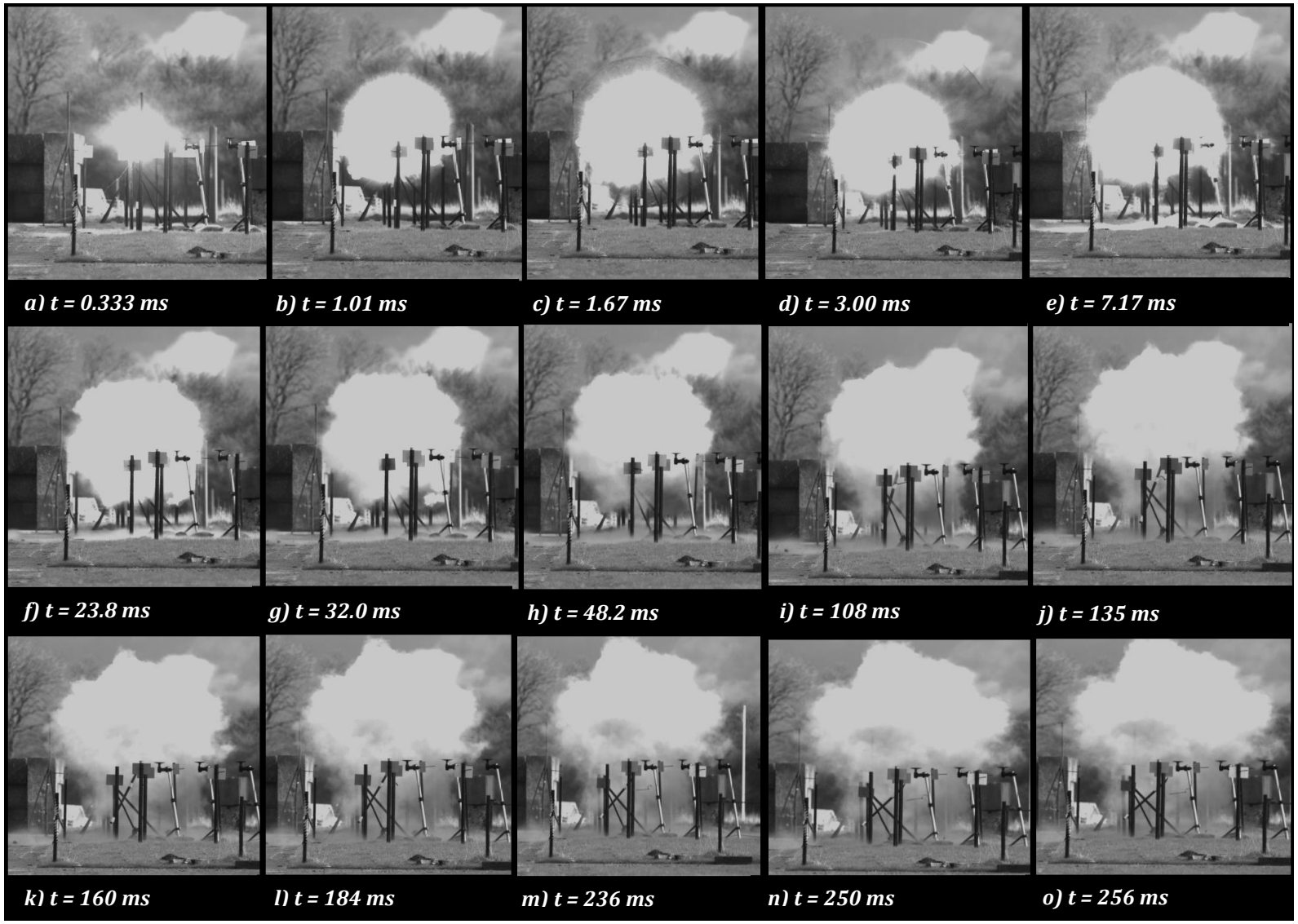

***Figure C.2**: Representative HSI footage stills of a 0.5 kg AlAN detonation showing the growth of the fireball (a-f) and subsequent smoke cloud (g-o).*

The detonation phases between t = 0.333 ms and t = 256 ms from a representative 0.5 kg AlAN detonation is shown in figure C.2. The blast wave was visible in stills b–d; within these frames, regions of speckled light in-between the fireball and blast wave were seen. The HSI showed the spherical nature of the fireball from one camera angle around the detonation centre; as the fireball grew through stills a–f in figure C.2 it impinged on the closest sampling sites 1 m from the detonation centre. The formation of the smoke between stills g–o showed the larger, more irregular shaped smoke cloud extending across sampling sites at least 4 m from the centre.

Figure C.3, comprised of stills a–o depicts the detonation phases of the 1 kg AlAN charge between t = 0.750 ms and t = 258 ms. Despite the near spherical shape of the charge mould, the fireball was not spherical but elongated vertically compared to the 0.5 kg charges, and this subsequently decayed into a more irregular and larger smoke cloud (C.3 m–o). The fireball extended across sample sites as far as 3 m from the charge centre (visible in C.3 h–i) and the smoke cloud further still to at least 5 m from the charge centre (C.3 o); both of which extended further than those produced from the 0.5 kg charges. Material ejected horizontally from the centre of the charge (equator region) was seen clearly in stills C.3 h–j and was in line with the 2 m high sampling plates.

***Figure C.3**: HSI footage stills of 1 kg AlAN detonation showing the growth of the fireball (a-j) and subsequent smoke cloud (k-o).*

RDX compositions

Figure C.4 displays video footage stills (a-f) of firing number 2 of the 0.5 kg PE4 charges and is representative of all 0.5 kg firings. Figure C.4a shows the spheroidal fireball, and is the earliest captured still (0.05 s) from the GoPro footage. Figure C.4b at 0.26 s shows the development of the fireball into smoke. Through stills c–f in figure C.4 the smoke cloud is seen to move past the north facing sites from the camera angle at t = 0.610 s to 3.82 s.

Figure C.4: *GoPro recording stills of a 0.5 kg PE4 charge showing the fireball and growth and movement of the smoke cloud following detonation between 0.05 s and 3.82 s.*

Figure C.5 shows the HSI footage stills from a representative 0.5 kg PE4 firing between t = 0.834 ms and t =350 ms.

Figure C.5: *Representative HSI footage stills of a 0.5 kg PE4 detonation showing the growth of the fireball (a-g) and subsequent smoke cloud (h-o)*

The blast wave was visible in stills C.5 b–e. Unlike that seen from the 0.5 kg AlAN HSI (figure C.3), no particulate matter was visible between the blast wave and fireball. The HSI showed the spherical nature of the fireball from one camera angle around the detonation centre; as the fireball grew through stills a–g it was seen to envelop sampling sites 1 m, 2 m and 3 m from the detonation centre. This was followed by the decay of the fireball (figure C.5; stills h–k) and the subsequent dispersion of the carbon rich smoke (figure C.5; stills l–o).

Figure C.6, comprised of stills a–o depicts the detonation phases of the 1 kg PE7 charge between t = 0.250 ms and 297 ms. Despite the near spherical shape of the charge mould, the subsequent fireball was not spherical as was the case for the 0.5 kg firings. The black carbon rim around the centre of the fireball, approximately at the charge height, (in stills c–e; 3.25 ms to 15.3 ms) was carbon. The fireball extended across sampling sites as far as 5 m from the charge centre (figure C.6 j) in the orientation visible through the camera angle. The smoke cloud was seen to have dispersed further still to 7 m from the detonation centre.

Figure C.7, comprised of stills a–o depicts the detonation phases of the 2 kg PE7 charge between t = 0.250 ms and 243 ms. Despite the near spherical shape of the charge mould, the fireball was not spherical, but more mushroom cloud shaped like that produced during the 1 kg charge firing. The black carbon rim around the centre of the fireball, approximately at the charge height, (in stills c–g of figure C.7) appeared to be carbon. The fireball extended across sampling sites further from the charge centre (figure C.7 h) in the orientation visible through the camera angle. The smoke cloud was larger than that produced following the 1 kg charge and extended across sample sites up to 10 m (figure C.7 o) away from the centre as well as vertically above the charge placement.

Figure C.6: *HSI footage stills of 1 kg PE7 detonation showing the growth of the fireball (a-i) and subsequent smoke cloud (j-o).*

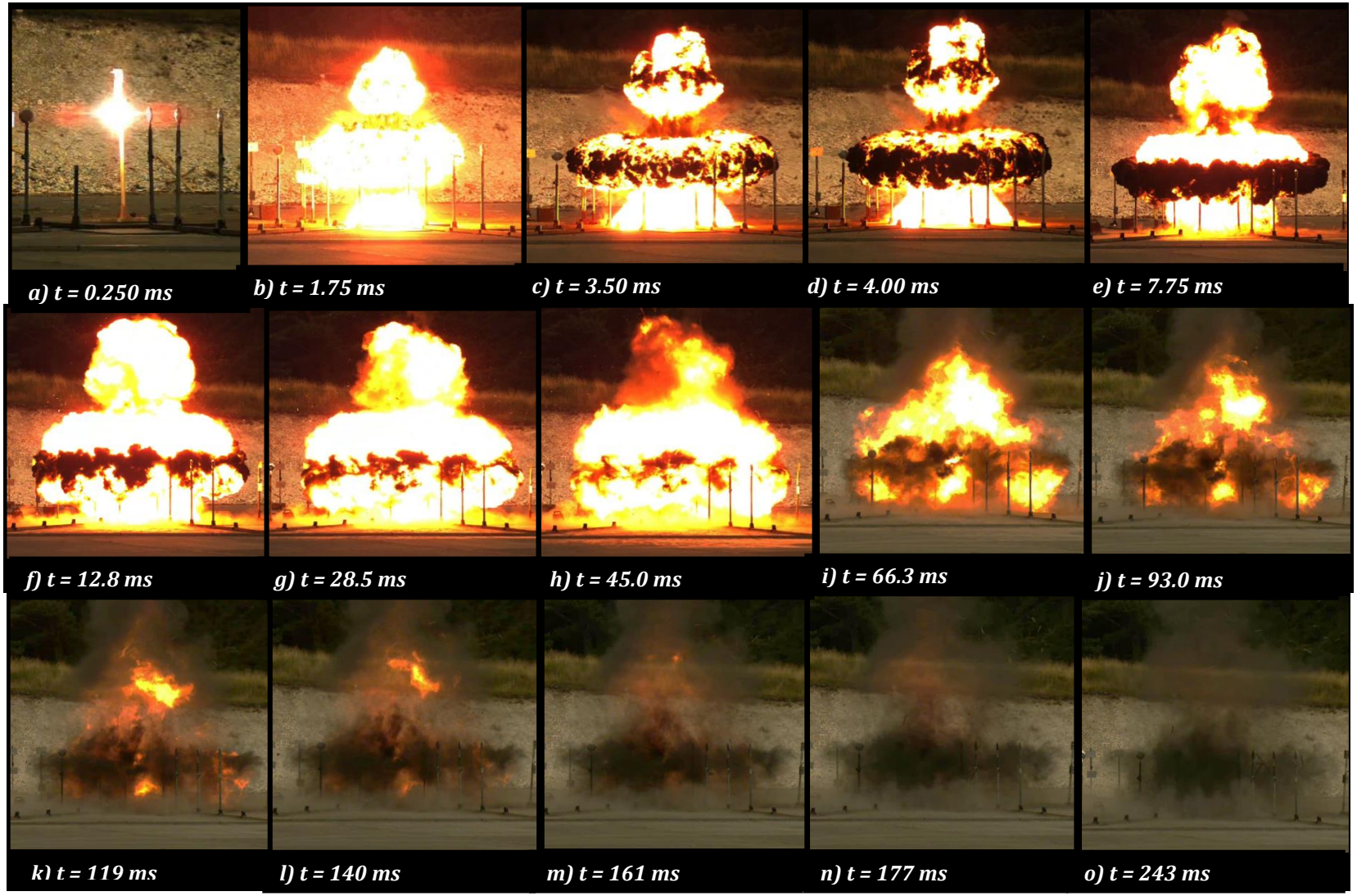

Figure C.7: *HSI footage stills of 2 kg PE7 detonation showing the growth of the fireball (a-h) and subsequent smoke cloud (i-o).*

Confined firings

Figure C.8 depicts the growth of the smoke around the vehicle during firing number 4, and its subsequent movement in the eastward direction. The smoke produced during all successful confined firings was grey.

Figure C.8*: Stills from real time video footage of car bomb firing number 4 between 0.80 s and 2.50 s. a) at time t = 0.80 s the firing had occurred and the smoke around the car was visible; b) at t = 1.20 s the plume had grown in size and engulfed the car and surrounding sample sites; c) and d) t = 1.70 s and 2.50 s, the plume was less dense and moving towards the east in line with the wind direction during firing.*